The Dissertation Committee for Bi-Qing For
certifies that this is the approved version of the following dissertation:

Probing Stellar Evolution Through Spectroscopy of Horizontal Branch Stars

Committee:

Christopher Sneden, Supervisor

Thomas G. Barnes III

Volker Bromm

Harriet Dinerstein

Robert Rood

J. Craig Wheeler

Probing Stellar Evolution Through Spectroscopy of Horizontal Branch Stars

by

Bi-Qing For, B.S., M.A.

DISSERTATION
Presented to the Faculty of the Graduate School of
The University of Texas at Austin
in Partial Fulfillment
of the Requirements
for the Degree of

DOCTOR OF PHILOSOPHY

THE UNIVERSITY OF TEXAS AT AUSTIN
August 2011

”If desire is your wishbone, then courage is your backbone. The successful person is the one who continually faces the problems and challenges that life brings and overcomes them all, no matter what the obstacle is.”

– Howard E. Ferguson

Acknowledgments

First of all, I would like to thank my supervisor, Chris Sneden, for sharing his precious time and knowledge. His great effort to explain things clearly and his patience in reading and helping with the journal manuscripts are greatly appreciated. It has been an honor to learn about stellar spectroscopy from him. I would also like to thank my committee members for their helpful comments and fruitful discussions.

For the RR Lyr work, I am in debt to George W. Preston, who shared his 2300+ spectra that he had collected over the past 4 years at the Las Campanas Observatory in Chile. This dissertation would not have been possible without these data. His ideas, comments on manuscripts and help on referee reports are much appreciated.

My time at the University of Texas was made enjoyable in large part due to the fellow graduate students and friends. I am grateful to have Amanda Heiderman, Hyo Jeong Kim, Randi Ludwig, Judith Mitchell and Melike Afsar for giving me support during the tough times; my officemate, Tim Weinzirl for solving the technical issues on my laptop and introduced me to Python; Amanda Bayless and John Barentine for the regular fun amazing P15 day; Ann Hsieh for taking care of my mail whenever I traveled down under.

I will never forget the person who has had a great impact in my career – my undergraduate research advisor, Betsy Green. I thank her for teaching me a lot about observing and giving me a chance to gain research experience as early as a freshman at the University of Arizona. Her inspiration on scientific projects related to hot subdwarf stars and constant support for my career in astronomy are much appreciated. It has been a truly enjoyable collaboration throughout the years.

Many thanks for the hospitality of CSIRO Astronomy and Space Science (CASS) during my numerous visits down under, especially for a financial support during June–August 2010. I would like to specially thank Bärbel Koribalski for giving me the Circinus galaxy project, which provided me a great opportunity to explore a different research field of astronomy that I had never been involved before. Her enthusiasm and fruitful discussions have inspired me in many ways.

I would also like to thank the staff at the McDonald observatory for cooking me good meals during my countless observing nights. A special thank go to Dave Doss for taking my late night calls when I encountered instrumental problems.

Most of all, I would like to thank my beloved husband, Tobias Westmeier, who encouraged me in every situation. This dissertation could not have been accomplished without him. His love and emotional support always comfort me in many ways. Without his understanding, I would not be able to finish my PhD here which is causing us to live apart for many years. Also, thanks to my parents who permitted me to study astronomy abroad, knowing that I most likely will not have a career back in Malaysia.

Finally, I would like to thank the generousity of Fritz Benedict for his approvals on conference travel support from Cox Funds and Sigma Xi grant-in-aid of research for supporting my observing trip to Las Campanas Observatory in Chile.

Probing Stellar Evolution Through Spectroscopy of Horizontal Branch Stars

Publication No. ____________________

Bi-Qing For, Ph.D.
The University of Texas at Austin, 2011

Supervisor: Christopher Sneden

This dissertation describes a new detailed abundance study of field red horizontal branch stars, RR Lyrae stars and blue horizontal branch stars. To carry out this study, we obtained high-resolution and high signal-to-noise ratio echelle spectra at the McDonald observatory and Las Campanas Observatory. In addition, new pulsational emphemerides were derived to analyze the spectra of RR Lyrae stars throughout the pulsational cycles. We find that the abundance ratios are generally consistent with those of field stars of similar metallicity in different evolutionary stages and throughout the pulsational cycles for RR Lyrae stars. We also estimated the red and blue edges of the RR Lyrae instability strip using the derived effective temperatures of RHB and BHB stars. New variations between microturbulence and effective temperature are found among the HB population. For the first time the variation of microturbulence as a function of phase is empirically shown to be similar to the theoretical calculations. Finally, through the study of a rare eclipsing sdB and M dwarf binary, we discovered an unusually low mass for this type of HB star, which observationally proved the existence of a new group of low-mass sdB stars that was theoretically predicted in the past.

Table of Contents

Chapter 1

Introduction: Physical Properties and Evolutionary Status of Horizontal Branch Stars

Horizontal branch (HB) stars are evolved objects that are fusing helium in their cores (Hoyle & Schwarzschild 1955). As low-mass main sequence stars age, they first ascend the red giant branch (RGB), undergo an internal helium-flash (losing some of their mass somewhere along the RGB), and finally take up residence on the HB while they complete their helium consumption. The helium core mass is relatively constant in all types of HB stars ($\sim 0.5\ M_{\odot}$), but they have a large range of hydrogen envelope masses.

HB stars are commonly found in globular clusters (GCs), as well as in field disk and halo populations of our Milky Way. They exhibit a range of photometric colors (or temperatures) which the distribution is known as the HB morphology. The distribution can be divided into several groups:

- Red horizontal branch (RHB) stars, which are all HBs cooler than the instability strip (IS).
- RR Lyraes (RR Lyr), named after their prototype. These are variable stars with intermediate temperature and color, located in the IS.
- Blue horizontal branch (BHB) stars, which are hotter than the RR Lyr IS. Their temperatures range from 8000–20,000 K, which is also sub-

divided into HBA ($T_{\rm eff}$ < 10,000 K) and HBB stars ($T_{\rm eff}$ > 10,000 K) (Möhler 2004). This subdivision corresponds roughly to A and B spectral types.

- Extreme horizontal branch (EHB) stars, which are hotter extension of HB. These stars often lie below the main sequence in the Hertzsprung-Russell diagram, and thus they are also referred to as hot subdwarfs. This group is subdivided into sdB (20,000 K $\lesssim T_{\rm eff} \lesssim$ 32,000 K), sdOB (32,000 K $\lesssim T_{\rm eff} \lesssim$ 40,000 K), and sdO stars (40,000 K $\lesssim T_{\rm eff} \lesssim$ 70,000 K) (see review by Heber 2009 for detailed classification of the hot subdwarfs).

Most horizontal branch studies are conducted in globular clusters (GCs), which provide a complete range of stellar population. In these studies, the assignment of a star to a particular HB group is based on color (or proxy for temperature), but the physical cause that determines the position could be affected by multiple parameters and is not easy to solve. Metallicity, also referred to as the first parameter, suggested by Sandage & Wallerstein (1960), certainly has an influence on the redundant of HB morphology as seen in the GCs. Metal-rich clusters have mostly RHB stars and metal-poor clusters have mostly BHB and/or EHB stars. However, this is not the full story of the HB morphology. Globular clusters that possess similar metallicity often exhibit different HB morphologies. For example, the color-magnitude diagrams of the pair M3 and M13 ([Fe/H]~ -1.34) (see Rosenberg et al. 2000) clearly indicate that HB morphology is influenced by other parameter(s). This is referred as second parameter(s) problem in the literature.

The early study of Searle & Zinn (1978) suggested that the cluster age could be the second parameter, but later investigation by, e.g, Peterson et al.

(1995) and Behr (2003a) argued that stellar rotation could also be a significant contributor. Alternative explanations, such as different CNO abundances (Rood & Seitzer 1981), mixing and helium abundance (Sweigart 1997), central concentration of the cluster (Fusi Pecci et al. 1993), and Na–O anticorrelation (Gratton et al. 2007) also have been proposed. Lee et al. (1994) demonstrated that various second parameters can produce different HB morphologies. To what extent these potential second parameters influence the variety of observed HB distributions in GCs remains an open question.

While cluster HB stars have been useful for studying the HB morphology, they are faint and hard to observe. On the other hand, field horizontal branch (FHB) stars are significantly brighter than cluster stars and and could be useful in many aspects. In the following sections, we describe the role of HB stars in studies of Galactic structure and formation, and the initiative of carrying out the chemical abundances study of HB stars.

1.1 Horizontal Branch Stars as Tracers in Studies of Galactic Structure

The current cold dark matter (CDM) cosmological model suggests that the formation of galaxies is via hierrachical merging, with smaller galactic systems merging to form the massive galaxies that we see today. Evidence of such cannabalism and hierrachical assembly are observed in our Milky Way halo, such as the tidal Sagittarius stream (Ibata et al. 1994) and numerous dwarf galaxies.

Recent large surveys, such as the Sloan Digital Sky Survey (SDSS, York et al. 2000), have improved our understanding of the Galactic structure with the discoveries of a large population of faint Local Group dwarf galaxies and stellar streams. Horizontal branch stars play an important role in these discoveries; in particular they are used to trace the spatial and kinematic distribution of the old stellar populations of the Galactic disk and halo components (see e.g., Ivezić et al. 2004; Vivas et al. 2004).

Field horizontal branch stars blueward of instability strip (i.e., HBB stars), which are brighter than those in the streams, are excellent tracers of old stellar populations due to their unique properties. The prominent Balmer lines as seen in their spectra can be used to derive accurate radial velocities and physical parameters (i.e., T_{eff} and log g). They can also easily be identified via photometric color from intermediate to high Galatic latitude. Unlike RHB, HBA and RR Lyrae stars, their absolute magnitudes are not influenced by the metallicity effects.

Field RR Lyrae stars are also a suitable as tracers. Their variability makes them very easy to be identified. However, they are less numerous than other HB populations.

1.2 Metal-Poor Stars as Tracers in Studies of Galactic Chemical Evolution

The early chemical evolution of the Milky Way involves mixing and continuous exchange of material between stars and the interstellar medium (ISM). The study of different elemental abundance ratios not only traces the Galaxy's enrichment history, but also provides rich information about the Galaxy's formation and the origin of our Galaxy's multi-component structure (e.g., thin disk and thick disk). Chemical compositions of the oldest low-mass metal-poor stars is particularly important because nearly all of their elements are not produced internally but inherited from the nucleosynthesis output of early massive Galactic supernova explosions in situ.

Metal-poor stars have chemical compositions that are enriched in the α-elements (e.g., Mg, Si, S, Ca and possibly Ti). These elements are overabundant as compared to the Fe-peak elements, i.e. $[\alpha/\mathrm{Fe}] \approx 0.2$. A ready explanation for the normal α-rich behavior of metal-poor halo stars begins with the presumed predominance of short-lived massive stars that resulted in core collapse type II supernovae (SNe II) in the early Galactic time. The resulting explosions contributed large amounts of light α-elements (e.g., O, Ne, Mg and Si), smaller amounts of heavier α-elements (e.g., Ca and Ti) and small amounts of Fe-peak elements to the ISM (Woosley & Weaver 1995). The detonation of neutron-rich cores is alleged to produce heavier isotopes through rapid neutron-capture nucleosynthesis (r-process) where synthesis occurs faster than the β-decay. By contrast, longer-lived, lower-mass stars begin to contribute their ejecta by adding more Fe-peak elements through type Ia supernovae (SNe Ia) which exploded due to the thermonuclear runaway process of accreting binary stars. The asymptotic giant branch (AGB) stellar wind contributes isotopes for slow neutron-capture nucleosynthesis (s-process) at later Galactic times. Large amount of iron pollutes the ISM and lowers the α/Fe at higher metallicity, i.e. $[\mathrm{Fe/H}] \simeq -1$.

In the past decades, the studies of chemical compositions of metal-poor stars have been concentrated on the low-mass F and G dwarfs, giants and subgiants. There are only a handful of detailed abundance studies of metal-poor FHB stars to date. Since horizontal branch stars are sensitive to the composition and structure of main-sequence stars prior to the exhaustion of their hydrogen fuel (Behr 2003b), they presumably can be used as an additional tracer for studying the Galactic chemical evolution. This may be interesting:

Are their chemical abundances similar to other metal-poor stars? Do they exhibit any chemical anomalies? Can we derive consistent chemical abundances throughout the pulsational cycle of RR Lyrae stars?

1.3 Overview

In this dissertation, we present first detailed chemical abundance study of field horizontal branch stars that span an effective temperature range of 4000 K. In chapter 2, we present a new compiled line list that is suitable for analyzing the chemical abundances of HB stars in this T_{eff} range. Chemical abundance ratios of non-variable red and blue field horizontal branch [1] stars are examined and compared to similar metallicity field stars in different evolutionary stages. In Chapter 3, we provide the radial velocity information of the RR Lyrae stars in our program and describe the methods of deriving their ephemerides, which are needed for performing the subsequent chemical abundance analysis. Chapter 4 describes the methodologies of determining chemical abundances of RR Lyrae stars throughout the pulsational cycle and the results are presented. Chapter 5 provides an introduction to the methodologies and data production of a medium-resolution survey to identify a larger sample of field horizontal branch and main-sequence A-type stars. We present the discovery of an unusual low-mass, rare reflection effect sdB and M dwarf binary system in chapter 6. Finally, chapter 7 considers the future outlook of this field.

---

[1] In chapter 2 of this dissertation, we analyzed only the HBA stars, referring to them collectively as BHB stars

Chapter 2

The Chemical Compositions of Non-Variable Red and Blue Field Horizontal Branch Stars

2.1 Introduction

Chemical abundance studies of GCs provide ideal laboratories for testing predictions of stellar evolution and nucleosynthesis [1]. Unfortunately, HBs in GCs are faint and as such, hard to observe at high spectral resolution. On the other hand, field horizontal branch (FHB) stars are significantly brighter than cluster stars, and could be useful in many aspects. For example, FHB stars have been used as tracers of Galactic structure (see Wilhelm et al. 1996; Altmann 2000). In addition, field RR Lyrae stars (easy to identify from their variability) yield important information on stellar evolution and pulsation. Their absolute magnitudes and metallicities provide powerful constraints on synthetic HB models (see Cassisi et al. 2004; Demarque et al. 2000).

While FHB kinematics have been widely used to study Galactic structure, their chemical compositions have received scant attention. There are only a handful of detailed abundance studies of FHB stars to date (see Adelman & Hill 1987; Adelman & Philip 1990; Lambert et al. 1996). Behr (2003b) conducted a rotational velocity study of FHB stars, with only the derivation of Mg abundances for all HB stars. He performed a more extensive chemical

---

[1] Significant portions of this chapter have been published previously in For, B.-Q. & Sneden, C. 2010, AJ, 140, 1694.

abundance study for BHB stars in GCs (Behr 2003a). A recent large survey of FHB stars was carried out by Preston et al. (2006a), but their sample was limited to very metal-poor RHB stars ([Fe/H] < -2) that were selected from the HK objective-prism survey. Their primary objectives were to investigate any abundance anomalies in these stars, and to derive the fundamental $T_{\rm eff}$ red edge of the metal-poor RR Lyr IS. They concluded that: (a) FRHB stars generally possess normal enhancements of α-elements; (b) there is a [Si/Fe] dependence on $T_{\rm eff}$ which is unrelated to nucleosynthesis issues; (c) [Mn/Fe] is subsolar; and (d) the n-capture elements have large star-to-star relative abundance scatter. They also derived the temperature of the red edge of the metal-poor RR Lyr IS, by interfacing the temperature distributions of field metal-poor RHB and RR Lyr stars with stars of similar metallicities in globular clusters.

In this chapter, we present the first detailed abundance study of field RHB and BHB stars. We explore possible abundance anomalies and their implications for HB evolution. This work potentially can provide a different point of view toward understanding HB morphology, and results should aid in application of HB chemical compositions to stellar stream investigations. §2.2 describes the target selection and interstellar reddening. The observations and reduction are given in §2.3. In §2.4 and 2.5, we present the line list compilation, equivalent width measurements and analysis methods. The results of individual elemental abundances and evolutionary states of HB stars are given in §2.6 and §2.7. We discuss the implication of several elemental abundances of our HB samples in §2.8. Lastly, we summarize the results of this work in §2.9.

2.2 Target Selection and Reddening

The observed targets for this program were selected from Behr (2003b). That paper contains a compilation of known FHB stars that he used for his rotational velocity study. We selected the FHB stars that have $V < 11$, [Fe/H] ≤ -1.2 and $T_{\mathrm{eff}} < 9000$ K. The temperature restriction was chosen to avoid abundance anomalies due to gravitational settling and diffusion processes that are observed in the hotter BHB stars (e.g, Behr 2003a). RR Lyr stars were deliberately excluded in this program; a companion study of their chemical compositions will be presented in chapter 4.

We also included metal-poor field red horizontal branch (MPFRHB) stars studied by Preston et al. (2006a) in our program. We did not re-observe the MPFRHB stars, but we analyzed them in a manner consistent with that of the newly observed targets. We refer the reader to the description of target selection and observational details in Preston et al. (2006a). Table 2.1 gives basic information for our program stars.

Reddening estimates $E(B-V)$ of individual stars were obtained from the NASA/IPAC Extragalactic Database[2] (NED) extinction calculator. This technique is based on the *Infrared Astronomical Satellite* (IRAS) and *Diffuse Infrared Background Experiment* (DIRBE) measurements of dust IR emission maps of Schlegel et al. (1998) (hereafter SFD). We chose this method in preference to the older Burstein & Heiles (1982) maps, which are based on H I 21-cm column density and galaxy counts, because the H I maps suffer from the general problem of saturation in the 21-cm line in high extinction regions and have lower spatial resolution than the SFD maps.

---

[2] http://nedwww.ipac.caltech.edu/forms/calculator.html

Some uncertainties in $E(B-V)$ values estimated from the SFD maps might arise from missing cold dust that is not detected by IRAS. In fact, $E(B-V)$ values determined from SFD are systematically larger by $\sim$0.02 mag as compared to those of Burstein & Heiles (1982) (e.g., see comments in Meléndez et al. 2006 and references therein). The Burstein & Heiles (1982) maps are not error free. In fact, their maps contain systematic effects that arises from fluctuations in galaxy counts and variations in gas-to-dust ratio. To be consistent and to reduce the degree of systematic effects in our analysis, we only adopted extinctions from SFD maps. To correct these systematic effects of SFD maps, we used a 10 % correction factor as suggested by Meléndez et al.:

$$cE(B-V) = 0.9E(B-V) - 0.01, \tag{2.1}$$

where $cE(B-V)$ is the corrected $E(B-V)$. We employed the corrected $E(B-V)$ for calculating the photometric $T_{\rm eff}$, which we used to compare with our independent spectroscopic $T_{\rm eff}$ values. The details will be given in §2.5.1.

Table 2.1. Program stars.

Star	R.A.(J2000) (hr m s)	Decl.(J2000) (° ′ ″)	$B^{\rm a}$ (mag)	$V^{{\rm a},b}$ (mag)	$J^{\rm c}$ (mag)	$H^{\rm c}$ (mag)	$K_s{}^{\rm c}$ (mag)	$B-V$ (mag)	$V-K$ (mag)	E$(B-V)^{\rm d}$ (mag)	cE$(B-V)$ (mag)
RHB											
HD 6229	01 03 36.5	+23 46 06.4	9.31	8.60	7.088	6.646	6.575	0.71	2.025	0.034	0.021
HD 6461	01 05 25.4	−12 54 12.1	8.4	7.65	6.149	5.676	5.587	0.75	2.063	0.025	0.013
HD 25532	04 04 11.0	+23 24 27.1	8.85	8.24	6.688	6.327	· · ·	0.61	1.057	0.191	0.162
HD 105546	12 09 02.7	+59 01 05.1	9.4	8.61	7.152	6.756	6.674	0.79	0.980	0.022	0.010
HD 119516	13 43 26.7	+15 34 31.1	9.52	9.13	7.771	7.431	7.366	0.39	1.764	0.031	0.018
BD+18° 2890	14 32 13.5	+17 25 24.3	10.49	9.77	8.241	7.837	7.744	0.72	2.026	0.020	0.008
BD+11° 2998	16 30 16.8	+10 59 51.7	9.70	9.07	7.619	7.271	7.185	0.63	1.885	0.057	0.041
BD+09° 3223	16 33 35.6	+09 06 16.3	9.81	9.25	7.760	7.335	7.277	0.56	1.007	0.076	0.058
BD+17° 3248	17 28 14.5	+17 30 35.8	9.99	9.37	7.876	7.391	7.338	0.62	0.956	0.059	0.043
HD 184266	19 34 15.4	−16 19 00.2	8.16	7.57	6.252	5.913	5.830	0.59	1.740	0.142	0.118
HD 229274	20 24 36.1	+41 30 02.6	9.63	9.06	7.622	7.288	7.213	0.57	1.847	· · ·	· · ·
CS 22882−001	00 20 25.3	−31 39 04.0	15.22	14.82	13.677	13.362	13.317	0.40	1.503	0.018	0.006
CS 22190−007	03 52 21.7	−16 24 30.0	14.66	14.20	13.059	12.706	12.656	0.46	1.544	0.031	0.018
CS 22186−005	04 13 09.1	−35 50 38.7	13.33	12.96	11.902	11.625	11.581	0.37	1.379	0.012	0.001
CS 22191−029	04 47 42.2	−39 07 26.0	14.46	14.05	12.947	12.646	12.614	0.41	1.436	0.019	0.007
CS 22883−037	14 24 19.4	+11 29 25.0	15.28	14.73	13.733	13.425	13.378	0.55	1.352	0.028	0.015
CS 22878−121	16 47 50.1	+11 39 12.0	14.53	13.99	12.620	12.288	12.169	0.54	1.821	0.043	0.029
CS 22891−184	19 26 12.5	−60 34 09.0	14.33	13.83	12.574	12.274	12.187	0.50	1.643	0.070	0.053
CS 22896−110	19 35 48.0	−53 26 17.0	14.09	13.56	12.180	11.791	11.780	0.53	1.780	0.060	0.044
CS 22940−077	20 41 33.5	−59 50 36.0	14.66	14.13	12.679	12.300	12.220	0.53	1.910	0.070	0.053
CS 22955−174	20 42 05.0	−23 49 12.7	14.88	14.38	13.179	12.843	12.770	0.50	1.610	0.049	0.034
CS 22940−070	20 42 39.2	−61 40 41.0	15.35	14.87	13.686	13.368	13.312	0.48	1.558	0.056	0.040
CS 22879−103	20 47 10.1	−37 26 52.6	14.79	14.30	13.095	12.747	12.661	0.49	1.639	0.044	0.030
CS 22879−097	20 48 46.6	−38 30 49.4	14.68	14.22	13.031	12.684	12.617	0.46	1.603	0.048	0.033
CS 22940−121	20 55 10.8	−58 00 54.0	14.71	14.16	12.738	12.339	12.267	0.55	1.893	0.053	0.038
CS 22898−043	21 10 36.8	−21 44 51.8	14.49	14.06	12.909	12.674	12.650	0.43	1.410	0.050	0.035
CS 22937−072	21 14 40.6	−37 24 51.8	14.55	14.02	12.646	12.301	12.221	0.53	1.799	0.040	0.026
CS 22948−006	21 33 17.7	−39 39 42.8	15.56	15.07	13.774	13.405	13.334	0.49	1.736	0.030	0.017
CS 22944−039	21 45 12.2	−14 41 22.0	14.85	14.30	12.976	12.616	12.500	0.55	1.800	0.049	0.034
CS 22951−077	21 57 53.4	−43 08 06.0	14.11	13.61	12.258	11.944	11.845	0.50	1.765	0.016	0.004

Table 2.1 (cont'd)

Star	R.A.(J2000) (hr m s)	Decl.(J2000) (° ′ ″)	B^{a} (mag)	$V^{\mathrm{a},b}$ (mag)	J^{c} (mag)	H^{c} (mag)	$K_s{}^{\mathrm{c}}$ (mag)	$B-V$ (mag)	$V-K$ (mag)	E$(B-V)^{\mathrm{d}}$ (mag)	cE$(B-V)$ (mag)
CS 22881−039	22 09 35.4	−40 25 51.2	15.52	15.12	13.915	13.746	13.646	0.40	1.474	0.014	0.003
CS 22886−043	22 22 33.9	−10 14 11.0	15.18	14.72	13.564	13.247	13.178	0.46	1.542	0.047	0.032
CS 22875−029	22 29 25.1	−38 57 47.5	14.08	13.68	12.584	12.298	12.267	0.40	1.413	0.013	0.002
CS 22888−047	23 20 19.9	−33 45 46.9	15.01	14.61	13.460	13.194	13.127	0.40	1.483	0.019	0.007
CS 22941−027	23 34 58.1	−36 52 05.7	14.40	14.05	13.060	12.721	12.747	0.35	1.303	0.016	0.004
CS 22945−056	23 53 19.8	−65 29 41.0	14.485	14.09	12.984	12.692	12.616	0.40	1.474	0.020	0.008
BHB											
HD 2857	00 31 53.8	−05 15 42.9	10.12	9.95	9.481	9.354	9.323	0.17	0.627	0.041	0.027
HD 8376	01 23 28.3	+31 47 12.3	9.72	9.59	9.248	9.163	9.130	0.13	0.460	0.051	0.036
HD 252940	06 11 37.3	+26 27 30.1	9.4	9.096	8.440	8.371	8.302	0.30	0.794	···	···
HD 60778	07 36 11.8	−00 08 15.6	9.19	9.12	8.746	8.662	8.666	0.07	0.454	0.104	0.084
HD 74721	08 45 59.3	+13 15 48.7	8.76	8.71	8.521	8.525	8.522	0.05	0.188	0.031	0.018
HD 86986	10 02 29.6	+14 33 25.2	8.11	8.01	7.610	7.499	7.499	0.10	0.511	0.031	0.018
HD 87047	10 03 12.7	+31 03 19.0	9.86	9.72	9.309	9.251	9.214	0.14	0.506	0.019	0.007
HD 93329	10 46 36.6	+11 11 02.9	8.86	8.76	8.475	8.399	8.416	0.10	0.344	0.029	0.016
HD 109995	12 38 47.6	+39 18 31.6	7.643	7.598	7.304	7.317	7.265	0.04	0.333	0.017	0.005
BD+25° 2602	13 09 25.6	+24 19 25.1	10.18	10.14	9.877	9.844	9.800	0.04	0.340	0.017	0.005
HD 161817	17 46 40.6	+25 44 57.0	7.123	6.988	6.413	6.339	6.290	0.14	0.698	0.093	0.074
HD 167105	18 11 06.3	+50 47 32.4	8.97	8.93	8.743	8.748	8.735	0.04	0.195	0.049	0.034

[a] SIMBAD. http://simbad.u-strasbg.fr/simbad/

[b] Beers et al. (1992).

[c] 2MASS All-Sky Point Source Catalog (Skrutskie et al. 2006). http://tdc-www.harvard.edu/catalogs/tmpsc.html

[d] Nasa/IPAC extragalactic database.

2.3 Observations and Reductions

The observations were made with the McDonald 2.7-m Smith telescope, using the "2dcoudé" cross-dispersed echelle spectrograph. We used this instrument with a 1.2″ slit and in its "cs23-e2" configuration; it gives a 2-pixel resolving power of $R \equiv \lambda/\Delta\lambda \sim 60,000$ with spectra projected onto a Tektronix 2048 × 2048 CCD chip with no binning. The total wavelength range is $\sim 3700 - 8200$ Å with complete spectral coverage for $\lambda < 5900$ Å, and with gaps in coverage increasing toward the red. We usually integrated on the target stars for 1.5 hr, yielding S/N per resolution element of ~ 70 near 4000 Å, ~ 140 near 5000 Å, and ~ 240 near 7000 Å. The typical seeing for our observing runs varied from 1.5″ to 2.2″. Our observations in 2007–2008 were taken in conjunction with another project, for which we positioned the grating so that more red portion of the spectrum was projected onto the CCD. This resulted in sacrificing some useful blue-spectral echelle orders, which meant that there were fewer lines available for analysis. Optimal spectral coverage was obtained for observing run in 2009.

ThAr comparison lamp exposures were taken at the beginning and the end of each night. We also took the spectra of hot, rapidly rotating, relatively featureless stars throughout the night at different airmasses. These spectra were used to aid in removing telluric features from the spectra of our program stars. Table 2.2 summarizes the observations and stars that are listed but lack sufficient numbers of detected Fe I & Fe II lines for stellar parameter estimations were excluded from abundance analysis.

We performed reductions of the spectra with the IRAF[3] ECHELLE

---

[3] The Image Reduction and Analysis Facility, a general purpose software package for as-

package. The raw data were bias, flat-field, and scattered-light corrected, then extracted to one-dimensional spectra and wavelength-calibrated in standard fashion. The wavelength calibration arc identification was based on the line list in the IRAF package data file (thar.dat) and the Th-Ar wavelength table for the 2dcoudé spectrograph (Allende Prieto 2001). The individual wavelength-corrected spectra were then average combined into a single spectrum.

Subsequently, we used the SPECTRE[4] (Fitzpatrick & Sneden 1987) code to normalize the spectra and to remove cosmic rays contamination from the spectral lines. Figure 2.1 shows typical normalized spectra of RHB and BHB stars. Several of the hotter BHB stars exhibit significant rotational broadening.

2.4 Line List and Equivalent Width Measurements

We compiled an input line list of various elements from previous studies on HB stars (i.e., Preston et al. 2006a,b; Hubrig et al. 2009; Khalack et al. 2007, 2008; Clementini et al. 1995 & Lambert et al. 1996). Species such as Si II and Ca II have been included in past HBB studies, but to our knowledge this is the first use of these species for RHB and BHB analysis. Excitation potentials (E.P.) and laboratory oscillator strengths ($\log gf$) are extracted from various sources, which we cite in Table 2.3.

For each star, we measured the equivalent widths (EWs) of unblended atomic absorption lines interactively with SPECTRE. We either adopted the

---

tronomical data, is written and supported by the IRAF programming group of the National Optical Astronomy Observatories (NOAO) in Tucson, AZ.

[4] An interactive spectrum measurement package, available at http://verdi.as.utexas.edu/spectre.html

Table 2.2. Observation Log.

Star	UT Date	No. Integration	t_{exp} (s)	S/N at 7000Å	S/N at 5000Å	S/N at 4000Å	Comments
BD+09° 3223	30 Jun 2007	3	1800	223	230	95	1
BD+11° 2998	01 Jul 2007	3	1800	230	128	88	1
BD+18° 2890	02 Jul 2007	3	1800	210	124	30	1
HD 180903	02 Jul 2007	3	1800	210	88	40	1,4
HD 229274	02 Jul 2007	3	1800	320	147	100	1
HD 119516	03 Jul 2007	3	1800	320	132	60	1
HD 184266	04 Jul 2007	2	900	360	140	75	1
BD+17° 3248	04 Jul 2007	2	1800	280	108	66	1
HD 252940	20 Feb 2008	3	1800	188	135	63	1
HD 117880	21 Feb 2008	3	1800	196	96	86	1,3
HD 60778	21 Feb 2008	4	1×1200, 1×1800	200	125	64	1
HD 87112	21, 22 Feb 2008	5	1800	250	112	56	1,3
HD 25532	22 Feb 2008	3	1800	247	235	122	1
HD 82590	23 Apr 2008	4	900	226	103	66	1,3
BD+25° 2602	24 Feb 2008	4	1800	176	70	45	1
BD+42° 2309	24 Feb 2008	4	1800	134	100	64	1,3
HD 86986	11 Apr 2009	4	2×1200, 2×1800	226	164	79	2
HD 109995	11 Apr 2009	4	3×1200, 1×870	370	124	72	2
HD 74721	11 Apr 2009	4	1×1200, 3×1800	200	156	86	2
HD 161817	11 Apr 2009	4	1200	430	270	73	2
HD 167105	11, 13 Apr 2009	4	3×1800, 1×2400	260	162	67	2
HD 93329	13 Apr 2009	5	1×1000, 3×2400	290	109	163	2
HD 87047	14 Apr 2009	3	2400	150	96	67	2
HD 105546	14 Apr 2009	4	3×1800, 1×1400	250	190	70	2
HD 8376	06 Oct 2009	3	1800	200	105	67	2
HD 2857	08, 09 Oct 2009	4	3×1800, 1×1000	170	100	34	2
HD 6229	09 Oct 2009	3	1200	200	166	74	2

[1] The echelle grating was blazed to obtain more red portion of the spectrum. See text for explanation.

[2] The echelle grating was blazed to obtain optima red and blue portion of the spectrum.

[3] Initial analysis was performed. Stellar parameters cannot be obtained due to the lack of measurable Fe I or Fe II lines. Excluded from this study.

[4] RR Lyr, excluded from this study.

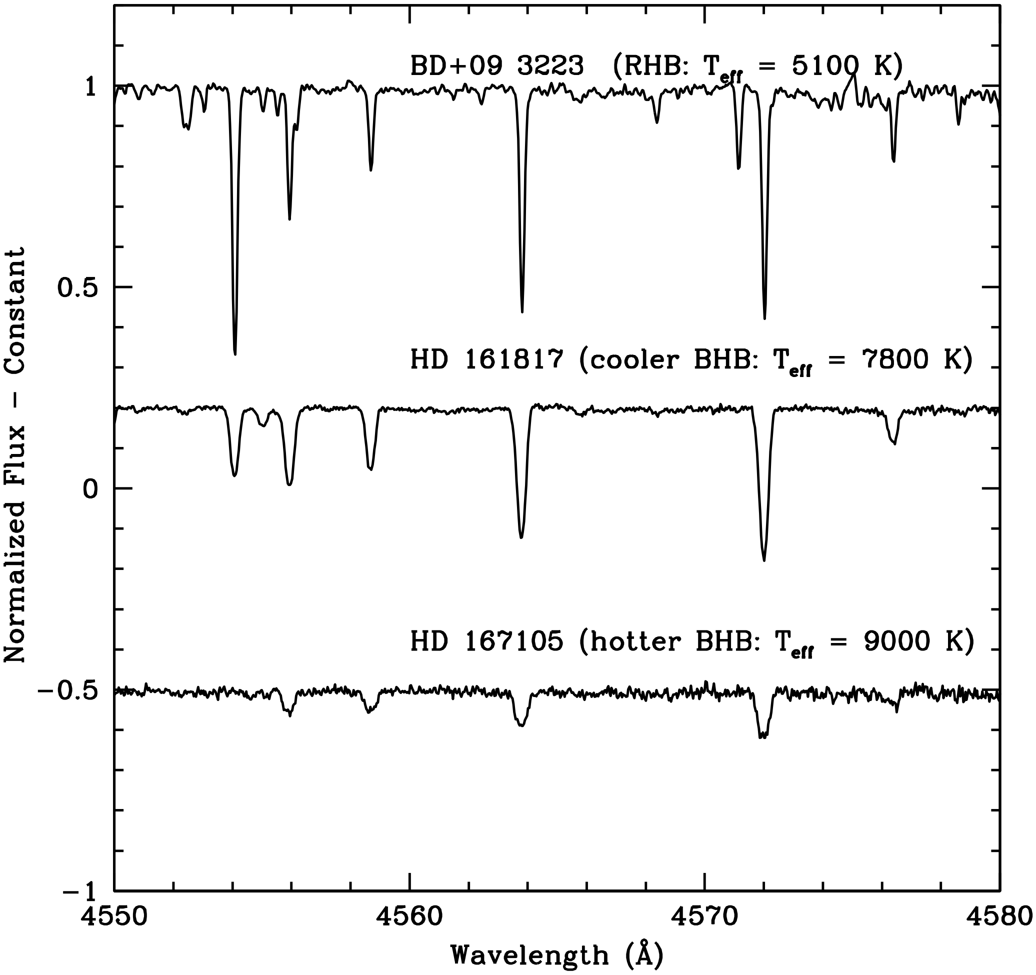

Figure 2.1 Typical reduced, normalized spectra of RHB and BHB stars obtained at McDonald 2.7 m telescope. Large rotational velocity is seen in hotter BHB stars.

EW value given by fitting a Gaussian to the line profile or by integrating over the relative absorption across a line profile. If a particular line was contaminated by cosmic rays or had an obviously distorted profile (especially lines in BHB stars can be blended with nearby lines due to rotational broadening), we excluded it. Very strong lines on the damping portion of the curve-of-growth (defined as those with reduced widths $\log \mathrm{RW} \equiv \log \mathrm{EW}/\lambda \gtrsim -4.0$) are relatively insensitive to abundance, and thus were not measured here. After initial trials, we also excluded very weak lines (EW < 5 mÅ) because the EW measurement errors were too large. Since our program stars have a wide range of T_{eff} and metallicity, the number of lines measured varied considerably. The lines used for each star, along with species, E.P., $\log gf$, its associated references, and measured EWs are listed in Table 2.3.

We may compare our EW measurements of stars with existing previous studies. Only a few high-resolution, detailed chemical abundance investigations of field BHB stars have been conducted to date. The only published iron EW measurements are from Adelman & Hill (1987) and Adelman & Philip (1990), which were measured on coudé spectrograms recorded with photographic plates. Figures 2.2–2.4 show the comparison of Fe I & Fe II EW measurements in four stars. The literature data for the cooler (CS 22951−077) and hotter (CS 22941−027) MPFRHB stars are from Preston et al. (2006a) and those for the two BHB stars (HD 161817 & HD 109995) are from Adelman & Hill (1987). Taking the EW measurements difference between Preston et al. (2006a), Adelman & Hill (1987) and this study (as shown in Figures 2.2–2.4), we find: for CS 22951−077, $\Delta\mathrm{EW} = 1.3 \pm 0.3$ mÅ, $\sigma = 2.7$ mÅ, 82 lines; for CS 22941−027, $\Delta\mathrm{EW} = 1.0 \pm 0.4$ mÅ, $\sigma = 2.7$ mÅ, 37 lines; for HD 161817, $\Delta\mathrm{EW} = -2.3 \pm 0.8$ mÅ, $\sigma = 4.4$ mÅ, 32 lines; and for HD 109995, ΔEW

Table 2.3. Equivalent width measurements of program stars.

Wavelength (Å)	Species	E.P. (eV)	$\log gf$	Ref.	EW (mÅ)
		HD 6229			
5682.63	Na I	2.102	−0.71	1	49
5688.19	Na I	2.104	−0.46	1	···
5339.93	Fe I	3.266	−0.72	1	101
5341.02	Fe I	1.608	−1.95	1	141
.	.	.	.	.	.
.	.	.	.	.	.
.	.	.	.	.	.

Note. — Table 2.3 is published in its entirety in the electronic edition of For & Sneden (2010). A portion is shown here for guidance regarding its form and content.

$= -2.4 \pm 1.3$ mÅ, $\sigma = 5.3$ mÅ, 16 lines. We only compute the EW difference of lines with EW < 75 mÅ in BHB stars because the larger EW difference in strong lines of HD 161817 is probably due to the different measurement techniques of the two studies. In our case, strong lines were treated by either fitting the damping wing or integrating over the line profile. Since the deviations (ΔEW) are small, we conclude that our EW measurements are in excellence agreement with others.

2.5 Analysis

Our analysis is based on equivalent width matching and spectrum synthesis. Both methods require a stellar atmosphere model that is characterized by four parameters: effective temperature ($T_{\rm eff}$), surface gravity (log g), metallicity ([M/H]) and microturbulence ($v_{\rm t}$). We constructed models by in-

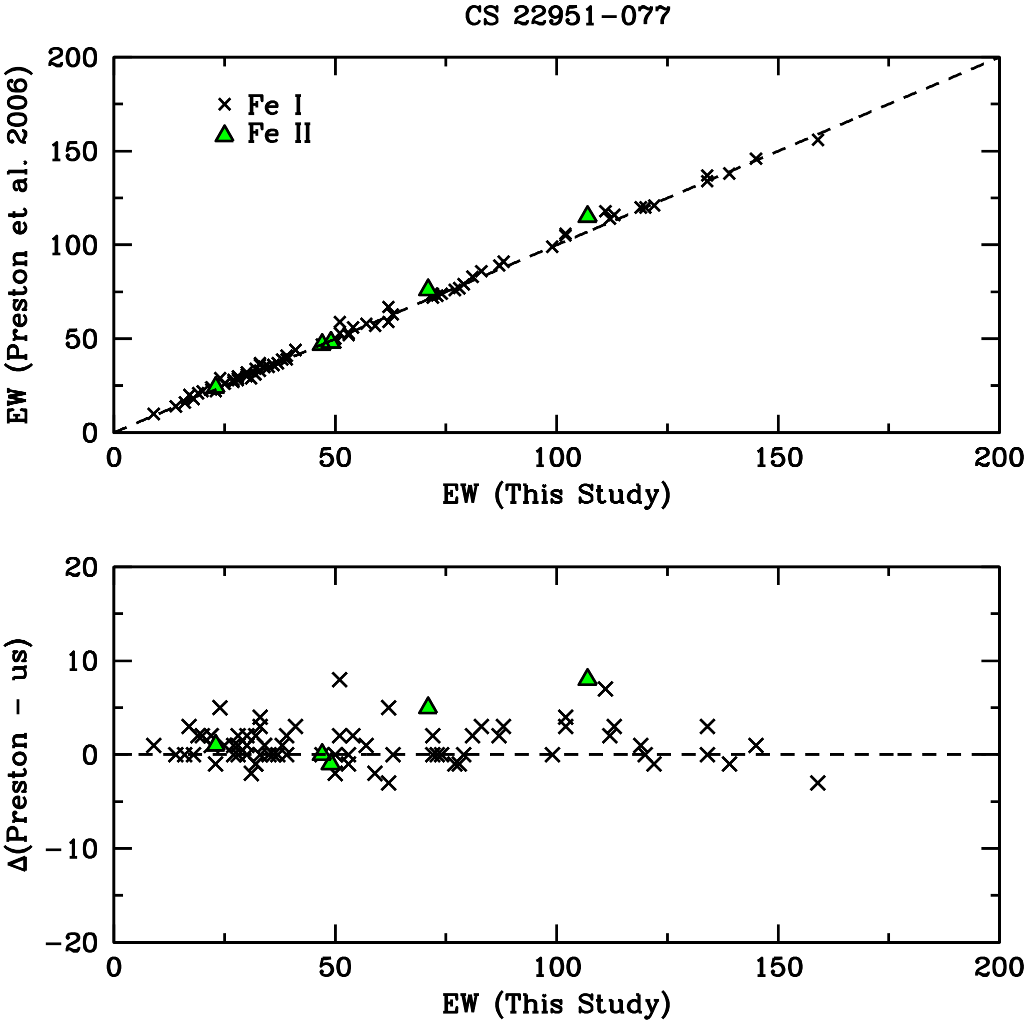

Figure 2.2 Comparison of our measured Fe I & II EWs of a cooler (CS 22951−077) MPFRHB star with Preston et al. (2006a). The top panels show 1:1 comparison of EW measurements. The bottom panels show the difference between our EW measurements and Preston et al. (2006a). The crosses and triangles represent Fe I and Fe II lines, respectively.

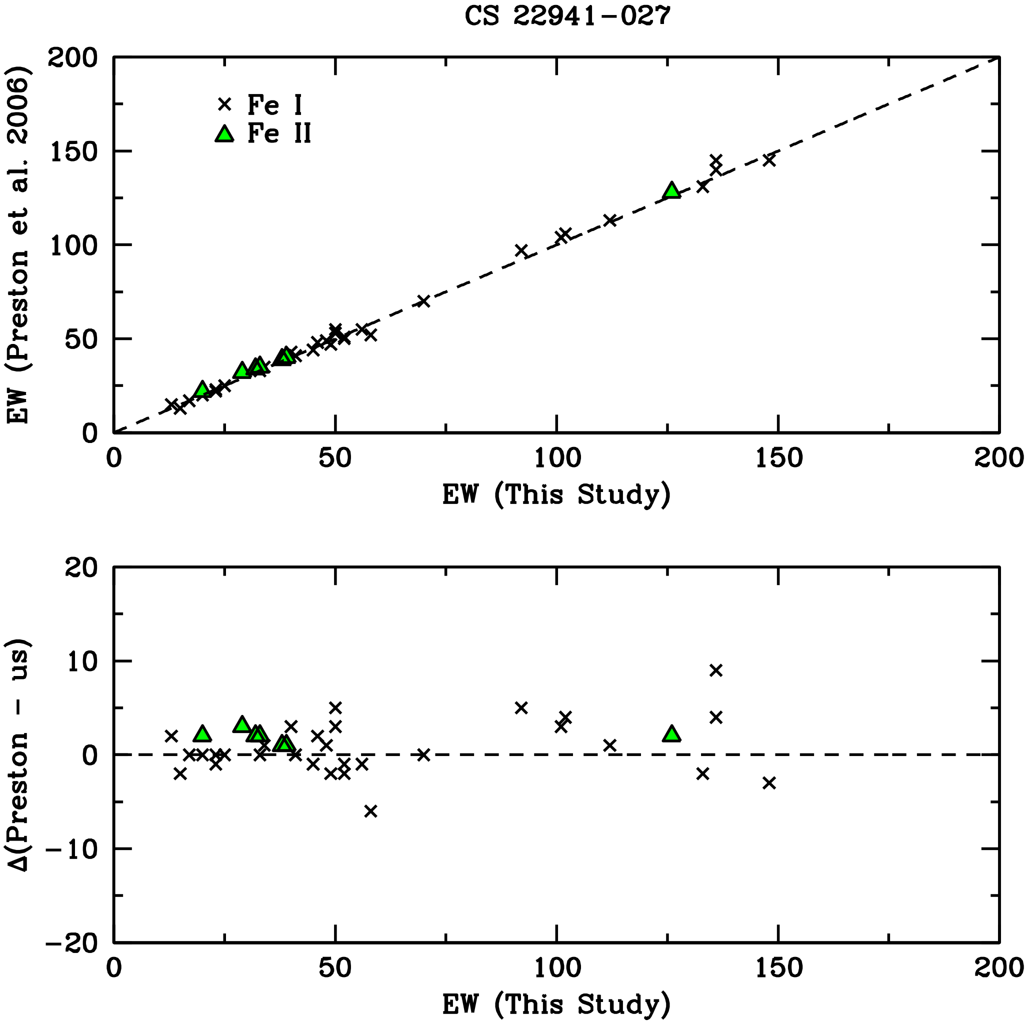

Figure 2.3 Same as Figure 2.2 except for a hotter (CS 22941−027) MPFRHB star.

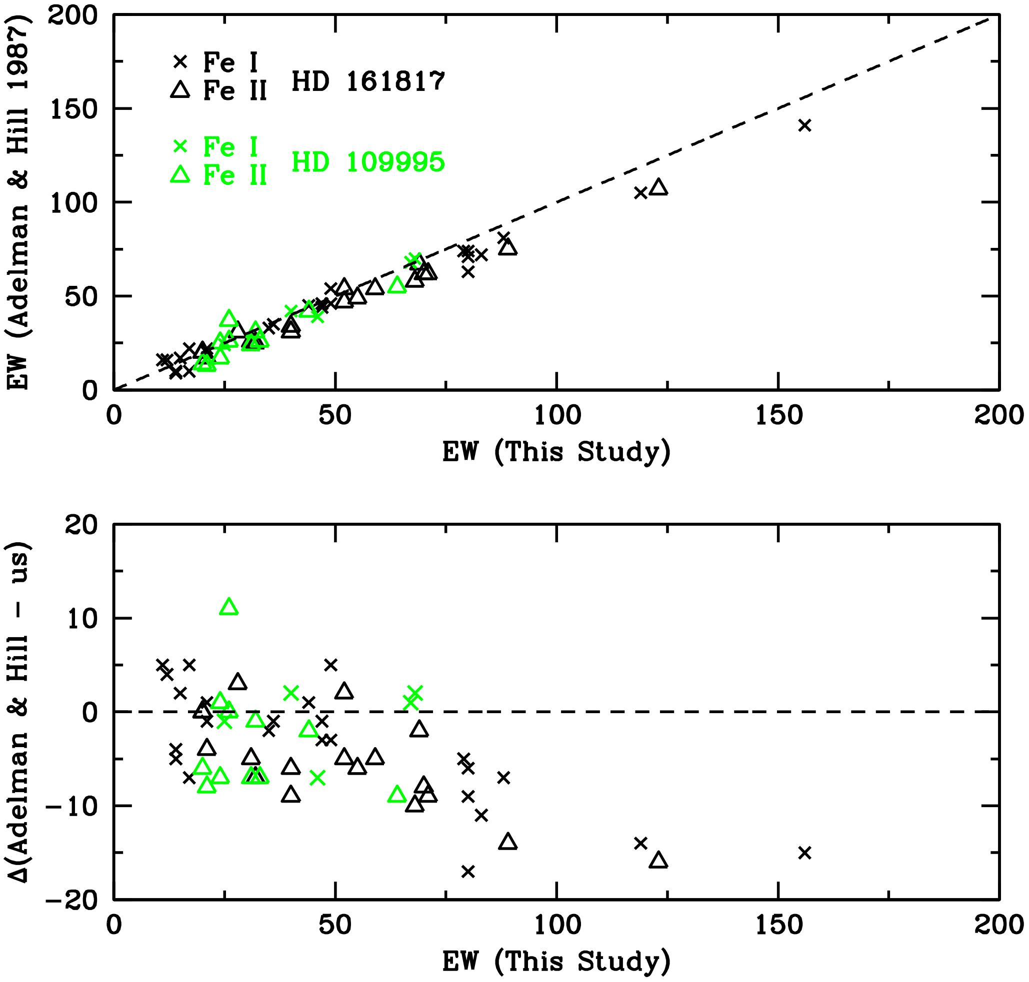

Figure 2.4 Comparisons of our measured Fe I & II EWs of HD 161817 and HD 109995 with Adelman & Hill (1987). The top panel shows 1:1 comparison of EW measurement. The bottom panel shows the difference between our EW measurements and Adelman & Hill (1987). See text for explanation on the large deviation between ours and Adelman & Hill (1987) measurements. The crosses and triangles represent Fe I and Fe II lines. The green and black correspond to lines measured in HD 109995 and HD 161817, respectively.

terpolation[5] in Kurucz's non-convective-overshooting atmosphere model grid (Castelli et al. 1997). The elemental abundances were derived using the current version of the local thermodynamic equilibrium (LTE) spectral line synthesis code MOOG[6] (Sneden 1973). With the exception of iron ($\log_\epsilon(\mathrm{Fe}) = 7.52$), this code adopted the solar and meteoritic abundances of Anders & Grevesse (1989). The details on determining the stellar parameters and methodologies are given in the following subsections.

2.5.1 Stellar Parameters

An initial stellar atmosphere model was created based on the stellar parameters of Preston et al. (2006a) and Behr (2003b). Final model atmosphere parameters were determined by iteration, through spectroscopic constraints: (1) for T_{eff}, that the abundances of individual Fe I lines show no trend with E.P.; (2) for v_{t}, that the abundances of individual Fe I lines show no trend with reduced width ($\log \mathrm{RW}$); (3) for log g, that ionization equilibrium be achieved between the abundances derived from the Fe I and Fe II species; and (4) for metallicity [M/H], that its value is consistent with the [Fe/H] determination. In the case of [Fe/H] < -2.5, we adopted [M/H]$= -2.5$ for the stellar atmosphere model due to no available models in our grid below this metallicity. Table 2.4 presents the derived stellar atmosphere model parameters and Fe metallicities of our program stars.

The standard spectroscopic constraints method has drawbacks. In particular, "spectroscopic" gravities derived from ionization balance may be lower than "trigonometric" gravities derived from stellar parallaxes (π) or "evolu-

---

[5] The interpolation code was kindly provided by Andrew McWilliam and Inese Ivans.

[6] Available at http://verdi.as.utexas.edu/moog.html .

tionary" gravities inferred from HR-diagram positions (see e.g., Allende Prieto et al. 1999). Such mismatches may arise from statistical equilibria that are not well described by LTE. These so-called NLTE effects are mainly due to the additional ionization of neutral-species by photoexcitation of UV photons. The problem can increase with decreasing metallicity due to smaller UV line opacities in metal-poor stars. Discrepancies in derived [Fe I/H] and [Fe II/H] are the result: Fe I lines yield lower abundances than do Fe II lines, which are then "corrected" by decreasing assumed gravities in LTE analysis (Thévenin & Idiart 1999). A full discussion of NLTE effects is beyond the scope of this chapter. In the following section, we consider the effects of log g uncertainties on our derived abundances.

We have compared our spectroscopic $T_{\rm eff}$'s to those based purely on photometry. We computed photometric temperatures using the metallicity-dependent $T_{\rm eff}$-color formula of giants developed by Alonso et al. (1999). These relationships are based on the infrared flux method (IRFM) (Blackwell & Shallis 1977). We employed only $V - K$ colors for this exercise. In contrast to $B - V$ colors, where blue continua are severely affected by line blanketing, $V - K$ colors are largely insensitive to the choice of metallicity and gravity.

The $(V - K)$ values of our stars, as listed in Table 2.1, are based on $V_{\rm Johnson}$ and 2MASS J and K_s magnitudes. The calibration curve of Alonso et al. (1999) is based on $(V - K)_{\rm TCS}$. Therefore, several color transformations were required. We converted these colors to the TCS system in two ways. First, we simply shifted the 2MASS K_s magnitudes to the $K_{\rm TCS}$[7] using Eq. 5(c) of Ramírez & Meléndez (2005a): $K_{TCS} = K_{\rm 2MASS} - 0.014 + 0.027(J - K)_{\rm 2MASS}$.

---

[7] $K_{\rm TCS}$ is the broad-band K magnitude in the photometric system developed for the Observatorio del Teide (Tenerife) 1.5m telescope (Alonso et al. 1994).

The $V_{\rm TCS}$ magnitudes are essentially equal to $V_{\rm Johnson}$, thus the K transformation should be sufficient to convert our $V-K$ values to $(V-K)_{\rm TCS}$. Second, a better method is to shift $(V_{\rm Johnson}-K_s)$ into $(V-K)_{\rm TCS}$ by two corrections as described in Johnson et al. (2005); we computed the $(V-K)_{\rm TCS}$ using their Eq. 6: $(V-K)_{\rm TCS} = 0.050+0.993(V_{\rm Johnson}-K_s)$. For each of these conversion attempts, we then applied extinction corrections to the colors, adopting an extinction ratio of $k = E(V-K)/E(B-V)$, where $k = 2.74$ for $(V-K)_{\rm TCS}$ (Ramírez & Meléndez 2005b). Photometric $T_{\rm eff}$ were subsequently calculated using polynomial relation described in Eq. 8 of Alonso et al. (1999). There are two BHB stars that possess $V-K$ colors that are smaller than $V-K$ range (< 0.2) of this equation's calibration. For these stars we simply assumed that the polynomial fit could be extrapolated to $V-K \simeq 0$.

We compared the calculated photometric $T_{\rm eff}$ of both methods and found that the difference is small ($\Delta T_{\rm eff}= 54\pm 1$ K, $\sigma = 6$ K, $N_{\rm star} = 34$) for RHB stars and somewhat larger ($\Delta T_{\rm eff}= 109\pm 3$ K, $\sigma = 11$ K, $N_{\rm star} = 11$) for BHB stars. The larger difference for BHB stars is most likely due to the color-$T_{\rm eff}$ transformation, because it is based mostly on cooler stars. The error of calculated photometric $T_{\rm eff}$ depends on the slope of the polynomial fit, $\Delta T_{\rm eff}/\Delta X$, where ΔX is a function of extinction ratio (k) and error in reddening ($\Delta E(B-V)$). The error is represented by 17 K per 0.01 mag for $V-K < 2.2$ (Alonso et al. 1999).

We show the comparison of the calculated photometric $T_{\rm eff}$ values that are adopted from the first color-transformation method to the derived spectroscopic $T_{\rm eff}$ values in Figure 2.5. Taking the difference (our spectroscopic $T_{\rm eff}$ minus photometric $T_{\rm eff}$), we show that the two sets of $T_{\rm eff}$ values of both RHB ($\Delta T_{\rm eff}= -73\pm30$ K, $\sigma = 177$ K, $N_{\rm star} = 34$) and BHB stars ($\Delta T_{\rm eff}= 59\pm91$ K,

$\sigma = 300$ K, $N_{\rm star} = 11$) are in good agreement.

Ideally our spectroscopic gravities should be compared with trigonometric or physical gravities, but such an exercise is not possible here. Our stars have no reliable parallax data from *Hipparcos* (Perryman et al. 1997); they are too distant. Most stars selected from the Behr (2003a) catalog have large errors in their parallaxes, and no parallaxes have been reported for stars selected from Preston et al. (2006a).

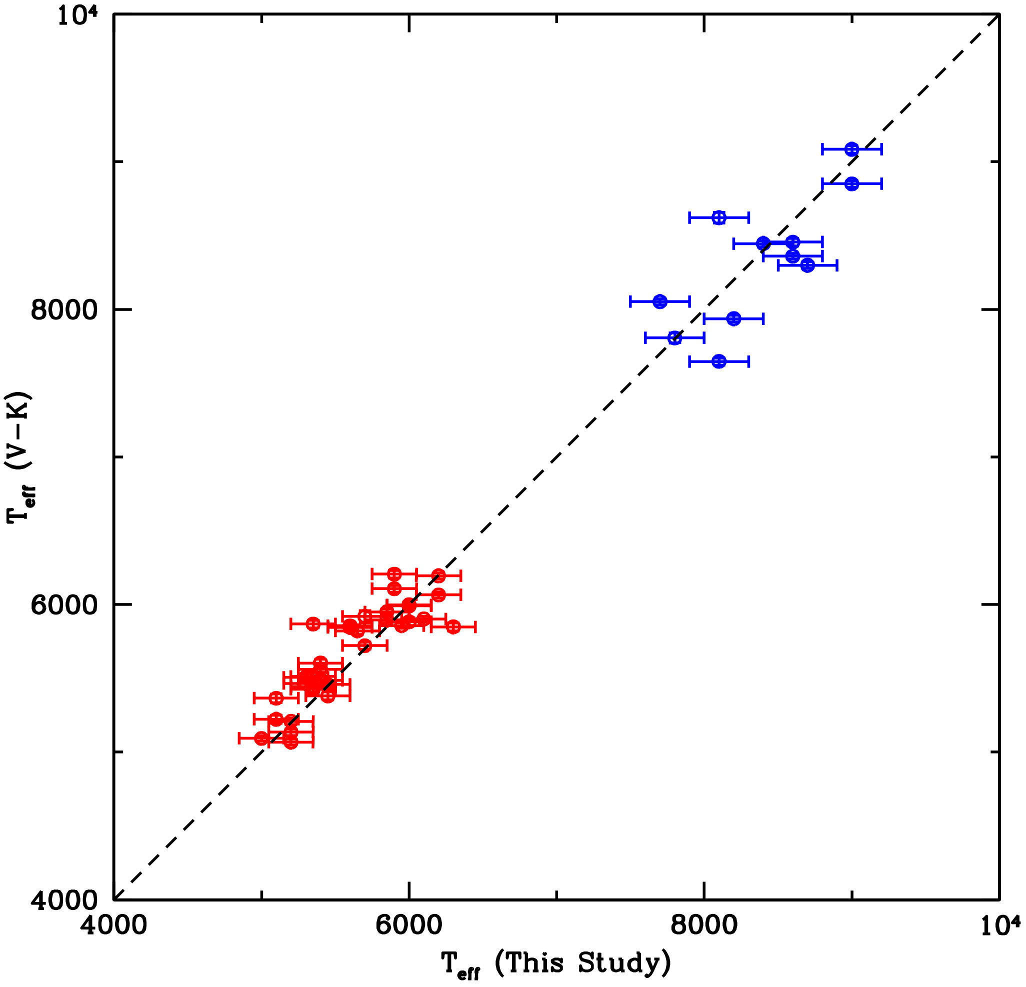

Figure 2.5 Comparison of spectroscopic $T_{\rm eff}$ with photometric $T_{\rm eff}$ derived from $(V-K)_{\rm TCS}$ metallicity–dependent $T_{\rm eff}$–color formula of Alonso et al. (1999). The formal error is equal to or smaller than the size of the dots.

Table 2.4. Final stellar atmosphere parameters and derived Fe metallicities.

Star	$T_{\rm eff}$ (K)	$\log g$ (dex)	[M/H][a]	v_t (km s^{-1})	[Fe I/H]	σ	N	[Fe II/H]	σ	N
					RHB					
HD 6229	5200	2.50	−1.07	1.60	−1.07	0.13	98	−1.06	0.13	20
HD 6461	5200	2.90	−0.75	1.40	−0.75	0.12	94	−0.74	0.10	13
HD 25532	5450	2.00	−1.41	2.10	−1.41	0.06	44	−1.42	0.09	8
HD 105546	5200	2.30	−1.54	1.80	−1.54	0.08	65	−1.54	0.06	20
HD 119516	5400	1.50	−2.16	2.20	−2.16	0.06	49	−2.16	0.05	15
BD+18° 2890	5000	2.40	−1.61	1.40	−1.61	0.07	51	−1.61	0.09	8
BD+11° 2998	5450	2.30	−1.28	1.90	−1.28	0.08	59	−1.29	0.06	10
BD+09° 3223	5100	1.30	−2.47	1.90	−2.47	0.05	48	−2.46	0.06	11
BD+17° 3248	5100	1.70	−2.24	1.80	−2.24	0.06	38	−2.23	0.07	13
HD 184266	5700	1.70	−1.79	2.70	−1.79	0.06	32	−1.78	0.05	8
HD 229274	5500	2.30	−1.41	2.00	−1.41	0.08	44	−1.42	0.08	12
CS 22882−001	5950	2.00	−2.50	3.05	−2.54	0.10	55	−2.54	0.07	14
CS 22190−007	5600	1.90	−2.50	1.90	−2.67	0.09	93	−2.67	0.07	15
CS 22186−005	6200	2.45	−2.50	3.20	−2.77	0.07	13	−2.78	0.08	6
CS 22191−029	6000	2.10	−2.50	2.90	−2.73	0.09	53	−2.72	0.06	10
CS 22883−037	5900	1.65	−1.95	2.80	−1.95	0.11	73	−1.94	0.10	17
CS 22878−121	5450	1.75	−2.38	1.90	−2.38	0.12	110	−2.37	0.07	24
CS 22891−184	5600	1.70	−2.50	2.05	−2.61	0.07	86	−2.61	0.07	16
CS 22896−110	5400	1.45	−2.50	2.05	−2.78	0.09	78	−2.78	0.07	16
CS 22940−077	5300	1.45	−2.50	1.90	−3.02	0.08	70	−3.02	0.09	15
CS 22955−174	5350	1.35	−2.50	2.20	−3.17	0.09	45	−3.17	0.08	7
CS 22940−070	6300	2.40	−1.41	3.20	−1.41	0.07	24	−1.42	0.06	7
CS 22879−103	5700	1.60	−2.20	3.00	−2.20	0.08	94	−2.20	0.06	16
CS 22879−097	5650	1.95	−2.50	2.20	−2.59	0.10	76	−2.58	0.10	14
CS 22940−121	5350	1.60	−2.50	2.10	−2.95	0.09	73	−2.94	0.12	14
CS 22898−043	5900	2.00	−2.50	3.40	−3.03	0.05	12	−3.03	0.08	2
CS 22937−072	5300	1.50	−2.50	1.80	−2.85	0.09	86	−2.85	0.06	16
CS 22948−006	5400	1.40	−2.50	2.15	−2.79	0.09	83	−2.79	0.09	13
CS 22944−039	5350	1.20	−2.43	2.20	−2.43	0.10	99	−2.44	0.09	16
CS 22951−077	5350	1.55	−2.44	2.00	−2.44	0.09	97	−2.43	0.09	13
CS 22881−039	6100	1.85	−2.50	2.70	−2.73	0.08	37	−2.72	0.12	7
CS 22886−043	6000	1.85	−2.17	3.05	−2.17	0.11	52	−2.17	0.10	21
CS 22875−029	6000	2.05	−2.50	3.00	−2.66	0.09	62	−2.66	0.08	12
CS 22888−047	5850	1.70	−2.50	3.20	−2.58	0.08	58	−2.57	0.06	11
CS 22941−027	6200	2.20	−2.50	3.30	−2.54	0.07	36	−2.53	0.09	10
CS 22945−056	5850	1.50	−2.50	3.00	−2.92	0.07	33	−2.92	0.08	7
					BHB					
HD 2857	8100	3.60	−1.39	3.70	−1.39	0.13	12	−1.38	0.14	14
HD 8376	8600	3.70	−2.39	1.00	−2.39	0.11	9	−2.38	0.11	6
HD 252940	7650	2.70	−1.69	3.10	−1.69	0.07	11	−1.68	0.07	10
HD 60778	8100	2.75	−1.43	2.20	−1.43	0.06	20	−1.43	0.03	11
HD 74721	9000	3.40	−1.23	1.40	−1.23	0.05	13	−1.21	0.06	13

Table 2.4 (cont'd)

Star	$T_{\rm eff}$ (K)	$\log g$ (dex)	[M/H][a]	v_t (km s^{-1})	[Fe I/H]	σ	N	[Fe II/H]	σ	N
HD 86986	8200	3.20	−1.61	2.30	−1.61	0.09	34	−1.59	0.07	23
HD 87047	7700	2.30	−2.38	1.30	−2.38	0.03	4	−2.37	0.11	7
HD 93329	8700	3.40	−1.10	2.80	−1.10	0.07	35	−1.11	0.07	27
HD 109995	8600	3.00	−1.60	2.00	−1.60	0.05	7	−1.59	0.07	18
BD+25° 2602	8400	2.80	−1.98	2.30	−1.98	0.07	5	−1.98	0.11	8
HD 161817	7800	3.00	−1.43	3.20	−1.43	0.09	57	−1.45	0.07	28
HD 167105	9000	3.10	−1.55	2.00	−1.55	0.03	3	−1.54	0.07	18

[a] Input model metallicity.

2.5.2 Parameter Uncertainties

To estimate the effects of uncertainties in our spectroscopically-based $T_{\rm eff}$ on derived abundances, we varied the assumed $T_{\rm eff}$'s of HD 119516 (RHB) and HD 161817 (BHB). For HD 119516, raising $T_{\rm eff}$ by 150 K from the derived 5400 K produced an unacceptably large trend of derived log ϵ(Fe) with excitation potential. For the BHB star, HD 161817, $T_{\rm eff}$ can be raised to 200 K before the trend of log ϵ(Fe) with E.P. becomes too large. Repeating these trials for other stars suggested that 150 K and 200 K are typical uncertainties for the RHB and BHB stars, respectively. The difference between the two groups is due to the lesser number of available Fe I lines in BHB spectra, which causes larger error in $T_{\rm eff}$ derivation.

We estimated $v_{\rm t}$ uncertainties in a similar manner, assessing the trends of Fe I abundances with log (RW). This yielded v_t errors of 0.2 km s^{-1} and 0.3 km s^{-1} for RHB and BHB stars, respectively. Finally, (assuming that $\log g$ based on the neutral/ion ionization balance of Fe abundance is correct) from the dependence Fe II abundances with $\log g$, we estimated the error of $\log g$ to be 2σ of Fe II abundance error. The mean error of log g to be $\sim$ 0.16 dex. We adopted the internal error (σ) of Fe I abundances as the model [M/H] error.

2.5.3 Comparisons with Previous Studies

We compared our derived $\log g$ and $T_{\rm eff}$ values with those of Preston et al. (2006a) and Behr (2003b), as shown in Figures 2.6 & 2.7. Behr (2003b) derived these quantities by comparing the synthetic photometric color and the observed color over a grid of $T_{\rm eff} - \log g$ values. Preston et al. (2006a) employed the same method as we do, i.e., from spectroscopic constraints, but they used both Fe and Ti abundances for determining log g from ionization-balance considerations. We decided here not to use Ti in the log g estimation, because the Ti I $\log gf$ values from the NIST atomic transition database[8] are of relatively high uncertainty and there are not many measurable Ti I lines ($N < 6$) in most cases for our RHB stars. Using small number of lines would cause larger error in log g estimation and could yield systematic error (see below). Additionally, we have no detections of Ti I lines in our BHB sample. Therefore to be consistent in our RHB and BHB star analyses, we decided to only use Fe I and Fe II abundances in estimations of log g.

Our $T_{\rm eff}$'s for RHB stars are $\Delta T_{\rm eff}$(Preston−us) = 59±20 K (σ = 100 K, N = 25) and $\Delta T_{\rm eff}$(Behr−us) = 154 ± 40 K (σ = 134 K, N = 11), which are in good agreement. Comparison of BHB stars can only be made with Behr. Our $T_{\rm eff}$ values generally agree with his, $\Delta T_{\rm eff}$(Behr-us) = −152 ± 43 K (σ = 134 K, N = 10) except for HD 8376 and possibly HD 93329. Our derived RHB log g values are systematically lower ($\Delta \log g$ (Preston−us) = 0.41 ± 0.06 dex, σ = 0.3 dex, N = 25) than those of Preston et al, which is due to different

---

[8] National Institute of Standards and Technology (NIST): http://www.nist.gov/physlab/data/asd.cfm .

derivation methods. To demonstrate such systematic effects, we performed tests using both Fe and Ti lines. Abundances of neutral species of Titanium is generally larger than ionized species by 0.12–0.2 dex. As such, this requires a larger log g, which is 0.2–0.5 dex, to achieve the ionization equilibrium for Ti.

Our derived log g values show no correlation with Behr's, and we note significant deviations for HD 8376, HD 6461 and HD 6229. For HD 6461 our derived [Fe I/H] is +0.6 dex higher than Behr's, which in turn forces a larger log g to achieve the ionization equilibrium. Our $T_{\rm eff}$ for HD 8376 is about 500 K larger than Behr's estimate, which forces a much larger log g value in our analysis. We do not have an explanation for the log g deviation of HD 6229.

2.5.4 Microturbulence vs Effective Temperature

We plot our $v_{\rm t}$ values against $T_{\rm eff}$ in Figure 2.8, where the correlations (dashed lines) were derived by fitting linear least squares regression lines to the RHB and BHB data. The clear positive correlation of microturbulent velocity with temperature in RHB stars has been found by others (see Preston et al. 2006a and references therein). It is possible that the BHB stars have an anti-correlation between these two quantities. The star-to-star scatter is large, but even if we exclude HD 8376[9], the anti-correlation remains. We have extended the dashed lines beyond their intersection in the figure; comparison of these lines with the RR Lyr data indicates that there is no $v_{\rm t}$ correlation with $T_{\rm eff}$ in this domain. This issue will be revisited in chapter 4.

---

[9] Our derived $v_{\rm t}$ for HD 8376 is rather uncertain because no $v_{\rm t}$ choice can eliminate the trend of log ϵ(Fe) with log(EW/λ) for this star. This is the only program star for which we have trouble in finding an acceptable $v_{\rm t}$ value.

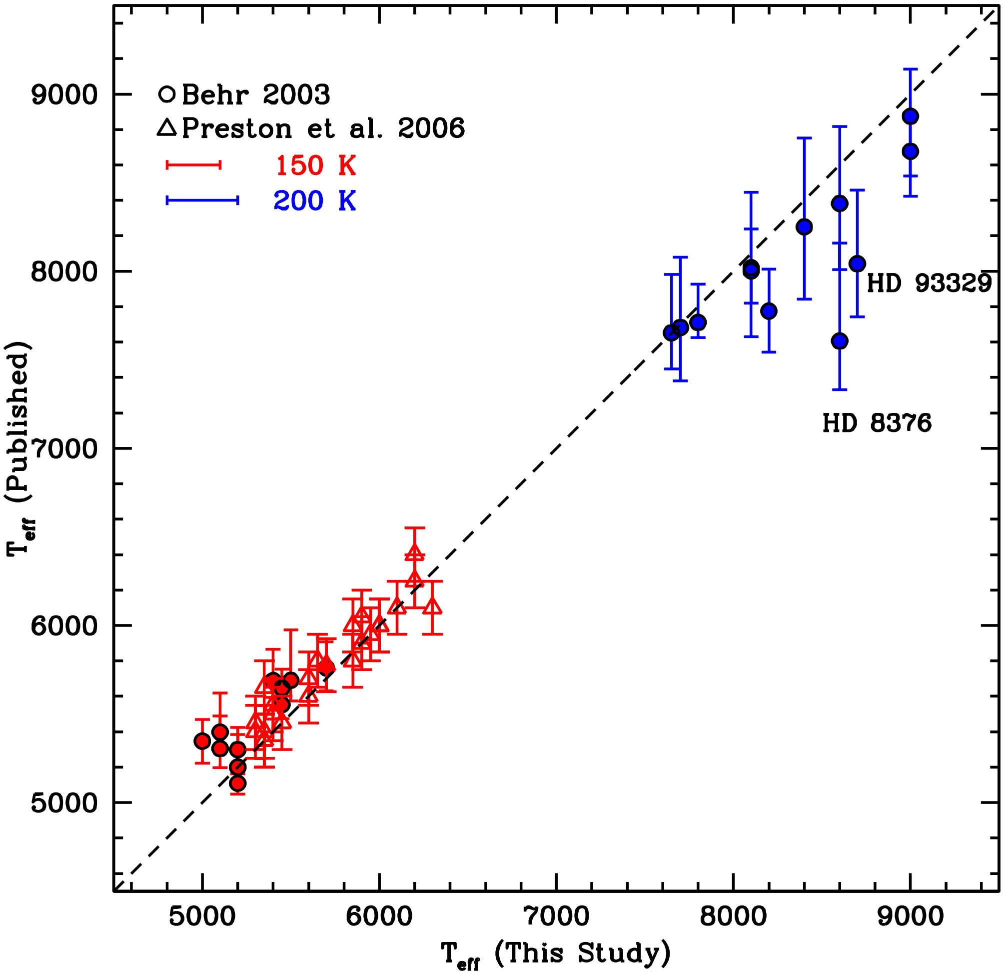

Figure 2.6 Comparison of spectroscopic $T_{\rm eff}$ derived from this study with $T_{\rm eff}$ values from Preston et al. (2006a) and Behr (2003b). The triangles and circles represent Preston et al. (2006a) and Behr (2003b) study, respectively. The red and blue colors correspond to RHB and BHB stars. For clarity in the figure, we do not plot error bars from our work for each star, but instead indicate typical $T_{\rm eff}$ uncertainties for this study, 150 K and 200 K for RHB and BHB stars. Comparison of BHB stars can only be made with Behr (2003b).

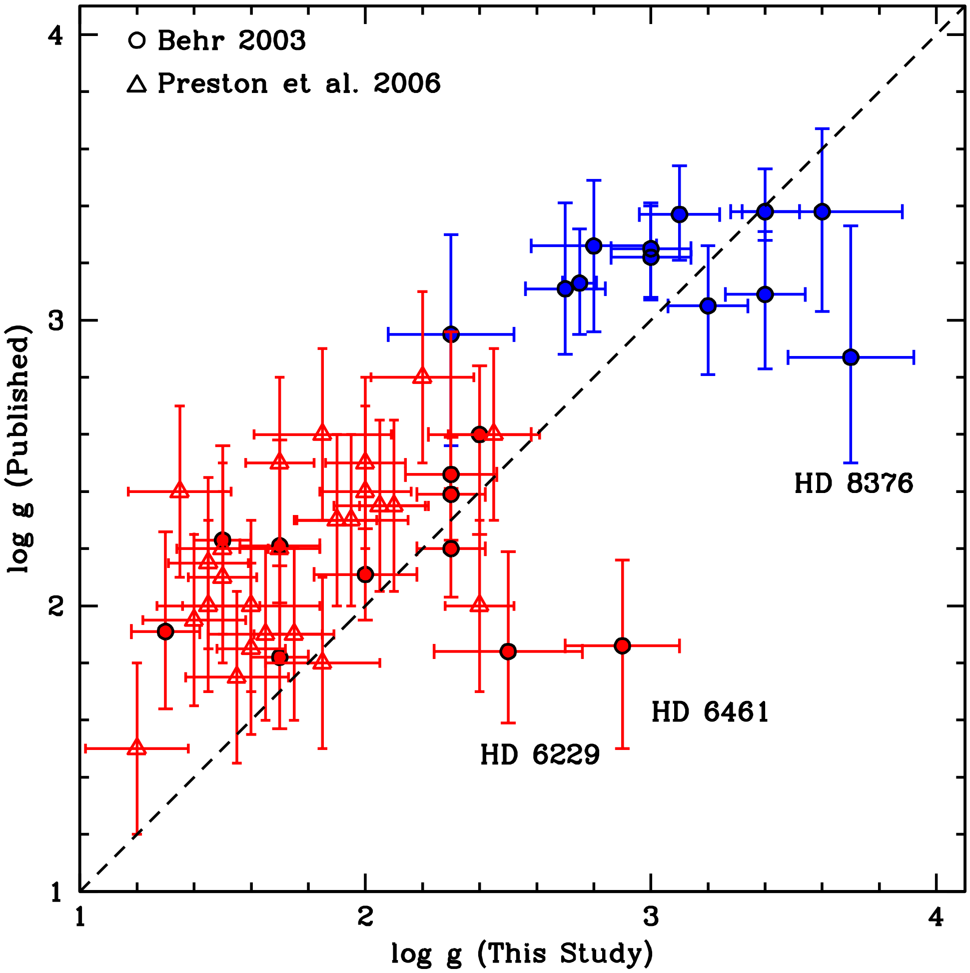

Figure 2.7 Comparison of spectroscopic log g derived from this study with log g derived by Preston et al. (2006a) and Behr (2003b). The triangles and circles represent Preston et al. (2006a) and Behr (2003b) study, respectively. The red and blue colors correspond to RHB and BHB stars.

These trends in derived v_t with $T_{\rm eff}$ undoubtedly are related to the envelope/atmosphere instabilities of RR Lyr stars. The evolutionary track of a HB star indicates that it evolves from the hot end, crosses the RR Lyr IS into the cool HB region, before ascending to the AGB. As an HB star evolves toward the RR Lyr IS blue edge, its atmosphere begins to be unstable, which results in increasing line widths that we model as increasing microturbulence. And as the HB star evolves away from the RR Lyr IS red edge, the line widths decrease as the stability is regained. We caution here that our microturbulence values are simple compensations for complex physical changes that are occurring in HB stars near the instability strip, and thus should be interpreted with caution.

2.6 Chemical Abundances

With the model atmosphere parameters listed in Table 2.4, we derived the abundances of most elements from their EW measurements. In the cases of Ca II, Mn I, Ni II, Sr II, Zr II, Ba II, La II, and Eu II, the detectable transitions are complex: they are either partially blended, or have significant hyperfine and/or isotopic substructure, or all of these things. We employed spectrum synthesis to determine abundances for these species. That is, for each line we computed theoretical spectra of a wavelength region within ±10Å of the line for a variety of assumed abundances, then broadened the computed spectrum with Gaussian line profile (or a combination of Gaussian plus rotational velocity line profile), and finally compared these spectra to the observed ones. The assumed abundances were changed iteratively to obtain acceptable synthetic/observed spectrum matches. For stars with detectable rotational line broadening, we began with the $v\sin i$ estimates of Behr (2003b) and derived the final $v\sin i$ based on the fit to observed line profile. Our final numbers were always in

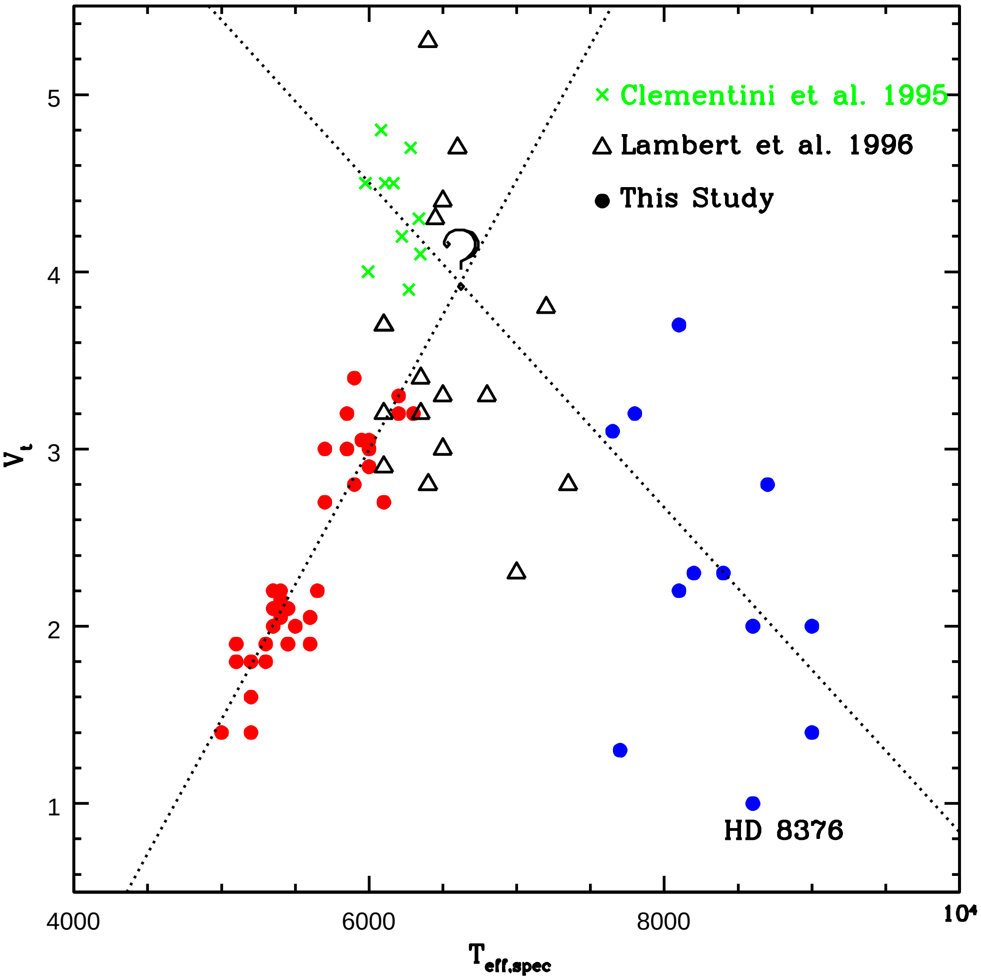

Figure 2.8 The correlation and anti-correlation between v_t and $T_{\rm eff}$ for RHB and BHB stars. Linear least square equations were fitted to all the RHB stars and BHB stars, excluding HD 8376. The crosses and open triangles represent the v_t and $T_{\rm eff}$ of RR Lyrs studies by Clementini et al. (1995) and Lambert et al. (1996), respectively. The readers are warned that there is no correlation in the RR Lyr IS region and beyond the intersection of dashed lines, where question mark is marked.

good agreement ($\Delta v \sin i \simeq 1 - 2$ km s^{-1}) with initial values. The damping constant of Barklem & O'Mara (1998) was adopted whenever possible in both EW analyses and spectrum syntheses method.

We present the derived abundance ratios [X/Fe] in Tables 4.8–4.11, and plot these as functions of metallicity in Figure 2.9–2.11 and $T_{\rm eff}$ in Figures 2.12–2.14. Non-LTE corrections have been applied to the data on these figures and tables wherever applicable. The mean [X/Fe] values of RHB and BHB stars are summarized in Table 2.9. In the following subsections we comment on individual elements.

The total error in the abundances is a combination of internal error (line-to-line scatter), and external errors (induced by stellar model atmosphere parameter uncertainties). The line-to-line scatter is given by the abundance standard deviation (σ) from individual spectral lines. To estimate the errors caused by model parameter uncertainties, we performed numerical experiments for four stars, in which we varied the model parameter errors as estimated in §2.5.2. These stars are CS 22898−043 (very metal-poor), HD 25532 (moderately metal-poor), HD 93329 (BHB) and BD+18° 2890 (RHB). They were selected because they are representative of our whole sample. The results of [X/Fe] sensitivity to different stellar model atmosphere parameter variations are shown in Table 2.10 & 2.11. In most cases Δ[X/Fe] $\lesssim$ 0.05 in response to changes in log g, [M/H] and $v_{\rm t}$. On the other hand, varying $T_{\rm eff}$ by 150 K has a larger effect on the abundance ratios of cool, metal-poor RHB star BD+18° 2890, especially on the neutral species. The overall average variations in [X/Fe] are small, $\simeq$0.05. Thus, in general external error from stellar model atmosphere parameters do not greatly influence the derived abundance ratios. For abundances derived from one spectral line, we adopted an error of

0.2 dex, judging from the statistical source of error (ie., sensitivity of Δ [X/Fe] with stellar parameters error, uncertainties in measuring the EW or matching a synthetic spectrum etc).

Table 2.5. Abundance ratios, [X/Fe], of Na, Mg, Si and Ca

Star	Na I	σ	N	Mg I	σ	N	Si I	σ	N	Si II	σ	N	Ca I	σ	N	Ca II	σ	N
RHB																		
HD 6229	0.03	0.06	5	0.36	0.04	3	0.28	0.06	5	0.32	0.03	2	0.15	0.11	12	···	···	···
HD 6461	−0.02	0.10	3	0.35	0.15	2	0.29	0.02	6	0.47	0.16	2	0.17	0.09	13	···	···	···
HD 25532	0.64	···	1	0.56	···	1	0.53	0.07	5	0.54	0.18	2	0.29	0.05	4	···	···	···
HD 105546	0.17	···	1	0.50	0.08	3	0.40	0.10	6	0.61	0.20	3	0.42	0.09	12	···	···	···
HD 119516	0.54	···	1	0.28	···	1	0.40	···	1	0.48	0.17	2	0.26	0.07	7	···	···	···
BD+18° 2890	−0.04	0.02	4	−0.06	···	1	0.41	0.08	6	0.74	···	1	0.35	0.07	12	···	···	···
BD+11° 2998	0.24	···	1	0.56	0.12	2	0.41	0.07	5	0.52	0.07	3	0.29	0.09	7	···	···	···
BD+09° 3223	···	···	···	0.27	···	1	0.73	···	1	0.86	0.16	2	0.50	0.06	11	···	···	···
BD+17° 3248	0.59	···	1	0.43	0.26	2	0.45	···	1	0.84	···	1	0.38	0.05	7	···	···	···
HD 184266	0.98	···	1	0.50	0.03	2	0.56	0.02	2	0.44	···	1	0.38	0.09	7	···	···	···
HD 229274	0.39	0.02	2	0.32	0.05	3	0.40	0.08	7	0.38	0.17	2	0.24	0.07	7	···	···	···
CS 22882−001	···	···	···	0.37	0.01	2	0.00	···	1	0.48	0.06	2	0.40	0.09	6	···	···	···
CS 22190−007	0.80	0.10	2	0.53	0.13	3	0.65	···	1	0.66	···	1	0.35	0.08	10	···	···	···
CS 22186−005	−0.04	···	1	0.38	0.06	2	−0.11[a]	···	1	0.36[a]	···	1	0.19	···	1	···	···	···
CS 22191−029	0.13	0.02	2	0.57	0.15	4	0.15[a]	···	1	0.55	···	1	0.39	0.10	9	···	···	···
CS 22883−037	0.81	···	1	0.04	···	1	−0.14	···	1	0.60	0.20	2	0.40	0.08	8	···	···	···
CS 22878−121	0.47	0.26	2	0.41	0.08	5	0.69	···	1	0.30	0.14	2	0.38	0.08	13	···	···	···
CS 22891−184	···	···	···	0.40	0.13	5	0.37	···	1	0.45	0.08	2	0.32	0.05	9	···	···	···
CS 22896−110	0.87	0.02	2	0.59	0.10	3	0.61	···	1	0.53	0.12	3	0.41	0.06	8	···	···	···
CS 22940−077	0.67	0.00	2	0.61	0.07	4	0.33	···	1	0.62	···	1	0.49	0.08	9	···	···	···
CS 22955−174	···	···	···	0.74	0.04	4	0.30	···	1	1.34	···	1	0.58	0.09	6	···	···	···
CS 22940−070	···	···	···	0.44	···	1	0.66	0.11	4	0.33	0.05	2	0.19	0.06	6	···	···	···
CS 22879−103	···	···	···	0.50	0.09	3	0.38	···	1	0.63	0.05	3	0.44	0.06	12	···	···	···
CS 22879−097	···	···	···	0.79	0.03	2	0.22	···	1	0.88	0.20	2	0.45	0.10	9	···	···	···
CS 22940−121	···	···	···	0.61	0.04	4	0.85	···	1	0.83	···	1	0.45	0.07	4	···	···	···
CS 22898−043	···	···	···	0.52	0.02	3	−0.14	···	1	···	···	···	0.41	0.03	3	···	···	···
CS 22937−072	0.49	0.08	2	0.70	0.10	3	0.50	···	1	1.12	0.02	2	0.55	0.07	8	···	···	···
CS 22948−006	0.39	0.13	2	0.57	0.06	2	0.41	···	1	0.90	0.16	2	0.59	0.09	12	···	···	···
CS 22944−039	0.56	0.15	2	0.41	0.02	2	0.55	···	1	0.52	0.15	2	0.40	0.07	10	···	···	···
CS 22951−077	0.26	0.04	2	0.45	0.09	4	0.51	···	1	0.44	0.01	2	0.39	0.07	15	···	···	···
CS 22881−039	0.12	0.05	2	0.70	0.01	2	0.08[a]	···	1	0.27[a]	···	1	0.52	0.09	4	···	···	···
CS 22886−043	0.65	0.18	2	0.45	0.08	3	0.40[a]	···	1	0.29	···	1	0.35	0.09	6	···	···	···
CS 22875−029	0.41	···	1	0.59	···	1	0.17[a]	···	1	0.53[a]	0.10	3	0.45	0.04	6	···	···	···
CS 22888−047	−0.16	···	1	0.27	0.01	2	0.06	···	1	0.61	···	1	0.34	0.09	7	···	···	···
CS 22941−027	−0.14	0.10	2	0.32	0.10	2	0.16[a]	···	1	0.33[a]	···	1	0.22	0.11	4	···	···	···
CS 22945−056	0.27	···	1	0.78	0.18	2	0.12	···	1	0.86	···	1	0.41	0.11	3	···	···	···
BHB																		
HD 2857	···	···	···	0.31	0.14	2	−0.22[a]	···	1	0.13[a]	0.08	2	0.33	···	1	0.30	···	1
HD 8376	···	···	···	0.05	0.05	2	−0.04[a]	···	1	0.34[a]	···	1	−0.19	···	1	0.40	···	1
HD 252940	···	···	···	0.36	0.01	2	−0.08[a]	···	1	0.16[a]	···	1	0.40	0.07	4	0.35	···	1
HD 60778	···	···	···	0.38	0.02	2	−0.11[a]	···	1	0.19[a]	0.22	2	0.21	0.08	5	0.12	···	1
HD 74721	−0.41[a]	···	1	0.35	0.02	2	0.07[a]	···	1	0.45[a]	0.21	2	−0.11	···	1	0.00	···	1
HD 86986	···	···	···	0.31	0.02	2	−0.10[a]	···	1	0.18[a]	0.18	3	0.14	0.07	2	0.23	···	1

Table 2.5 (cont'd)

Star	Na I	σ	N	Mg I	σ	N	Si I	σ	N	Si II	σ	N	Ca I	σ	N	Ca II	σ	N
HD 87047	···	···	···	0.65	···	1	0.04[a]	···	1	0.22[a]	···	1	0.15	···	1	0.15	···	1
HD 93329	−0.49[a]	···	1	0.24	···	1	−0.05[a]	···	1	0.02[a]	0.22	3	−0.12	···	1	0.16	···	1
HD 109995	···	···	···	0.47	···	1	0.03[a]	···	1	0.17[a]	0.18	3	0.04	···	1	0.08	···	1
BD+25° 2602	···	···	···	0.50	0.05	2	0.15[a]	···	1	0.41[a]	0.17	2	−0.03	···	1	0.11	···	1
HD 161817	···	···	···	0.26	0.00	2	−0.09[a]	···	1	0.06[a]	0.15	3	0.24	0.05	8	0.32	···	1
HD 167105	···	···	···	0.39	0.06	2	0.05[a]	···	1	0.16[a]	0.20	3	−0.21	···	1	−0.12	···	1

[a] NLTE correction.

Table 2.6. Abundance ratios, [X/Fe], of Al, Ti, Sc and Cr

Star	Al I	σ	N	Ti I	σ	N	Ti II	σ	N	Sc II	σ	N	Cr I	σ	N	Cr II	σ	N
RHB																		
HD 6229	···	···	···	0.07	0.08	13	0.34	0.14	10	0.34	0.12	4	−0.15	0.08	5	0.03	0.14	5
HD 6461	···	···	···	0.19	0.10	13	0.43	0.10	9	0.35	0.11	4	−0.11	0.05	2	0.10	0.20	5
HD 25532	···	···	···	0.18	0.07	8	0.22	0.09	7	0.12	0.06	2	−0.21	0.12	4	−0.08	0.17	5
HD 105546	···	···	···	0.25	0.02	9	0.40	0.10	8	0.25	0.08	3	−0.17	0.11	7	0.25	0.19	6
HD 119516	−0.82	···	1	0.23	0.06	5	0.06	0.13	5	−0.06	···	1	−0.18	0.06	5	0.01	0.10	5
BD+18° 2890	···	···	···	0.15	0.09	6	0.00	0.08	3	0.06	0.09	2	−0.17	0.01	2	0.26	···	1
BD+11° 2998	···	···	···	0.19	0.04	10	0.22	0.12	6	0.16	0.05	3	−0.22	0.08	4	−0.05	0.12	3
BD+09° 3223	···	···	···	0.28	0.08	8	0.16	0.09	9	0.06	0.02	3	−0.21	0.07	4	0.12	0.18	2
BD+17° 3248	···	···	···	0.28	0.06	6	0.26	0.09	8	0.16	0.07	2	−0.27	0.08	5	0.25	0.09	4
HD 184266	···	···	···	0.30	0.07	6	0.21	0.10	5	0.09	0.02	3	−0.06	0.06	3	0.14	0.17	5
HD 229274	···	···	···	0.16	0.05	9	0.22	0.12	6	0.13	0.02	3	−0.26	0.03	3	0.17	0.18	4
CS 22882−001	−0.77	···	1	0.55	···	1	0.30	0.09	22	0.22	0.02	2	−0.19	···	1	0.39	···	1
CS 22190−007	−0.80	0.17	2	0.37	0.10	4	0.17	0.08	23	0.06	0.13	4	−0.11	0.16	6	0.25	0.04	2
CS 22186−005	−0.82	···	1	···	···	···	0.03	0.04	6	−0.01	···	1	−0.15	0.11	4	0.76	···	1
CS 22191−029	−0.62	0.08	2	0.51	0.03	3	0.30	0.09	14	0.28	0.05	3	−0.16	0.08	3	0.49	···	1
CS 22883−037	−0.70	···	1	0.36	···	1	0.23	0.11	10	0.04	0.04	3	−0.01	0.16	5	0.20	0.08	3
CS 22878−121	−0.88	···	1	0.34	0.11	6	0.21	0.10	27	0.15	0.09	6	−0.09	0.12	9	0.20	0.12	4
CS 22891−184	−0.84	0.05	2	0.29	0.04	4	0.08	0.06	21	−0.01	0.04	3	−0.20	0.06	5	0.25	0.06	2
CS 22896−110	−0.46	0.21	2	0.45	0.08	5	0.19	0.11	17	0.06	0.01	3	−0.14	0.14	6	0.48	0.11	2
CS 22940−077	−0.76	···	1	0.50	0.12	6	0.28	0.10	17	0.15	0.11	5	−0.16	0.13	5	0.30	···	1
CS 22955−174	−0.51	···	1	0.69	0.02	2	0.27	0.06	14	0.11	0.05	2	−0.24	0.10	3	0.61	0.05	2
CS 22940−070	···	···	···	0.38	0.09	4	0.26	0.06	9	0.14	0.04	2	0.11	···	1	−0.01	0.16	2
CS 22879−103	−0.59	0.14	2	0.41	0.09	6	0.28	0.06	15	0.18	0.00	2	−0.07	0.09	6	−0.05	0.07	3
CS 22879−097	−0.74	···	1	0.52	0.12	5	0.25	0.08	16	0.29	0.13	4	−0.15	0.15	3	0.23	0.16	3
CS 22940−121	−0.48	···	1	0.43	0.13	3	0.27	0.10	15	0.19	0.12	3	−0.19	0.13	4	0.14	···	1
CS 22898−043	−0.72	···	1	0.47	···	1	0.31	0.08	10	0.20	···	1	−0.12	0.11	2	0.45	···	1
CS 22937−072	−0.49	···	1	0.43	0.09	9	0.23	0.09	20	0.11	0.05	4	−0.22	0.07	3	0.50	···	1
CS 22948−006	−0.72	···	1	0.31	0.04	5	0.16	0.08	16	−0.03	0.01	2	−0.17	0.23	4	0.15	0.13	4
CS 22944−039	−0.68	0.16	2	0.28	0.14	3	0.10	0.11	19	−0.14	0.08	3	−0.17	0.05	4	0.00	0.06	4
CS 22951−077	−0.75	0.17	2	0.22	0.03	3	0.11	0.07	17	−0.05	0.14	3	−0.17	0.10	7	0.04	0.15	3
CS 22881−039	−0.63	0.02	2	0.69	···	1	0.24	0.08	15	0.20	0.05	2	−0.20	0.11	4	0.25	···	1
CS 22886−043	−0.58	0.14	2	0.45	0.05	3	0.38	0.13	6	0.29	0.18	2	0.03	0.13	6	0.02	0.11	2
CS 22875−029	−0.42	···	1	0.63	0.01	3	0.33	0.08	18	0.30	0.10	3	−0.11	0.08	3	0.37	0.11	3
CS 22888−047	−0.75	0.03	2	0.40	0.13	3	0.13	0.08	17	0.07	0.14	3	−0.05	0.11	4	0.34	0.13	2
CS 22941−027	−0.73	0.07	2	0.36	···	1	0.28	0.08	12	···	···	···	−0.02	0.12	3	0.38	0.10	5
CS 22945−056	−0.48	···	1	0.79	···	1	0.19	0.06	8	0.18	0.04	3	−0.13	0.06	3	···	···	···
BHB																		
HD 2857	0.20[a]	···	1	···	···	···	0.36	0.07	8	0.25	0.08	2	0.31	···	1	−0.04	0.14	2
HD 8376	···	···	···	···	···	···	0.43	0.07	11	···	···	···	···	···	···	···	···	···
HD 252940	···	···	···	···	···	···	0.36	0.07	8	0.07	···	1	0.07	0.06	2	0.14	0.02	2
HD 60778	···	···	···	···	···	···	0.27	0.12	11	0.10	···	1	−0.17	···	1	0.17	0.06	2
HD 74721	···	···	···	···	···	···	0.28	0.09	11	0.08	0.05	2	0.02	0.06	4	0.03	0.15	7
HD 86986	···	···	···	···	···	···	0.34	0.05	12	0.15	0.04	2	−0.04	0.12	5	0.15	0.12	7

Table 2.6 (cont'd)

Star	Al I	σ	N	Ti I	σ	N	Ti II	σ	N	Sc II	σ	N	Cr I	σ	N	Cr II	σ	N
HD 87047	···	···	···	···	···	···	0.18	0.06	4	0.02	···	1	···	···	···	···	···	···
HD 93329	0.29[a]	···	1	···	···	···	0.33	0.09	14	0.21	0.08	2	0.00	0.09	4	0.02	0.14	7
HD 109995	0.59[a]	···	1	···	···	···	0.39	0.08	10	0.12	···	1	···	···	···	0.23	0.09	3
BD+25° 2602	···	···	···	···	···	···	0.28	0.07	8	0.19	···	1	···	···	···	0.51	···	1
HD 161817	···	···	···	···	···	···	0.35	0.13	25	0.21	0.03	3	−0.08	0.09	3	0.04	0.14	8
HD 167105	···	···	···	···	···	···	0.17	0.05	6	···	···	···	···	···	···	0.29	0.11	3

[a] NLTE correction.

Table 2.7. Abundance ratios, [X/Fe], of Fe-peak elements: V, Mn, Co, Ni and Zn

Star	V II	σ	N	Mn I	σ	N	Co I	σ	N	Ni I	σ	N	Ni II	σ	N	Zn I	σ	N
RHB																		
HD 6229	···	···	···	0.12	0.27	3	0.80	···	1	−0.04	0.09	9	···	···	···	0.11	0.04	2
HD 6461	···	···	···	0.30	···	1	0.84	···	1	−0.01	0.1	9	···	···	···	0.24	···	1
HD 25532	···	···	···	0.05	0.07	3	0.37	···	1	0.05	0.12	4	···	···	···	0.04	···	1
HD 105546	···	···	···	−0.09	0.16	5	0.30	0.08	2	−0.03	0.13	5	···	···	···	0.13	0.05	2
HD 119516	···	···	···	−0.30	0.08	3	−0.01	···	1	−0.04	···	1	···	···	···	0.05	0.04	2
BD+18° 2890	···	···	···	−0.70	0.08	3	0.22	···	1	−0.03	0.09	3	···	···	···	0.04	···	1
BD+11° 2998	···	···	···	−0.06	0.15	4	0.32	0.04	2	0.06	0.03	2	···	···	···	···	···	···
BD+09° 3223	0.03	···	1	−0.10	0.11	4	0.42	···	1	···	···	···	···	···	···	0.20	···	1
BD+17° 3248	···	···	···	−0.18	0.08	4	···	···	···	···	···	···	···	···	···	0.07	0.01	2
HD 184266	0.15	···	1	−0.19	0.11	4	−0.03	···	1	0.12	···	1	···	···	···	···	···	···
HD 229274	···	···	···	−0.06	0.24	4	0.34	0.15	2	−0.03	0.11	6	···	···	···	0.01	0.01	2
CS 22882−001	0.31	···	1	−0.39	0.05	3	···	···	···	···	···	···	···	···	···	···	···	···
CS 22190−007	0.20	···	1	−0.50	0.02	3	···	···	···	···	···	···	···	···	···	···	···	···
CS 22186−005	···	···	···	−0.46	0.05	3	···	···	···	···	···	···	···	···	···	···	···	···
CS 22191−029	0.32	···	1	−0.54	0.05	3	···	···	···	···	···	···	···	···	···	···	···	···
CS 22883−037	−0.02	···	1	−0.47	0.05	3	···	···	···	···	···	···	···	···	···	0.57	···	1
CS 22878−121	···	···	···	−0.33	0.17	3	0.44	···	1	0.41	···	1	···	···	···	0.10	···	1
CS 22891−184	···	···	···	−0.49	0.07	3	···	···	···	···	···	···	···	···	···	···	···	···
CS 22896−110	0.13	···	1	−0.45	0.09	3	···	···	···	···	···	···	···	···	···	···	···	···
CS 22940−077	···	···	···	−0.58	0.08	3	···	···	···	···	···	···	···	···	···	···	···	···
CS 22955−174	···	···	···	−0.63	0.02	3	···	···	···	···	···	···	···	···	···	0.54	···	1
CS 22940−070	···	···	···	−0.37	0.05	3	0.50	···	1	0.69	···	1	···	···	···	0.06	···	1
CS 22879−103	···	···	···	−0.50	0.04	3	···	···	···	···	···	···	···	···	···	0.31	···	1
CS 22879−097	0.13	0.02	2	−0.58	0.05	3	0.78	···	1	···	···	···	···	···	···	···	···	···
CS 22940−121	0.30	···	1	−0.58	0.02	3	···	···	···	···	···	···	···	···	···	···	···	···
CS 22898−043	···	···	···	−0.30	0.05	3	···	···	···	···	···	···	···	···	···	···	···	···
CS 22937−072	0.11	0.01	2	−0.53	0.06	3	···	···	···	···	···	···	···	···	···	···	···	···
CS 22948−006	0.10	···	1	−0.61	0.02	3	···	···	···	0.59	···	1	···	···	···	0.42	···	1
CS 22944−039	0.05	···	1	−0.45	0.04	3	0.35	···	1	0.43	···	1	···	···	···	0.10	···	1
CS 22951−077	−0.04	0.02	2	−0.33	0.17	3	···	···	···	0.39	···	1	···	···	···	0.19	···	1
CS 22881−039	···	···	···	−0.37	0.02	3	···	···	···	···	···	···	···	···	···	···	···	···
CS 22886−043	···	···	···	−0.45	0.04	3	0.58	···	1	0.71	···	1	···	···	···	0.27	···	1
CS 22875−029	0.23	···	1	−0.57	0.05	3	···	···	···	···	···	···	···	···	···	···	···	···
CS 22888−047	···	···	···	−0.57	0.08	3	···	···	···	···	···	···	···	···	···	···	···	···
CS 22941−027	···	···	···	−0.36	0.04	3	···	···	···	···	···	···	···	···	···	···	···	···
CS 22945−056	···	···	···	−0.51	0.05	3	···	···	···	···	···	···	···	···	···	···	···	···
BHB																		
HD 2857	···	···	···	···	···	···	···	···	···	···	···	···	···	···	···	···	···	···
HD 8376	···	···	···	···	···	···	···	···	···	···	···	···	···	···	···	···	···	···
HD 252940	···	···	···	···	···	···	···	···	···	···	···	···	···	···	···	···	···	···
HD 60778	0.12	···	1	···	···	···	···	···	···	···	···	···	−0.40	···	1	···	···	···
HD 74721	0.17	0.04	2	···	···	···	···	···	···	···	···	···	−0.30	···	1	···	···	···
HD 86986	0.14	0.09	2	0.06	0.32	3	···	···	···	···	···	···	···	···	···	···	···	···

Table 2.7 (cont'd)

Star	V II	σ	N	Mn I	σ	N	Co I	σ	N	Ni I	σ	N	Ni II	σ	N	Zn I	σ	N
HD 87047	...	...	...	...	...	...	...	...	...	...	...	...	...	...	...	...	...	...
HD 93329	0.11	0.07	2	−0.10	0.02	2	...	...	...	...	...	...	−0.35	...	1	...	...	...
HD 109995	...	...	...	...	...	...	...	...	...	...	...	...	...	...	...	...	...	...
BD+25° 2602	...	...	...	...	...	...	...	...	...	...	...	...	...	...	...	...	...	...
HD 161817	0.21	0.06	2	−0.33	0.10	3	0.28	...	1	...	...	...	...	...	...	...	...	...
HD 167105	...	...	...	...	...	...	...	...	...	...	...	...	...	...	...	...	...	...

Table 2.8. Abundance ratios, [X/Fe], of neutron-capture elements: Sr, Y, Zr, Ba, La and Eu

Star	Sr II	σ	N	Y II	σ	N	Zr II	σ	N	Ba II	σ	N	La II	σ	N	Eu II	σ	N
							RHB											
HD 6229	0.05	0.05	2	−0.11	0.07	2	0.05	0.05	2	0.33	0.09	3	0.07	···	1	0.10	0.15	2
HD 6461	0.10	0.10	2	···	···	···	0.45	0.15	2	0.53	0.12	3	0.07	···	1	0.10	···	1
HD 25532	0.25	···	1	0.01	0.10	2	0.35	0.04	3	0.52	0.19	3	0.09	0.08	2	0.24	0.01	2
HD 105546	0.33	0.02	2	−0.02	0.04	4	0.43	0.06	3	0.40	0.16	3	0.20	0.08	2	0.33	0.03	2
HD 119516	0.10	···	1	−0.36	0.06	5	0.30	···	1	0.32	0.22	3	0.12	···	1	0.45	0.05	2
BD+18 2890	−0.35	···	1	−0.17	···	1	···	···	···	0.32	0.08	3	0.15	0.28	2	0.45	0.10	2
BD+11 2998	0.28	0.02	2	−0.08	0.12	2	0.30	···	1	0.43	0.09	3	0.02	0.02	2	0.18	0.03	2
BD+09 3223	0.30	0.10	2	−0.23	0.07	2	0.40	···	1	0.08	0.11	4	0.07	···	1	0.34	0.06	2
BD+17 3248	0.23	0.08	2	−0.09	0.08	2	0.53	0.03	2	0.68	0.16	3	0.46	0.04	2	0.89	0.01	2
HD 184266	0.50	···	1	−0.23	···	···	0.32	0.08	3	0.28	0.24	3	0.05	0.03	2	0.38	0.03	2
HD 229274	0.15	0.05	2	−0.14	0.06	2	0.40	···	1	0.48	0.18	2	0.32	0.05	2	0.75	0.02	2
Cs22882-001	0.22	0.03	2	0.06	0.04	2	···	···	···	0.16	0.02	3	···	···	···	0.84	···	1
Cs22190-007	0.35	0.03	2	−0.40	···	1	···	···	···	−0.11	0.06	3	0.34	···	1	0.37	···	1
Cs22186-005	−1.03	0.05	2	···	···	···	···	···	···	−0.58	···	1	···	···	···	···	···	···
Cs22191-029	0.33	0.05	2	···	···	···	···	···	···	−0.22	0.02	2	···	···	···	···	···	···
Cs22883-037	0.13	0.18	2	−0.23	0.02	2	···	···	···	0.13	0.08	4	0.09	0.02	2	0.40	0.02	2
Cs22878-121	0.48	0.13	2	−0.04	0.16	3	0.33	0.12	3	0.13	0.08	4	0.17	···	1	0.40	0.02	2
Cs22891-184	0.11	0.00	2	···	···	···	···	···	···	−0.01	0.02	3	···	···	···	···	···	···
Cs22896-110	0.26	0.02	2	−0.38	···	1	0.28	···	1	−0.32	0.02	3	···	···	···	···	···	···
Cs22940-077	0.52	0.02	2	0.14	···	1	0.82	···	1	−0.51	0.23	2	···	···	···	···	···	···
Cs22955-174	0.52	0.05	2	−0.23	···	1	···	···	···	−0.18	0.05	2	···	···	···	···	···	···
Cs22940-070	0.80	···	1	0.07	···	1	0.40	···	1	0.15	0.15	2	0.07	···	1	0.40	0.02	2
Cs22879-103	0.55	0.05	2	0.02	0.03	2	0.48	0.08	2	0.29	0.09	4	0.15	0.08	2	0.40	0.02	2
Cs22879-097	0.24	0.05	2	···	···	···	0.29	···	1	−0.51	0.07	3	···	···	···	···	···	···
Cs22940-121	0.40	0.05	2	−0.03	0.06	3	0.65	···	1	0.18	0.05	3	···	···	···	···	···	···
Cs22898-043	−0.27	0.10	2	···	···	···	···	···	···	−0.47	···	1	···	···	···	···	···	···
Cs22937-072	0.30	0.05	2	−0.26	0.05	2	0.45	···	1	−0.28	0.03	2	···	···	···	···	···	···
Cs22948-006	−0.26	0.05	2	···	···	···	···	···	···	−0.61	0.10	2	···	···	···	···	···	···
Cs22944-039	0.48	0.03	2	−0.36	0.06	3	0.30	···	1	−0.15	0.05	4	−0.08	0.05	2	0.13	0.03	2
Cs22951-077	0.05	0.05	2	−0.50	0.05	3	0.30	···	1	−0.19	0.05	4	···	···	···	0.10	0.05	2
Cs22881-039	0.18	0.05	2	···	···	···	···	···	···	−0.57	···	1	···	···	···	···	···	···
Cs22886-043	0.85	0.05	2	0.21	0.03	2	0.62	0.05	3	0.46	0.10	4	0.47	0.02	2	0.83	0.03	2
Cs22875-029	0.86	0.02	2	0.39	0.17	3	0.69	0.03	2	0.44	0.06	3	0.73	···	1	0.91	0.05	2
Cs22888-047	0.31	0.02	2	0.13	0.12	2	0.53	0.05	2	0.23	0.07	3	···	···	···	0.93	0.02	2
Cs22941-027	−0.11	0.05	2	−0.29	···	1	···	···	···	−0.36	···	1	···	···	···	···	···	···
Cs22945-056	−0.06	0.13	2	···	···	···	···	···	···	−0.43	···	1	···	···	···	···	···	···
							BHB											
HD 2857	−0.15	0.05	2	···	···	1	0.50	···	1	···	···	···	···	···	···	···	···	···
HD 8376	···	···	···	···	···	···	···	···	···	···	···	···	···	···	···	···	···	···
HD 252940	−0.33	0.03	2	···	···	···	0.70	···	1	−0.10	···	1	···	···	···	···	···	···
HD 60778	−0.35	0.02	2	···	···	···	0.55	0.05	2	−0.10	···	1	···	···	···	···	···	···
HD 74721	−0.10	0.02	2	0.42	···	1	0.60	···	1	0.20	···	1	···	···	···	···	···	···
HD 86986	−0.43	0.02	2	−0.03	···	1	0.50	···	1	−0.10	···	1	···	···	···	···	···	···

Table 2.8 (cont'd)

Star	Sr II	σ	N	Y II	σ	N	Zr II	σ	N	Ba II	σ	N	La II	σ	N	Eu II	σ	N
HD 87047	−0.45	0.02	2	...	...	...	...	...	...	−0.10	...	1	...	...	...	...	...	...
HD 93329	−0.30	0.02	2	0.13	...	1	0.75	0.05	2	0.10	...	1	...	...	...	...	...	...
HD 109995	−0.40	...	1	...	...	...	...	...	...	...	...	...	...	...	...	...	...	...
BD+25 2602	−0.55	...	1	...	...	...	...	...	...	...	...	...	...	...	...	...	...	...
HD 161817	0.02	0.08	2	0.36	0.01	2	0.65	...	1	0.08	0.03	2	...	...	...	...	...	...
HD 167105	...	...	...	...	...	...	...	...	...	...	...	...	...	...	...	...	...	...

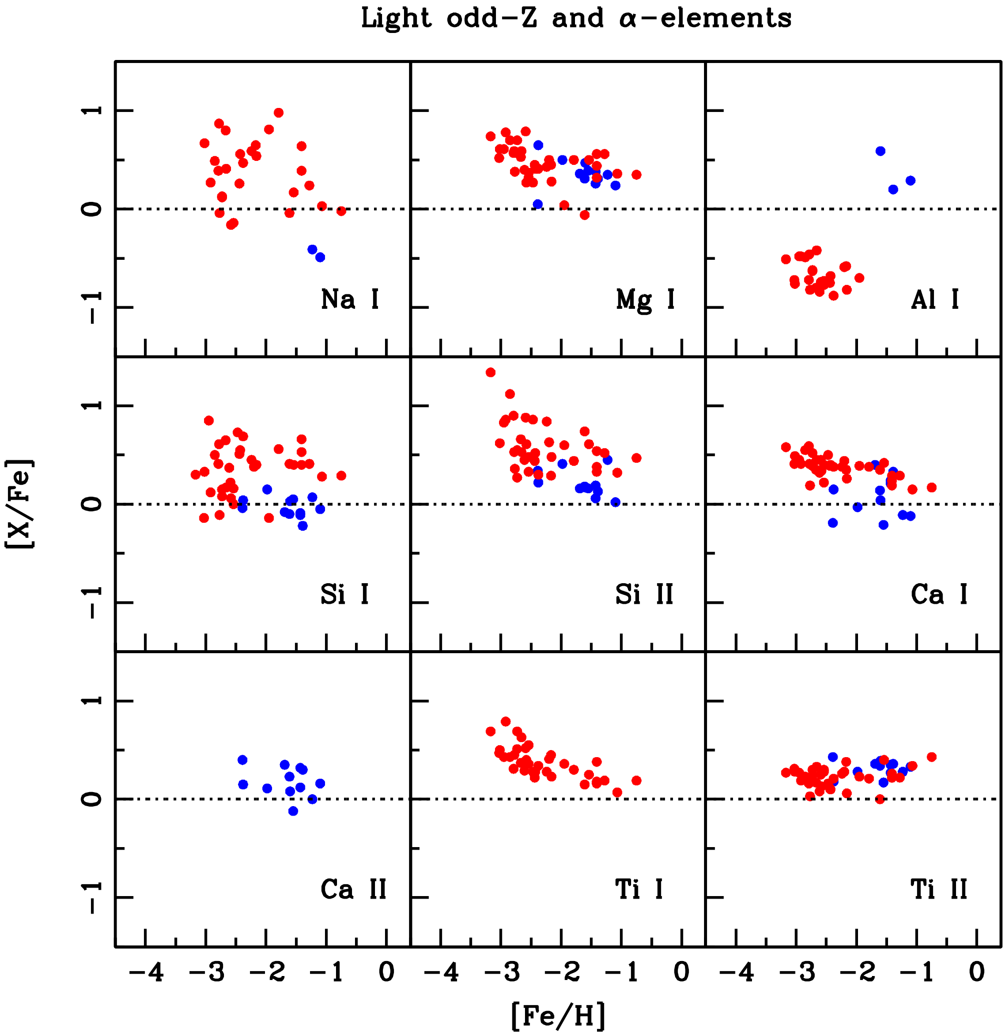

Figure 2.9 Abundance ratios of odd-Z and α-elements as a function of metallicity. NLTE corrections applied to Na I, Al I, Si I & Si II as described in text. The red and blue dots represent RHB and BHB stars.

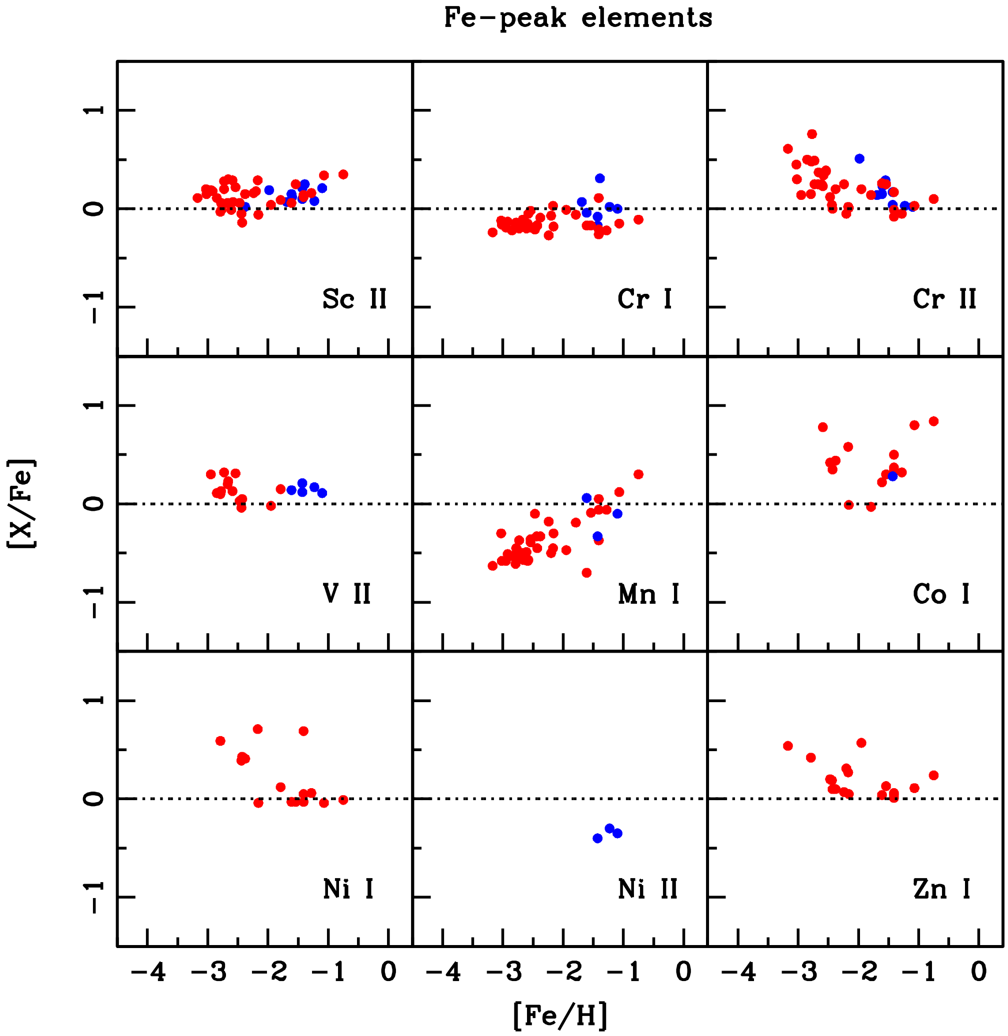

Figure 2.10 Abundance ratios of Fe-peak elements as a function of metallicity. The red and blue dots represent RHB and BHB stars.

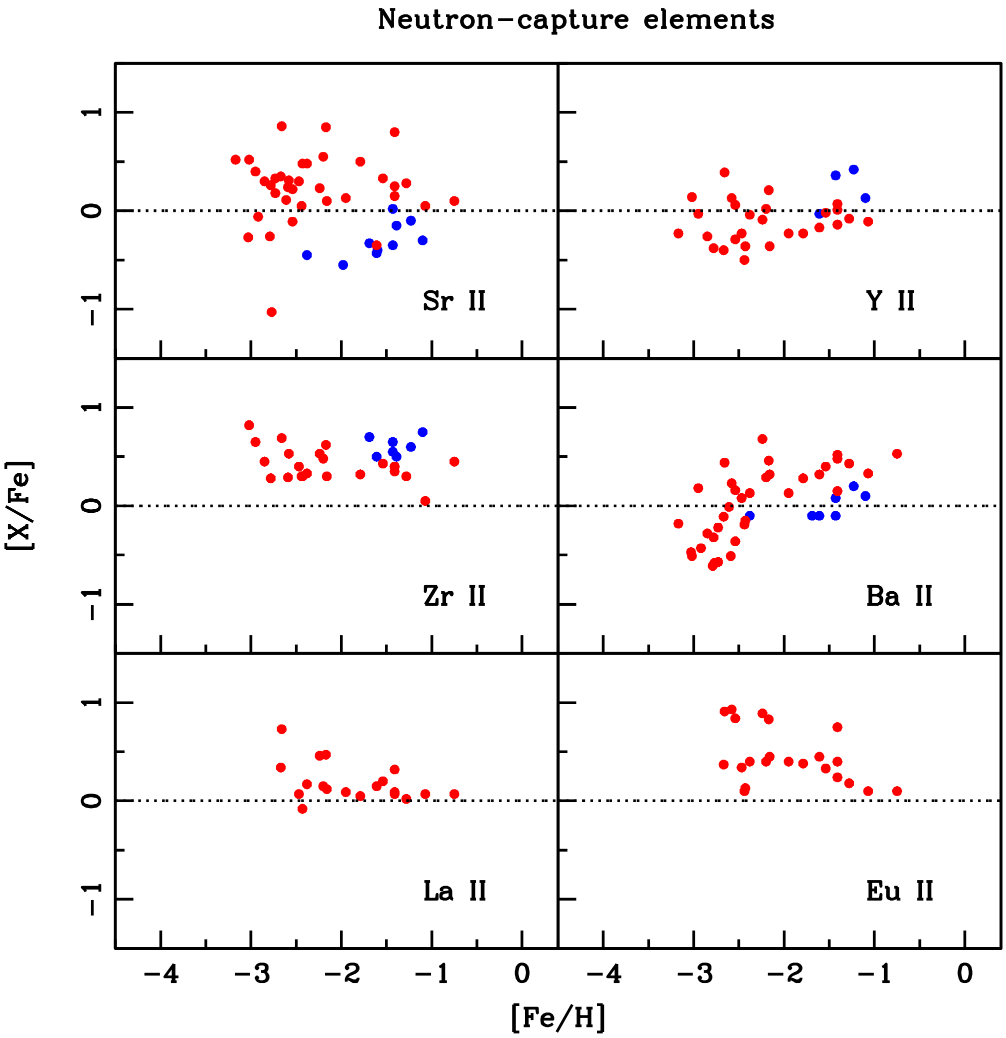

Figure 2.11 Abundance ratios of neutron-capture elements as a function of metallicity. The red and blue dots represent RHB and BHB stars.

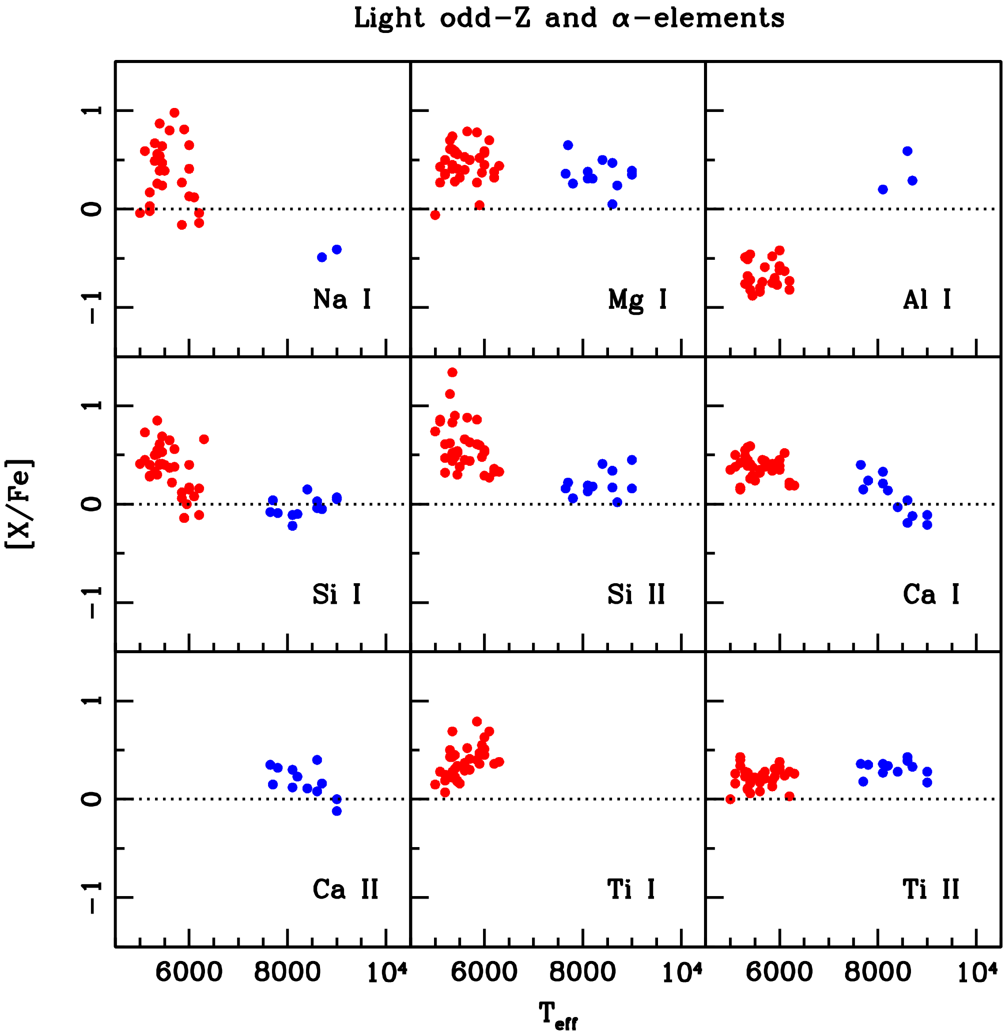

Figure 2.12 Abundance ratios of odd-Z and α-elements as a function of spectroscopic $T_{\rm eff}$. NLTE corrections applied to Na I, Al I, Si I & Si II as described in text. The red and blue dots represent RHB and BHB stars.

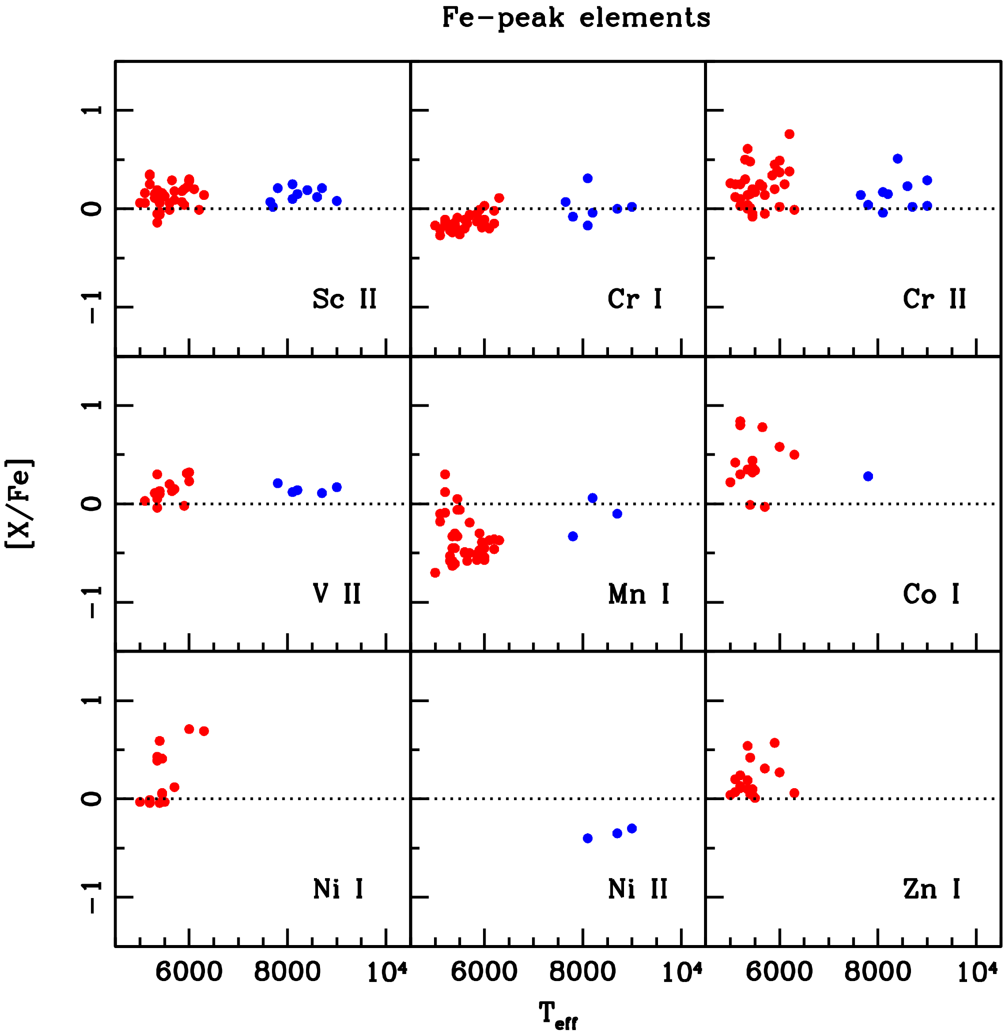

Figure 2.13 Abundance ratios of Fe-peak elements as a function of spectroscopic $T_{\rm eff}$. The red and blue dots represent RHB and BHB stars.

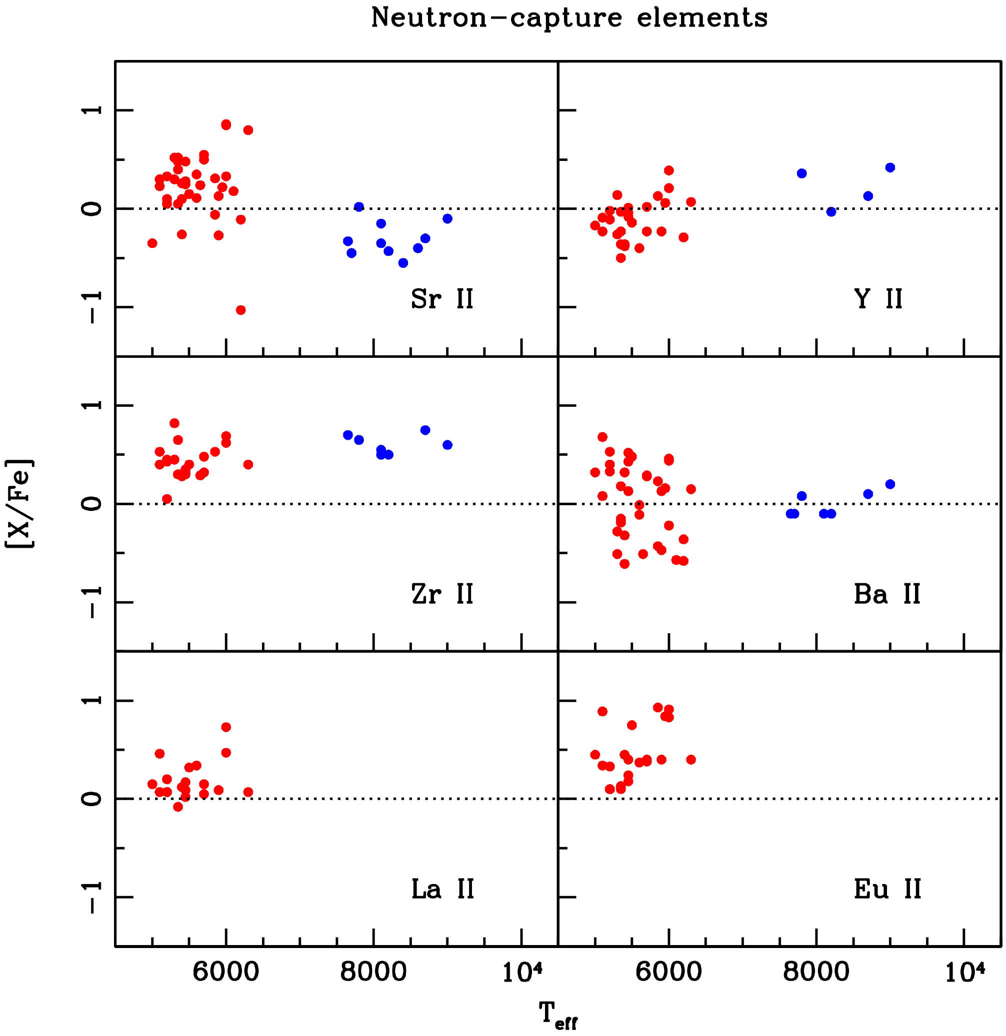

Figure 2.14 Abundance ratios of neutron-capture elements as a function of spectroscopic $T_{\rm eff}$. The red and blue dots represent RHB and BHB stars.

Table 2.9. Mean abundance ratios of various elements.

Element	RHB	*N*	BHB	*N*
Na I	0.37	27	−0.45	2
Mg I	0.47	36	0.36	12
Al I	−0.67	25	0.36	3
Si I	0.35	36	−0.03	12
Si II	0.59	35	0.21	12
Ca I	0.37	36	0.07	12
Ca II	···	···	0.18	12
Sc II	0.13	35	0.14	10
Ti I	0.37	35	···	···
Ti II	0.23	36	0.31	12
V II	0.14	14	0.15	5
Cr I	−0.14	36	0.02	7
Cr II	0.23	35	0.15	10
Mn I	−0.37	36	−0.13	3
Co I	0.41	15	0.28	1
Ni I	0.22	15	···	···
Ni II	···	···	−0.35	3
Zn I	0.19	18	···	···
Sr II	0.23	36	−0.30	10
Y II	−0.12	27	0.22	4
Zr II	0.42	23	0.61	7
Ba II	0.03	36	0.00	7
La II	0.19	19	···	···
Eu II	0.45	22	···	···

Table 2.10. Sensitivity of [X/Fe] with stellar parameters.

Stellar Parameters	Species Δ[X/Fe]	Star CS 22898−043	 HS 25532	 BD+18° 2890
$T_{\rm eff}$ + 150	Na I	···	+0.16	+0.16
(K)	Mg I	+0.09	+0.08	+0.25
log g+0.15	Na I	···	−0.05	−0.03
(dex)	Mg I	+0.01	−0.02	−0.01
[M/H]+0.1	Na I	···	−0.01	+0.00
(dex)	Mg I	···	−0.01	−0.01
$v_{\rm t}$+0.2	Na I	···	−0.01	−0.05
(km s^{-1})	Mg I	−0.05	−0.10	−0.07

Note. — Table 2.10 is published in its entirety in the electronic edition of For & Sneden (2010). A portion is shown here for guidance regarding its form and content.

2.6.1 Magnesium, Calcium and Titanium

It has been known for decades that metal-poor stars are generally overabundant in α-elements (e.g., Wallerstein et al. 1963). Our HB stars show standard enhancements in these elements, with neutral species <[Mg,Ca,Si,Ti/Fe]> $\simeq$ +0.3 (see Figure 2.9).

Two RHB stars, BD+18° 2890 and CS 22883−037, exhibit relatively low [Mg/Fe]. However, they exhibit normal abundances in other α-elements. Only a single Mg I line was analyzed in both of these cases, which resulted in larger abundance uncertainties. Caution is advised in interpreting the Mg abundances of BD+18° 2890 and CS 22883−037.

The calcium abundances of BHB stars have a larger scatter than those

Table 2.11. Sensitivity of [X/Fe] with stellar parameters for BHB star.

Stellar Parameters	Species Δ[X/Fe]	Star HD 93329
$T_{\rm eff} + 200$	Na I	+0.18
(K)	Mg I	+0.14
log $g + 0.15$	Na I	−0.03
(dex)	Mg I	−0.04
[M/H]+0.1	Na I	+0.01
(dex)	Mg I	+0.00
$v_{\rm t}$+0.2	Na I	−0.02
(km s^{-1})	Mg I	−0.01

Note. — Table 2.11 is published in its entirety in the electronic edition of the For & Sneden (2010). A portion is shown here for guidance regarding its form and content.

of RHB stars. There is also an offset, ~ 0.3 dex of mean [Ca/Fe] of RHB and BHB stars. We investigated this offset by synthesizing the Ca II 3933Å K-line of BHB stars. This line is rarely used in abundance analyses, as it is extremely strong in cool stars. In our case, the K-line could be analyzed in BHB stars, in which the line is not very strong and uncontaminated in most cases. There are weak interstellar contamination for HD 2857 and BD+25° 2602. However, it does not affect our abundances derivation, which is based on a Gaussian line profile fitting to the line. The abundances in BHB stars for Ca I and Ca II are approximately consistent with each other. The presence of the BHB/RHB offset is currently unknown. We also note that there is an unexplained trend of decreasing [Ca/Fe] with increasing $T_{\rm eff}$ for BHB stars (see Figure 2.12). Investigation of larger sample of BHB stars might resolve this puzzle.

There are no Ti I lines detectable in our BHB stars. Additionally, our log gf values for the Ti I lines are taken from the NIST compilation, for which the estimated uncertainties are large. In the RHB stars, Ti I lines are visible, but there are not many measurable lines. The analysis yields a trend of increasing [Ti I/Fe] with increasing $T_{\rm eff}$ (see Figure 2.12). This trend is opposite the sense of Si (discussed below) and has been noted by others (see Lai et al. 2008 and references therein). The abundance ratios derived from Ti II, unlike those of the other α-elements, do not decline as the metallicity increases. The mean value is flat, with small scatter, across the entire metallicity range. The Ti II-based titanium abundances should be trustworthy as many Ti II lines were used to determine the abundances.

2.6.2 The Alpha Element Silicon: A Special Case

Substantial dependence of [Si I/Fe] with temperature has been found in previous studies of metal-poor field stars (see Cayrel et al. 2004, Cohen et al. 2004, Preston et al. 2006a, Sneden & Lawler 2008 & Lai et al. 2008). This effect seems to depend entirely on $T_{\rm eff}$; there is no apparent trend with log g. To address this puzzle, Shi et al. (2009) investigated NLTE effects in warm metal-poor stars. They showed that the Si I 3905.53 Å lines and Si II 6347 Å, 6371 Å lines exhibit significant NLTE departures in warm metal-poor stars. Their study was limited to a sample of metal-poor dwarfs and a single cool giant. Observationally however, warmer FRHB stars (6000 K $\lesssim T_{\rm eff} \lesssim$ 6400 K) have similar Si abundances to those of metal-poor main sequence turnoff stars, [Si/Fe] $\simeq$ 0 (see Figure 10 of Preston et al. or Figure 5 of Sneden & Lawler), in spite of their large gravity differences ($<\Delta\log g> \sim 2$). Thus, the effect seems to be most dependent on $T_{\rm eff}$, so we assume that the predicted NLTE effects for main sequence stars will also affect our low gravity, metal-poor, warm RHB and BHB stars. Taking the offsets of +0.1 dex and −0.1 dex to the Si I and

Si II abundances from these lines, as suggested by Shi et al., we corrected the abundances of these two species in our program stars with $T_{\rm eff} \geq 6000$ K. Note that there is a large star-to-star scatter for RHB and BHB stars even after this adjustment (see Figure 2.12). This suggests, in agreement with the conclusions of Shi et al., that addition of an offset is inadequate to produce abundance consistency for this species.

The Si I abundances of all the BHB stars and the CS stars, with the exception of CS 22940−070, were exclusively derived from the 3905.53 Å line. As always, the reader is cautioned about the abundances derived from a single line. The blue-spectral region of hot stars are not overcrowded with lines, so blending is not an issue in this case. For cool stars, 3905.53 Å might be blended with a weak CH transition (Cohen et al. 2004) which would become stronger with decreasing temperature. However, Preston et al. (2006a) argue that the CH contamination in metal-poor RHB stars is very weak, and will not seriously affect the derived Si abundance. The line is thus essentially unblended and weak enough for abundance determinations in all BHB stars, and in RHB stars with $T_{\rm eff} \geq 5400$ K and $[{\rm Fe/H}] \leq -2$[10]. Lines of Si I in the red-spectral region ($>$ 5600Å) were used to derive abundances for the rest of the RHB stars. There are eight stars for which we used at least four lines for determining the abundances. For these stars, we derived $<$[Si I/Fe]$>$ = +0.42, which is consistent with the mean of typical α-enhancement in metal-poor stars.

In Figure 2.15, we summarize the Si I abundances found in large-sample studies and the spectral regions that were used to derive the Si I abundances. All investigators agree on the declining trend of [Si I/Fe] with increasing $T_{\rm eff}$

---

[10] We could not determine a Si abundance for HD 119516 because our spectrum of the 3905Å line was corrupted by cosmic rays.

among cooler metal-poor stars, and we have shown that the abundances reach a (low) plateau in BHB stars. Resolution of this unsatisfactory situation is beyond the scope of this study.

An important check on the Si abundances is provided by our detection of Si II, which has mainly been studied in stars with $T_{\rm eff} > 10{,}000$ K. Only a handful of dwarfs have reported Si II abundances (see Stephens & Boesgaard 2002), and no prior investigation has been done for RHB stars. In general, Si II lines are very weak for RHB stars, only becoming strong (EW > 30 mÅ) in BHB stars. We caution that weak lines and 1–3 Si II lines were used for deriving the Si II abundances.

In Figure 2.16, we illustrate the mixture of lines that have been used to derive Si II abundances for both RHB and BHB stars. The scatter of [Si II/Fe] is large but the mean abundances agree with the general α-enhancement indicated by Mg and Ca for our HB stars. We find unusually large Si II abundances for CS 22955−174 and CS 22937−072. However, they show normal enhancement in Si I (i.e., +0.3 and +0.5 dex, respectively). Unfortunately, in both cases, only 1–2 Si I or Si II lines were used to derive their abundances, so these abnormally large abundances should be viewed with caution.

2.6.3 Light Odd-Z Elements Sodium and Aluminum

For sodium abundances, we used mainly the Na I resonance D-lines (5889.9 Å, 5895.9 Å). Only a few of the cooler RHB stars have detectable, albeit weak, higher excitation Na I lines (the 5682.6 Å, 5688.2 Å and the 6154.2 Å, 6160.7Å doublets). We visually inspected the D-line spectral region to search for ISM contamination of the stellar lines. Any suspected line blending resulted in dropping the D-line measures for a star. The derived [Na/Fe] values

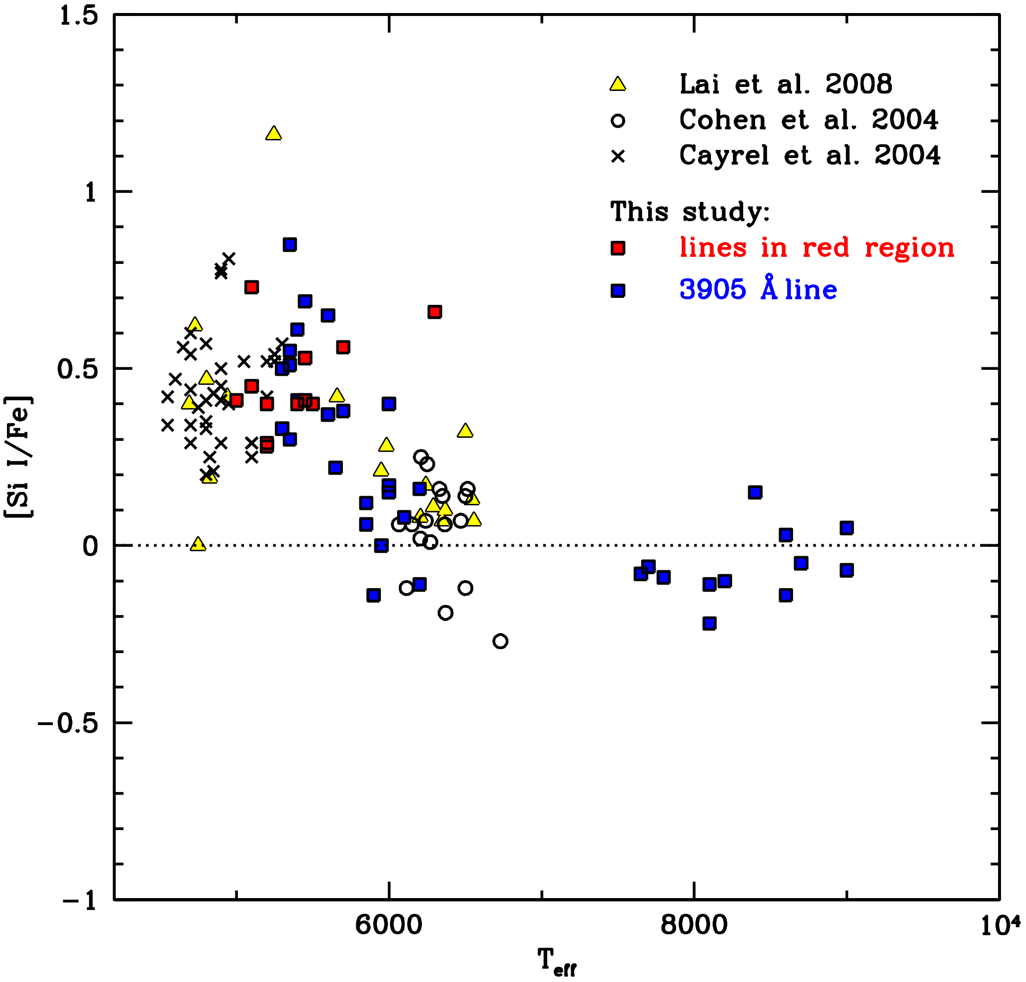

Figure 2.15 Abundance ratios of [Si I/Fe] vs spectroscopic $T_{\rm eff}$, with the addition of data of very metal-poor stars giants from Cayrel et al. (2004) (crosses), low-luminosity near-turnoff stars from Cohen et al. (2004) (open circles) and stars in different evolutionary states from Lai et al. (2008) (yellow triangles). The derived [Si I/Fe] in this study is represented by filled rectangles. NLTE correction applied to [Si I/Fe] as described in text. The red and blue colors represent Si I lines in red spectral region and 3905 Å line, respectively.

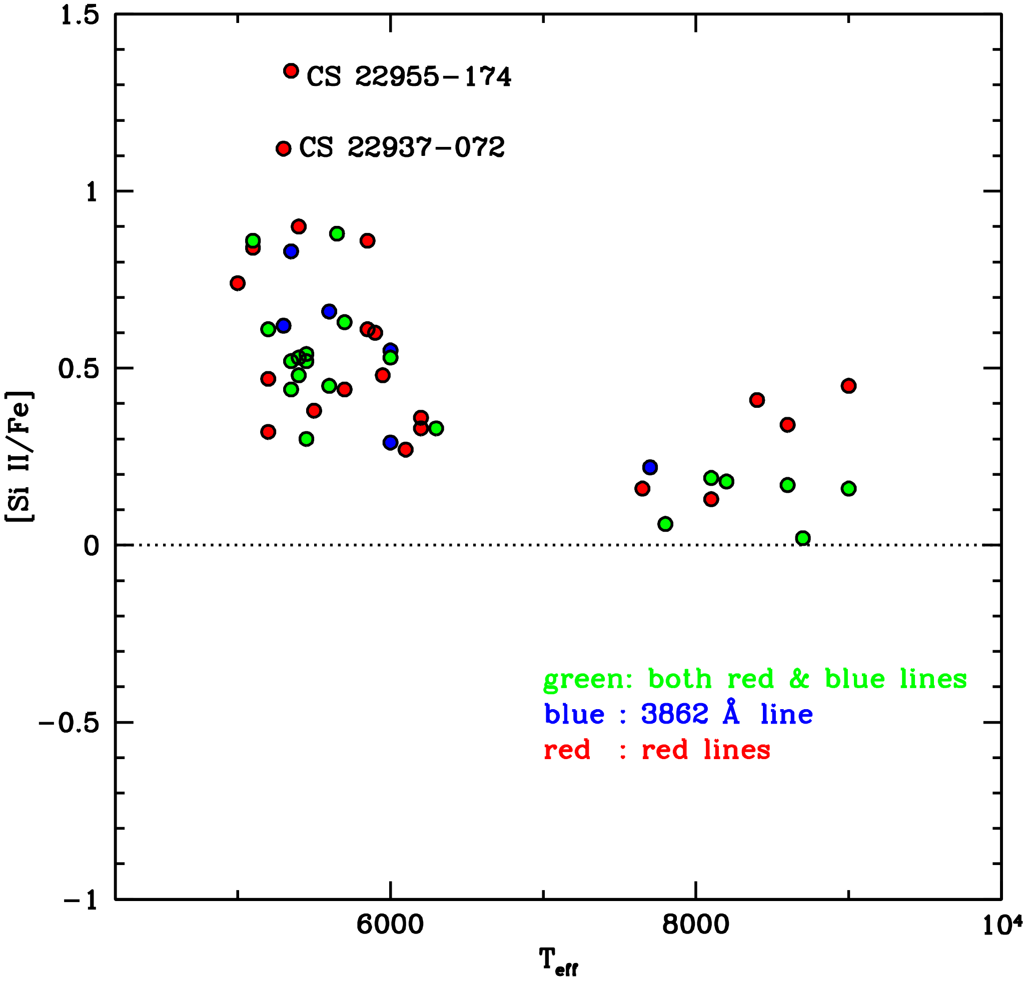

Figure 2.16 Abundance ratios of [Si II/Fe] vs spectroscopic $T_{\rm eff}$. NLTE correction applied to [Si II/Fe] as described in text. The colors represent the usage of lines in different spectral regions for EW analysis.

exhibit a large star-to-star scatter (see Figure 4.43). We warn the reader that the Na I D-lines are relatively strong in the RHB stars as compared to the BHB stars. Unfortunately, there are only two BHB stars in our samples that have measurable, clean D-lines. Therefore, we could not make direct comparison with the star-to-star scatters in BHB and RHB stars. Nevertheless, the large variations derived here are consistent with those seen in previous field metal-poor star studies (see Pilachowski et al. 1996; Venn et al. 2004 and references therein).

Aluminum is underabundant in RHB stars, $<$[Al/Fe]$>\simeq -0.64$, and overabundant in BHB stars, $<$[Al/Fe]$>\simeq +0.36$ (see Figure 2.9). There are only two Al I lines, the resonance transitions 3944 Å and 3961 Å in the blue spectral region, which we can employ for this study. The 3944 Å line can be contaminated by CH transition (Arpigny & Magain 1983). However, it is not an issue in our very warm BHB stars and it is even undetectable in our metal-poor RHB stars. Additionally, the 3961 Å line can only be a reliable abundance indicator in metal-poor stars, as it is affected by the strong wing of Ca II H and Hϵ features in higher metallicity stars (Sneden & Lawler 2008). Higher excitation Al lines in the red spectral region, e.g., the 6696 Å, 6698 Å pair, generally result in higher [Al/Fe] (see discussion of Francois 1984). The discrepancy of [Al/Fe] between the transitions of red and the blue spectral region is currently not completely understood. Unfortunately we could not detect the red Al I lines in our stars.

As noted by others, Na D lines and the Al I red and blue resonance spectral region can be significantly altered from NLTE effects. These corrections are important for warm, metal-poor turnoff stars with $T_{\rm eff}\gtrsim$ 6000 K (Baumueller et al. 1998). The suggested NLTE corrections are -0.5 dex for Na

(Baumueller et al. 1998) and +0.65 dex for Al (Baumueller & Gehren 1997). Since the majority of our RHB stars are below this T_{eff} we only applied NLTE corrections of suggested values to Na and Al abundance ratios of our BHB stars.

2.6.4 The iron-peak elements: Scandium through Zinc

.

Scandium lines can have substantial hyperfine substructure. We synthesized a few Sc II lines with their full substructure, and found that the abundances derived from synthesis do not differ by more than 0.05 dex from those derived by the single-line EW method. Thus, we used the EW method for deriving all final Sc II abundances. A study by Cohen et al. (2004) showed that there are discrepancies of [Sc II/Fe] among different evolutionary groups of metal-poor stars, in which they are generally enhanced in main sequence stars while RGB stars exhibit deficiencies. Our results are more in accord with those of main-sequence stars, $<$[Sc II/Fe]$>\simeq +0.13$ (see Figure 2.10).

Our vanadium abundances come exclusively from V II lines, which were detectable in both RHB and BHB stars. We find no trends of [V/Fe] with either [Fe/H] or T_{eff}.

Chromium abundances derived from Cr I transitions generally yield smaller abundances than those from Cr II lines in metal-poor stars (e.g, Preston et al. 2006a, Sobeck et al. 2007, and references therein). Ideally, we would have preferred to use recent laboratory transition probabilities for both Cr I (Sobeck et al. 2007) and Cr II (Nilsson et al. 2006) for our study. However, there are no Cr II lines studied by Nilsson et al. (2006) that are routinely detectable in our spectra. Therefore, we employed the transition probabilites of detectable Cr I and Cr II lines from Sobeck et al. (2007) and NIST, respectively. The offset between Cr I & Cr II remains (see Figure 2.10). The trend of increasing Cr II with decreasing metallicity is due to large line detection/measurement uncertainty; only 1–2 lines were used in relatively metal-poor, RHB stars. This offset is also present in the detailed Cr transition probability study of Sobeck et al. (2007). Ionization imbalance or non-LTE effects could be the cause.

A trend of increasing [Cr I/Fe] with increasing $T_{\text{eff}} < 7000\ K$ has also been found for RHB stars (see Figure 2.13). This was first pointed out by Lai et al. (2008) (see their Figure 21). Clearly no such trend is apparent in our BHB stars.

Manganese has been shown to be substantially underabundant in field and halo metal-poor dwarf and giant stars (see, e.g, Sobeck et al. 2006, Lai et al. 2008, and references therein). Our analysis yields $<$[Mn/Fe]$>\simeq -0.35$. The general trend of increasing [Mn/Fe] with at higher [Fe/H] metallicities in our HB sample is in agreement with those and other previous studies. We refer the reader to review the extensive discussion of Sobeck et al. (2006) regarding the production of Mn.

We derived nickel abundances via spectrum synthesis of the Ni II 4067 Å line and the remaining iron-group elements from EW analysis. The reader should be cautious in interpreting the Co I, Ni II, and Zn I abundances, as they were determined with only 1–2 lines each. There are insufficient data to define an abundance pattern of Ni II at this point. Our [Ni I/Fe] values are generally near solar for moderately metal-poor stars ([Fe/H] > 2.0). The larger star-to-star scatter for very metal-poor stars ([Fe/H] < 2.0) is probably not real, as only one weak Ni I line was used in our analysis, resulting in uncertain Ni abundances for individual stars.

Zinc has multiple abundant isotopes (^{64,66,67,68}Zn), but the isotopic / hyperfine substructure of Zn I lines are not large and the observed features are weak (Timmes et al. 1995). Therefore we treated Zn I lines as single absorbers. The discussion of [Zn/Fe] will be given in §2.8.1.

2.6.5 The neutron capture elements: Strontium, Yttrium, Zirconium, Barium, Lanthanum and Europium

We derived the strontium abundances using the available Sr II lines, namely 4077 Å, 4161 Å and 4215 Å. These lines are particularly hard to analyze in RHB stars because they are strong and/or partially blended. For example, the 4077.8 Å resonance line can be affected by Dy II 4078.0 Å and possibly La II 4077.3 Å. We illustrate this in Figure 2.17, which shows an example of the Sr II 4077 Å synthesis superimposed on the observed spectrum of an RHB star. The Dy abundance cannot be determined reliably with the spectra. Therefore, the adopted Dy abundance was arbitrarily changed to produce the best fit to the red wing of the observed Sr II line profile.

The star-to-star scatter in Sr abundances is large (see Figure 2.11). These variations are intrinsic to the stars, as can be easily seen in the spectra. In Figure 2.18 we show a few examples. Comparison of stars with similar stellar parameters (i.e., CS 22186−005 and CS 22875−029 in this figure) shows that the large scatter in [Sr/Fe] ratios is real. We also note an offset (~ 0.5 dex) of Sr abundance ratios between the RHB and BHB stars, which is not present in Yttrium and Zirconium abundance ratios (see Figure 2.11 & 2.14). This offset may be related to the large Sr II line strength difference between the two HB groups. Additionally, contamination of the lines by other species, which plagues the RHB spectra, is not an issue in the BHB stars.

We performed EW analysis for Yttrium lines. The star-to-star scatter is also large in this element but the analytical uncertainties are smaller for Y abundances than for Sr abundances. We compare a Y II line in stars with similar metallicity in Figure 2.19. The comparison shows that stars with similar metallicity possess different [Y II/Fe].

Syntheses were performed for Zr II 4149 Å, 4161 Å, 4090 Å and 4317 Å lines, whenever present in the spectra. Generally Zr appears to be overabundant as compared to its neighboring light *n*-capture elements Sr and Y. We caution that the Zr II lines are generally very weak, and the resulting abundance uncertainties are thus large.

Barium is a much-studied member of the heavier *n*-capture element group. Its lines are affected by both hyperfine substructure and isotopic splitting. A line list with full Ba II substructure is given in McWilliam (1998). We adopted the solar abundance ratio distribution among the $^{134-138}$Ba isotopes (Lodders 2003), and synthesized the Ba II lines at 4554 Å, 5853 Å, 6141 Å, and 6496 Å, whenever present in the spectra. We note that the 4554 Å line is always substantially stronger than the other lines, and Ba abundances derived from this line can be severely affected by microturbulence and damping.

The spectral lines of La have significant hyperfine substructure, and those of Eu have both hyperfine substructure and isotopic substructure. There are two natural occurring isotopes, ^{151,153}Eu, for which we adopted the solar abundance ratio distribution (Lodders 2003). We employed La II 4086 Å and 4123 Å lines and Eu II 4129 and 4205 Å lines for abundance analysis. In general, Eu and La lines are very weak. None are detectable in BHB stars, and only 1–2 lines are available in RHB stars.

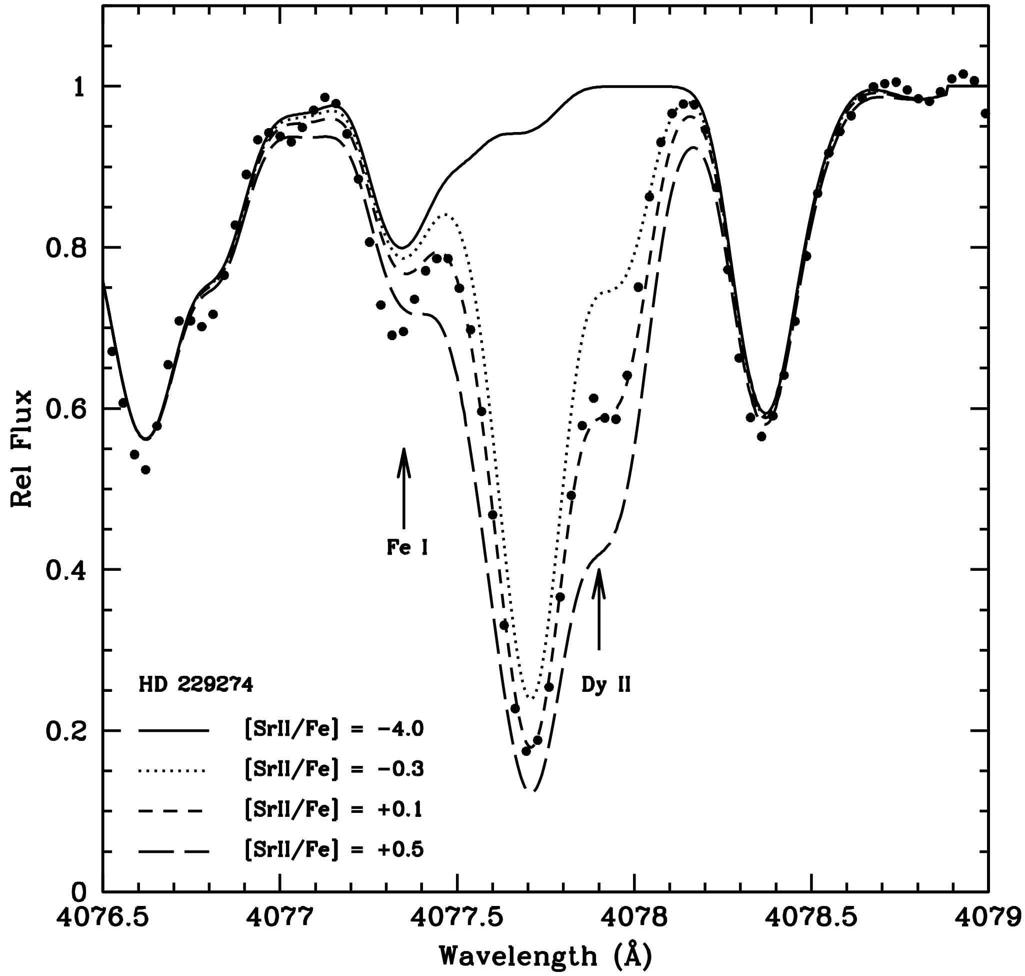

Figure 2.17 An example of synthesized Sr II 4077 Å line superimposed on the observed spectrum. The assumed Fe abundance is the same as the metallicity used in the stellar parameters. The solid and medium dashed lines represent no Sr contribution and derived Sr abundance ratio for this line. The dotted and long dashed lines are ±0.4 dex of derived Sr abundance ratio.

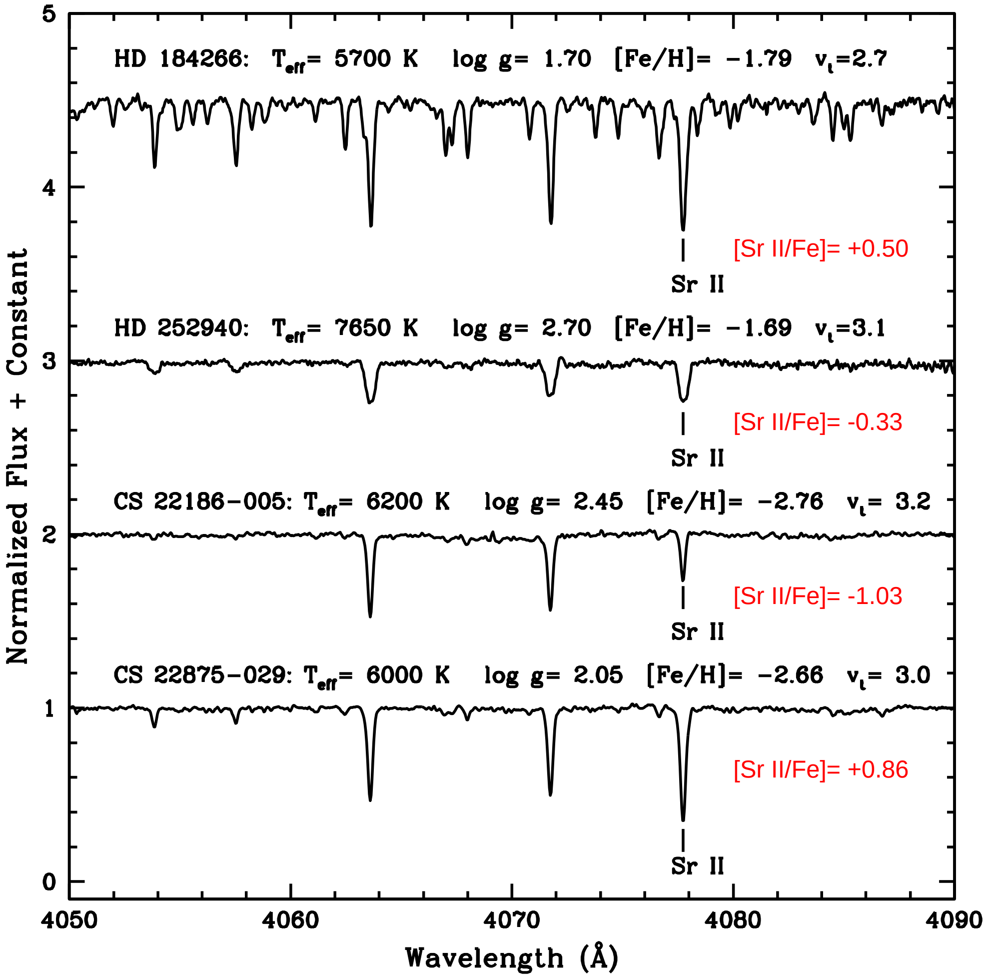

Figure 2.18 The top two spectra show the different Sr II line strength between RHB and BHB stars. As shown, Sr II line in BHB stars is not as strong as in RHB stars. The bottom two stars posses similar stellar parameters but show different line strength in Sr II line.

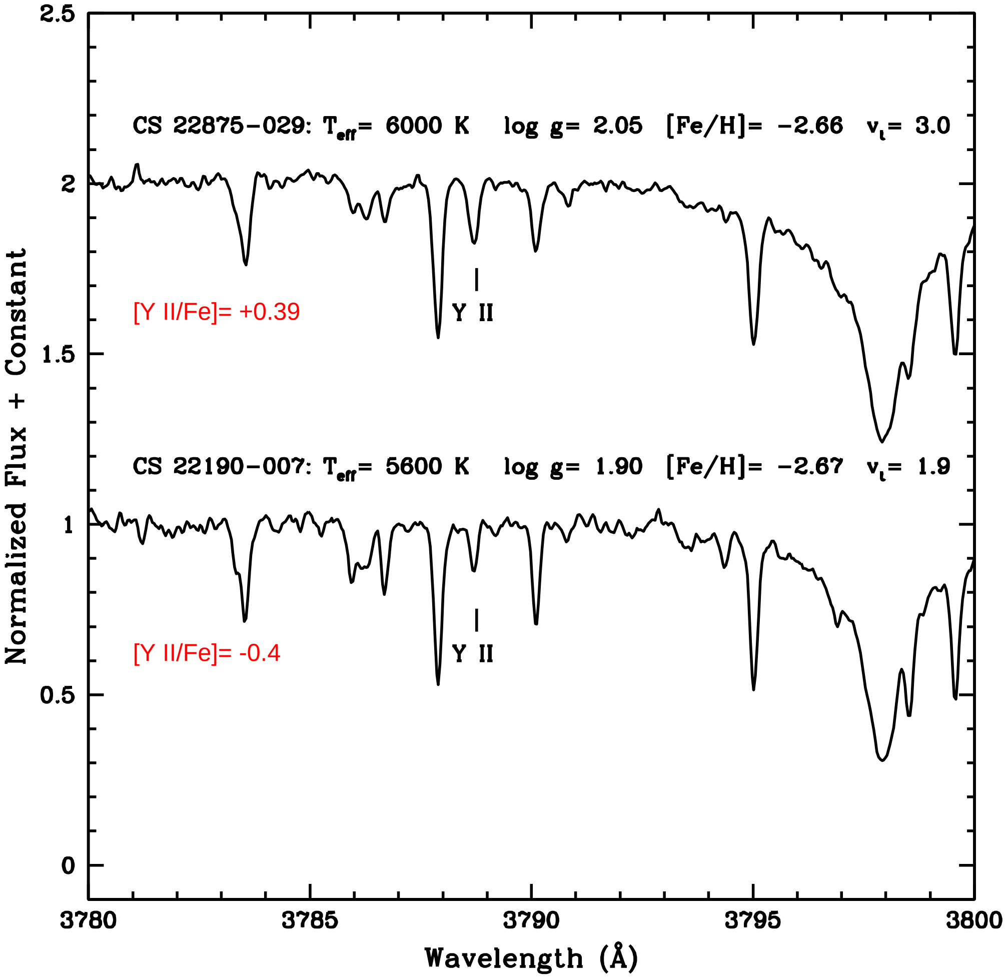

Figure 2.19 Comparison of Y II line strength of stars with similar [Fe/H]. The low and high Y II abundance ratios of these two stars contribute to the scatter of [Y II/Fe] vs [Fe/H].

2.7 Evolutionary States

2.7.1 $T_{\rm eff} - \log g$ Plane

We investigated the physical properties of our HB samples, by comparing our derived temperatures and gravities using the α-enhanced, HB models of Pietrinferni et al. (2006). These models implemented the low T-opacities of Ferguson et al. (2005) and an α-enhanced metal distribution that represents typical Galactic halo and bulge stars. The α-enhancement treatment is particularly important because the α-elements are overabundant in metal-poor stellar atmospheres, and they are major donors of electrons for the $\rm H^-$ continuum opacity. We adopted the HB canonical models of various metallicities with $\eta = 0.4$. The models of Pietrinferni et al. were chosen because they provide a fine grid of masses and time steps in contrast to other available HB models.

In order to convert the bolometric luminosities $L/L_\odot$ of the models for each mass to log g values, we adopted Eq. (2) of Preston et al. (2006a),

$$\log\, g = \log(M/M_\odot) + 4\log T_{\rm eff} \; - \log(L/L_\odot) - 10.607, \tag{2.2}$$

in which the constant was evaluated by using the solar $T_{\rm eff}$ and log g values. In Figure 2.20, we show the spectroscopic $T_{\rm eff}$ and log g values of our stars and the field RR Lyraes that are based on spectroscopic $T_{\rm eff}$ and log g of Lambert et al. (1996), and, photometric $T_{\rm eff}$ and Baade-Wesselink log g of Clementini et al. (1995), on the $T_{\rm eff}$–log g plane. Both their data and our samples exhibit similar gravity scatter at fixed temperature.

To estimate the uncertainties associated with the Pietrinferni et al. (2006) HB models, we compare their luminosities (as translated into log g) for a given mass with Lee & Demarque (1990)'s HB model (i.e., [Fe/H]$= -2.26$,

Table 2.12. Comparison of HB model

Model	Mass ($M/M_\odot$)	$\log T_{\rm eff}$ (K)	$\Delta \log g^{\rm a}$	$\Delta \log L^{\rm a}$
Lee & Demarque (1990)	0.56	4.22	+0.02	−0.02
Lee & Demarque (1990)	0.56	4.26	+0.11	−0.11
Lee & Demarque (1990)	0.78	3.86	−0.01	+0.01
Lee & Demarque (1990)	0.78	3.72	+0.09	−0.09

[a] Pietrinferni et al. (2006) minus Lee & Demarque (1990) model

$Z = 0.0001$, $Y = 0.23$).[11] The comparison is summarized in Table 2.12. The difference in log g in the two studies is $\lesssim$0.1 dex, much smaller than the uncertainties in our spectroscopic log g values. Therefore, model choice is not an issue in contributing significant error on the mass derivation.

2.7.2 Derivation of HB Masses

Our mass estimation uses HB evolutionary tracks in the $T_{\rm eff} - \log g$ plane. As discussed in §2.5.1, spectroscopic log g values are generally lower than the photometric ones, which would result in deriving more low mass HB stars. Therefore, a correction of the spectroscopic gravities is necessary and adopting the photometric gravities is more appropriated to represent the physical gravities.

Preston et al. (2006a) derived an empirical relation for computing photometric gravities (log $g_{\rm phot}$) by using their spectroscopic gravities (log $g_{\rm spec}$)

---

[11] Dorman et al. (1993) also published HB models with similar parameters, but their time steps are too large to be useful in this exercise.

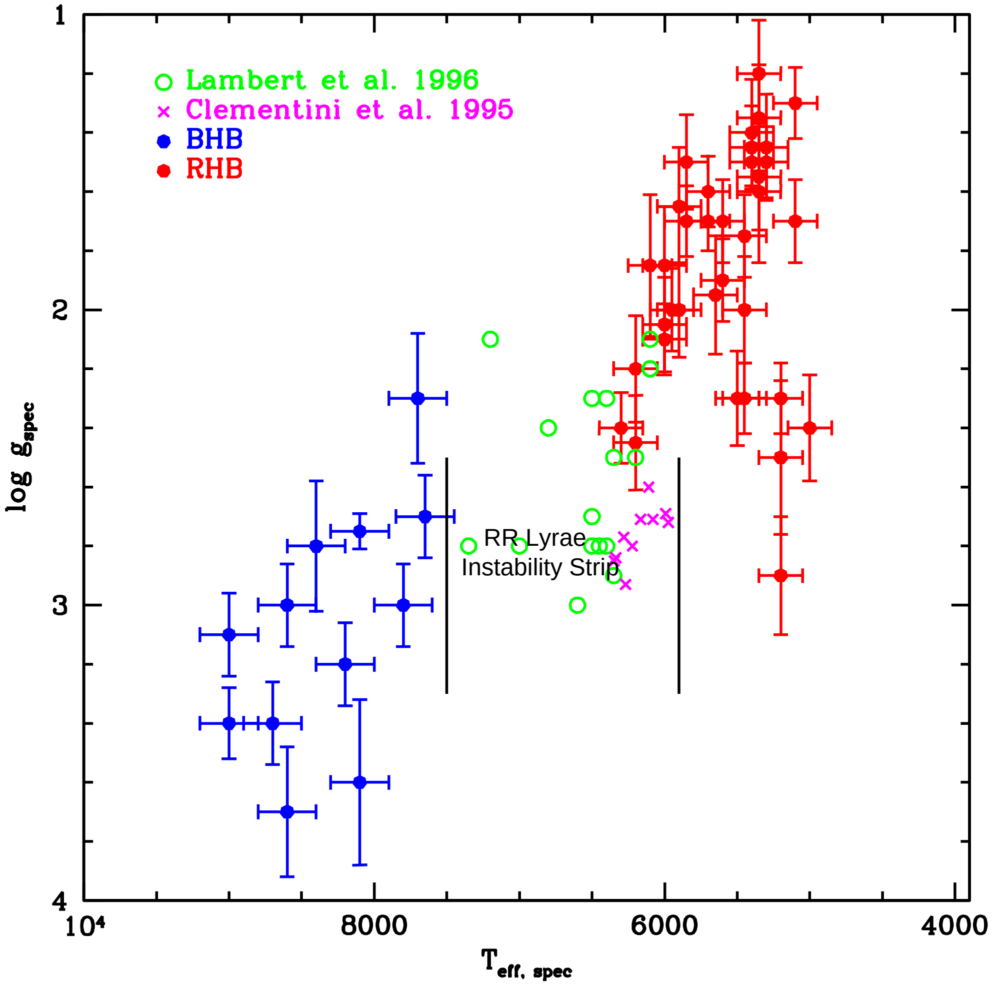

Figure 2.20 The spectroscopic $T_{\rm eff}$ and $\log g$ of our RHB and BHB stars (red and blue dots), and $T_{\rm eff}$ and $\log g$ of field RR Lyraes from Lambert et al. 1996 and Clementini et al. 1995) (green open circles & magenta crosses) on the $T_{\rm eff}$–log g plane.

in conjunction with the existing log $g_{\rm phot}$ of M 15. We adopted this relation,

$$\log\, g_{\rm phot} = \log\, g_{\rm spec} + 28.802 - 7.655 \log T_{\rm eff,spec} \tag{2.3}$$

to obtain the log $g_{\rm phot}$ for all our RHB stars. While there are published log $g_{\rm phot}$ data for BHB stars in other GCs (Behr 2003a), there are no useful log $g_{\rm spec}$ values for comparison (Behr 2003a suggested that their measurements are too uncertain to provide any useful information on this issue). Additionally, Preston et al. showed that the corrections to log $g_{\rm spec}$ decline with increasing $T_{\rm eff}$ and essentially disappear at the red edge of the RR Lyr IS (see their Figure 17). This can be understood by noting that the continuous opacity of a hotter star is dominated by H^-, and the dominant electron donor is hydrogen itself rather than the metals. The electron density rises sharply with increasing $T_{\rm eff}$ among RHB stars. Examination of atmosphere models for the M15 RHBs (from Preston et al.) suggests that in the line-forming regions, the electron pressure increases by a factor of more than 30 from the coolest ($T_{\rm eff}$ = 5000 K) to the warmest ($T_{\rm eff}$ = 6250 K) stars. This higher electron pressure helps to enforce LTE in the ionization equilibria in warmer HB stars. Thus, we assume the spectroscopic log g for our BHB stars is correct and no correction is applied. Future spectroscopic investigation of log g for BHB stars in GCs would be welcome.

After calculating RHB log $g_{\rm phot}$ values, we estimated the masses of individual HB stars by employing an interpolation scheme. To account for different metallicities of our program stars, we first chose two models that closely match a star's [Fe/H] and superimposed them on the $T_{\rm eff}$-log g plane along with the $T_{\rm eff,spec}$ and log $g_{\rm phot}$. Then, calculating the linear interpolation between these two metallicities and masses:

$$M_{\rm star} = M_1 + \frac{(M_2 - M_1)}{([Fe/H]_2 - [Fe/H]_1)} \times ([Fe/H]_{\rm star} - [Fe/H]_1) \qquad (2.4)$$

where M_1, M_2 are estimated masses from the two models, and $[\mathrm{Fe/H}]_1$,$[\mathrm{Fe/H}]_2$ are the two models' iron abundances. For stars positioned outside the model mass range ($0.503M_\odot \le M \le 0.80M_\odot$), we chose the mass that is within the $\log g$ and $T_{\rm eff}$ errors of the star on $T_{\rm eff}$–$\log g$ plane. If there is no mass track lies within the errors, we constrain the upper mass limit to be 0.8 $M_\odot$, the approximate turnoff mass of a old metal-poor main-sequence star. In Figure 2.21, we show an example of a set of HB stars superimposed on the HB tracks ([M/H]$= -1.79$ and -2.27) that were used to derive their masses. We summarize the derived masses as a histogram in Figure 2.22 and parameters used to derive the masses is listed in Table 2.13.

The inferred mass distributions have means at 0.59 $M_\odot$ and 0.56 $M_\odot$ for RHB and BHB stars, respectively (see Figure 2.22). If we exclude those RHB stars that have masses set to the upper limit ($M > 0.8M_\odot$), the mean masses for RHB and BHB stars are both 0.56 $M_\odot$, and the median masses are 0.54 $M_\odot$ and 0.56 $M_\odot$.

This estimated mean mass is smaller than the HB masses found in some GCs, e.g. M3, for which Valcarce & Catelan (2008) derived mean masses of 0.633 $M_\odot$ and 0.650 $M_\odot$ for RHB and BHB stars, respectively. We also do not find a bimodal or multi-modal HB mass distribution that appears to exist in many GC's (see Valcarce & Catelan; Catelan 2004). Several reasons could contribute to these differences. (1) GC's are mostly mono-metallic, in contrast to the large metallicity range of our FHB stars. We have needed to use multiple evolutionary tracks that correspond most closely to the individual metallicities of our FHB stars (refer back to the interpolation method as described above). (2) Our sample sizes of RHB and BHB stars are too small to clearly indicate statistically significant mass distributions. (3) We have used an empirical correction to spectroscopically-determined log g values, which directly impacts the derived masses. (3) Our samples consist more RHB than BHB stars, where the majority agglomerate near the low mass end, resulting in more low mass HB estimates. (4) Finally, Valcarce & Catelan cautioned about over-interpretation of masses derived from the GC CMD method, because they are biased against stars in later evolutionary states. Thus, it is not clear that our mean masses are substantially different than those reported for M3.

Additionally, other GC HB mass studies have reported mean masses in reasonable agreement with ours. For example, de Boer et al. (1993) obtained $< M_{\rm HB} >= 0.5\ M_\odot$ for NGC 6397. Masses of nearby HB stars derived via *Hipparcos* parallaxes have slightly smaller mean masses, $< M_{\rm HB} >= 0.38\ M_\odot$, than ours (de Boer et al. 1997). Finally, the evolutionary and structural models of Sweigart (1987) suggest a wide range of individual HB masses (0.2–1.2 $M_\odot$). We conclude that our derived mean masses for the field HB stars are reasonable.

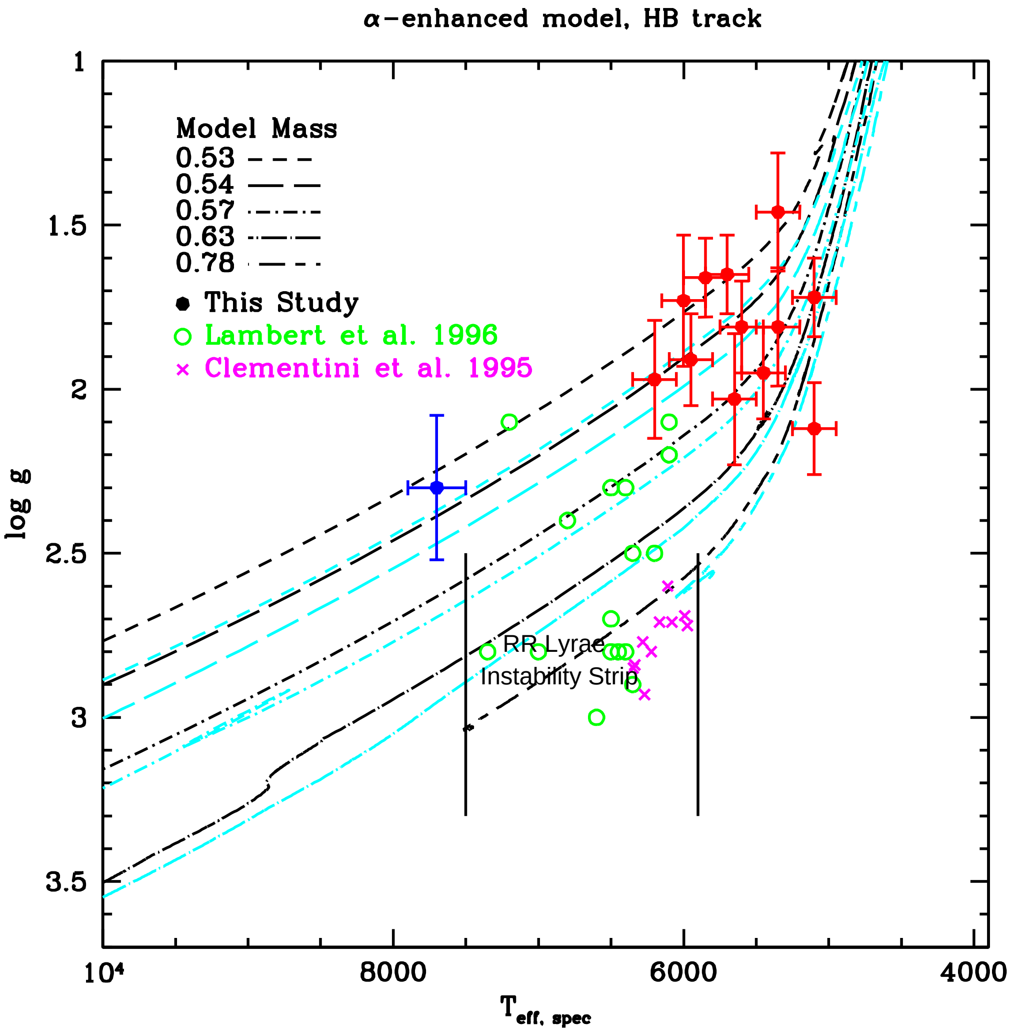

Figure 2.21 The spectroscopic $T_{\rm eff}$ and photometric/spectroscopic $\log g$ of a set of our RHB and BHB stars (red and blue dots) overlaid on α-enhanced HB tracks of [M/H]$= -1.79$, $Z = 0.0003$, $Y = 0.245$ (black) and [M/H]$=-2.27$, $Z = 0.0001$, $Y = 0.245$ (cyan). These HB tracks were used to derive the masses of this set of HB stars. The $T_{\rm eff}$ and $\log g$ of field RR Lyraes are from Lambert et al. 1996 and Clementini et al. 1995 (green open circles & magenta crosses).

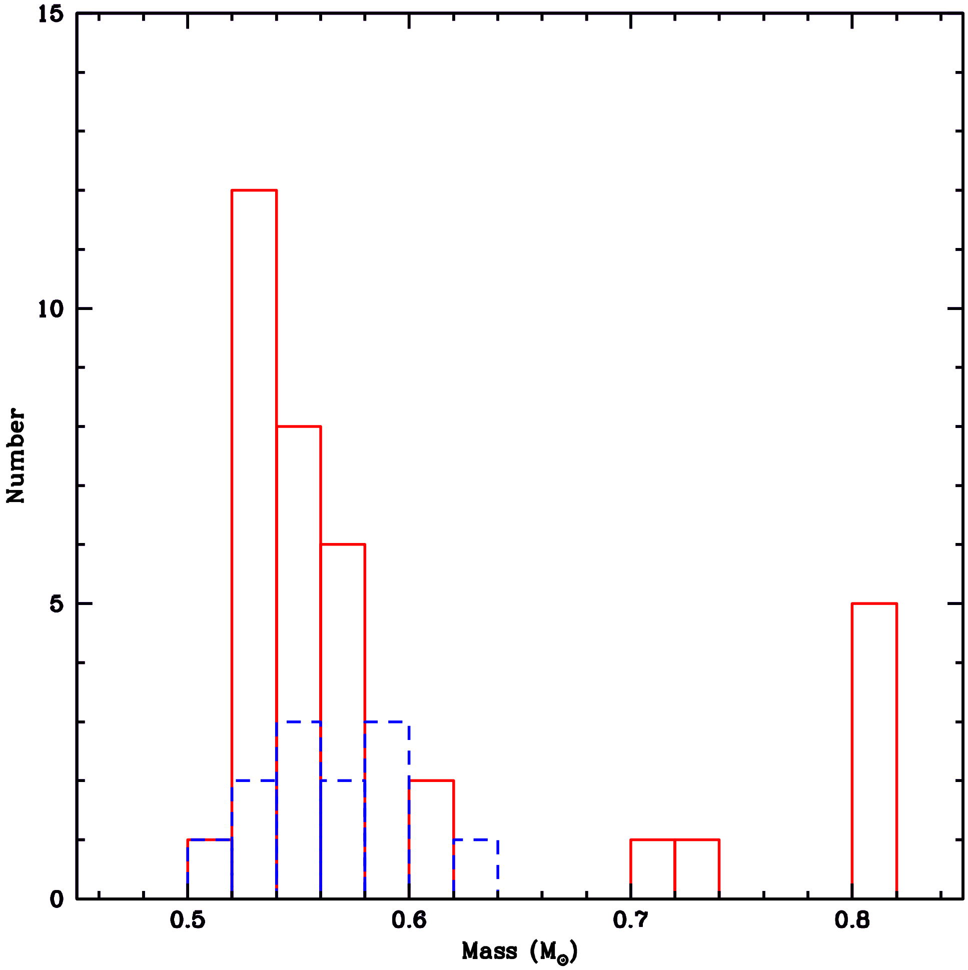

Figure 2.22 The red (solid) and blue (dashed) histograms represent the estimated RHB and BHB masses. The mean masses for RHB and BHB stars are 0.59 $M_\odot$ and 0.56 $M_\odot$. Excluding the upper mass limit RHB stars ($M > 0.7\ M_\odot$), the mean masses are 0.56 $M_\odot$ for both RHB and BHB stars. The median masses for RHB and BHB stars are 0.54 $M_\odot$ and 0.56 $M_\odot$, respectively.

Table 2.13. Estimated HB masses and Parameters Used

Stars	$T_{\mathrm{eff,spec}}$ (K)	$\log g$ (dex)	[Fe/H] (dex)	Mass $M_{\odot}$
		RHB		
HD 6229	5200	2.86^{a}	-1.07	0.80
HD 6461	5200	3.26^{a}	-0.75	0.80
HD 25532	5450	2.20^{a}	-1.41	0.60
HD 105546	5200	2.66^{a}	-1.54	0.80
HD 119516	5400	1.73^{a}	-2.16	0.54
BD+18° 2890	5000	2.89^{a}	-1.61	0.80
BD+11° 2998	5450	2.50^{a}	-1.28	0.72
BD+09° 3223	5100	1.72^{a}	-2.47	0.61
BD+17° 3248	5100	2.12^{a}	-2.24	0.80
HD 184266	5700	1.75^{a}	-1.79	0.52
HD 229274	5500	2.47^{a}	-1.41	0.73
CS 22882−001	5950	1.91^{a}	-2.54	0.54
CS 22190−007	5600	2.01^{a}	-2.67	0.58
CS 22186−005	6200	2.22^{a}	-2.77	0.57
CS 22191−029	6000	1.98^{a}	-2.73	0.55
CS 22883−037	5900	1.59^{a}	-1.95	0.52
CS 22878−121	5450	1.95^{a}	-2.38	0.57
CS 22891−184	5600	1.81^{a}	-2.61	0.54
CS 22896−110	5400	1.68^{a}	-2.78	0.54
CS 22940−077	5300	1.74^{a}	-3.02	0.56
CS 22955−174	5350	1.61^{a}	-3.17	0.54
CS 22940−070	6300	2.12^{a}	-1.41	0.53
CS 22879−103	5700	1.65^{a}	-2.20	0.52
CS 22879−097	5650	2.03^{a}	-2.59	0.57
CS 22940−121	5350	1.86^{a}	-2.95	0.57
CS 22898−043	5900	1.94^{a}	-3.03	0.55
CS 22937−072	5300	1.79^{a}	-2.85	0.57
CS 22948−006	5400	1.63^{a}	-2.79	0.54
CS 22944−039	5350	1.46^{a}	-2.43	0.52
CS 22951−077	5350	1.81^{a}	-2.44	0.56
CS 22881−039	6100	1.68^{a}	-2.73	0.53
CS 22886−043	6000	1.73^{a}	-2.17	0.52
CS 22875−029	6000	1.93^{a}	-2.66	0.54
CS 22888−047	5850	1.66^{a}	-2.58	0.53
CS 22941−027	6200	1.97^{a}	-2.54	0.54
CS 22945−056	5850	1.46^{a}	-2.92	0.52
		BHB		
HD 2857	8100	2.48^{b}	-1.39	0.52
HD 8376	8600	2.38^{b}	-2.39	0.52
HD 252940	7650	1.77^{b}	-1.69	0.56
HD 60778	8100	1.63^{b}	-1.43	0.54
HD 74721	9000	1.93^{b}	-1.23	0.59

Table 2.13 (cont'd)

Stars	$T_{\mathrm{eff,spec}}$ (K)	$\log g$ (dex)	[Fe/H] (dex)	Mass $M_{\odot}$
HD 86986	8200	2.04^{b}	-1.61	0.63
HD 87047	7700	1.35^{b}	-2.38	0.53
HD 93329	8700	2.04^{b}	-1.10	0.59
HD 109995	8600	1.68^{b}	-1.60	0.56
BD+25° 2602	8400	1.56^{b}	-1.98	0.55
HD 161817	7800	2.01^{b}	-1.43	0.59
HD 167105	9000	1.63^{b}	-1.55	0.56

[a] Photometric $\log g$.

[b] Spectroscopic $\log g$.

2.7.3 Blue and Red Edges of the RR Lyrae Instability Strip: [Fe/H]> -2.5

Locations of the blue and red edges (BE and RE) of the RR Lyr IS provide powerful constraints on stellar pulsation theory. They can be determined directly by examining the color-magnitude diagram of GCs that are well populated with RR Lyrs. Unfortunately, this requirement eliminates most clusters.

Additionally, accurate cluster reddenings must be known to transformation from colors to T_{eff} values. Determining the blue and red edges from bright field RR Lyr stars via spectroscopic method can avoid these complications. For the metallicity regime [Fe/H]< -2.0, Preston et al. (2006a) estimated the fundamental red edge from the T_{eff} distributions of field RHB stars and GC RR Lyrs. Since HB colors are affected by metallicity, shifting slightly blueward with decreasing [Fe/H] (e.g., see Figure 1 of Sandage 1990), we repeated the exercise with our sample. We considered only those stars with [Fe/H]> -2.5, and compared the T_{eff} distributions of our field RHB and BHB with the distribution for field RR Lyr stars.

In Figure 2.23, the top and bottom panels show the distributions of spectroscopic and photometric T_{eff}'s of BHB and RHB stars with [Fe/H]> -2.5, respectively. The data for field RR Lyr stars (fundamental mode RR-ab and first overtone RR-c variables) in both middle panels are extracted from Lambert et al. (1996) and Clementini et al. (1995). It shows the RR Lyr distribution drops at T_{eff} = 5900 K and 7000 K. Both photometric and spectroscopic T_{eff} RHB distributions decline at $T_{\text{eff}} > 5700$ K and overlap with the RR Lyr distributions (bottom panels). We suggest that the weak overlap region, $\simeq$5900 K, is the red edge of field HB with [Fe/H]> -2.5. The T_{eff}'s of our BHB sample have no overlap with those of the RR Lyr stars. This is expected since RR-c type variables, which are bluer than the RR-ab type variables, are generally used for determining the BE, and there are only two RR-c type variables from Lambert et al. (1996) being included in the histogram (middle panels). Assuming the RR-c type variables defined the blue edge in this case, we approximated it to be 7400 K.

While field HB stars can be used for deriving red and blue edges, we warn that the method is not very robust. The lack of large BHB samples and uncertainties in T_{eff} values of field RR-c stars are limiting factors on our blue edge estimates. The overlapping distributions of field RHB and RR-ab stars also limit the red edge accuracy. Perhaps semi-empirical work (i.e., simulations to map the observed distributions) would provide a better constraints on the red and blue edges of FHB stars. Before then, deriving T_{eff}'s for a large sample of field BHB and RR-c will be needed.

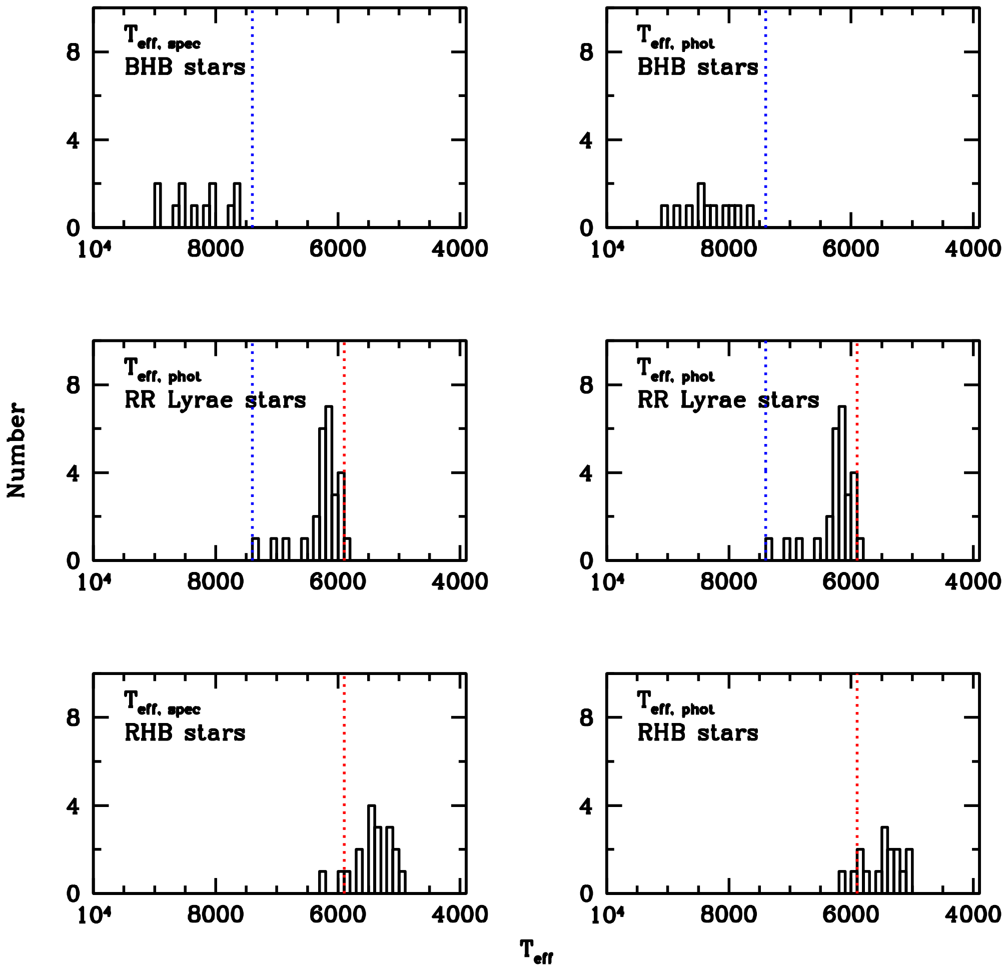

Figure 2.23 The top and bottom panels show the histograms of spectroscopic and photometric $T_{\rm eff}$ of BHB and RHB stars. The middle panels (same) are the photometric $T_{\rm eff}$ of field RR Lyr stars extracted from Lambert et al. (1996) and Clementini et al. (1995). The red and blue dotted lines represent the estimated fundamental red and blue edges of field RR Lyr IS for [Fe/H]> -2.5.

Table 2.14. Data Sources

References	Element
Venn et al. (2004)	Na, Mg, Ca, Ti, Ni, Y, Ba, La, Eu
Cohen et al. (2004)	Si, Al, Sc, Cr, Mn, Sr
Lai et al. (2008)	Si, Al, Sc, V, Mn, Zn, Sr, Zr
Fulbright (2000)	Si, Al, Cr, V, Zr
Reddy et al. (2003)	Al, Sc, Cr, V, Mn, Ni, Zn
Sobeck et al. (2006)	Mn
Cayrel et al. (2004)	Si, Zn
Stephens & Boesgaard (2002)	Si, Ni
Nissen et al. (2007)	Ni

2.8 Discussion

In this chapter we have explored the chemical compositions of non-variable RHB and BHB field stars. Here we will compare our results with abundances in other evolutionary groups of halo field stars, and discuss some of the possible nucleosynthetic implications. The comparisons of our [X/Fe] values with those of field stars are presented in Figures 2.24−2.26, where neutral and ionized species abundances of several elements have been averaged. We did not combine Cr I & Cr II abundances, since their distributions conspicuously diverge at lower metallicities (as discussed in §2.6.4). Data for field stars were mainly taken from the compilation of Venn et al. (2004). For those [X/Fe] that are not listed in Venn et al. (2004), we assembled the comparison samples from several references, which we summarize in Table 2.14.

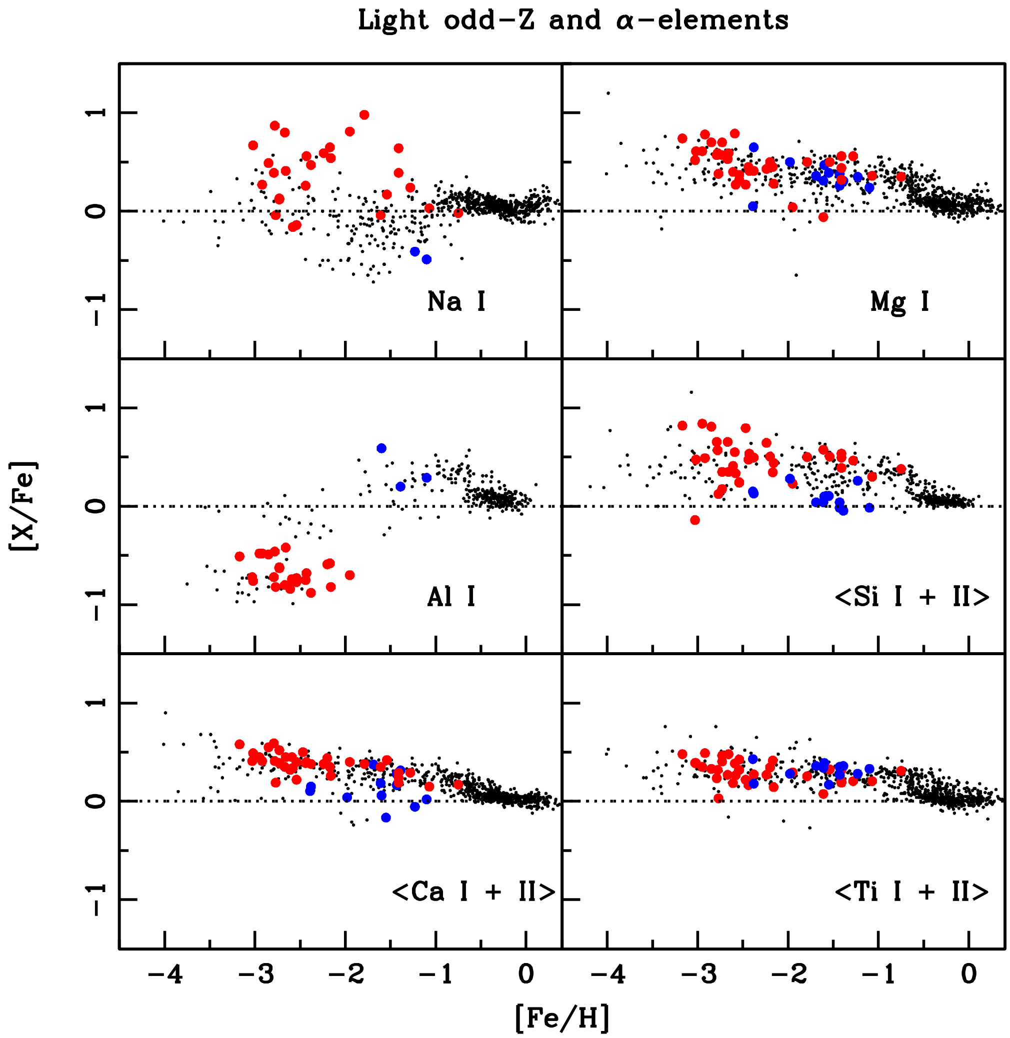

Figure 2.24 Abundance ratios of light odd-Z and α-elements in this study superimposed on the data assembled by Venn et al. (2004) and us. Mean of neutral and ionized species are used for comparisons. NLTE corrections applied to Na I, Al I, Si I & Si II for our HB stars. The red and blue dots correspond to RHB and BHB stars.

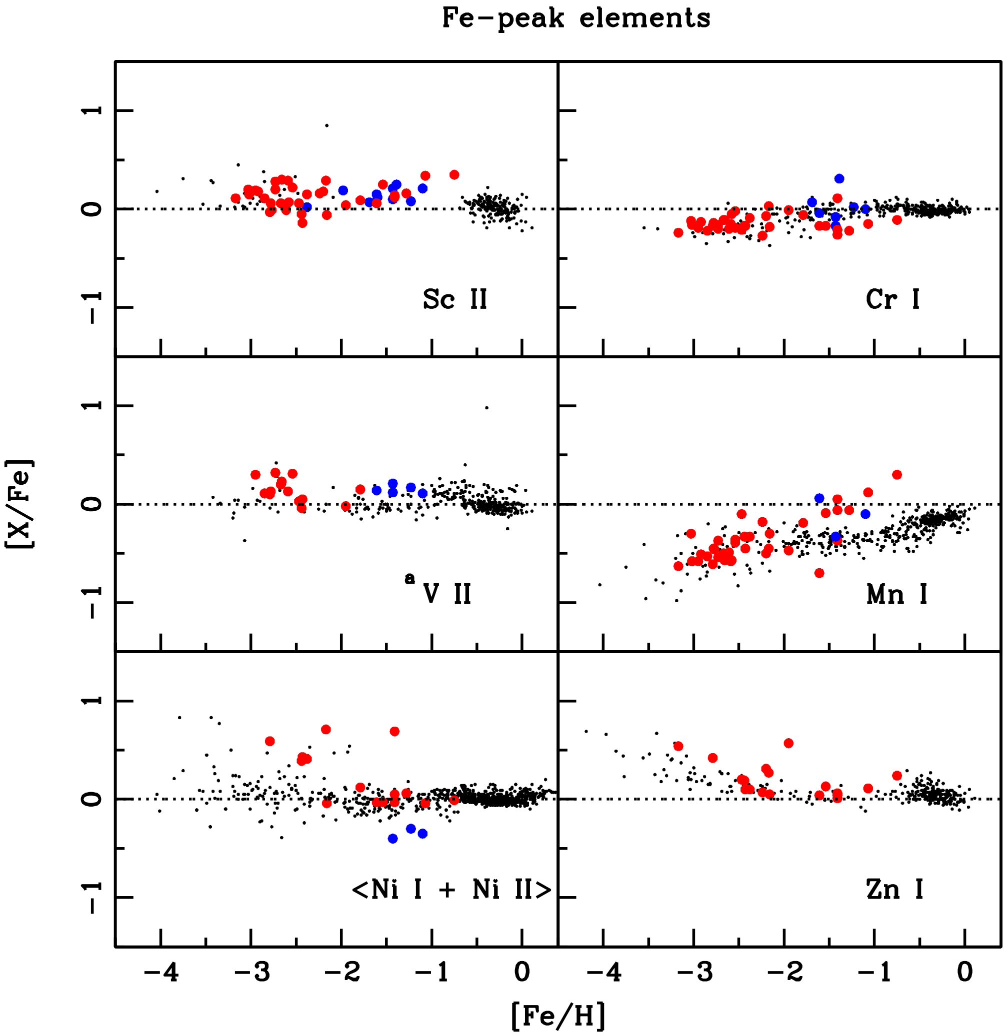

Figure 2.25 Same as Figure 2.24, except for Fe-peak elements. a: [V I/Fe] for stars possess [Fe/H] > 2.0 is used for comparison. The red and blue dots correspond to RHB and BHB stars.

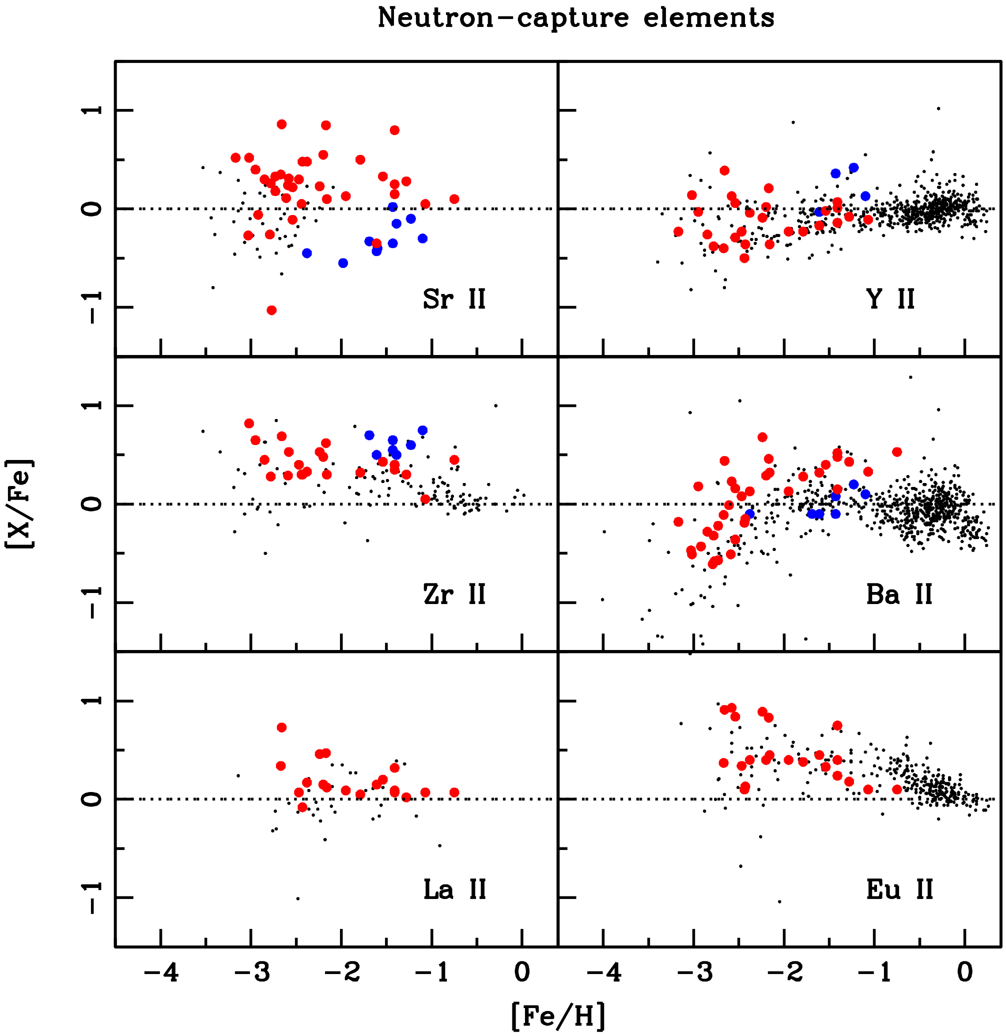

Figure 2.26 Same as Figure 2.24, except for n-capture elements. The red and blue dots correspond to RHB and BHB stars.

2.8.1 Light and Iron-peak Elements

Enrichment of α-elements in metal-poor stars has been known for decades. The explanation for this behavior presumes predominance of nucleosynthetic contributions from short-lived massive stars that died in core-collapse type II supernovae (SNe II) in early Galactic times. The resulting explosions contributed large amounts of light α-elements (e.g., O, Ne, Mg and Si), smaller amounts of heavier α-elements (e.g., Ca and Ti) and small amounts of Fe-peak elements to the ISM (Woosley & Weaver 1995). Longer-lived, lower-mass stars began to contribute their ejecta by adding more Fe-peak elements through Type Ia supernovae (SNe Ia) from lower-mass progenitors which exploded in thermonuclear runaway processes at later times. When SNe Ia became significant polluters of the ISM, a lowering of the [α/Fe] values (at higher metallicities) occurred.

In general our HB α-element abundances agree with those of other halo star populations. We illustrate this in Figure 2.24, where [Mg I/Fe] and [Ti I/Fe] of our RHB and BHB are in close accord with other field stars. The <[Si I+II/Fe]> and <[Ca I+II]> of RHB stars follow the general field star trend but these ratios tend to be lower for BHB stars in the same metallicity range (i.e., $\sim$ 0.35 dex lower). The offset of mean Ca abundances is mainly due to the lower [Ca I/Fe] of BHB stars (see description in §2.6.1). Similar lines were used in both BHB and RHB stars, as such, line selection is probably not the cause of the offset. As for <[Si I+II/Fe]>, the star-to-star scatter is large and the offset between RHB and BHB stars is dominated by the RHB star [Si I/Fe] dependence on $T_{\rm eff}$ (see §2.6.2).

Our BHB and RHB sodium abundance pattern looks quite different than in other field stars. However, little weight should be attached to our results because they have large uncertainties. We must rely solely on the Na D lines, and they are very strong in RHB stars. Aluminum is produced in massive stars, similarly to magnesium, but significantly deficient with respect to iron in metal-poor stars. The production of Al rises as it reaches the disk-to-halo transition at higher metallicity, i.e., [Fe/H] $\gtrsim 1.5$ (e.g., Timmes et al. 1995). Our abundances confirm this, with the caution that our derived trend with metallicity depends solely on RHB stars at low [Fe/H] and all BHB stars at high [Fe/H].

Iron-peak elements are believed to be largely produced during Type Ia and Type II SNe explosion events. In our metallicity regime the iron-peak abundances of main-sequence and RGB stars generally have their solar values, with the exception of Mn and Cu. The derived Fe-peak abundance ratios (i.e., Sc II, Cr I, and V II) of our RHB and BHB stars are also in agreement with those found in field dwarfs and giants (see Figure 2.25). Most of them are expected to be constant in all metallicity regimes. Manganese and Zinc are the exceptions. In common with previous studies, [Mn/Fe] ratios of our HB stars increase as metallicity increases, but the slope of this relation may be larger in our sample. We do not have a clear physical explanation to this, and caution that, (a) the trend is based on relatively few points, and (b) [Mn/Fe] is quite sensitive to stellar parameter choices (refer to Table 2.10 & 2.11). Again, we refer the reader to Sobeck et al. (2006) for the production of Mn.

For nickel abundances we must rely on Ni I lines for RHB stars and Ni II lines for BHB stars. The low Ni II abundances of BHB stars should not be given large weight, as they are solely derived from one line. The very large [Ni I/Fe] values of several RHB stars, substantially at variance with the general trend of field stars, are most likely due to the lack of many detectable lines.

The RHB stars with more than four lines contributing to their Ni abundance have ratios in good agreement with the field stars.

We find [Zn/Fe] $\simeq 0.0$ throughout the metallicity regime of [Fe/H] > -2.0, which is consistent with the study of Sneden et al. (1991). Recent work by Cayrel et al. (2004) shows increasing [Zn/Fe] at decreasing metallicities. Such a trend could indicate an α-rich freezeout process contribution to Fe-group element production at low metallicities. Our Zn abundance at low metallicity range, i.e., [Fe/H] < -2.0, perhaps consistent with this recent finding, but our data points are too sparse for firm conclusions on this point. Unfortunately, the comparison can only be made for RHB stars since the Zn I lines in BHB stars are too weak to be detected.

2.8.2 Neutron-Capture Elements

Elements heavier than the iron-peak (Z $>$ 30) cannot be efficiently synthesized by charged-particle fusion because of Coulomb repulsion and the endothermic nature of such reactions. They are produced in the late stages of stellar evolution via neutron-capture events, namely the *s*- and *r*-processes (see review by Sneden et al. 2008). The *s*-process occurs quiescently in the He-fusion zones of low or intermediate mass AGB stars, while the *r*-process is believed to occur explosively in neutron rich sites, e.g., Type II SNe or merging events of two neutron stars (Rosswog et al. 1999).

We have abundances for six *n*-capture elements in HB stars. Strontium, Yttrium and Zirconium are relatively light *n*-capture elements. In the solar system, they are attributed mostly to the “main” *s*-process (Arlandini et al. 1999). Barium and Lanthanum are heavier *n*-capture elements also primarily *s*-process elements in solar-system material. Europium is our sole representative of solar-system *r*-process elements.

Our HB *n*-capture abundance ratios are generally in accord with field star studies (see Figure 2.26). The offset of [Sr/Fe] between RHB and BHB stars are discussed in §2.6.5. Unfortunately, we do not have [Sr/Fe] for field stars with [Fe/H] > -2.0 for comparison. The resonance lines of Sr II are very strong for moderately metal-poor cooler stars and thus Strontium is not well represented in previous field-star surveys in this metallicity regime. We conclude that $<$[Sr/Fe]$>$ ~ 0 for [Fe/H] > -2.0.

Increasing star-to-star scatter with decreasing metallicity is apparent in the heavier *n*-capture elements Ba, La, and Eu, in accord with trends seen in other field star samples. A sharp downward trend of [Ba II/Fe] with decreasing metallicity becomes apparent for [Fe/H]< -2.0. This pattern is present in field stars studies as well. The [La/Fe] should roughly correlate with [Ba/Fe]. Unfortunately, we cannot easily detect La II lines in HB stars below [Fe/H] $\simeq -2.5$, where the drop in Ba abundance becomes apparent. The simplest explanation for the rise of [Ba/Fe] at [Fe/H] > -2.0 is that the *r*-process dominates Ba production at lowest metallicities while the *s*-process plays a more important role at higher metallicities (Busso et al. 1999).

The initial examination of our derived Europium abundances yielded six RHB stars with [Eu/Fe] > 0.5, well above the mean trend. However, high [Eu/Fe] has also been found in some field stars (as shown in Figure 2.26). For example, *n*-capture rich star CS 22892$-$052 has [Eu/Fe] $= +1.64$ (Sneden et al. 2003) and CS 31082$-$001 has [Eu/Fe] $= +1.63$ (Hill et al. 2002). The other *n*-capture elements of three of the Eu-rich RHB stars in our samples, i.e., CS 22875$-$029, CS 22886$-$043 and BD+17° 3248 are also high, implying that these three are truly *n*-capture rich stars. The overall *n*-capture abundance distributions for the other three RHB stars with Eu excesses are less certain. These six RHB stars deserve followup spectroscopic investigation of the *n*-capture elements.

2.8.3 Heavier vs Lighter Neutron-Capture Elements

Abundances of light *n*-capture elements Sr, Y, and Zr appear to be highly correlated with each other, and clearly they share a common nucleosynthetic origin (e.g., McWilliam et al. 1995; François et al. 2007; Aoki et al. 2005). In Figure 2.27, we compare the mean Sr-Y-Zr abundances the heavier element Ba for our HB stars, adding in the data of François et al. (2007). Only stars with detections of all of these elements are included in this plot. The comparison shows a tight correlation (i.e., increasing overabundant as decreasing Barium abundances), which suggests the correlation exists regardless of metallicity regime and evolutionary state.

To examine the contributions of the *r* and *s*-process ratios of metal-poor stars, abundances of Y, Ba, La and Eu are generally used. As discussed above, Y, Ba and La can be formed via *r* and *s*-processes, while Eu is largely formed via the *r*-process. In Figure 2.28, we plotted the [La/Eu], [Ba/Eu] and [Y/Eu] vs [Fe/H] of our HB samples along with those of Venn et al. (2004), Simmerer et al. (2004) and Woolf et al. (1995), and compare them with estimated pure *r*-process solar system abundances (Arlandini et al. 1999; Sneden et al. 2008).

The top panel shows the [La/Eu] distribution, which the rise of [La/Eu] as metallicity increases progresses slower than [Ba/Eu] and [Y/Eu]. The comparison between [La/Eu] and middle panel of [Ba/Eu] demonstrates that the larger scatter of [Ba/Eu] is due to the Barium not Europium abundances. The middle and bottom panels of [Ba/Eu] and [Y/Eu] show large scatter in very metal-poor stars regime, which suggests an inhomogeneous mixing in early Galactic time. We also find a slow increase of [Ba/Eu] and [Y/Eu] as the metallicity increases. The rise is further evidence of the increasing contribution of the *s*-process as metallicity increases (with time in the Galaxy). The slope of [Ba/Eu] for our HB stars is steeper than the field stars but the overall trend is indistinguishable from the large scatter. Also, the [Y/Eu] abundances are above the estimated pure *r*-process solar-system abundances, which again suggests that the *s*-process (from AGB stars) plays a significant role in Yttrium production.

2.8.4 CS 22186−005

The RHB star CS 22186−005 has an extremely low Sr abundance, i.e., [Sr II/Fe] = −1.03 (see Figures 2.18 and 2.26). As expected, there is no detection of the weaker Zr II and Y II in this star. However, we detected Barium, with an abundance ratio of [Ba II/Fe] = −0.58. Its Barium abundance follows the general declining trend of metal-poor stars that has metallicity below −2.0 (see Figure 2.26). The resulting abundance ratio, [Ba/Sr] = +0.45, is somewhat surprising because in most *n*-capture metal-poor cases, the heavier *n*-capture elements are underabundant with respect to lighter ones (as summarized in see Figure 7 of Sneden et al. 2008). Other heavier *n*-capture elements (i.e., Eu and La) were not detectable with our spectra of CS 22186−005, This star does not appear to have obvious abundance anomalies among the lighter elements.

In Figure 2.29, we extend Sneden et al's Figure 7 by adding in Sr and Ba abundances of our RHB and BHB stars. It is clear that CS 22186−005 is not the only metal-poor star that exhibits unusually large [Ba/Sr] ratios at

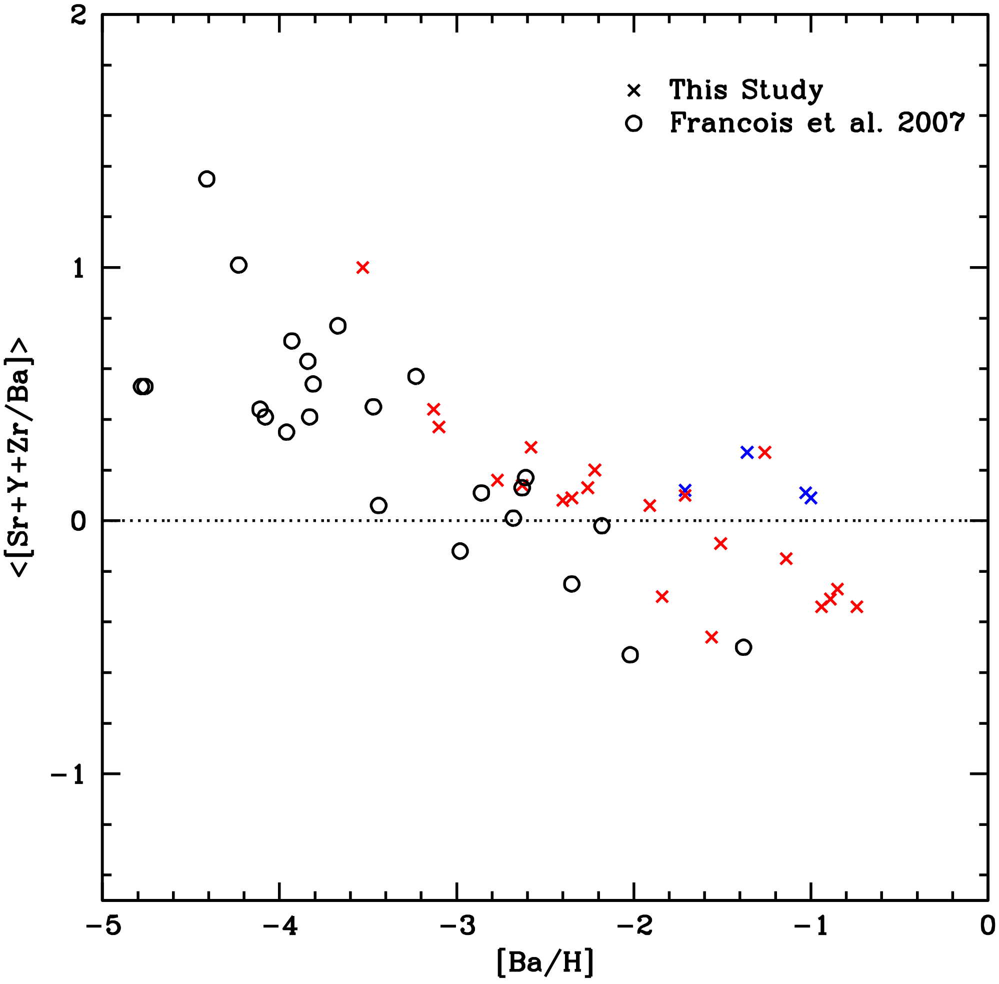

Figure 2.27 Mean abundance ratios of [Sr+Y+Zr/Ba] vs [Ba/H] (red crosses), with the additional data from François et al. (2007) (black open circles).

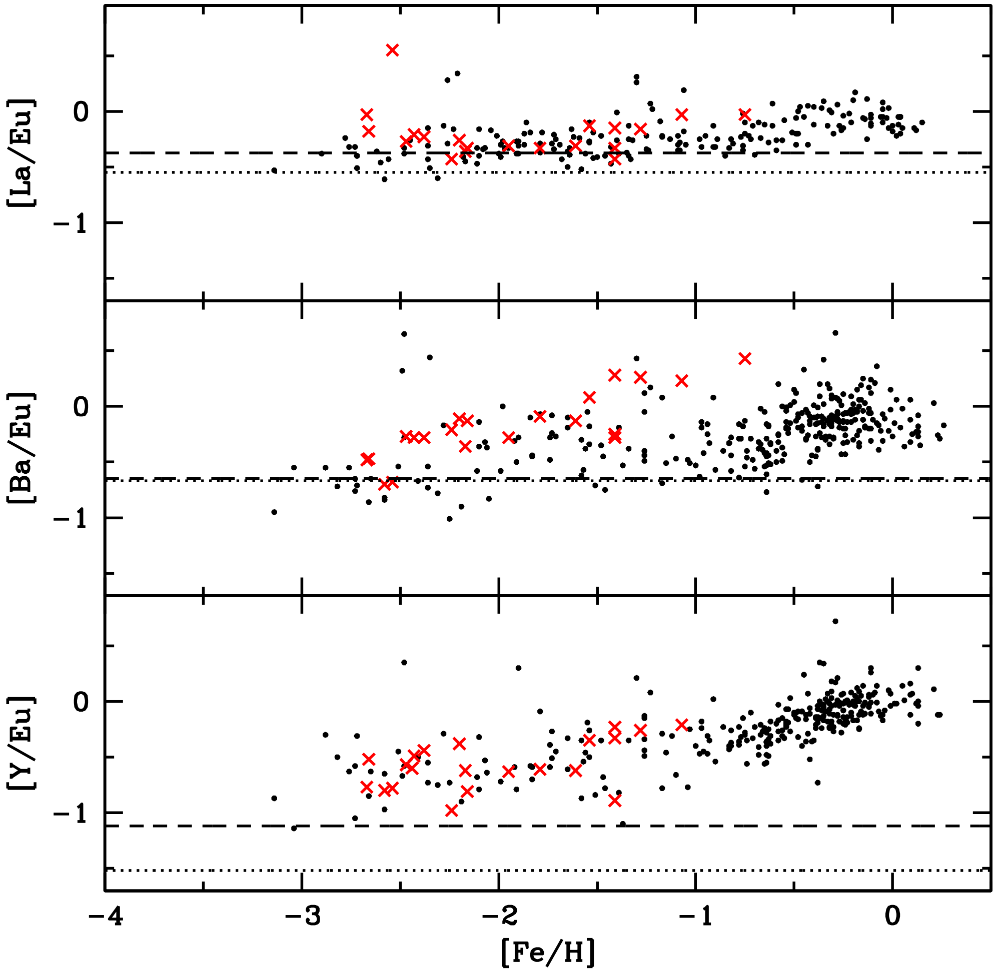

Figure 2.28 Comparison of light vs heavier n-capture elemental abundance ratios as a function of metallicity. These ratios are used to examine s and r-process enrichment. The dashed and dotted lines represent the estimated pure r-process from solar system abundances of Arlandini et al. (1999) and Sneden et al. (2008), respectively. The red crosses correspond to our RHB stars. The black dots represent La, Ba, Y, Eu from Venn et al. (2004), La, Eu from Simmerer et al. (2004) and Woolf et al. (1995).

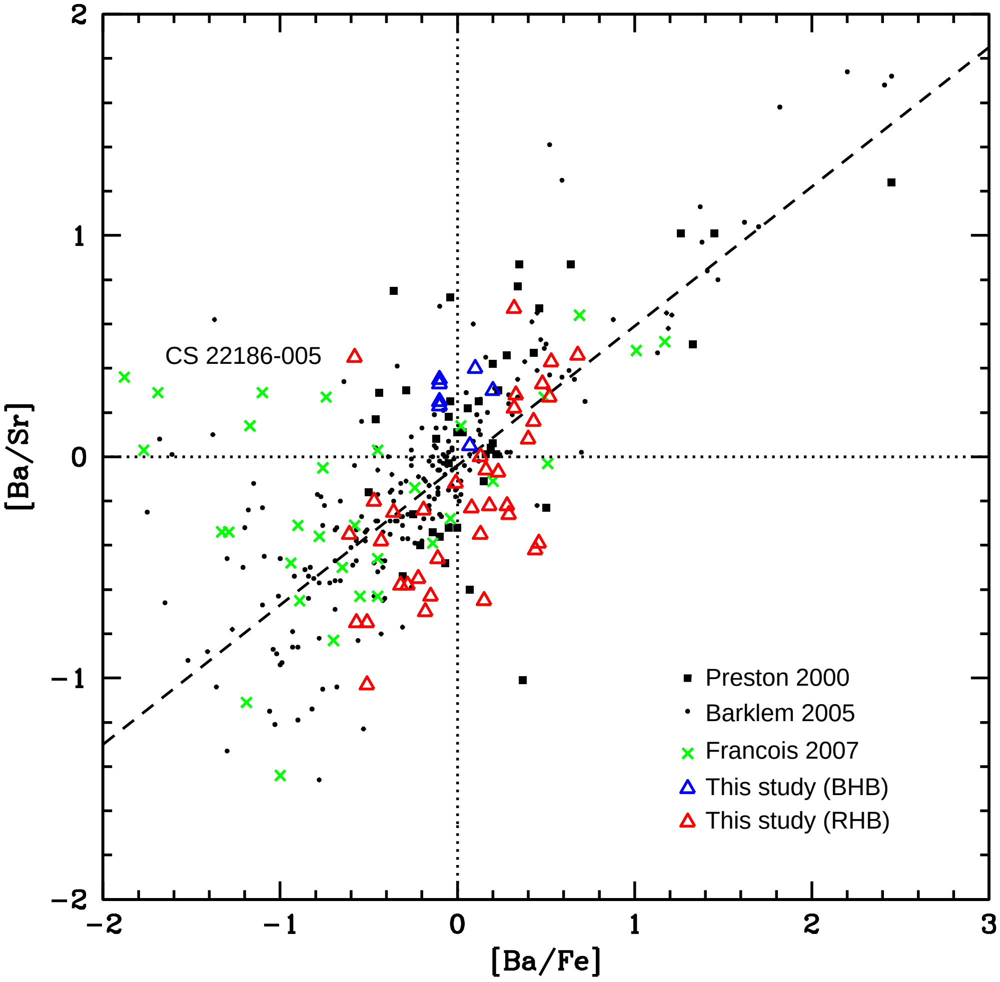

Figure 2.29 Abundance ratios of [Ba/Sr] vs [Ba/Fe]. The long dashed line represent the linear correlation between [Ba/Sr] and [Ba/Fe] (see Sneden et al. 2008). Solid, black rectangulars and dots represent studies of Preston & Sneden (2000a) and Barklem et al. (2005), respectively. Study by François et al. (2007) is represented in green crosses. Our RHB and BHB stars are represented by red and blue open triangles.

low [Ba/Fe]. Such stars have mainly been found among the very metal-poor giant sample of François et al. (2007). Clearly these stars provide further evidence that n-capture synthesis events cannot easily be characterized by single nucleosynthesis processes. Followup observations at higher S/N and resolution of this type of star should be undertaken.

2.9 Conclusions

We present the first large-sample detailed chemical composition study of non-variable field RHB and BHB stars. The high resolution spectra for our work were obtained with the 2.7-m telescope at the McDonald Observatory. The sample was selected from the survey of Behr (2003b). Additional RHB spectra from Preston et al. (2006a) were also added to the analysis. We derived the model stellar atmospheric parameters, $T_{\rm eff}$, log g, [Fe/H], and $v_{\rm t}$ for all program stars based on spectroscopic constraints. Of some interest is that the microturbulence of RHB stars increases with increasing $T_{\rm eff}$, in agreement with Preston et al. (2006a), while microturbulence appears to decline with increasing $T_{\rm eff}$ in BHB stars. More data on BHB stars to solidify this conclusion would be welcome.

Employing these stellar parameters, we derived relative abundance ratios, [X/Fe], of the α-elements, Fe-peak elements and n-capture elements for these stars. The abundance ratios vs metallicity of our RHB and BHB stars are generally in accord with other field star studies. In particular, the α-elements are overabundant, [Al I/Fe] (RHB stars only) and [Mn I/Fe] are underabundant for metal-poor stars. Large star-to-star scatter is present in [n-capture/Fe] abundance ratios.

Finally we investigated the physical properties of our RHB and BHB stars by locating them in the $T_{\rm eff}-\log g$ plane, and comparing them to HB evolutionary tracks of Pietrinferni et al. (2006), in order to estimate individual stellar masses. The mass distribution suggests that the majority of our stars have $M \sim 0.56\ M_{\odot}$. By comparing the $T_{\rm eff}$ distribution of our field RHB and BHB stars with the field RR Lyraes of Lambert et al. (1996) and Clementini et al. (1995), we estimated the temperatures of red and blue edges of the RR Lyr IS for stars with [Fe/H]> -2.5. We derived 5900 K and 7400 K, respectively for these edges.

The general consistency of HB abundance ratios with those of other dwarf and giant halo star samples justifies that HB stars can be used routinely in the future for Galactic sturcture-metallicity studies (such as investigations of stellar streams). More importantly, this work provides a starting point for our study on chemical compositions of RR Lyr stars (see chapter 4). Determinations of abundances of these stars throughout their pulsational cycles will be examined in detail with the same methods as have been employed in this chapter.

Chapter 3

Radial Velocities and Pulsation Ephemerides of 11 Field RR Lyrae Stars

3.1 Introduction

RR Lyraes (RR Lyr), named after their prototype, are old, low-mass stars that reside in the instability strip of the horizontal branch (HB)[1]. They are powerful tools in the studies of many fundamental astrophysical problems. Due to their variability and relatively high luminosity, they are easily identified even at large distances. Their small dispersion in intrinsic mean luminosity makes them good standard candles in contrast to other stellar tracers, such as M giants (Majewski et al. 2003). In addition to the distance scale, RR Lyr play an important role in studying Galactic structure and formation. They are generally used to trace the spatial and kinematic distribution of the old stellar populations of the Galactic disk and halo components. For example, recent optical RR Lyrae surveys, such as QUEST (Vivas et al. 2004) and SDSS (Ivezić et al. 2004), have revealed halo substructures and dynamically young stellar streams that are associated with the formation of the outer halo.

RR Lyr are also commonly used to study the chemical evolution of the disk and halo of our Milky Way. This effort began with the pioneering low-resolution spectroscopic survey by Preston (1959), who introduced the

---

[1] Significant portions of this chapter have been published in For, B.-Q., Preston, G. & Sneden, C. 2011, ApJS, in press.

ΔS index that describes the relation between Hydrogen and calcium K-line absorption strengths. The ΔS index varies during RR Lyrs pulsational cycle, so the standard ΔS index is defined at light minimum (i.e., near phase 0.8). High-resolution studies generally have concentrated on limited phases near minimum light, because of the relatively slow variations in photometric effective temperature that occur at these pulsation phases.

Our work in this area began as an investigation of the systematics of chemical abundances along the HB in the Galactic Halo (For & Sneden 2010). The primary objectives of that paper were to investigate any abundance anomalies in non-variable RHB and BHB stars, to derive masses of these stars and to determine the red and blue edges of the RR Lyrae instability strip. They concluded that: (1) the abundance ratios of these stars are generally consistent with those of similar-metallicity field stars in other evolutionary stages, (2) the stars possess masses of $\sim 0.5\ M_{\odot}$, and (3) the effective temperatures for the red and blue edges of HB stars in the metallicity range $-0.8 \gtrsim$ [Fe/H] $\gtrsim 2.5$ are 5900 K and 7400 K, respectively.

We are applying the analytical techniques of For & Sneden (2010) to a controlled sample of RR Lyr stars. The spectra have been gathered by GWP for his investigation of many issues in RR Lyr atmospheric dynamics, such as shocks, turbulent and Blazhko effect. This RR Lyr spectral study was also initiated partly to better understand the nature of a carbon-rich and s-process rich RR-ab star, TY Gru (Preston et al. 2006b). This star was identified as CS 22881$-$071 in the HK objective-prism survey (Beers et al. 1992) and was initially included in the study of chemical abundance of a sample of metal-poor red horizontal branch stars (Preston et al. 2006a). The enrichment of carbon and n-capture species suggests that this star might have gone through binary mass transfer from a primary star during its Asymptotic Giant Branch (AGB) evolution (Preston et al. 2006b and references therein). To further investigate the abundance anomalies as seen in TY Gru and to detect the possible orbital motion caused by the relic companion of an AGB star (Preston 2011), GWP selected a sample of RR-ab stars with $P \sim 0.57$ day that are broadly representative of the metal-poor halo. Numerous observations at all pulsation phases provide a dataset that can be used to investigate the dependence of derived abundances on the various thermodynamic conditions that occur during pulsation cycles.

In this chapter, we present radial velocities (RVs) and improved ephemerides of 11 field RR-ab stars. In chapter 4, we will report stellar parameter and chemical abundance analyses throughout the pulsational cycles. We provide the basic information on targets and describe the observations and reduction methods in §3.2 and §3.3. In §3.4, we present the derived radial velocities and improved ephemerides.

3.2 Targets and Observations

The observations were made with echelle spectrograph of the du Pont 2.5-m telescope at the Las Campanas Observatory (LCO) during 2006–2009. We used this instrument configured with the $1.5'' \times 4''$ entrance slit, which gives a resolving power of $R \equiv \lambda/\Delta\lambda \sim 27,000$ at the Mg I b lines (5180 Å). The total wavelength coverage is $3500 - 9000$ Å. Integration times ranged from a minimum value of 200 s (to insure reasonably uniform illumination of the slit by starlight) to an upper limit of 600 s (to avoid excessive blurring of the spectrum due to changing radial velocity). The values of S/N achieved by such integrations can be estimated by observations of CS 22175−034 (Preston

Table 3.1. Program stars.

Star	R.A.(J2000) (hr m s)	Decl.(J2000) (° ′ ″)	$V_{\max}$[a] (mag)	$V_{\rm amp}$[a] (mag)	Note
CD Vel	09 44 38.24	−45 52 37.2	11.66	0.87	Blazhko[c]
WY Ant	10 16 04.95	−29 43 42.4	10.37	0.85	···
DT Hya	11 54 00.18	−31 15 40.0	12.53	0.98	···
AS Vir	12 52 45.86	−10 15 36.4	11.66	0.72	Blazhko
RV Oct	13 46 31.75	−84 24 06.4	10.53	1.13	Blazhko
XZ Aps	14 52 05.43	−79 40 46.6	11.94	1.1	···
BS Aps	16 20 51.51	−71 40 15.8	11.9	0.68	Blazhko
UV Oct	16 32 25.53	−83 54 10.5	9.19	0.82	Blazhko
V1645 Sgr	20 20 44.47	−41 07 05.7	10.99	0.84	Blazhko
Z Mic	21 16 22.71	−30 17 03.1	11.32	0.64	Blazhko
TY Gru	22 16 39.42	−39 56 18.0	13.6[d]	0.9[d]	Blazhko

[a] Maximum light in V magnitude from ASAS.

[b] Pulsational amplitude in V-band from ASAS.

[c] Szczygieł & Fabrycky (2007).

[d] Values extracted from Preston et al. (2006b).

et al. 1991), which is a star with similar colors to RR Lyr. Spectra of this star ($V = 12.60$, $B - V = 0.37$) obtained near the zenith under typical observing conditions with an exposure time of 600 s achieved S/N∼ 10 at 4050Å, S/N∼ 15 at 4300 Å, S/N∼ 20 at 5000 Å, S/N∼ 30 at 6000 Å and S/N∼ 30 at 6600 Å. Wavelength calibrations were achieved by taking Thorium-Argon comparison lamp exposures at least once per hour at each star position. Basic information about our program stars is given in Table 3.1.

3.3 Data Reduction

The raw data were bias subtracted, flat-fielded, background subtracted, then extracted to one-dimensional (1D) spectra and wavelength-calibrated by use of IRAF[2] ECHELLE package. Thorium-Argon identifications were based on the line list in the IRAF package data file (thar.dat) and the Th-Ar wavelength table[3] provided by the LCO. We paid particular attention to scattered light corrections, and in the following subsection we describe our own (non-global) approach to this problem.

3.3.1 Scattered Light Correction

Some of the incident photons at each wavelength are scattered into all echelle orders by optical imperfections in the optical train of the spectrograph. A generic method for making scattered light corrections is use of the IRAF apscatter task, in which the scattered light pixels are fitted by a series of 1D functions across the dispersion. The independent fits are then smoothed along the dispersion by again fitting low order functions. These fits then define the smooth scattered light surface to be subtracted from the image. Application of this method to du Pont echelle spectra is complicated by a number of considerations discussed below.

A fraction of the photons of every wavelength that passed through the $1.5'' \times 4.0''$ entrance slit were scattered into the image plane of the du Pont spectrograph by imperfect transmission/reflection at surfaces in the optical

---

[2] The Image Reduction and Analysis Facility, a general purpose software package for astronomical data, written and supported by the IRAF programming group of the National Optical Astronomy Observatories (NOAO) in Tucson, AZ.

[3] http://www.lco.cl/telescopes-information/irenee-du-pont/instruments/website/echelle-spectrograph-manuals/echelle-spectrograph-manuals/atlas

train. Longward of 6500 Å the inter-order space became too small to measure pure scattered light. To circumvent this difficulty, we obtained observations of 4 standard stars through a small $0.75'' \times 0.75''$ slit, for which the inter-order space was more than adequate. Additional difficulties in data reduction arose due to our adopted observing procedure. Long experience at the du Pont had shown that accurate sky subtraction could not be achieved by use of light adjacent to the star image because of centering and guiding errors. If sky background is important, it must be measured by sky observations before and/or after the stellar observation, and only under good photometric conditions. For stars brighter than magnitude 13, sky was unimportant at the 1% level except near the full moon, which we avoided, so we ignored it. To save the precious time between observations that would be required to rotate the spectrograph, we made all observations with an east-west oriented slit. Furthermore, we guided with a red-sensitive detector, so that at many telescope positions significant fractions of blue-violet light did not pass through the slit due to atmospheric dispersion: the observed spectra were thus somewhat "reddened" and mimicked those of lower color temperature. In addition, this could affect the velocity differences between the red and blue lines.

To investigate such effects on our spectral line widths, we calculated the velocity shifts between spectral regions at 4000–6000 Å using the following procedures: (1) calculate the parallactic angle for each of our stars at different 7 hour angles (from 0.01–6 hr with increment of 1 hr); (2) calculate the angle between east–west slit of Cassegrain spectrograph on equatorially–mounted telescope and direction to zenith; (3) calculate the sine of the inclination of the spectrum to the slit; (4) calculate the altitude of each star; (5) calculate differential atmospheric dispersion by linear approximate of data shown in Figure 2 of Simon (1966) for elevation 2811 m, which is close to du Pont elevation at 2200 m; (6) calculate the differential atmospheric dispersion perpendicular to the slit; (7) finally, convert angular displacement in arcsec to velocity displacement by use of scale factor 8 km s^{-1} $arcsec^{-1}$ (assuming $1.5''$ slit width projects to 12 km s^{-1}) The upper limit of 6 km s^{-1} was set for the conversion, which corresponds to an illumination centroid at the edge of the slit. During the observation, seeing and guiding errors will diminish atmospheric displacements, e.g., producing centroids nearer to aperture center. Our velocity displacement calculations over 7 hr angles of each star range from 0–2 km s^{-1}, which are small compared to intrinsic RR Lyr line width of > 20 km s^{-1}. Thus, the broadening effects of these displacements on individual spectra are small.

To further investigate if such broadening would have any effect on the co-added spectra, we measured the equivalent widths of several metal lines of individual spectra and co-added spectra of the same phase. The comparisons of measured equivalent width are consistent with an overall difference of ±3 mÅ. As such, we conclude that the equivalent widths are unaffected in these cases. However, we warn the reader that the shifts certainly contribute to systematic errors of individual radial velocities, especially for stars with large Sourthern declinations (DEC < -70). Inspecting the scatter of RV data for the stable RRab stars (WY Ant, DT Hya, CD Vel, XZ Aps, RV Oct and Z Mic) of our RV curves, the errors due to blue image decentering cannot be much greater than 1 km s^{-1}.

The raw spectra of the observed standard stars were bias-subtracted and flat fielded. Then, individual spectra were combined into a single spectrum. We extracted each combined spectrum with 6 pixel aperture to two 1D

Table 3.2. Basic Information and Observing Log of Standard Stars

Star	Spectral Type	R.A. (h m s)	Decl. (° ′ ″)	V (mag)	UT Date	$N_{\rm exp}$
HD 142629	A3 V	15 56 53.498	−33 57 58.08	5.095	08,09 Aug 2008	2,2
HD 135153	F1 III	15 14 37.319	−31 31 08.84	4.924	09 Aug 2008	3
HD 144880	F7 V	16 09 11.123	−32 06 01.20	7.45	09 Aug 2008	5
HD 136014	G6 III-IV	15 19 31.720	−37 05 49.78	6.189	09 Aug 2008	4

spectra with one for star and one for inter-order background. Subsequently, the 1D spectra were continuum normalized with the continuum task in IRAF ECHELLE package. To obtain the contribution of scattered light in each order, we calculated the fractional contribution of the inter-order background light to the on-order starlight as a function of spectral order (or wavelength), b_λ/s_λ, for each standard star. Because a 10 pixel aperture was used to extract the spectra of our program RR Lyr, the extracted 1D spectra are expected to contain more scattered light than the extracted scattered light frames. Thus, we applied a correction factor of 5/3 to the calculated b_λ/s_λ ratios.

In Table 3.2, we provide the basic information and observing log for our standard stars. The calculated fraction as a function of spectral order for each standard star is presented in Table 3.3. We summarize our results in Figure 3.1. The success of this calibration procedure depends on the stability of the scattered light distribution produced by the spectrograph. Recalibration performed from time to time by the procedure described above has shown that the scattered light distribution has changed little, if at all, during the past two decades. We will consider this issue more fully in chapter 4.

Table 3.3. Mean background fractions b_λ/s_λ for Du Pont echelle spectrograph.

		HD 142629		HD 135153		HD 144880		HD 136014	
Order	λ_c[a]	$\langle b_\lambda/s_\lambda \rangle$	$c\langle b_\lambda/s_\lambda \rangle$[b]	$\langle b_\lambda/s_\lambda \rangle$	$c\langle b_\lambda/s_\lambda \rangle$[b]	$\langle b_\lambda/s_\lambda \rangle$	$c\langle b_\lambda/s_\lambda \rangle$[b]	$\langle b_\lambda/s_\lambda \rangle$	$c\langle b_\lambda/s_\lambda \rangle$[b]
46	7575	0.068	0.113	0.069	0.115	0.070	0.117	0.073	0.122
47	7415	0.064	0.107	0.064	0.107	0.066	0.110	0.066	0.110
48	7260	0.061	0.102	0.061	0.102	0.064	0.107	0.061	0.102
49	7108	0.057	0.095	0.058	0.097	0.059	0.098	0.055	0.092
50	6962	0.054	0.090	0.055	0.092	0.056	0.093	0.053	0.088
51	6825	0.052	0.087	0.051	0.085	0.054	0.090	0.048	0.081
52	6688	0.047	0.078	0.048	0.080	0.052	0.087	0.046	0.077
53	6560	0.047	0.078	0.047	0.078	0.051	0.085	0.044	0.073
54	6435	0.045	0.075	0.045	0.075	0.050	0.083	0.043	0.072
55	6315	0.043	0.072	0.045	0.075	0.049	0.082	0.043	0.071
56	6202	0.043	0.072	0.044	0.073	0.048	0.080	0.042	0.070
57	6092	0.043	0.072	0.043	0.072	0.048	0.080	0.041	0.069
58	5987	0.043	0.072	0.043	0.072	0.047	0.078	0.042	0.069
59	5880	0.044	0.073	0.044	0.073	0.047	0.078	0.042	0.070
60	5780	0.045	0.075	0.044	0.073	0.047	0.078	0.042	0.071
61	5686	0.045	0.075	0.045	0.075	0.046	0.077	0.042	0.071
62	5592	0.046	0.077	0.045	0.075	0.046	0.077	0.043	0.071
63	5502	0.047	0.078	0.046	0.077	0.046	0.077	0.044	0.073
64	5413	0.049	0.082	0.046	0.077	0.047	0.078	0.044	0.073
65	5330	0.050	0.083	0.047	0.078	0.049	0.082	0.045	0.074
66	5250	0.051	0.085	0.049	0.082	0.050	0.083	0.045	0.076
67	5170	0.052	0.087	0.049	0.082	0.050	0.083	0.047	0.078
68	5090	0.053	0.088	0.050	0.083	0.051	0.085	0.048	0.080
69	5017	0.052	0.087	0.051	0.085	0.053	0.088	0.047	0.079
70	4945	0.052	0.087	0.051	0.085	0.055	0.092	0.048	0.080
71	4870	0.057	0.095	0.052	0.087	0.056	0.093	0.049	0.082
72	4805	0.053	0.088	0.052	0.087	0.062	0.103	0.049	0.082
73	4740	0.050	0.083	0.051	0.085	0.059	0.098	0.050	0.084
74	4672	0.053	0.088	0.051	0.085	0.057	0.095	0.054	0.090
75	4610	0.052	0.087	0.049	0.082	0.064	0.107	0.053	0.089
76	4548	0.053	0.088	0.049	0.082	0.063	0.105	0.054	0.090
77	4490	0.050	0.083	0.048	0.080	0.061	0.102	0.056	0.093
78	4430	0.049	0.082	0.048	0.080	0.060	0.100	0.060	0.100
79	4375	0.057	0.095	0.050	0.083	0.063	0.105	0.045	0.074
80	4320	0.050	0.083	0.047	0.078	0.055	0.092	0.054	0.090
81	4265	0.044	0.073	0.044	0.073	0.057	0.095	0.053	0.088
82	4210	0.046	0.077	0.045	0.075	0.064	0.107	0.047	0.078
83	4160	0.047	0.078	0.048	0.080	0.069	0.115	0.058	0.097
84	4110	0.053	0.088	0.046	0.077	0.067	0.112	0.063	0.105
85	4060	0.046	0.077	0.046	0.077	0.070	0.117	0.062	0.104
86	4012	0.049	0.082	0.044	0.073	0.082	0.137	0.099	0.166
87	3966	0.057	0.095	0.047	0.078	0.123	0.205	0.099	0.165
88	3920	0.061	0.102	0.046	0.077	0.100	0.167	0.105	0.175

[a] Central wavelength of the order.

[b] Mean b_λ/s_λ corrected with 5/3 factor.

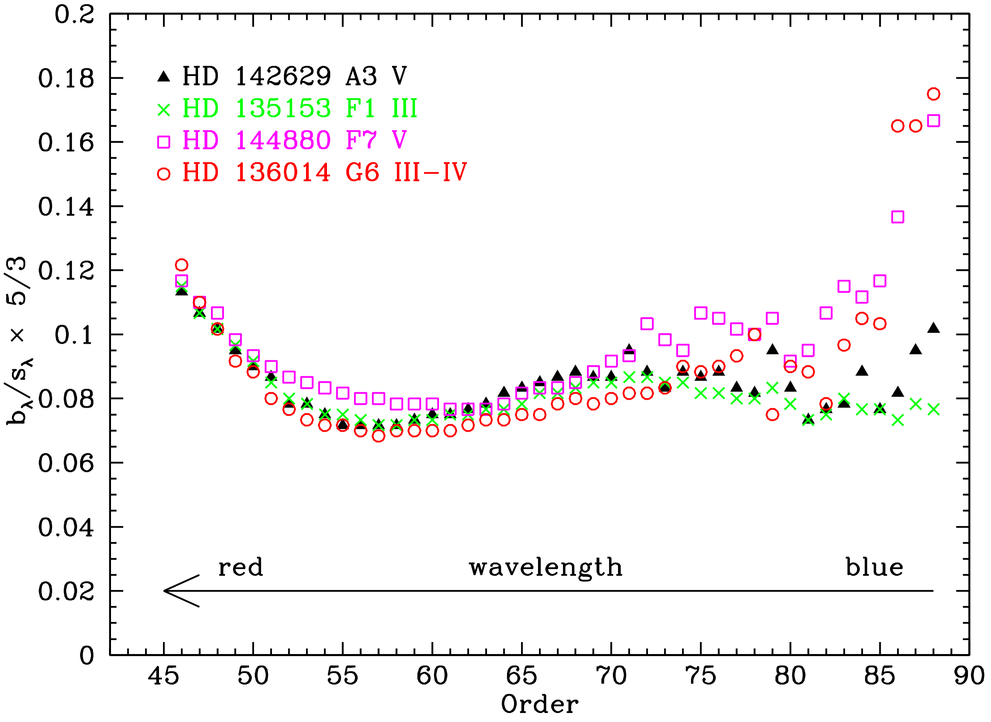

Figure 3.1 Fractional contribution of the inter-order background light to the on-order starlight as a function of spectral order (wavelength), b_λ/s_λ, for each standard star. Wavelength decreases with increasing order.

3.4 Analysis

3.4.1 Radial Velocities

The spectra that we used for deriving the RVs were not corrected for scattered light. It is not important for deriving the RVs but will be required for the the subsequent atmospheric analysis. We derived the RVs by use of the cross-correlation FXCOR task in IRAF, in which the individual spectra were cross-correlated against a template by fitting a Gaussian to the cross-correlation peak. We constructed the individual spectra from 13 echelle orders covering the spectral region of 4000-4600 Å, which were then flattened, normalized, and stitched together with an IRAF script. In order to get strong cross-correlations that minimizes RV errors, we created a template from several spectra of CS 22874−009, a blue metal-poor radial velocity standard star (Preston & Sneden 2000b), which possesses a spectrum similar to those of RR Lyr stars at most phases. The typical RV error calculated from FXCOR is ~ 0.5 km s^{-1}. We present the observed HJD midpoints, phases (see §3.4.2), derived RVs and their associated errors in Table 3.4.

3.4.2 Pulsation Ephemerides

A pulsation ephemeris is commonly written as HJD (max light) = $T_0 + n \times$P, where T_0 is epoch, n is the number of elapsed pulsation cycles and P is the pulsational period in days. The All Sky Automated Survey[4] (ASAS) (Pojmanski 2002) provides a starting point to obtain ephemerides for our program stars. This photometric survey has been carried out over many years at the LCO and Haleakala, Maui stations. Using the ASAS reported pulsation period

---

[4] http://www.astrouw.edu.pl/asas/

Table 3.4. Radial Velocities

Star	HJD at midpoint (2450000+)	Phase (ϕ)	RV (km s^{-1})	err (km s^{-1})
CD Vel	3836.48565	0.00	210.76	0.50
	3836.49453	0.02	210.97	0.48
	3836.54295	0.10	216.80	0.35
	3836.54928	0.11	218.06	0.35
	.	.	.	.
	.	.	.	.
	.	.	.	.

Note. — Table 3.4 is published in its entirety in the electronic edition of For et al. (2011). A portion is shown here for guidance regarding its form and content.

and T_0, the folded lightcurves as shown on the ASAS website were slightly out of phase. This suggests that the quoted values could be improved. Here we present the methods of improving both pulsation periods and T_0 values of our program stars.

3.4.2.1 Pulsation Period

We improved the pulsation periods of our 10 RR-ab stars using the classified "grade A" V-band photometric data listed in the ASAS database. The pulsation period of TY Gru was adopted from Preston et al. (2006b) since those authors derived it by use of additional observations obtained with the LCO Swope telescope. The pulsational periods were derived using the Lomb-Scargle periodogram (Scargle 1982). We set a short period range of 0.5–0.6 day to minimize the chance of selecting spurious peaks caused by aliasing sidelobes (due to large observational gap and unevenly spaced time series data) in a different frequency domain. In addition, the pulsational period of our RR-ab stars is known to lie within this range, so that a smaller time step can be set to achieve accuracy while cutting down the computing time. The advantages of this algorithm are: (1) less computing time than the lightcurve template fitting method, which requires continuous sampled data sets that are not available from the ASAS database and (2) the ability to compute Fourier Transform for unevenly spaced time series data. While we have continuously sampled RV data, we still cannot use the template fitting method because it is designed for lightcurve fitting, not for RV curves of RR Lyr stars. We warn the reader that there is a caveat for this algorithm. It is optimized to identify sinusoidal-shaped periodic signal in time-series data. The lightcurves of RR Lyrae stars are non-sinusoidal.

Given that we have a huge amount of photometric data, the highest peak, which represents the most probable repeating signal, in a periodogram is always more than 4σ above the mean noise level (see Figure 3.2). The highest peak of each periodogram is selected as the pulsational period of our program stars. We evaluated the error of the periods by comparing the periods derived from Lomb-Scargle algorithm and Box-fitting least squares method (BLS) (Kovács et al. 2002). The BLS algorithm fits the input time series with "box"-shaped function, which makes it more suitable for obtaining period for transiting lightcurve than RR Lyrs lightcurve.

In Table 3.5, we present the pulsation periods quoted in the ASAS catalog in column 5, the derived pulsation periods and their associated errors in column 6 and 7. The error of the period is within 0.000001–0.000007 day, which is 10 times better than the periods accuracy quoted at the ASAS website.

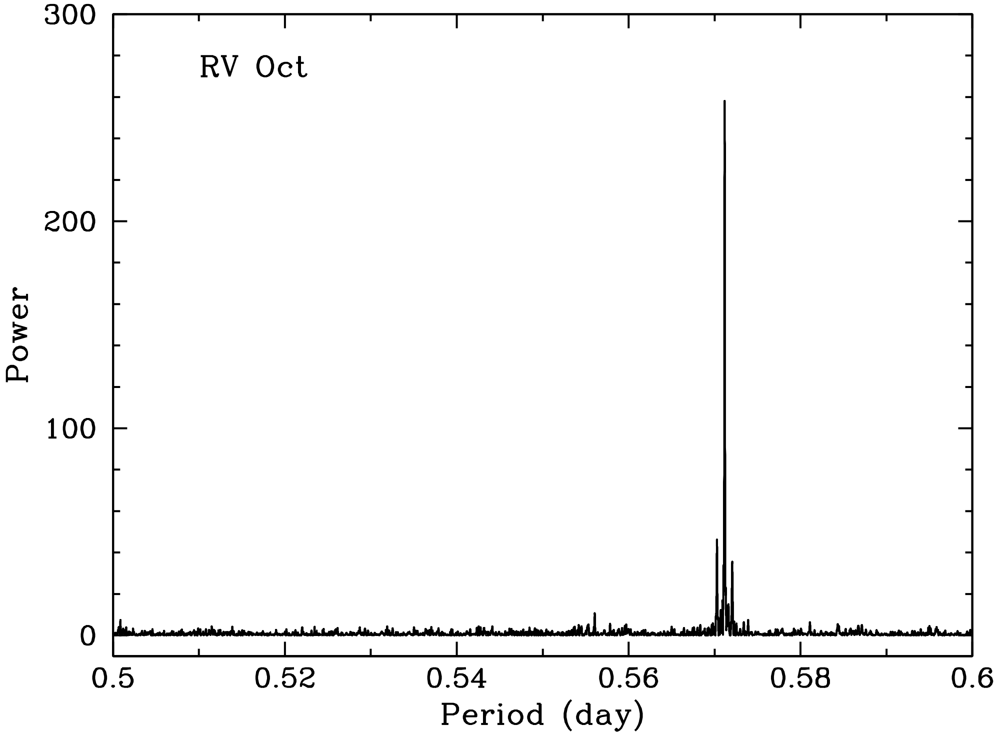

Figure 3.2 An example of typical periodogram used for searching the pulsational period. The sidelobes that caused by the large observing gap is clearly seen in the periodogram. The highest peak defines the pulsational period of RV Oct.

Table 3.5. Ephemerides of our program stars

Star	Data used (HJD 2450000+)	T_0[a] (HJD 2450000+)	err (HJD 2450000+)	Period[b] (day)	Period (day)	error (day)
CD Vel	all	3837.632	0.0003	0.57351	0.573510	0.000003
WY Ant	all	4191.685	0.0097	0.57434	0.574344	0.000002
DT Hya	all	4583.637	0.0089	0.56797	0.567978	0.000001
AS Vir	all	4907.709	0.0098	0.553439	0.553412	0.000002
RV Oct	all	3841.602	0.0016	0.571184	0.571170	0.000002
XZ Aps	all	3842.735	0.0052	0.5873	0.587264	0.000002
BS Aps	all	4583.785	0.0045	0.582577	0.582561	0.000007
UV Oct	3836.843842.91, 4306.465021.84	3837.875	0.0072	0.542561	0.542578	0.000003
	3931.584194.92, 5070.485073.59	5070.605	0.0072	···	···	···
V1645 Sgr	4191.894306.90	4306.775	0.0150	0.552979	0.552948	0.000005
	4579.854583.91	4579.895	0.0150	···	···	···
	3932.733946.75, 4687.665074.71	4687.703	0.0170	···	···	···
Z Mic	all	5075.606	0.0015	0.58693	0.586926	0.000001
TY Gru	3933.793935.65, 5071.50–5073.66	3933.785	0.0120	···	0.570065	0.000005
	3945.634306.89	4304.885	0.0120	···	···	···

[a] Epoch at time of light maxima or radial velocity minima.

[b] Listed in ASAS catalog.

3.4.2.2 Epoch

The reference epoch (T_0) of a pulsating variable star is usually chosen to occur at visual light maximum, which closely coincides with RV minimum (see discussion by Preston 2009 and particularly Figure 3.4 as an example). Because the periodogram does not calculate an epoch, we derived values of T_0 by use of the Kwee-van Woerden method (Kwee & van Woerden 1956). This method is generally used for computing the epoch of minimum of eclipsing variables accurately but it is also suitable to determine the epoch of light maxima of variable stars. We prefer to use our RV curves for this purpose because adequate data points near the RV minima (light maxima) were available during individual cycles, in constrast to the ASAS lightcurve data that were collected over long time intervals, with few observations per cycle and relatively large scatter near light maxima.

For each star, we selected the cycles that cover the RV minima and calculated several equidistant midpoints between the rising and descending branch near the RV minima for a given cycle. Then, we fitted a linear least square equation to these midpoints, which the intersection of the straight line and the RV curve gives the T_0 of RV minima. We typically computed more than one T_0 using the above method per star to evaluate the error. Assuming the pulsational period and the first derived T_0 are accurate, we can calculate the predicted T_0 after n pulsation cycles using the defined pulsation ephemeris above. The predicted T_0 should be close to the second derived T_0. The difference between the predicted and the derived value provides an estimate for the error. Due to the possibility of period change for the Blazhko RRab stars, several epochs were determined and used for folding their RV curves.

In Figure 3.3, we show the schematic diagram that determines the times of RV minima of our asymmetric RV curves. We refer the reader to Kwee & van Woerden (1956) for the mathematical description of the method (for symmetric lightcurve only). In Table 3.5, we summarize the ephemerides of 11 field RR-ab stars. We tabulate epochs for the particular RV minima used to derive them. The table also gives the range of data in HJD that are associated with the corresponding T_0 and pulsational periods. We present the folded RV curves and ASAS lightcurves with our derived ephemerides in Figures 3.4–3.25. The figures are arranged by ascending right ascension.

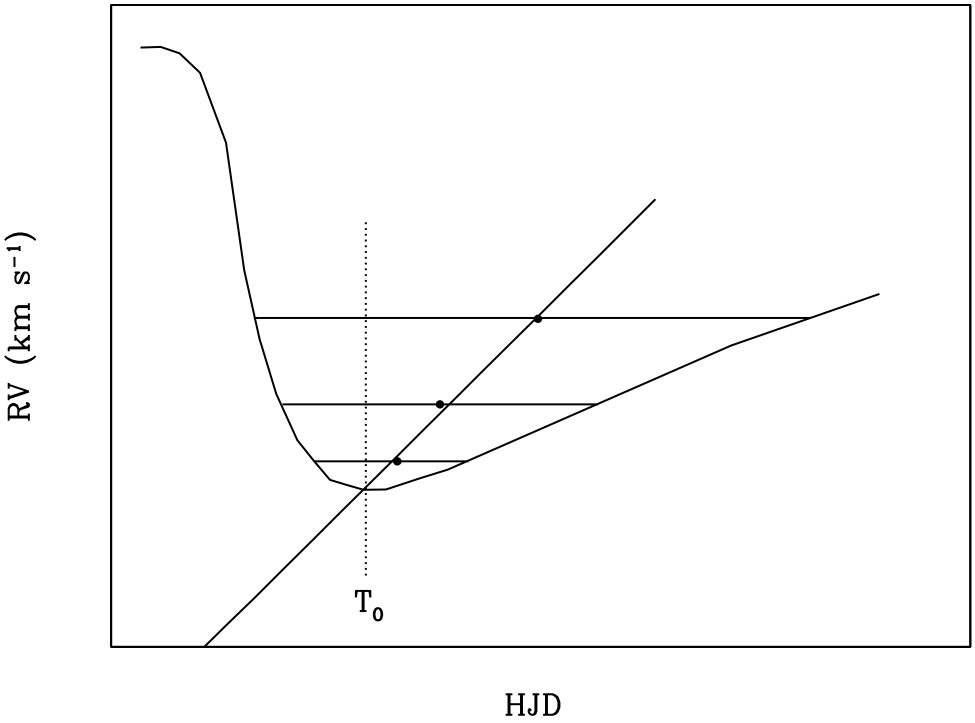

Figure 3.3 A schematic diagram that shows the typical radial velocity curve near minima (or equivalent to light maxima) of a RRab variable star. It also shows the Kwee-van Woerden method (Kwee & van Woerden 1956) that we applied to determine the epochs of our RR Lyrae stars.

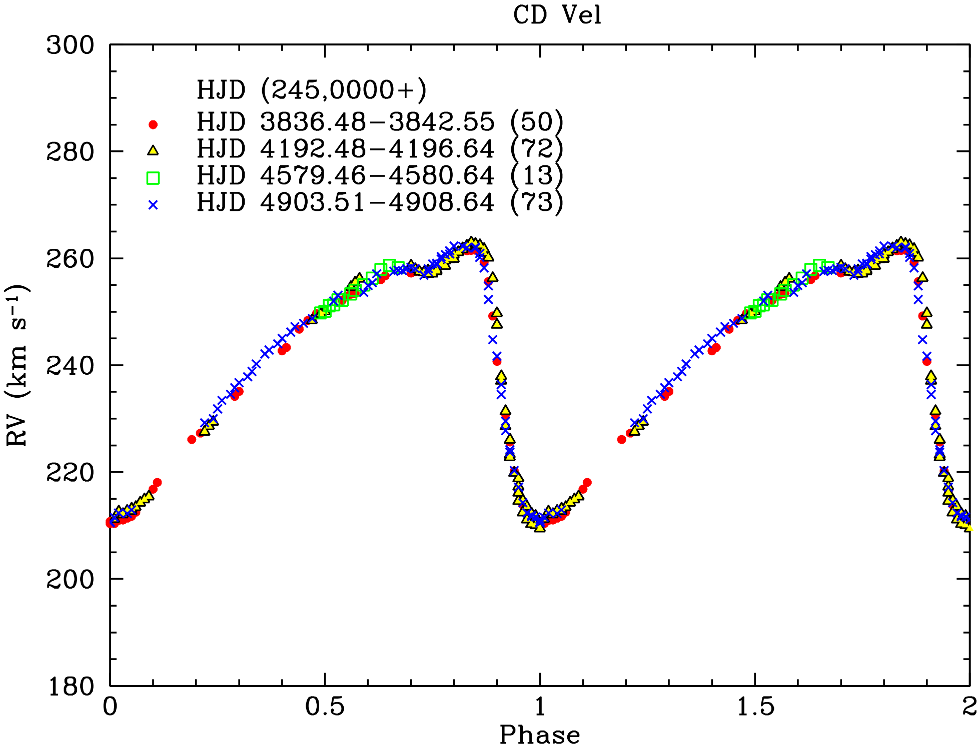

Figure 3.4 Folded radial velocity curve by using our derived ephemeris for this star (Table 3.5). Radial velocity vs pulsational phase for all of our spectra. The different symbols and colors represent different times of observations in HJD. The total numbers of observed spectra per cycle are listed in the parentheses.

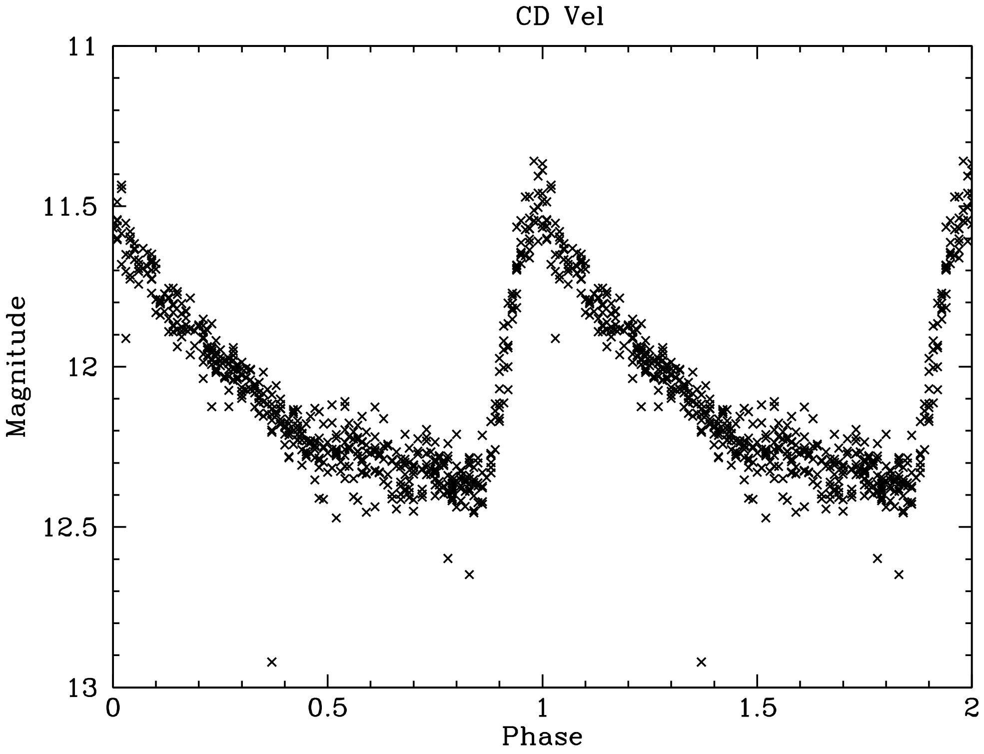

Figure 3.5 Folded lightcurve of CD Vel by using our derived ephemeris for this star (Table 3.5). The ASAS photometric lightcurve vs pulsational phase. The scatter of data points at a given phase for CD Vel and for the other program stars is highly related to the mean apparent brightness of the observed star.

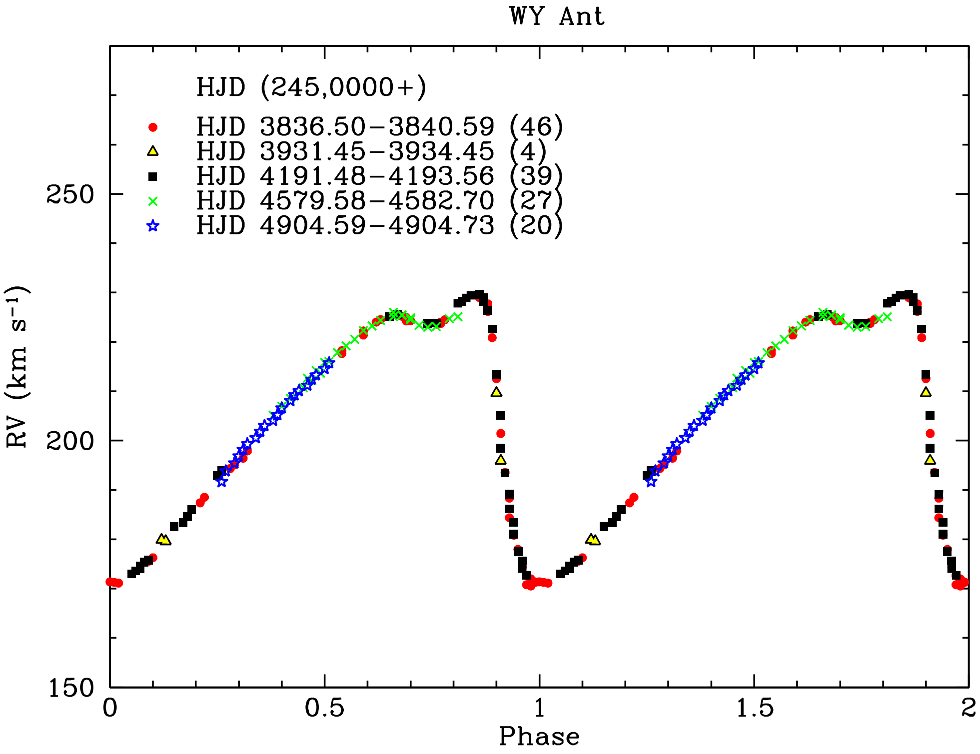

Figure 3.6 Same as Figure 3.4.

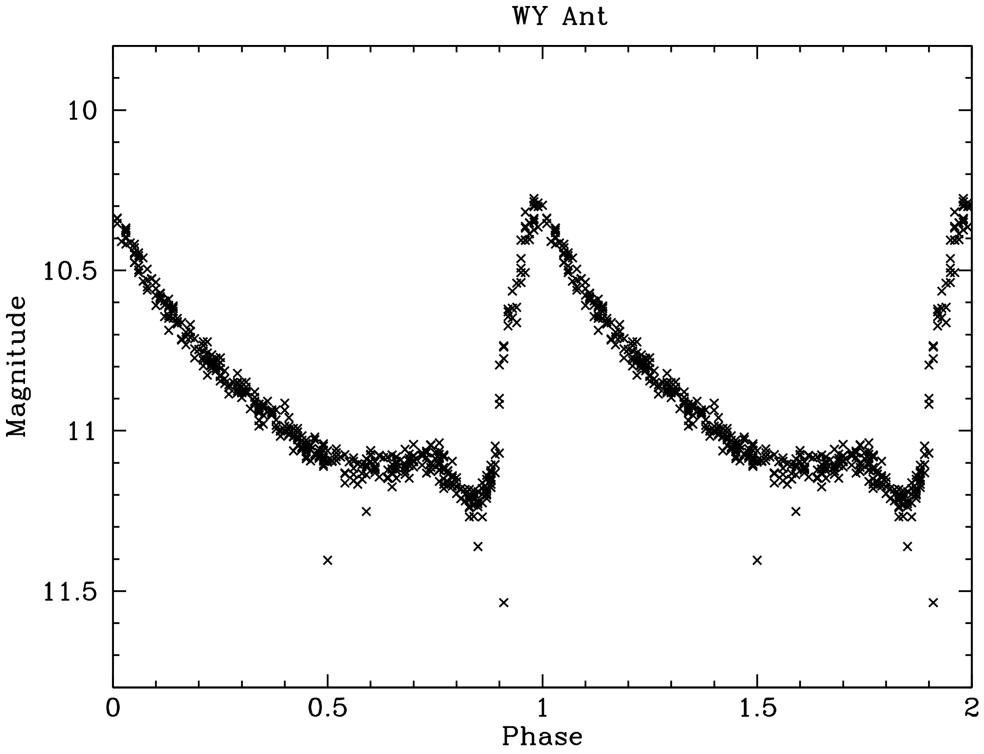

Figure 3.7 Same as Figure 3.5.

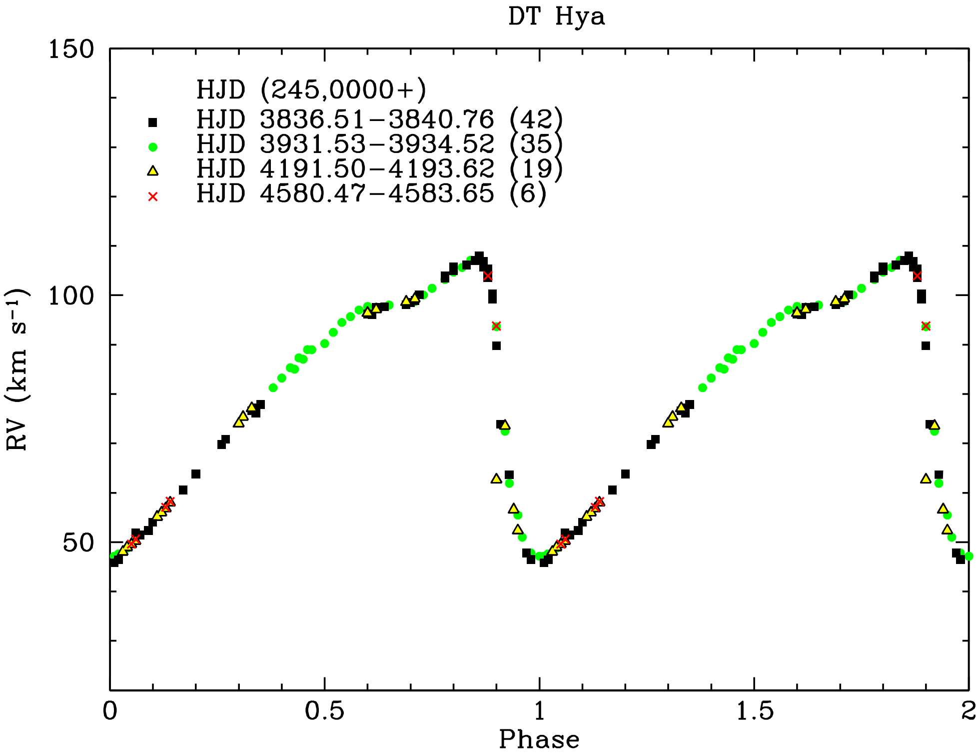

Figure 3.8 Same as Figure 3.4.

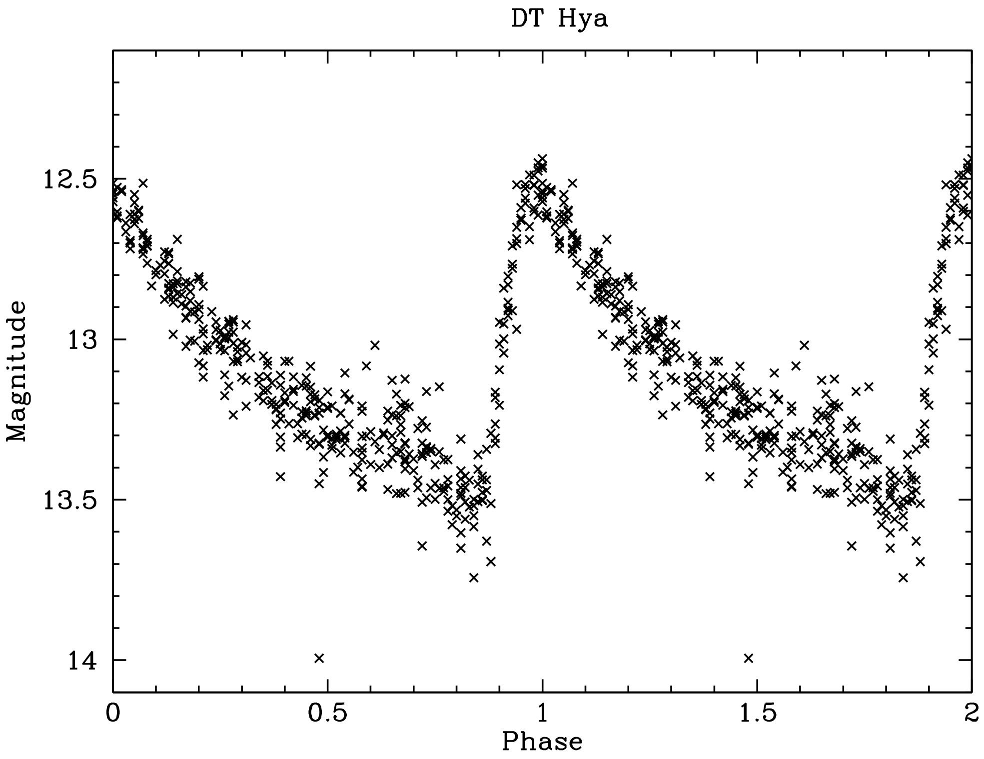

Figure 3.9 Same as Figure 3.5.

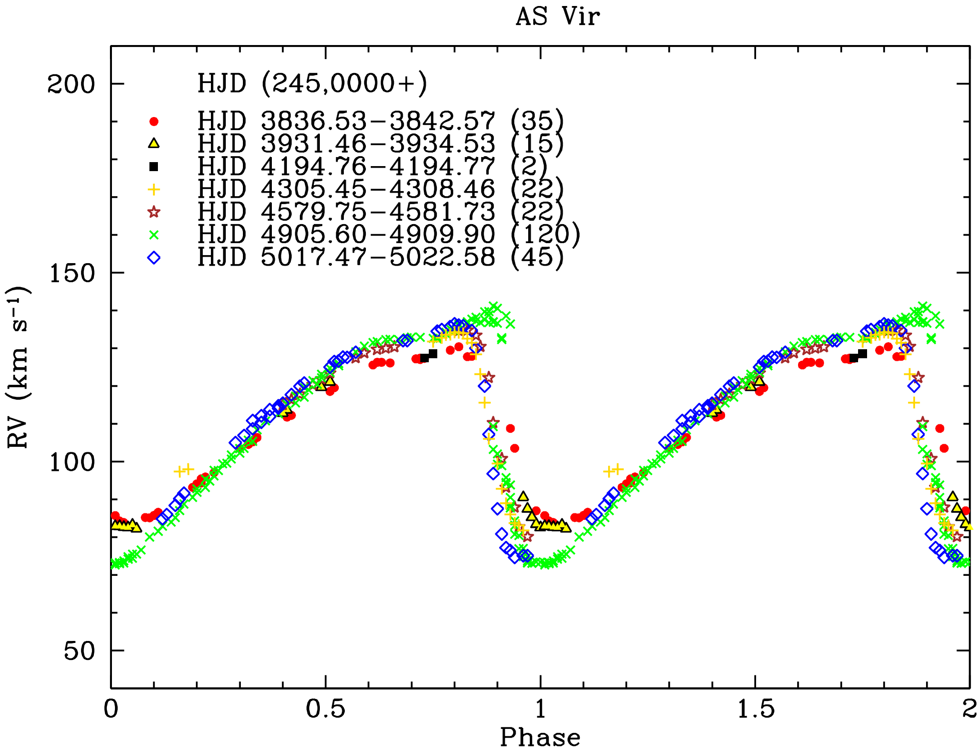

Figure 3.10 Same as Figure 3.4.

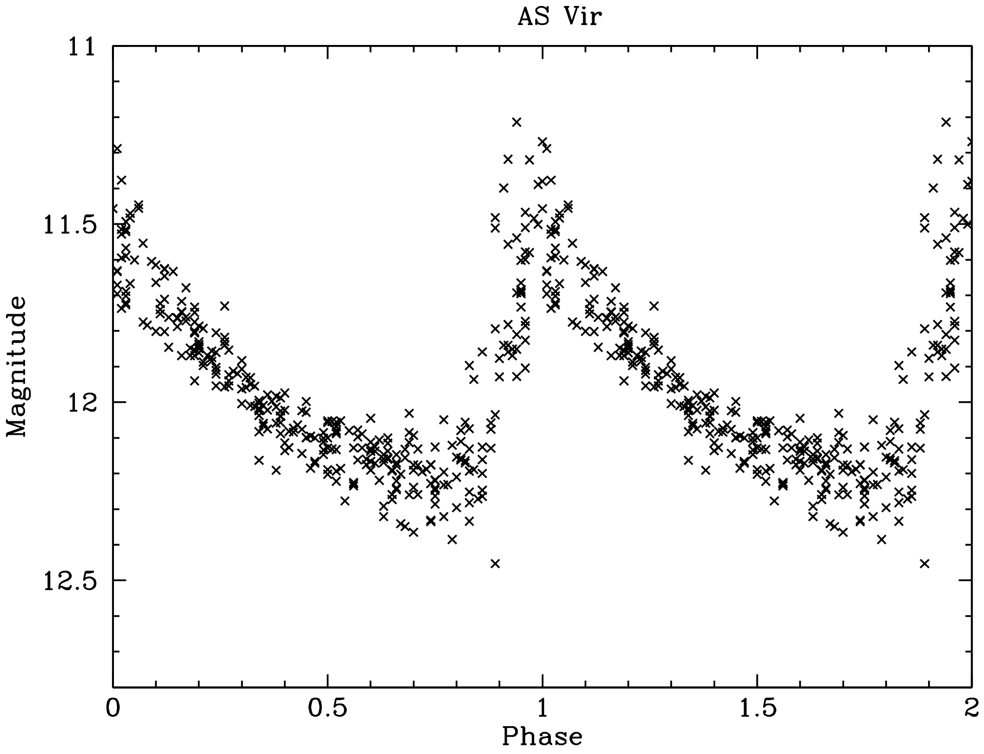

Figure 3.11 Same as Figure 3.5.

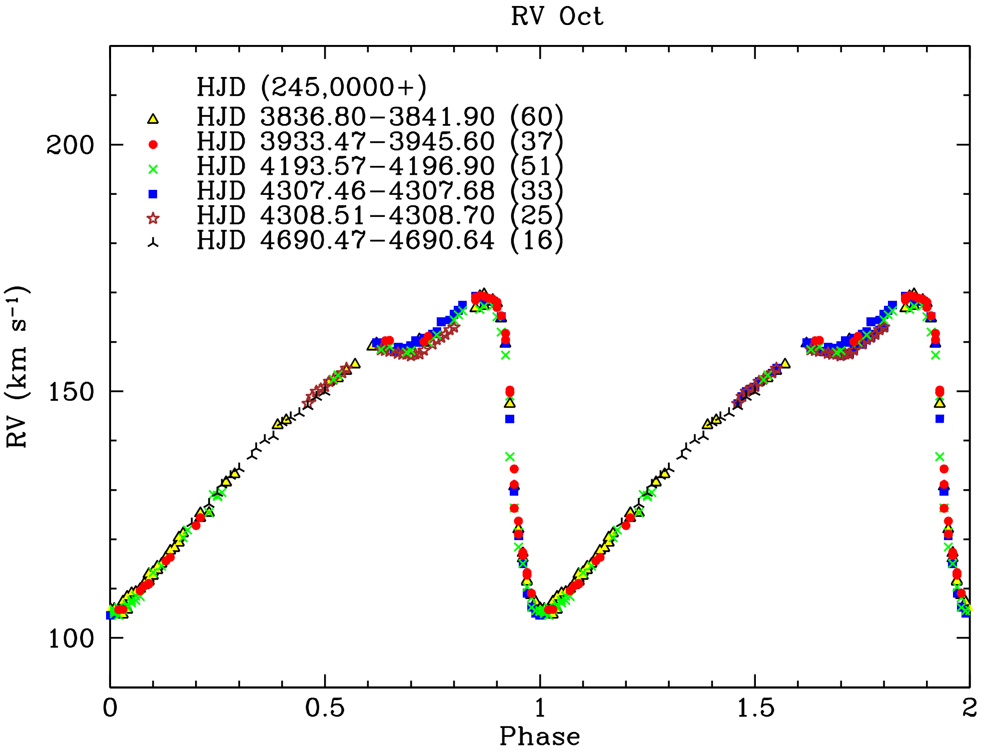

Figure 3.12 Same as Figure 3.4.

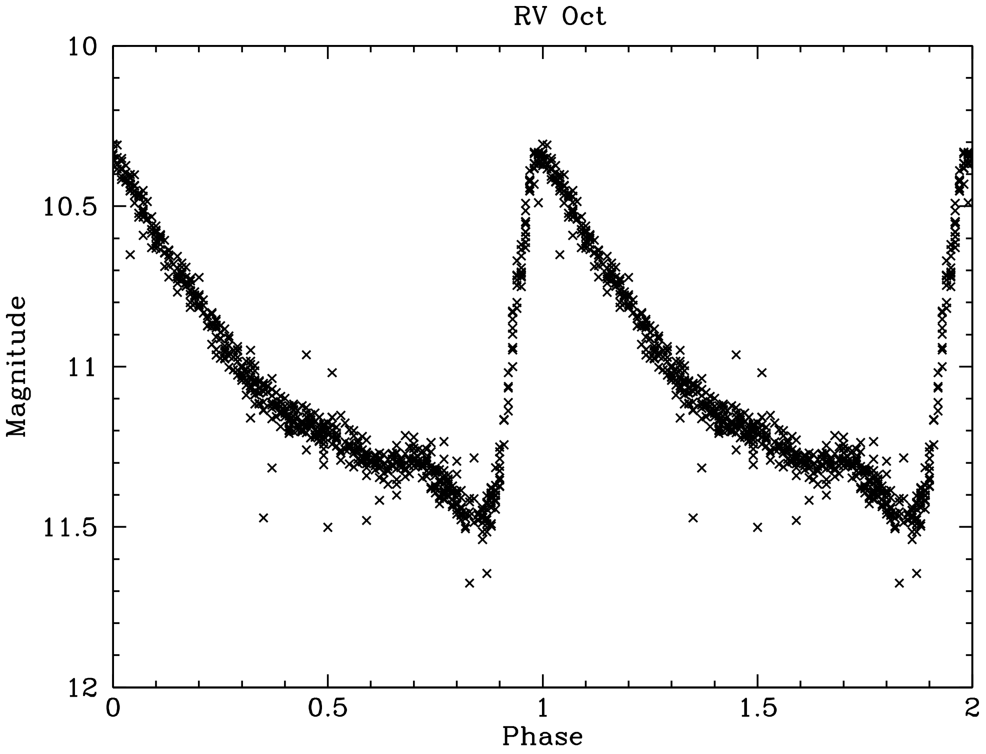

Figure 3.13 Same as Figure 3.5.

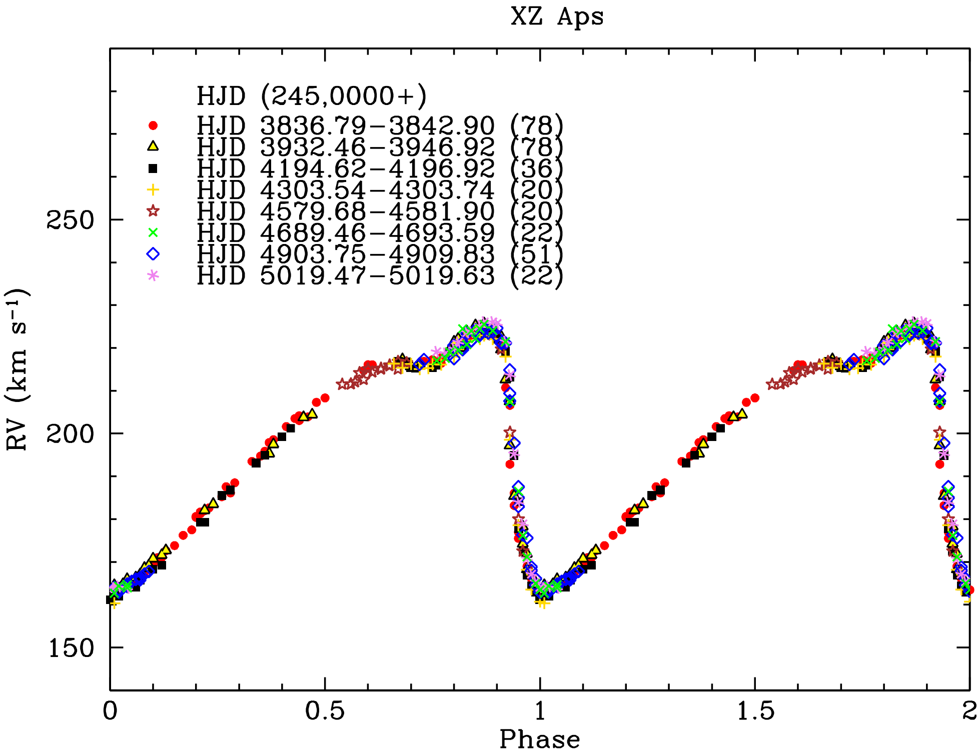

Figure 3.14 Same as Figure 3.4.

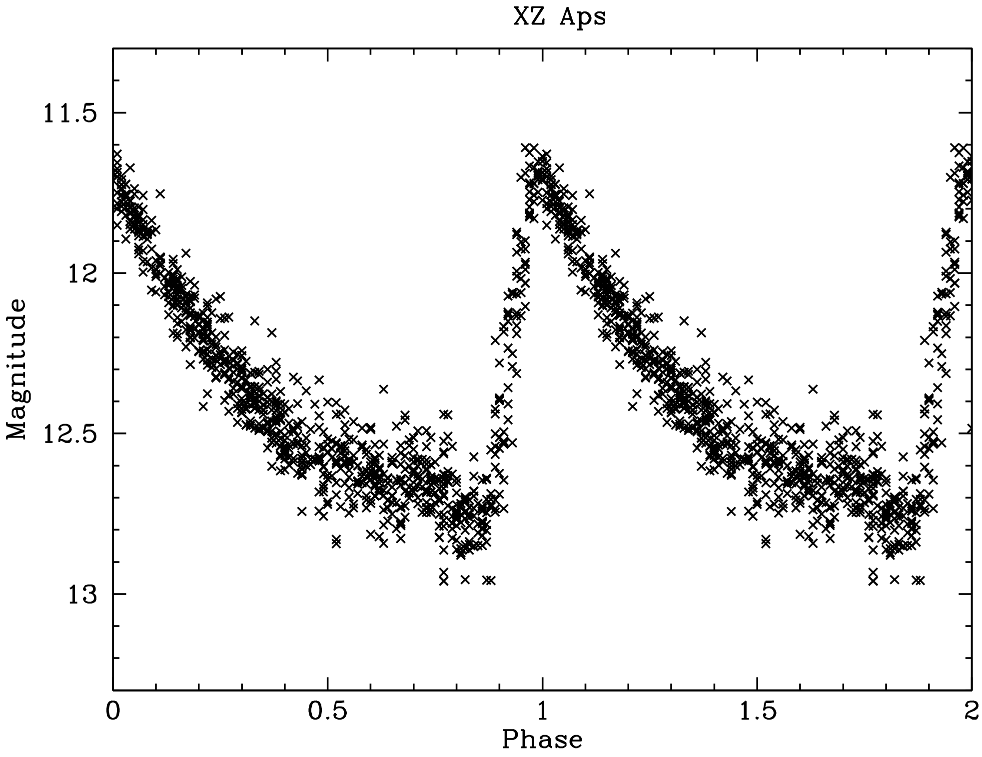

Figure 3.15 Same as Figure 3.5.

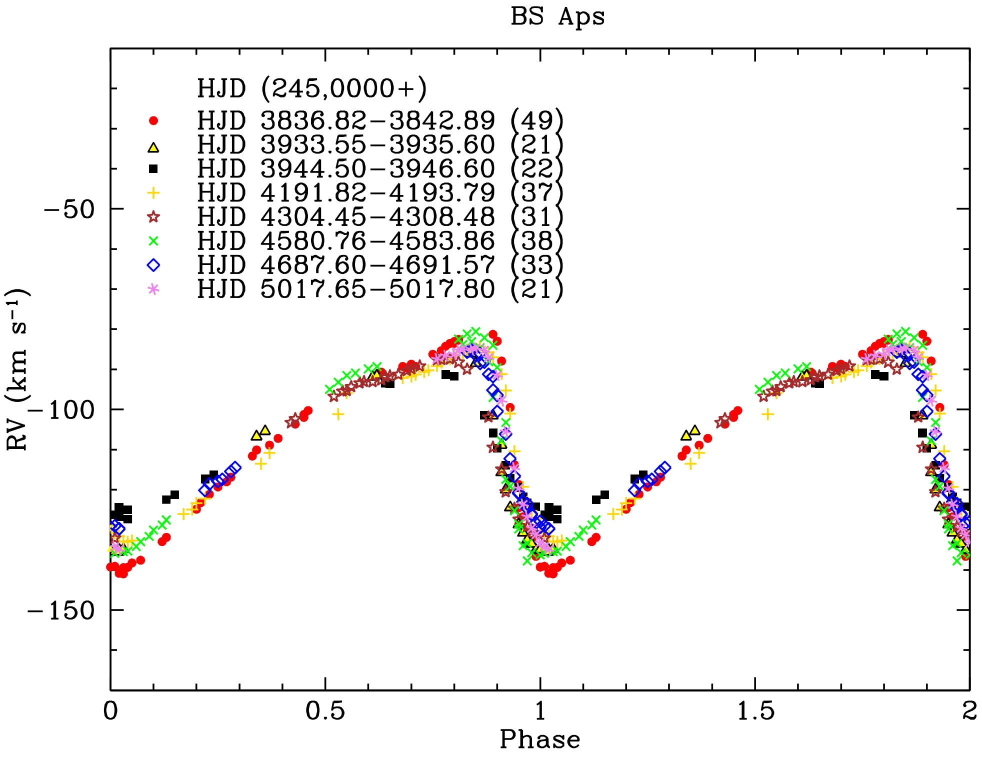

Figure 3.16 Same as Figure 3.4.

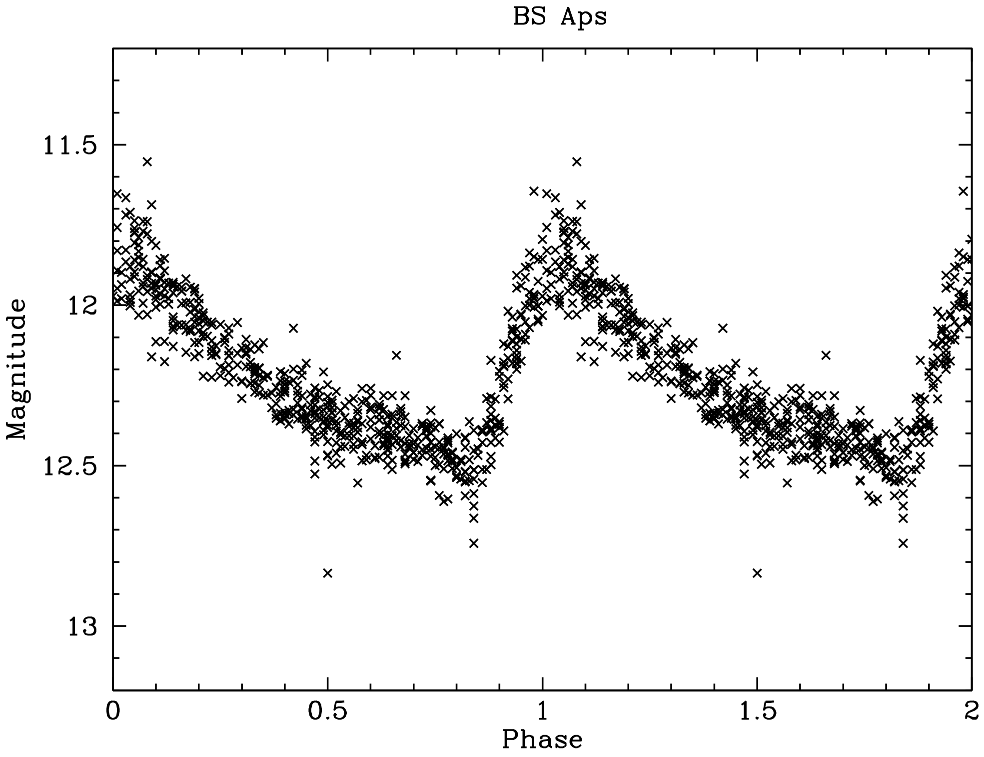

Figure 3.17 Same as Figure 3.5.

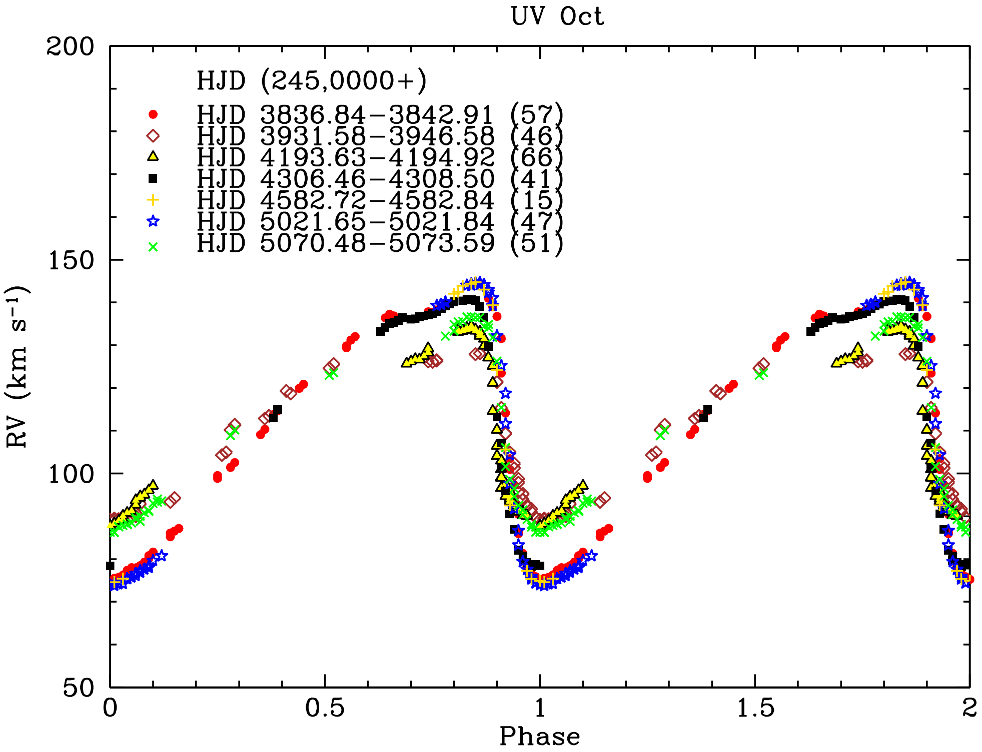

Figure 3.18 Same as Figure 3.4.

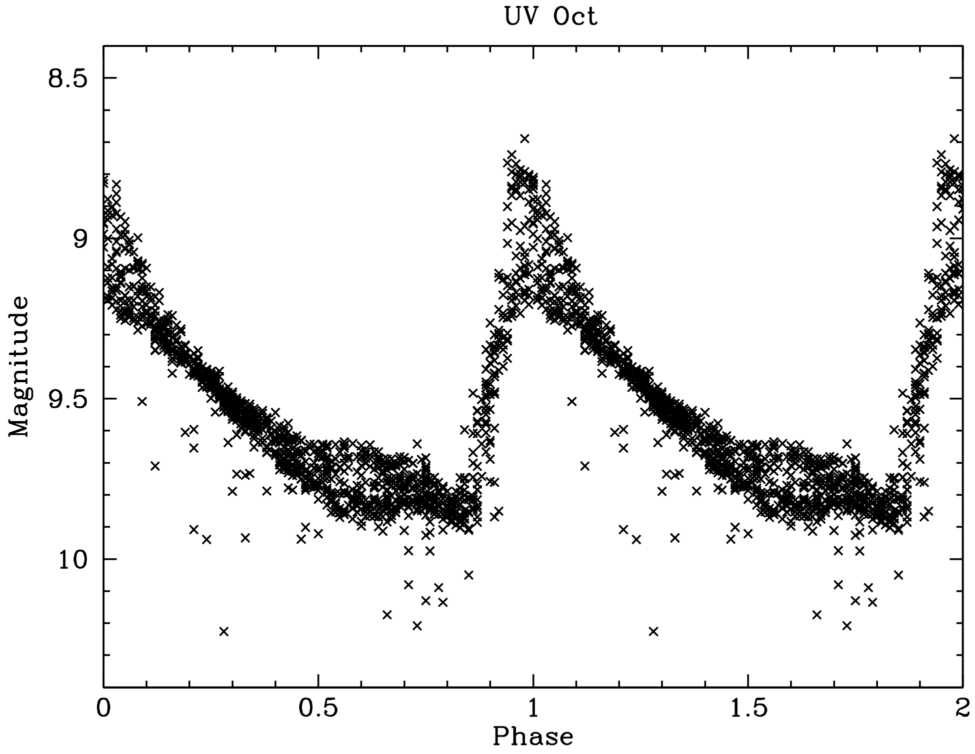

Figure 3.19 Same as Figure 3.5.

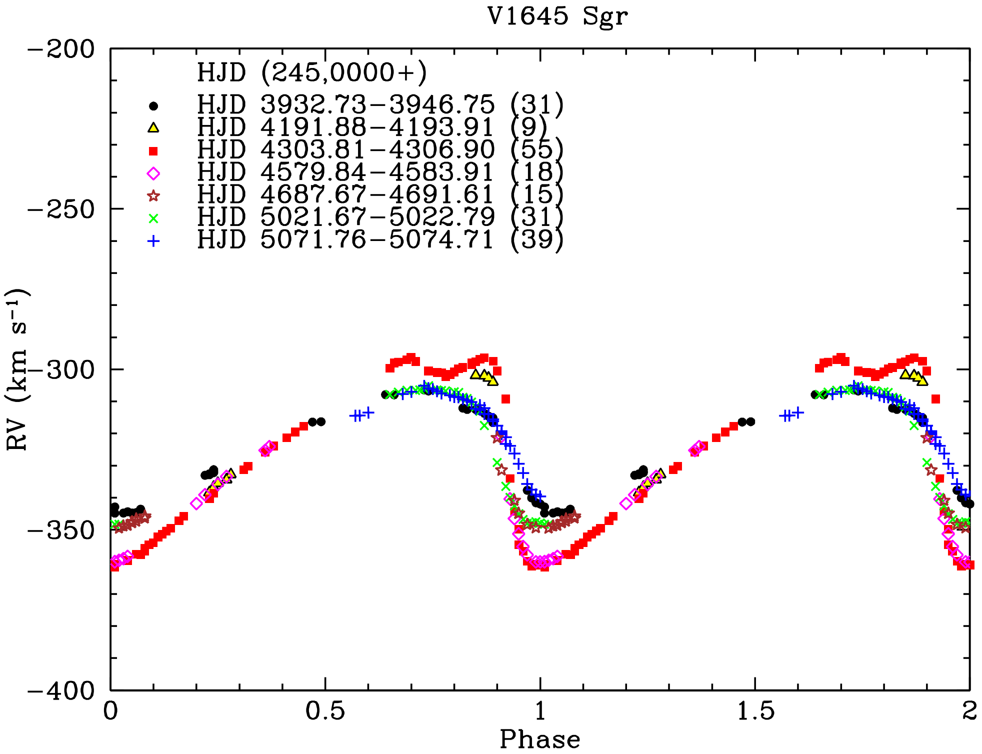

Figure 3.20 Same as Figure 3.4.

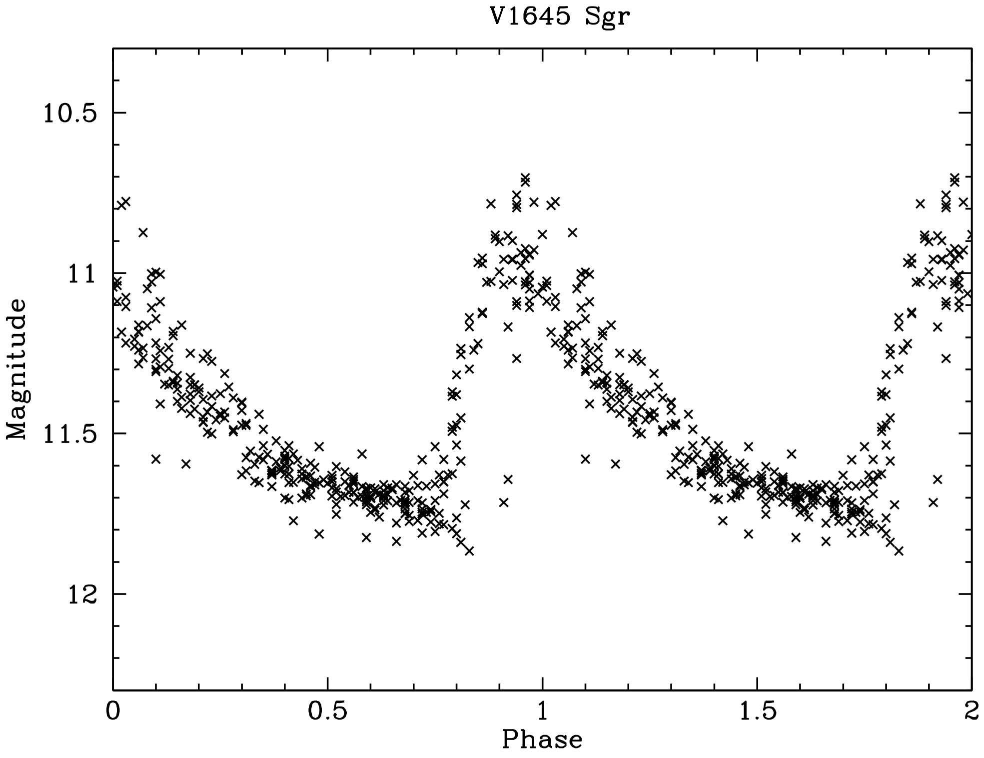

Figure 3.21 Same as Figure 3.5.

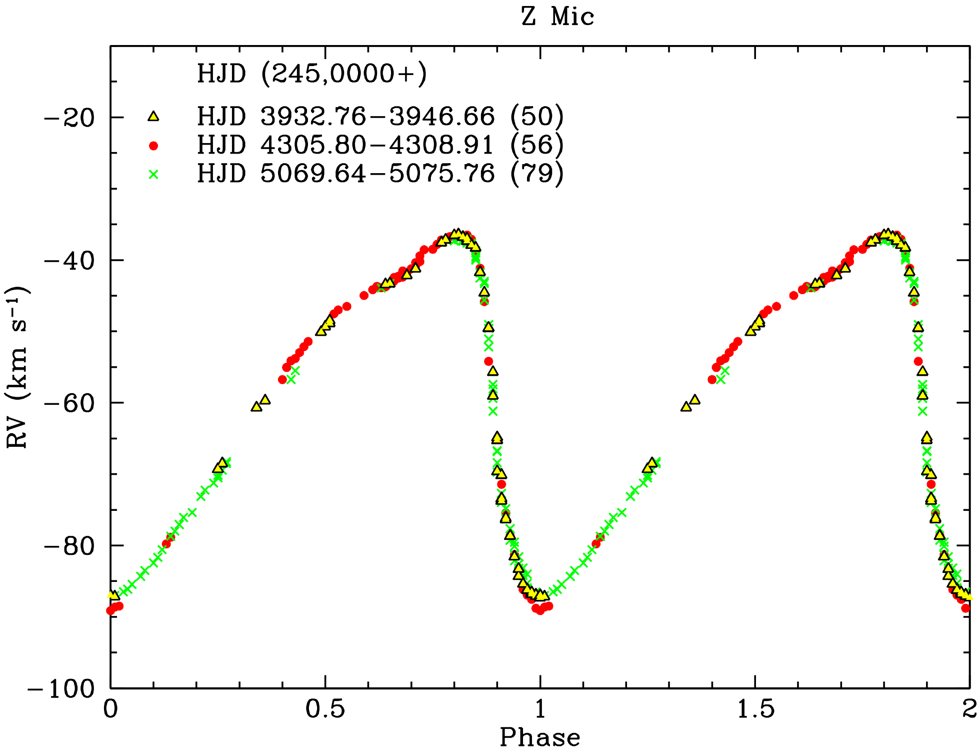

Figure 3.22 Same as Figure 3.4.

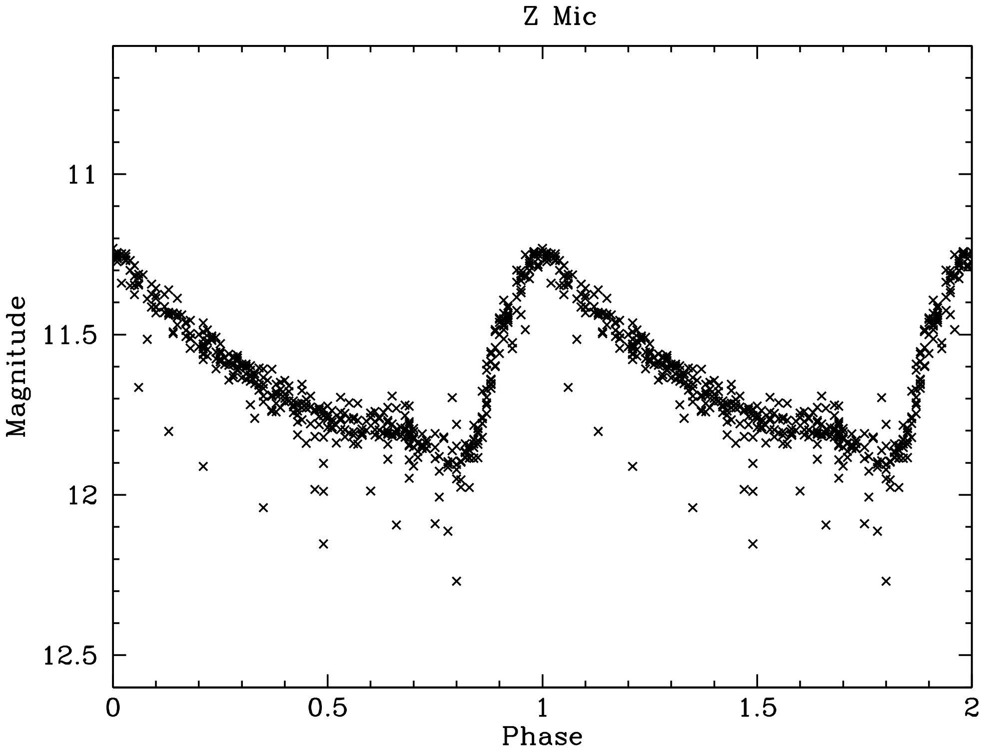

Figure 3.23 Same as Figure 3.5.

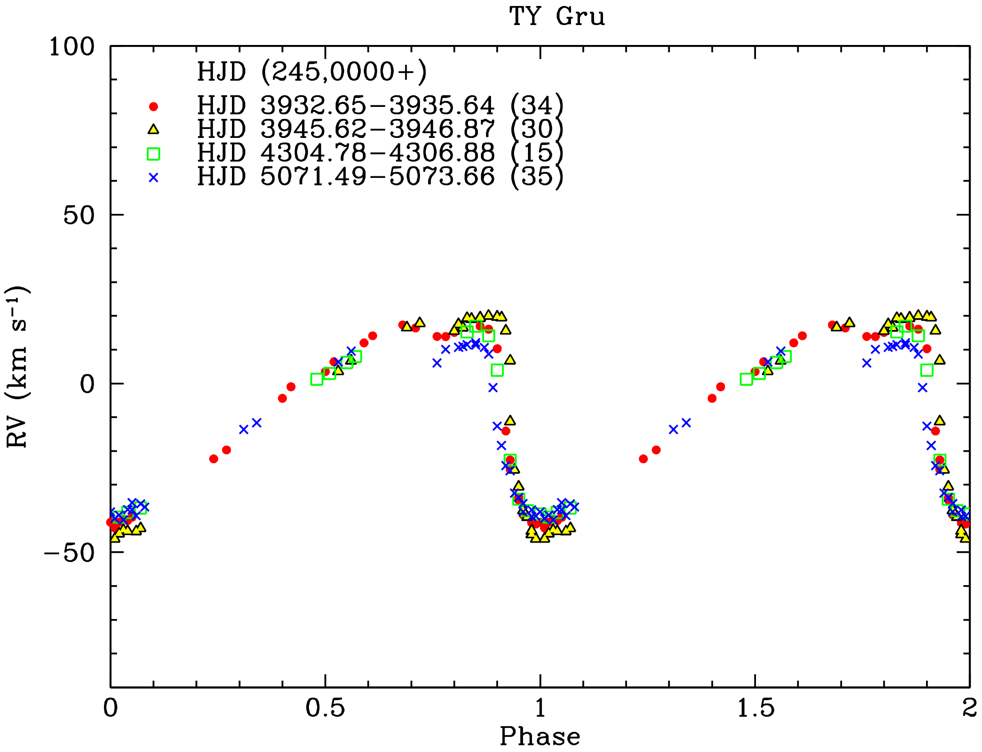

Figure 3.24 Same as Figure 3.4.

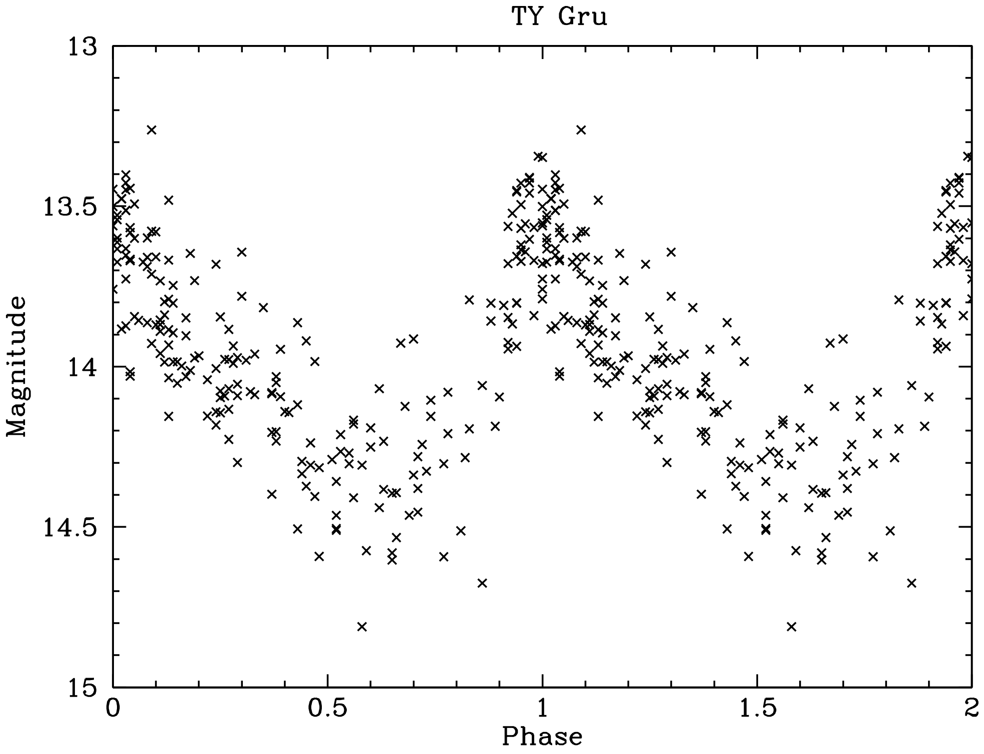

Figure 3.25 Same as Figure 3.5.

Chapter 4

The Chemical Compositions of Variable Field Horizontal Branch Stars: RR Lyrae stars

4.1 Introduction

The distinctive characteristics of RR Lyraes make them good standard candles for Galactic and extragalactic populations. In the past decades, many studies have been carried out to determine the mean absolute magnitudes of RR Lyr and hence their distances. For example, investigators have used the statistical parallax method (Fernley et al. 1998; Gould & Popowski 1998), main-sequence fitting in globular clusters (Gratton et al. 1997), and the Baade-Wesselink method (Liu & Janes 1990; see Gautschy 1987 for a review of this method). The distance scales are also essential to derive the cluster ages, which have significant impact for our understanding of stellar structure, evolution and ultimately the age of the universe.

Observations of RR Lyr pulsational properties are important in constraining both their pulsation models and the physics of their interiors. RR Lyr have typical periods of 0.2–1.0 day, with magnitude variation of 0.3–2.0 mag. Most of them pulsate in radial fundamental mode (RR-ab stars), radial first overtone (RR-c stars) and in some cases, in both modes simultaneously (RR-d stars). Additionally there is a special case, in which the light variations of RR Lyraes are modulated with respect to phase and amplitude on time scales of days to months, and even years. Such modulation is known as the Blazhko effect, named after the Russian astronomer who first identified it (Blažko 1907). This behavior has been attributed on the one hand to interference of radial and non-radial modes of similar frequency (see review by Preston 2009, 2011), and on the other hand to changes in pulsation period induced by changes in envelope structure (Stothers 2006, 2010). Vigorous debate about these possibilites is in progress.

The application of RR Lyr to study the chemical evolution of the Milky Way disk and halo began with the pioneering low-resolution spectroscopic survey by Preston (1959). That paper introduced a ΔS index that describes the relation between Hydrogen and calcium K-line absorption strengths. The standard ΔS index is defined at light minimum (i.e., near phase 0.8). Early analyses of model stellar spectra (Manduca 1981) and observed high-resolution spectra (Preston 1961; Butler 1975) showed a correlation between the ΔS index and metallicity. This relation has been calibrated through the studies of metal abundances in globular clusters (e.g., Smith & Butler 1978, Clementini et al. 1994, 2005) and presented in various forms (see e.g., Carney & Jones 1983).

While metallicities of RR Lyraes have widely been studied, there are only a handful of high-resolution detailed chemical abundance studies of field RR Lyraes to date (see Clementini et al. 1995; Lambert et al. 1996; Wallerstein & Huang 2010; Kolenberg et al. 2010; Hansen et al. 2011). These investigations generally have concentrated on limited phases near minimum light, because of the relatively slow variations in photometric effective temperature that occur at these pulsation phases and longer-lived than phases near maximum light. Clementini et al. (1995) deliberately selected RR-ab type variables that have accurate photometric and radial velocity data, so that atmospheric parameters could be derived independently of excitation and ionization equilibria. They obtained 2-6 individual spectra of 10 RR Lyr at pulsational phases 0.5–0.8, and co-added these spectra to increase signal-to-noise for chemical composition analysis. They suggested that lines of most elements are formed in conditions of local thermodynamic equilibrium (LTE) and that the abundances of RR Lyr share similar patterns to other stars of their metallicity domains. Lambert et al. (1996) gathered spectra of 18 targets; all stars except the prototype RR Lyr itself were observed on single occasions at a variety of mid-observation phases. They used photometric information to assist their derivation of iron and calcium abundances. Recent studies by Wallerstein & Huang (2010), Kolenberg et al. (2010) and Hansen et al. (2011) also reported results of a new detailed abundance study of several elements.

In this chapter, we present atmospheric parameters, metallicities, and detailed chemical compositions of 11 RR Lyr stars which have been observed intensively throughout multiple pulsational cycles. On average more than 200 individual spectra were gathered for each target. These spectra have been described in chapter 3, which discusses the observational data set, and reports the complete set of radial velocities and new pulsational ephemerides for the program stars. In §4.2 we briefly summarize the observations and reductions, and in §4.3 we describe the co-addition of spectra to prepare them for abundance analysis. §4.4 discusses the atomic line list and equivalent width measurements, §4.5 and 4.6 describe the initial and derived model atmosphere parameters, §4.7 describe the optimal phases and §4.8 presents the results of chemical abundances. Finally, we describe the evolutionary state of these RR Lyr in §4.9 and draw a conclusion in §4.10.

4.2 Observations and Data Reduction

Photometric data from the All Sky Automated Survey (ASAS) and radial velocities were presented in chapter 3 for a sample of 11 field RR-ab type variable stars, along with their corresponding folded lightcurves and radial velocity curves determined from ephemerides derived in that chapter. The RR Lyraes being analyzed here are AS Vir, BS Aps, CD Vel, DT Hya, RV Oct, TY Gru, UV Oct, V1645 Sgr, WY Ant, XZ Aps and Z Mic. There are no previous detailed chemical abundances study of these stars, except TY Gru (Preston et al. 2006b). In Table 4.1 we give the basic information about our program stars and refer the readers to §3 of chapter 3 for details of data reduction. Here we summarize the observations.

The spectroscopic data were obtained with the du Pont 2.5-m telescope at the Las Campanas Observatory (LCO), using a cross-disperesed echelle spectrograph. We used this instrument with a $1.5'' \times 4''$ entrance slit, which gives a resolving power of $R \equiv \lambda/\Delta\lambda \sim 27,000$ at the Mg I b triplet lines (5180 Å), and a total wavelength coverage of $3500 - 9000$ Å. Integration times ranged from 200–600 s. The values of S/N achieved by such integrations can be estimated by observations of a star with similar colors to RR Lyr, CS 22175−034 (Preston et al. 1991), for which an intergration time of 600 s yielded S/N$\sim$ 10 at 4050Å, S/N$\sim$ 15 at 4300Å, S/N$\sim$ 20 at 5000Å, S/N$\sim$ 30 at 6000Å and S/N$\sim$ 30 at 6600Å. We took Thorium-Argon comparison lamp exposures at least once per hour at each star position for wavelength calibration.

The pulsational periods of our program stars tightly cluster around 0.56 days, and so the 600 s maximum integration time corresponds to at most ∼1.2% of the period. The radial velocity excursions over a pulsational cycle are typically ~65 km s^{-1}. If we neglect the phase interval 0.85-1.0, in which very rapid velocity changes occur, then during a 600 s integration the radial velocity typically changes by only ~0.9km s^{-1}, smaller than a typical absorption line width. Even during the rapid velocity changes observed in the phase interval 0.85–1.0, the radial velocity changes by only about 5 km s^{-1} during the maximum integration time; the velocity smearing is still relatively small in this complex pulsational domain.

4.3 Creation of Spectra for Abundance Analysis

In this section, we discuss the method of combining spectra for Blazhko and non-Blazhko stars. Then we describe the scattered light subtraction from the combined spectra and the preparation of final spectra for equivalent width (EW) measurements and chemical abundance analysis.

We first shifted individual spectra to rest wavelength by use of the IRAF DOPCOR task in the ECHELLE package, having calculated RV_{obs} with the FXCOR task. The goal is to create as many spectra (or phase bins) as possible throughout the pulsational cycle per star. However, phase contamination due to rapid changes in the atmosphere from phase to phase during a pulsational cycle, must be minimized. A balance between having enough number of spectra for combining to achieve high S/N and avoiding phase contamination is needed.

We designated a series of phase bins per star. Using the phase information in Table 4 of chapter 3, we selected about 10–15 spectra with similar phases for combining, in order to significantly increase the signal-to-noise for abundance analysis. For a Blazhko star, we treated the cycles of different RV amplitudes separately, which resulted in more than one series of phase bins.

Table 4.1. Basic information of our program stars.

Star	R.A.(J2000) (hr m s)	Decl.(J2000) (° ′ ″)	Data Used[a] (HJD 2450000+)	T_0 (HJD 2450000+)	err (HJD 2450000+)	Period (day)	err (day)	N[b]
CD Vel	09 44 38.24	-45 52 37.2	all	3837.632	0.0003	0.573510	0.000003	208
WY Ant	10 16 04.95	-29 43 42.4	all	4191.685	0.0097	0.574344	0.000002	136
DT Hya	11 54 00.18	-31 15 40.0	all	4583.637	0.0089	0.567978	0.000001	102
AS Vir	12 52 45.86	-10 15 36.4	all	4907.709	0.0098	0.553412	0.000002	262
RV Oct	13 46 31.75	-84 24 06.4	all	3841.602	0.0016	0.571170	0.000002	222
XZ Aps	14 52 05.43	-79 40 46.6	all	3842.735	0.0052	0.587264	0.000002	289
BS Aps	16 20 51.51	-71 40 15.8	all	4583.785	0.0045	0.582561	0.000007	252
UV Oct	16 32 25.53	-83 54 10.5	3836.843842.91, 4306.465021.84	3837.875	0.0072	0.542578	0.000003	323
			3931.584194.92, 5070.485073.59	5070.605	0.0072	⋯	⋯	⋯
V1645 Sgr	20 20 44.47	-41 07 05.7	4191.894306.90	4306.775	0.0150	0.552948	0.000005	198
			4579.854583.91	4579.895	0.0150	⋯	⋯	⋯
			3932.733946.75, 4687.665074.71	4687.703	0.0170	⋯	⋯	⋯
Z Mic	21 16 22.71	-30 17 03.1	all	5075.606	0.0015	0.586926	0.000001	185
TY Gru	22 16 39.42	-39 56 18.0	3933.793935.65, 5071.50–5073.66	3933.785	0.0120	0.570065	0.000005	114
			3945.634306.89	4304.885	0.0120	⋯	⋯	⋯

[a] Data with the corresponding HJDs were used to derive the T_0

[b] Total number of observed spectra

Prior to combination, the individual spectra were examined carefully, especially near the Hα profile, to guard against any obvious phase contamination in the averaged spectrum. The Hα profile was chosen because it varied significantly from phase-to-phase, and thus any anomalies in its appearance could be identified easily. The number of spectra for combining was decided on a case-by-case basis through these inspections of the individual spectra. We have listed/named the single combined spectrum as the mid-point of starting and ending phases (e.g., a spectrum at phase 0.015 is the combination of spectra that have phases from 0 to 0.03).

The shapes of metal line profiles of combined XZ Aps and RV Oct spectra and their associated Hα line profiles (after correction for scattered light, see below) are displayed in Figure 4.1–4.4. The figures show distinctive variations of Hα profiles from phase to phase.

To correct for scattered light in the RR Lyr spectra, we first measured the peak count of each order of the combined spectrum for each phase. This yielded the *relative* spectral energy distribution (SED). We did the same for the spectra of standard stars (see chapter 3) and for a family of combinations of their spectra (e.g., one such composite contained 50% of a G6 and 50% of an A3 spectral type). Subsequently, we compared the SEDs of standard stars and their combination family with the combined RR Lyr spectrum. We illustrate SED comparisons between the spectra of standard stars and their combination family with RR Lyr spectra in different phases in Figure 4.5.

Once the best match was found (as shown in Figure 4.5), we normalized the combined spectrum with IRAF CONTINUUM task in ONED package and then subtracted the corresponding fractional contribution of the inter-order background to the on-order starlight, b_λ/s_λ (corrected by a factor of 5/3 due to different aperture extractions, see chapter 3), of a particular spectral type from each order. The b_λ/s_λ values were listed in Table 3 of chapter 3[1].

The RR Lyr spectrum corrected for scattered light was then renomalized and stitched into 4 long wavelength spectra. These 4 long wavelength spectra per phase bin were used for the abundance analysis. The depths of spectral lines before and after the scattered light correction for the combined spectrum of CD Vel at phase 0.3 is presented in Figure 4.6. The effect of this correction of course deepens all lines; the effect was larger for strong lines more than weak ones, with $\sim 8\%$ change with respect to the line strength.

---

[1] The mean b_λ/s_λ of the family of spectra combinations are not listed in Table 3 but can be calculated. For example, scattered light correction for a 50% of G6 and 50% of A3 spectral type spectrum would be equal to adding 50% b_λ/s_λ of G6 and 50% b_λ/s_λ of A3 spectral type.

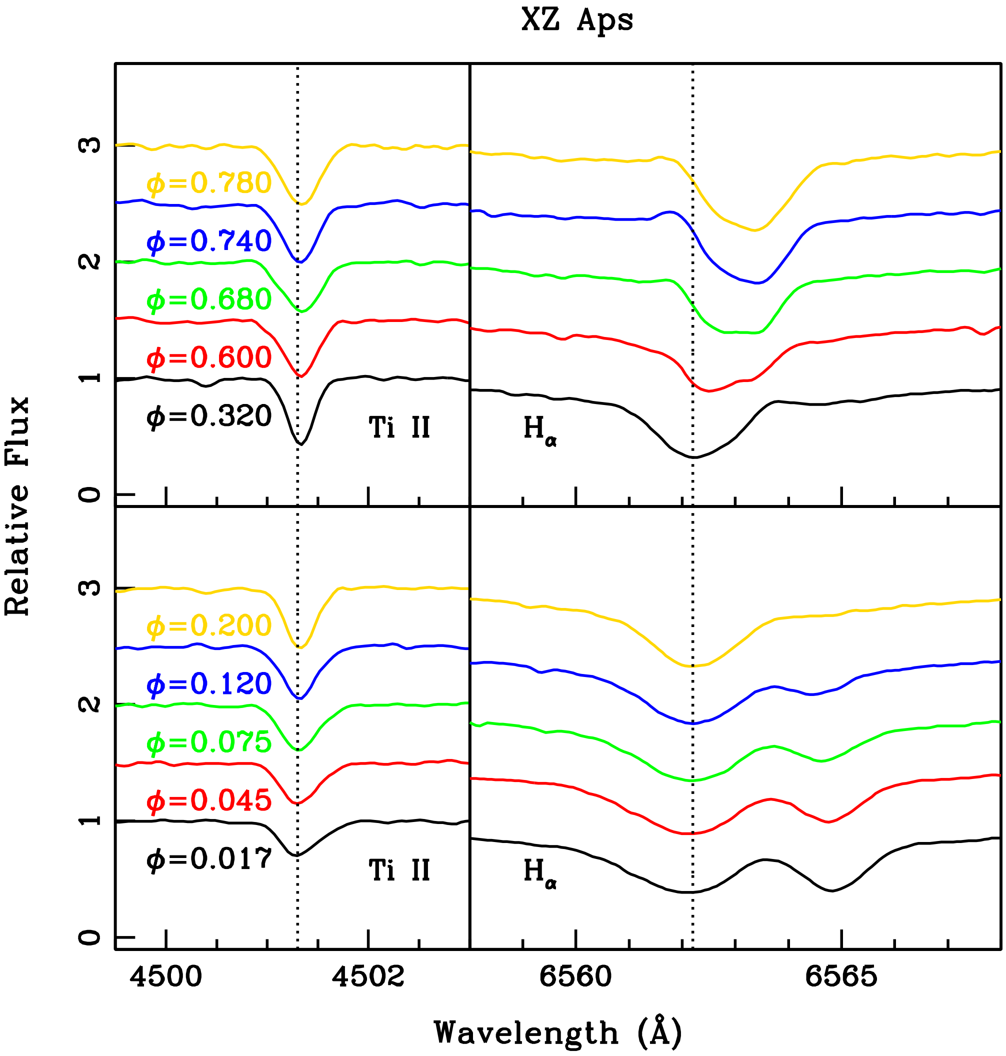

Figure 4.1 The left and right panels show the metal Ti I and Hα line profile variations of combined spectra of XZ Aps from ϕ =0.017–0.78. The metal line appears to be sharpest near $\phi = 0.32$.

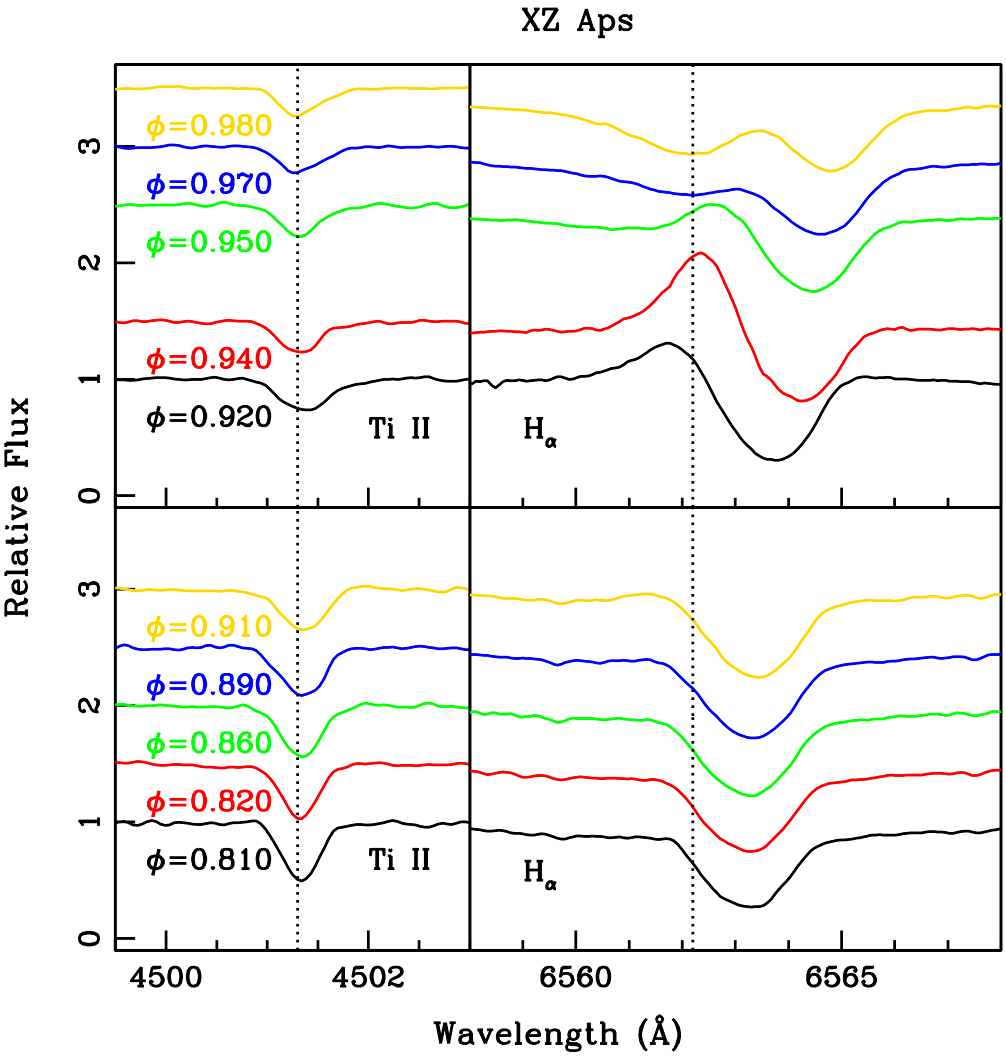

Figure 4.2 This is the continue presentation of Figure 4.1 for line profile variatons of combined spectra of XZ Aps from ϕ =0.81–0.98. The H_α emission occurs at its highest near $\phi = 0.94$.

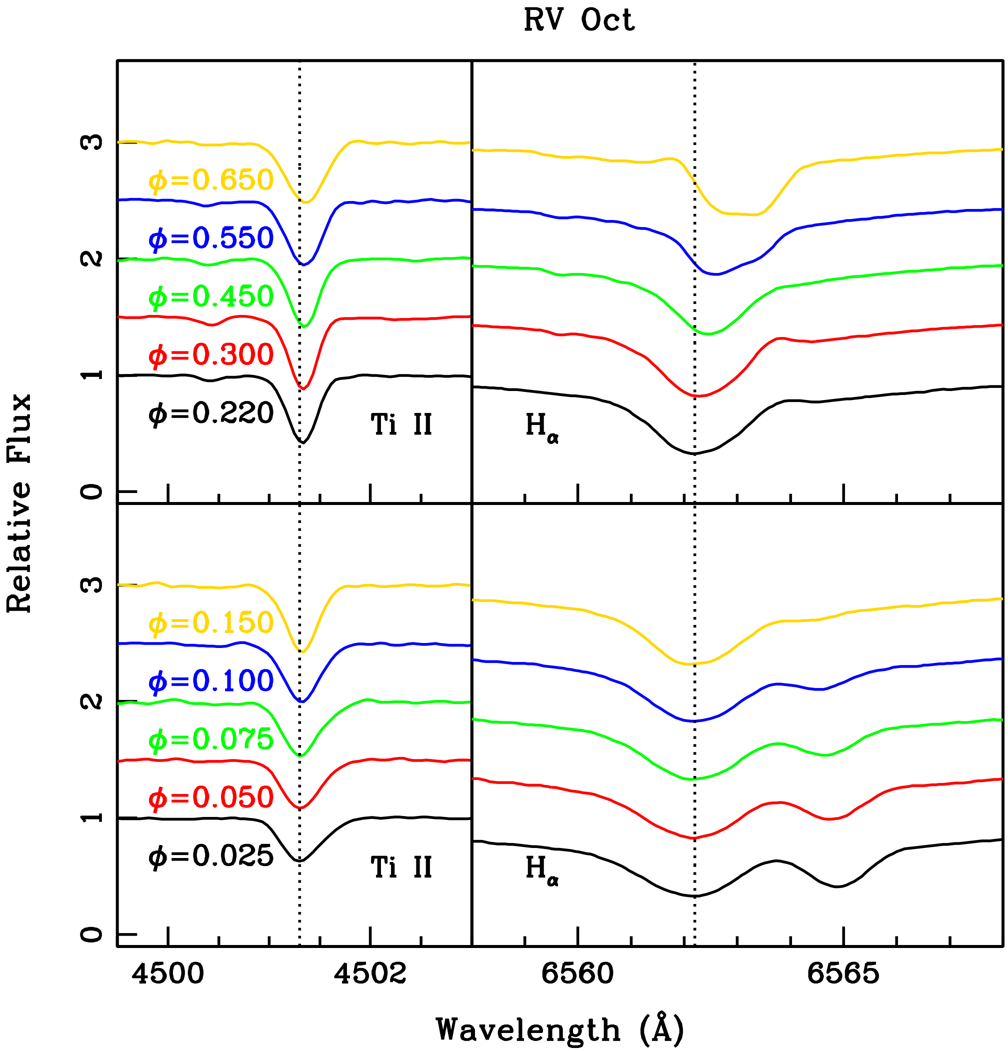

Figure 4.3 Same as Figure 4.1 except for RV Oct, which shows many more combined spectra between $\phi =\sim 0.2 - 0.6$. The metal lines are reasonable sharp (least distortion) between these phases.

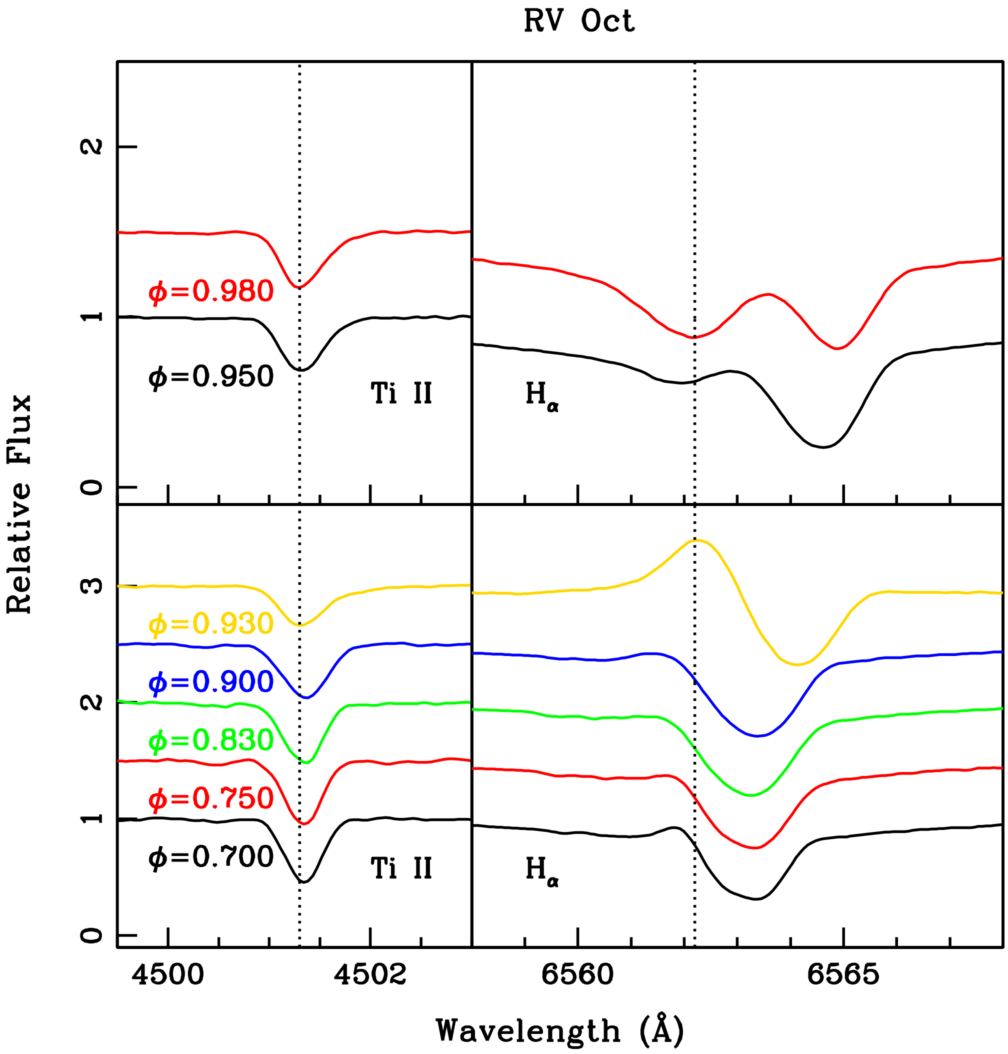

Figure 4.4 This is the continue presentation of Figure 4.3 for line profile variations of combined spectra of RV Oct from ϕ =0.7–0.98. The H_α emission occurs at its highest near $\phi = 0.93$.

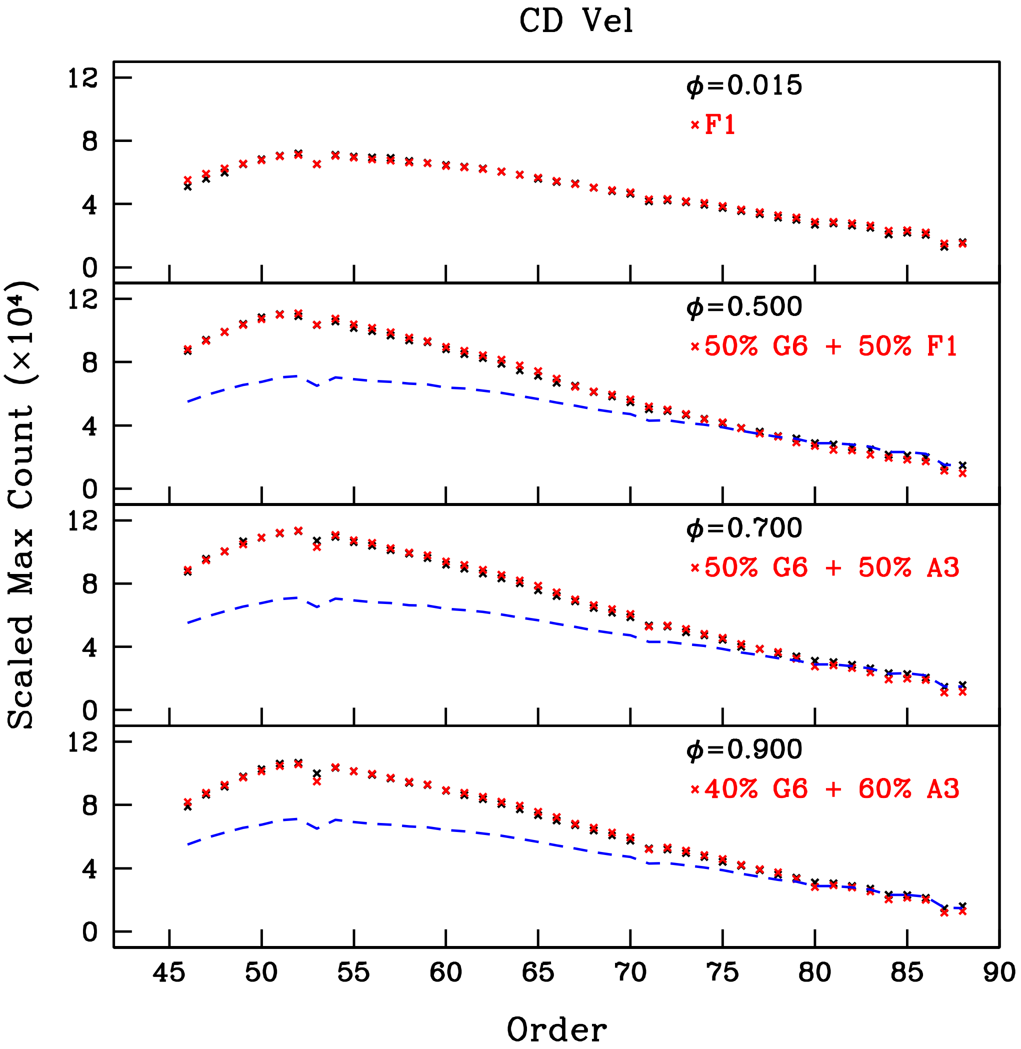

Figure 4.5 Comparisons between the spectral energy distribution of standard stars/family of their spectra combination and the combined spectra of CD Vel in different phases. The count of each order was scaled for comparisons. These comparisons were used to decide the amount of scattered light correction for each order. The blue dashed line (same as the top panel) represents the SED of F1 spectral type for comparisons.

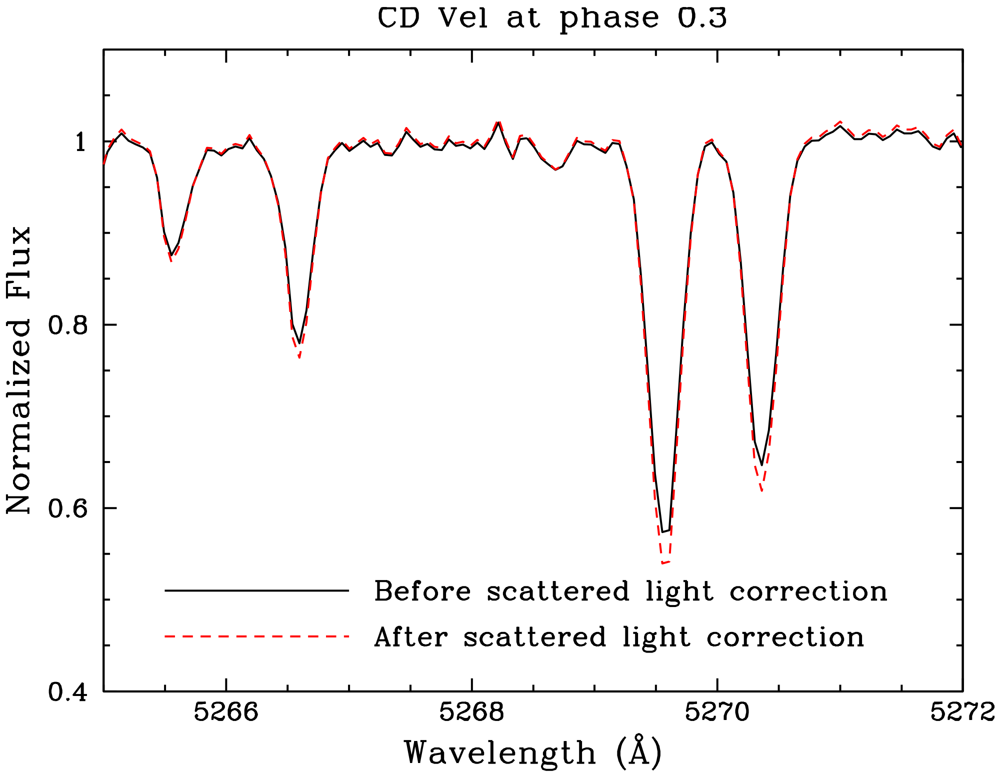

Figure 4.6 The black solid line and red dashed line represent the combined spectrum of CD Vel at phase 0.3 before and after scattered light correction, respectively. The lines are deeper after the scattered light correction.

4.4 Line List and Equivalent Width Measurements

We employed the atomic list compiled in chapter 2 for our analysis. The line wavelengths, excitation potentials (EP) and oscillator strengths ($\log gf$) and their sources are given in chapter 2. For each star, we measured the EWs of unblended atomic absorption lines semi-automatically with SPECTRE[2].

---

[2] An interactive spectrum analysis code (Fitzpatrick & Sneden 1987). It has been modified to integrate absorption line profiles to determine the EW values without manually specifying the wavelength.

Each line measurement was visually inspected prior to acceptance of its EW. Due to the asymmetric line profiles of RR Lyr stars over most of their cycle, we adopted the method of intergrating over the relative absorption across a line profile to determine the EW values. Fitting a Gaussian to the line profile was adopted only at the phase with sharp (symmetric), non-distorted absorption line profile. We excluded strong lines, defined as those with reduced widths, $\log \mathrm{RW} \equiv \log \mathrm{EW}/\lambda \gtrsim -4.0$, because they are relatively insensitive to abundance on the damping portion of the curve-of-growth. Very weak lines ($\log \mathrm{RW} < -5.9$) were also excluded because the EW measurement errors were too large.

There is no previous detailed chemical abundances study of any of our sample stars (except TY Gru), and thus no previous EWs reported in the literature. However, we may compare our EW measurements with EWs of other RR Lyr that possess similar stellar parameters. The only published EW measurements are from Clementini et al. (1995). In Figure 4.7 and 4.8, we compare Fe I & Fe II EW measurements in two groups of star. The literature data for RR Cet with [Fe/H]$= -1.38$ at $\phi \sim 0.75$ and VX Her with [Fe/H]$= -1.58$ at $\phi \sim 0.62$ were used to compare with our DT Hya with [Fe/H]$= -1.47$ at $\phi = 0.77$ and RV Oct with [Fe/H]$= -1.53$ at $\phi = 0.65$. Taking EW differences between Clementini et al. (1995) and this study (as shown in Figure 4.7), we find: for the RR Cet and DT Hya pair, $\Delta\mathrm{EW} = -9.5 \pm 3.8$ mÅ, $\sigma = 11.3$ mÅ, 9 lines; and for the VX Her and RV Oct pair, $\Delta\mathrm{EW} = -3.7 \pm 2.1$ mÅ, $\sigma = 8.8$ mÅ, 17 lines. Since the deviations (ΔEW) are small, we conclude that our EW measurements appear to be reasonable.

We may also compare the EW measurements among our stars. A correlation of Fe I and Fe II EWs for BS Aps and RV Oct at phase 0.3 is presented in Figure 4.9. Both stars have similar log g, metallicity and $v_{\rm t}$ but BS Aps has slightly cooler $T_{\rm eff}$ ($\sim$ 100 K) than RV Oct. The top panel of Figure 4.9 shows a slight offset, which indicates a larger EW measurements for BS Aps. We expect such deviation because metal lines are stronger in cooler star. Overall, the EW measurements are consistent among our stars.

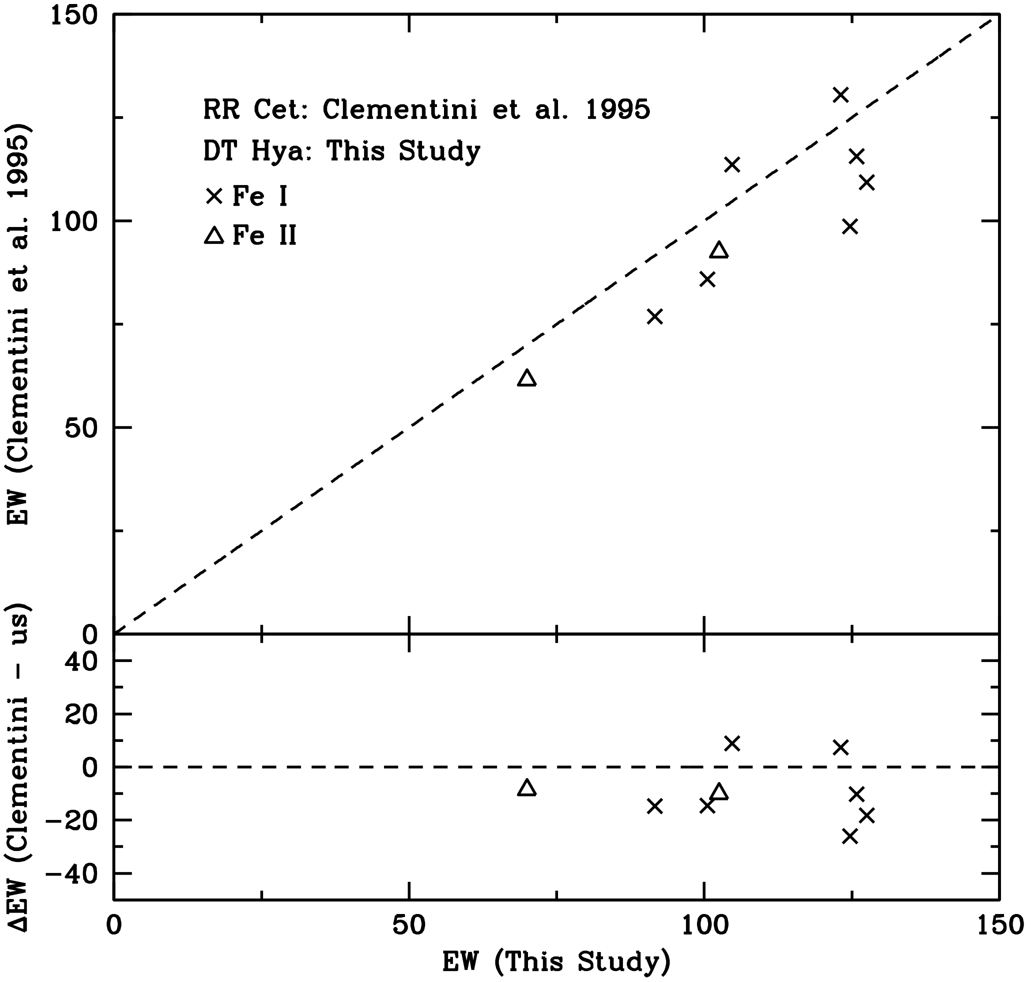

Figure 4.7 Comparisons of our measured Fe I & Fe II EWs of DT Hya with RR Cet of Clementini et al. (1995). The top panel shows 1:1 comparison of EW measurements. The bottom panel shows the differences between Clementini et al. (1995) EW measurements and ours. The crosses and triangles represent Fe I & Fe II lines, respectively.

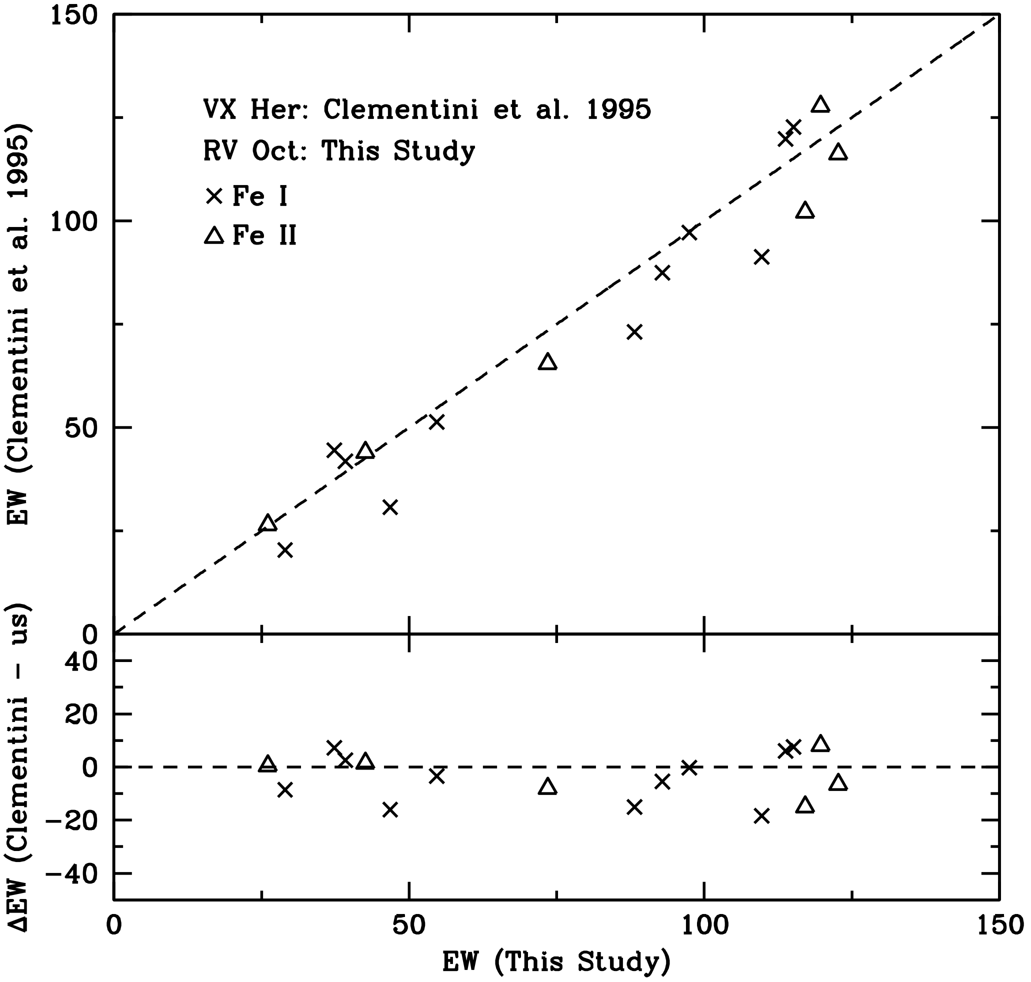

Figure 4.8 Comparisons of our measured Fe I & Fe II EWs of RV Oct with VX Her of Clementini et al. (1995). The top panel shows 1:1 comparison of EW measurements. The bottom panel shows the differences between Clementini et al. (1995) EW measurements and ours. The crosses and triangles represent Fe I & Fe II lines, respectively.

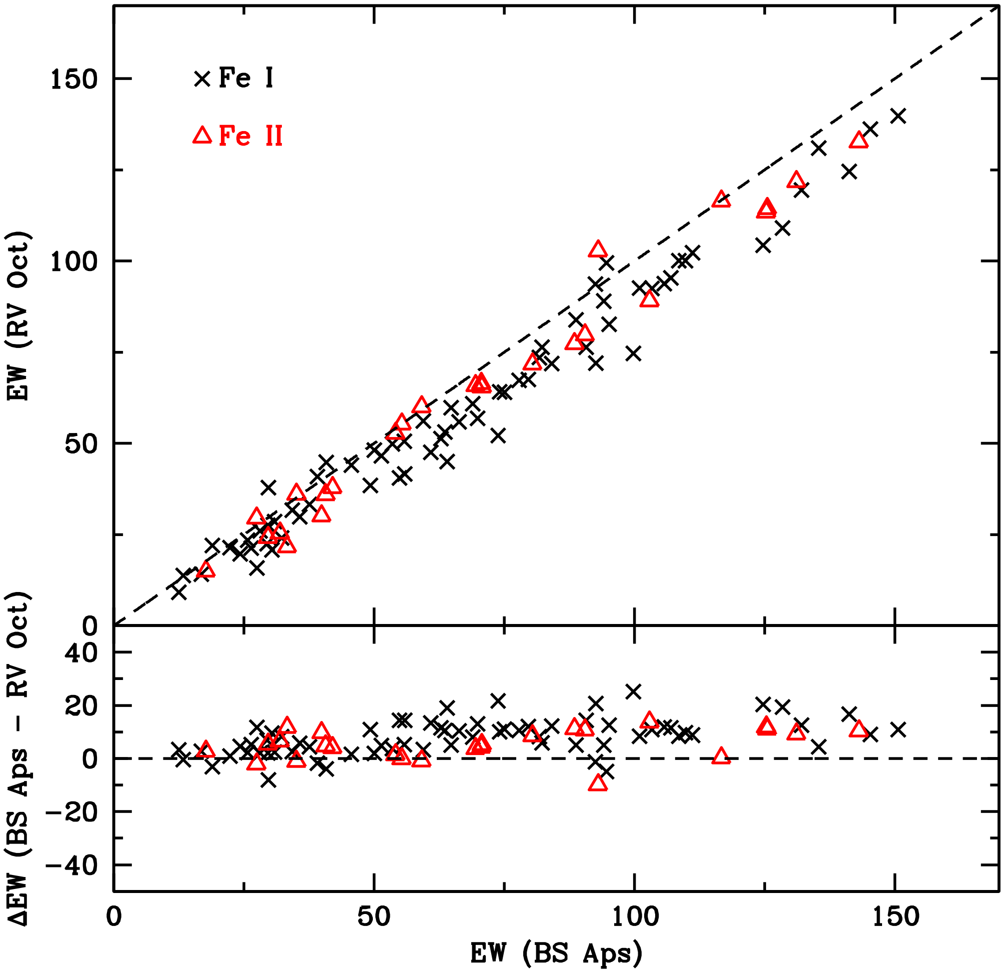

Figure 4.9 The top panel shows 1:1 comparison of Fe I & Fe II EW measurements between our RV Oct and BS Aps. Both stars have similar log g, metallicity and v_t but BS Aps has cooler $T_{\rm eff}$ than RV Oct. The small offset is expected because a cooler star should have stronger metal lines than its counterpart. The black crosses and red triangles represent Fe I & Fe II lines, respectively.

4.5 Analysis: Initial Model Atmosphere Parameters

We derived abundances in our RR Lyr stars through EW matching and spectrum syntheses. Both methods require a stellar atmosphere model that is characterized by parameters effective temperature ($T_{\rm eff}$), surface gravity (log g), metallicity ([M/H]) and microturbulence ($v_{\rm t}$). We constructed the models by interpolating in Kurucz's non-convective-overshooting atmosphere model grid (Castelli et al. 1997), using software developed by A. McWilliam and I. Ivans. The elemental abundances were subsequently derived using the latest 2010 version local thermodynamic equilibrium (LTE), plane-parallel atmosphere spectral line synthesis code MOOG[3] (Sneden 1973). This code includes treatment of electon scattering contributions to the near-UV continuum that have been implemented by Sobeck et al. (2011).

The details on determining the stellar parameters are given in the following subsections. Final model atmosphere parameters were determined by iteration through spectroscopic constraints: (1) for $T_{\rm eff}$, that the abundances of individual Fe I and Fe II lines show no trend with EP; (2) for $v_{\rm t}$, that the abundances of individual Fe I and Fe II lines show no trend with reduced width log (RW); (3) for log g, that ionization equilibrium be achieved between the abundances derived from the Fe I and Fe II species; and (4) for metallicity [M/H], that its value is consistent with the [Fe I/H] determination. An example of fulfilling the spectroscopic constraints of (1) and (2) is presented in Figure 4.10.

---

[3] Available at http://www.as.utexas.edu/ chris/moog.html .

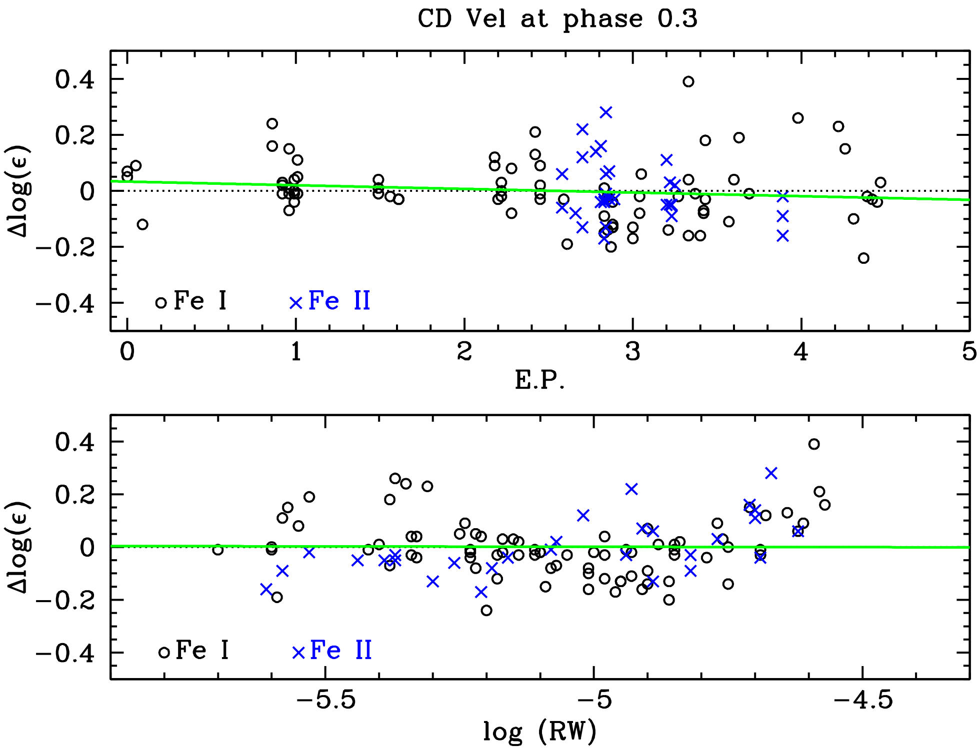

Figure 4.10 Demonstration of determining T_{eff} and v_{t} values based on spectroscopic constraints. The top and bottom panels show the difference of Fe abundances as a function of EP and log (RW), respectively. The black open circles and blue crosses represent Fe I and Fe II. The green solid line shows the trends in both panels.

4.5.1 Effective Temperature

Use of spectroscopic constraints alone to determine model atmosphere parameters can lead to ambiguous results, due to degeneracies in the responses of individual EWs to changes in various quantities. This is especially true for $T_{\rm eff}$ and $v_{\rm t}$: the lines with lower EPs are usually those with larger EWs, making it difficult to simultaneously solve for $T_{\rm eff}$ and $v_{\rm t}$ unambiguously. It is important to have a good initial guess at $T_{\rm eff}$ from other data, and the standard method involves photometric color transformations. Using color-temperature transformations (e.g., Alonso et al. 1996, Ramírez & Meléndez 2005b) is straightforward to obtain the temperatures of the RR Lyr throughout their pulsational cycles. However, our program stars lack the necessary photometric information. Extensive V magnitude data are available for all our stars at the All-Sky Automated Survey (ASAS) website[4] (Pojmanski 2002) but I magnitude data have not been gathered. Therefore we do not have any color information for our stars and developement of a new, indirect method to estimate initial $T_{\rm eff}$ values for at individual phases of our RR Lyr stars is needed.

4.5.1.1 Color–Temperature Transformation

Temperature transformations from photometric indices are generally achieved with either a stellar atmosphere model (see Liu & Janes 1990) or an empirical color–temperature calibration (see Clementini et al. 1995). The latter method can be problematic because it does not account easily for metallicity and surface gravity effects. Of particular importance is the gravity, which varies about a factor of ten during the pulsational cycle of an RR-ab star.

---

[4] http://www.astrouw.edu.pl/asas/

Ideally, hydrodynamical models would be more suitable to describe RR Lyr atmospheres (and thus their $T_{\rm eff}$ values at any phase) but no such models capable of dealing with the fast moving atmopheres of RR Lyr exist yet. Luckily the most dynamical phase (near minimum radius), in which a shock wave is produced during the rapid acceleration of an RR Lyr atmosphere, only occurs in a very short timescale ($\sim$ 15 min). In addition, the theoretical study by Castor (1972) has suggested that a dynamical atmosphere model produces a continious spectrum that is nearly indistinguishable from that of a hydrostatic atmosphere at the same temperature and gravity in most of the pulsational cycle. A non-linear pulsational model for the prototype star RR Lyr by Kolenberg et al. (2010) shows that the kinetic energy of its atmosphere reaches a minimum at two phases, $\phi \simeq 0.35$ and 0.90 (see their Figure 1), for which the dynamical effects are small. Therefore, atmosphere of RR Lyrs can be considered in some quasi-static equalibrium during most of the pulsational phases.

Liu & Janes (1989) suggested that the RV curve of an RR-ab variable, which is basically a "mirror image" of its photometric lightcurve, could be used to estimate $T_{\rm eff}$ values around the pulsational cycle. The RV curve shows a prominent "depression" feature near phase 0.7 that corresponds to the early shockwave "bump" feature as seen in the lightcurve (Gillet et al. 1989). Since RR-ab's pulsate in a certain temperature/luminosity range, and nearly all of them vary similarily throughout their cycles, we can obtain $T_{\rm eff}$–phase relations from published examples having both well-observed RV curves and color curves. Then, the derived relations can be applied to our RR Lyr stars.

The extensive work by Liu & Janes (1989, 1990), here after LJ89 and LJ90, were used to achieve this. We chose eight RR-ab stars from LJ89 (SW

And, RR Cet, SU Dra, RX Eri, RR Leo, TT Lyn, AR Per and TU Uma). For these stars we first extracted $B - V$, $V - R_c$ and $V - I_c$ color indices[5] and their RVs that correspond to our defined 11 phase bins (e.g., $\phi = 0$, 0.05, 0.1, 0.2, 0.3, 0.4, 0.5, 0.6, 0.7, 0.8 and 0.85, see Table 4.3 for details). The color index of a phase that most closely matches one of our phase bins was adopted (e.g., RV at phase 0.8525 in LJ89 was adopted as our RV for the defined phase 0.85). The published color curves were not corrected for the reddening. Thus, we corrected the color indices of $B - V$, $V - R_c$ and $V - I_c$ as follow:

$$c(colors) = (colors) - E(colors), \tag{4.1}$$

where $c(colors)$ is the corrected color indice and $E(colors) = kE(B-V)$. The values of k and $E(B-V)$ were adopted from Table 2 & 3 of LJ90. We refer the reader to §2b of LJ90 for the extensive discussion of their choice of reddenings.

To transform the color indices of LJ89 into $T_{\rm eff}$ values, a set of synthetic colors computed from model stellar atmosphere grids is needed. Calculated colors are given in Table 7 of LJ90, but those are based on relatively old model atmospheres (Kurucz 1979). Instead, we created grids that correspond to the metallicity of RR Lyr in LJ90 with Kurucz's non-convective-overshooting atmosphere models[6] (Castelli et al. 1997). A surface gravity of $\log g = 3.0$ was chosen initially because it is a better representation for the mean effective gravity (with only small variations) of an RR Lyr star during phases 0–0.8 (i.e., $3.2 < \log g < 2.8$; see Figure 1 of LJ90). However, the effective gravity (which will be described in detail in §4.5.2) is an approximation for compensating the

---

[5] LJ89 used Johnson-Cousins color system. The $V-K$ color indice was not chosen because the lack of photometric data points for most of the RR-ab variables in LJ89.

[6] The specific models are under the suffix ODFNEW on Kurucz's website: http://kurucz.harvard.edu/grids.html

dynamical nature of the RR Lyr atmospheres, which could be quite different than the actual surface gravity in the static model that we applied here. Our tests showed that the transformed $T_{\rm eff}$ with $\log g = 3.0$ model was persistently too high to fulfill the spectroscopic constraint for all phases of our RR Lyr during the initial spectroscopic analysis. We noted that the effective gravity calculated in LJ89 were based on the Baade-Wesselink (BW) method. For & Sneden (2010) showed that the log g derived from the BW method by others were systematically higher than indicated by the spectroscopic method for non-variable horizontal branch stars analysis (see Figure 19 of For & Sneden 2010). Therefore, we employed models with $\log g = 2.0$; the new grids are presented in Table 4.2.

The subsequent color–temperature transformation was carried out by employing a linear interpolation scheme:

$$T_{\rm eff} = T_{\rm eff\,1} + \frac{(T_{\rm eff\,2} - T_{\rm eff\,1})}{(c_2 - c_1)} \times (c_* - c_1), \tag{4.2}$$

where $T_{\rm eff\,1}$ and $T_{\rm eff\,2}$ are two effective temperatures from the grid, c_1 and c_2 are the color indices of $T_{\rm eff\,1}$, $T_{\rm eff\,2}$, and c_* is the color index of the star at a particular phase.

To derive the $T_{\rm eff}$–phase relations, we employed only the $V - I_c$ color because the color–temperature transformation became less sensitive to metallicity and gravity at longer wavelengths. We demonstrate the sensitivity of transformed $T_{\rm eff}$ as a function of metallicity in Figure 4.11. The strong dependence of $B - V$ on metallicity is caused by the line blanketing in the B filter. The calculated $T_{\rm eff}$ for a given observed color index was adopted at phase 0.3 of RR Cet for different metallicities with fixed log g. The difference was taken between the calculated $T_{\rm eff}$ at that particular [M/H] minus the $T_{\rm eff}$

at [M/H]$= -2.5$. We summarize the color–temperature transformations in Table 4.3. In Figures 4.12, 4.13, and 4.14 we show the transformed $T_{\rm eff}$ from $B-V$, $V-R_c$ and $V-I_c$, respectively, versus phase for eight selected RR-ab variables, which will be called "calibration stars" in the following sections.

Subsequently, we fitted 4$^{\rm th}$-order polynomials to $T_{\rm eff}$ values transformed from $V-I_c$ vs phase. The fitted curves are called "calibration curves" for our RR Lyr. Phases after the rising branch of RR Lyr (i.e., after phase $\sim$0.85) were excluded to avoid any artificial fit to the data. We considered the $T_{\rm eff}$ at those phases to be close to their descending branch (i.e., phase 0.9 equivalent to phase 0.1). The derived 4$^{\rm th}$-order polynomial equations are given in Table 4.4 and Figure 4.15 shows the fit to the $V-I_c$ data.

To decide which "calibration curves" to use for obtaining the initial $T_{\rm eff}$ throughout the pulsational cycle of our RR Lyr, we compared our RV curves to the RV curves of those eight RR-ab variables selected from LJ89. An example of such comparison is shown in Figure 4.16, where the RV curve of RV Oct matched the RV curve of RR Cet but not TT Lyn.

We found that comparing the RV curves of our Blazhko stars to the RV curves of calibration stars were particularly difficult. The RV curves of calibration stars represent typical pulsation RV amplitudes of non-Blazhko RR-ab variables. In the case of our Blazhko stars, the RV amplitudes vary significantly in numerous cycles. Thus, we did not find any exact match to the RV curves of our Blazhko stars with the calibration stars. Instead, we selected the closest match RV curve of a particular calibration star and used its calibration curve to obtain the initial $T_{\rm eff}$ in those cases.

Table 4.2. Synthetic Colors for Model $\log g = 2.0$.

	Effective Temperature (K)												
Color Indices	5500	5750	6000	6250	6500	6750	7000	7250	7500	7750	8000	8250	8500
[M/H]= −0.10 (SW And)													
$B-V$	0.755	0.650	0.555	0.470	0.394	0.323	0.249	0.177	0.124	0.081	0.044	0.014	-0.007
$V-R_c$	0.396	0.352	0.310	0.270	0.230	0.193	0.156	0.120	0.090	0.065	0.044	0.028	0.018
$V-I_c$	0.779	0.698	0.620	0.544	0.470	0.397	0.328	0.263	0.206	0.158	0.118	0.087	0.065
[M/H]= −0.30 (AR Per)													
$B-V$	0.722	0.619	0.528	0.447	0.375	0.307	0.237	0.167	0.115	0.074	0.039	0.011	-0.008
$V-R_c$	0.390	0.347	0.306	0.266	0.227	0.190	0.153	0.118	0.088	0.064	0.043	0.027	0.017
$V-I_c$	0.776	0.697	0.619	0.543	0.470	0.398	0.329	0.264	0.207	0.159	0.119	0.088	0.066
[M/H]= −1.15 (RR Leo)													
$B-V$	0.612	0.522	0.446	0.380	0.319	0.262	0.204	0.140	0.092	0.056	0.026	0.003	-0.011
$V-R_c$	0.375	0.334	0.294	0.256	0.218	0.182	0.146	0.112	0.083	0.059	0.040	0.026	0.016
$V-I_c$	0.773	0.694	0.618	0.545	0.472	0.401	0.332	0.268	0.210	0.162	0.122	0.092	0.071
[M/H]= −1.25 (RR Cet and TU Uma)													
$B-V$	0.603	0.515	0.441	0.376	0.316	0.259	0.202	0.138	0.091	0.055	0.026	0.003	-0.012
$V-R_c$	0.374	0.333	0.294	0.256	0.218	0.182	0.146	0.112	0.083	0.059	0.040	0.026	0.017
$V-I_c$	0.773	0.695	0.619	0.545	0.472	0.401	0.332	0.268	0.211	0.162	0.122	0.092	0.072
[M/H]= −1.35 (TT Lyn)													
$B-V$	0.594	0.508	0.435	0.371	0.312	0.256	0.199	0.136	0.089	0.054	0.025	0.003	-0.012
$V-R_c$	0.373	0.332	0.293	0.255	0.218	0.181	0.146	0.112	0.082	0.058	0.039	0.026	0.017
$V-I_c$	0.773	0.695	0.619	0.545	0.472	0.401	0.332	0.268	0.211	0.162	0.122	0.092	0.072
[M/H]= −1.40 (RX Eri)													

Table 4.2 (cont'd)

	Effective Temperature (K)												
Color Indices	5500	5750	6000	6250	6500	6750	7000	7250	7500	7750	8000	8250	8500
$B - V$	0.589	0.504	0.432	0.369	0.310	0.255	0.198	0.136	0.088	0.053	0.025	0.002	-0.012
$V - R_c$	0.367	0.328	0.290	0.252	0.215	0.178	0.143	0.109	0.081	0.057	0.038	0.026	0.018
$V - I_c$	0.773	0.695	0.619	0.546	0.473	0.402	0.333	0.269	0.211	0.163	0.123	0.093	0.072
[M/H]= -1.60 (SU Dra)													
$B - V$	0.574	0.493	0.424	0.362	0.305	0.250	0.195	0.133	0.086	0.051	0.024	0.002	-0.012
$V - R_c$	0.370	0.330	0.291	0.254	0.217	0.180	0.145	0.111	0.082	0.058	0.039	0.026	0.017
$V - I_c$	0.773	0.695	0.619	0.546	0.473	0.402	0.333	0.269	0.211	0.163	0.123	0.094	0.073

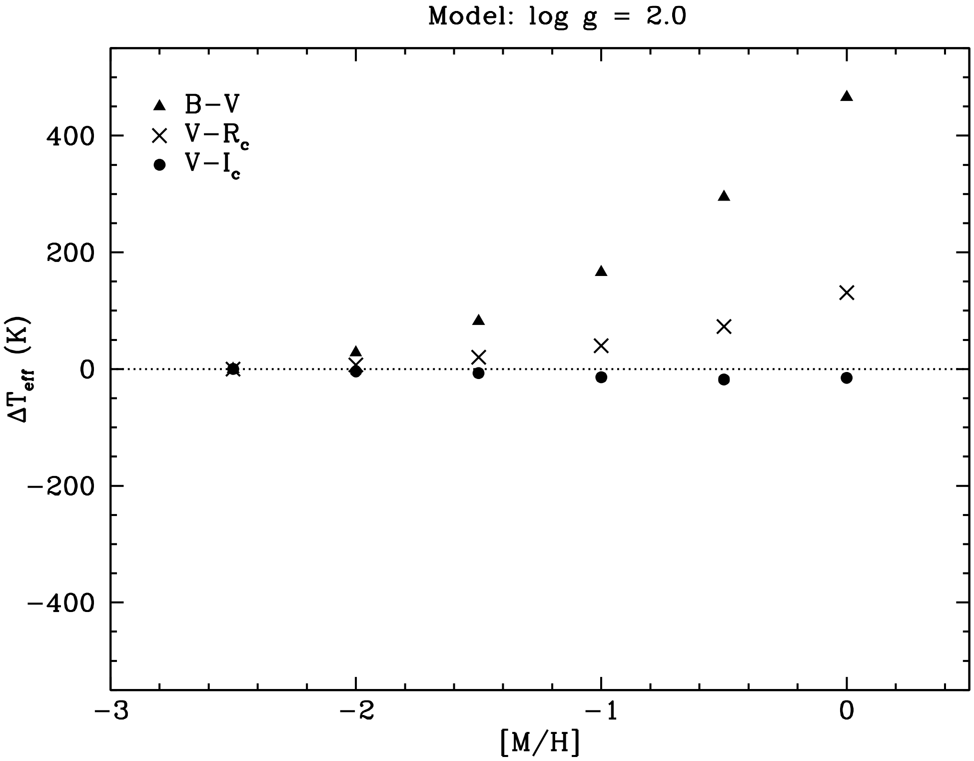

Figure 4.11 The deviation of effective temperature calculated from different synthetic color indices as a function of metallicity. The employed color indices are at phase 0.3 of RR Cet with fixed gravity. The difference was taken between the calculated $T_{\rm eff}$ at that particular [M/H] minus the $T_{\rm eff}$ at [M/H]$= -2.5$. Symbols represent $T_{\rm eff}$ values derived from the color indices: $B-V$ (triangles); $V-R_{\rm c}$ (crosses); $V-I_{\rm c}$ (circles).

Table 4.3. Basic Data for Deriving the $T_{\rm eff}$–Phase Relations.

Phase	RV$-$RV$_{\rm min}$	$B-V$	$c(B-V)$	$T_{\rm eff}$	$V-R_c$	$c(V-R_c)$	$T_{\rm eff}$	$V-I_c$	$c(V-I_c)$	$T_{\rm eff}$
SW And										
0.00	0	0.211	0.151	7373	0.131	0.097	7443	0.272	0.198	7544
0.05	2.72	0.237	0.177	7250	0.161	0.127	7203	0.325	0.251	7304
0.10	7.28	0.273	0.213	7125	0.187	0.153	7022	0.377	0.303	7098
0.20	16.83	0.346	0.286	6875	0.226	0.192	6758	0.458	0.384	6799
0.30	26.46	0.453	0.393	6504	0.276	0.242	6426	0.559	0.485	6451
0.40	34.47	0.491	0.431	6378	0.307	0.273	6233	0.614	0.540	6265
0.50	44.89	0.514	0.454	6303	0.318	0.284	6164	0.640	0.566	6179
0.60	48.73	0.526	0.466	6263	0.313	0.279	6195	0.630	0.556	6212
0.75	56.48	0.533	0.473	6241	0.322	0.288	6139	0.643	0.569	6169
0.80	61.36	0.541	0.481	6218	0.319	0.285	6158	0.637	0.563	6189
0.85	62.48	0.495	0.435	6365	0.299	0.265	6283	0.600	0.526	6312
AR Per										
0.00	0	0.460	0.140	7380	0.285	0.103	7378	0.597	0.200	7535
0.05	3.56	0.494	0.174	7225	0.311	0.129	7174	0.649	0.252	7301
0.10	7.57	0.528	0.208	7104	0.335	0.153	7003	0.692	0.295	7130
0.20	16.05	0.628	0.308	6746	0.395	0.213	6597	0.820	0.423	6663
0.30	28.04	0.701	0.381	6479	0.431	0.249	6362	0.893	0.496	6410
0.40	35.28	0.743	0.423	6333	0.456	0.274	6203	0.930	0.533	6284
0.50	44.80	0.759	0.439	6278	0.467	0.285	6134	0.956	0.559	6197
0.60	52.40	0.762	0.442	6267	0.469	0.287	6121	0.928	0.531	6290
0.75	58.62	0.762	0.442	6267	0.486	0.304	6015	0.952	0.555	6210
0.80	64.06	0.770	0.450	6241	0.478	0.296	6065	0.936	0.539	6263
0.85	65.73	0.766	0.446	6254	0.467	0.285	6134	0.937	0.540	6260
RR Leo										
0.00	0	0.086	0.036	7917	0.057	0.029	8205	0.140	0.078	8417
0.05	5.19	0.097	0.047	7825	0.074	0.046	7927	0.176	0.114	8067
0.10	9.56	0.157	0.107	7421	0.113	0.085	7487	0.241	0.179	7661
0.20	16.79	0.270	0.220	6931	0.197	0.169	6844	0.409	0.347	6946
0.30	29.62	0.341	0.291	6623	0.254	0.226	6451	0.501	0.439	6616
0.40	40.80	0.410	0.360	6332	0.282	0.254	6266	0.587	0.525	6319
0.50	47.49	0.439	0.389	6216	0.298	0.270	6161	0.616	0.554	6219
0.60	54.16	0.435	0.385	6231	0.311	0.283	6076	0.628	0.566	6178
0.70	60.85	0.447	0.397	6186	0.288	0.260	6227	0.603	0.541	6264
0.80	59.28	0.397	0.347	6385	0.285	0.257	6247	0.584	0.522	6329
0.85	59.54	0.424	0.374	6275	0.293	0.265	6194	0.595	0.533	6291
RR Cet										
0.00	0	0.171	0.141	7238	0.127	0.110	7268	0.276	0.239	7378
0.05	2.58	0.198	0.168	7133	0.148	0.131	7111	0.322	0.285	7184
0.15	13.17	0.284	0.254	6772	0.206	0.189	6702	0.444	0.407	6730

Table 4.3 (cont'd)

Phase	RV−RV$_{\rm min}$	$B-V$	$c(B-V)$	$T_{\rm eff}$	$V-R_c$	$c(V-R_c)$	$T_{\rm eff}$	$V-I_c$	$c(V-I_c)$	$T_{\rm eff}$
0.20	17.13	0.320	0.290	6614	0.228	0.211	6549	0.492	0.455	6561
0.30	28.62	0.395	0.365	6296	0.268	0.251	6284	0.559	0.522	6329
0.40	41.56	0.427	0.397	6169	0.282	0.265	6191	0.603	0.566	6180
0.50	45.29	0.447	0.417	6092	0.314	0.297	5981	0.633	0.596	6078
0.60	51.86	0.437	0.407	6131	0.316	0.299	5969	0.625	0.588	6105
0.70	55.11	0.425	0.395	6177	0.302	0.285	6060	0.614	0.577	6143
0.80	57.02	0.440	0.410	6119	0.297	0.280	6093	0.611	0.574	6153
0.85	60.94	0.441	0.411	6115	0.293	0.276	6119	0.602	0.565	6183
TU Uma										
0.00	0	0.158	0.138	7250	0.116	0.105	7314	0.265	0.240	7372
0.05	1.07	0.184	0.164	7148	0.142	0.131	7113	0.318	0.293	7152
0.10	1.67	0.237	0.217	6934	0.173	0.162	6892	0.369	0.344	6956
0.20	17.26	0.319	0.299	6575	0.224	0.213	6537	0.476	0.451	6573
0.30	29.74	0.377	0.357	6329	0.276	0.265	6193	0.565	0.540	6266
0.40	37.79	0.418	0.398	6165	0.295	0.284	6068	0.602	0.577	6141
0.50	43.69	0.440	0.420	6081	0.306	0.295	5996	0.618	0.593	6087
0.65	51.18	0.465	0.445	5986	0.288	0.277	6115	0.611	0.586	6111
0.70	52.19	0.446	0.426	6058	0.277	0.266	6187	0.577	0.552	6226
0.80	57.35	0.418	0.398	6165	0.300	0.289	6036	0.605	0.580	6131
0.85	59.37	0.437	0.417	6092	0.284	0.273	6141	0.605	0.580	6131
TT Lyn										
0.00	0	0.222	0.212	6943	0.173	0.167	6848	0.368	0.356	6914
0.05	3.11	0.257	0.247	6789	0.190	0.184	6728	0.416	0.404	6741
0.10	6.60	0.285	0.275	6665	0.210	0.204	6593	0.435	0.423	6674
0.20	14.37	0.363	0.353	6326	0.250	0.244	6322	0.517	0.505	6388
0.30	20.75	0.407	0.397	6148	0.270	0.264	6189	0.568	0.556	6214
0.40	33.74	0.426	0.416	6074	0.304	0.298	5966	0.614	0.602	6059
0.50	38.12	0.449	0.439	5986	0.311	0.305	5921	0.625	0.613	6022
0.60	47.08	0.450	0.440	5983	0.308	0.302	5940	0.626	0.614	6018
0.70	47.15	0.430	0.420	6051	0.295	0.289	6024	0.611	0.599	6069
0.80	50.20	0.448	0.438	5990	0.297	0.291	6011	0.619	0.607	6042
0.85	49.79	0.429	0.419	6063	0.304	0.298	5966	0.617	0.605	6049
RX Eri										
0.00	0	0.224	0.174	7097	0.158	0.130	7099	0.351	0.289	7172
0.05	3.36	0.250	0.200	6991	0.175	0.147	6975	0.384	0.322	7043
0.10	7.63	0.288	0.238	6825	0.200	0.172	6796	0.438	0.376	6844
0.20	17.49	0.353	0.303	6531	0.271	0.243	6314	0.522	0.460	6546
0.30	27.17	0.445	0.395	6147	0.291	0.263	6181	0.603	0.541	6267
0.40	34.87	0.468	0.418	6056	0.306	0.278	6082	0.650	0.588	6106
0.50	42.02	0.488	0.438	5979	0.323	0.295	5970	0.661	0.599	6069
0.60	47.76	0.501	0.451	5934	0.330	0.302	5924	0.690	0.628	5970
0.70	49.59	0.474	0.424	6032	0.324	0.296	5964	0.665	0.603	6055

Table 4.3 (cont'd)

Phase	RV$-$RV$_{\rm min}$	$B-V$	$c(B-V)$	$T_{\rm eff}$	$V-R_c$	$c(V-R_c)$	$T_{\rm eff}$	$V-I_c$	$c(V-I_c)$	$T_{\rm eff}$
0.80	56.47	0.495	0.445	5955	0.331	0.303	5918	0.672	0.610	6031
0.85	58.69	0.473	0.423	6036	0.328	0.300	5938	0.663	0.601	6062
SU Dra										
0.00	0	0.143	0.133	7250	0.113	0.107	7282	0.261	0.249	7338
0.05	1.40	0.174	0.164	7125	0.135	0.129	7115	0.306	0.294	7154
0.10	5.49	0.218	0.208	6941	0.174	0.168	6834	0.370	0.358	6911
0.20	16.05	0.287	0.277	6627	0.217	0.211	6539	0.464	0.452	6575
0.30	21.49	0.370	0.360	6259	0.260	0.254	6248	0.550	0.538	6279
0.40	32.49	0.417	0.407	6069	0.287	0.281	6066	0.607	0.595	6084
0.50	40.56	0.430	0.420	6016	0.304	0.298	5953	0.622	0.610	6032
0.60	44.52	0.437	0.427	5989	0.301	0.295	5972	0.622	0.610	6032
0.70	45.85	0.414	0.404	6081	0.291	0.285	6039	0.604	0.592	6094
0.80	53.85	0.411	0.401	6093	0.290	0.284	6045	0.600	0.588	6108
0.85	55.06	0.418	0.408	6065	0.282	0.276	6099	0.597	0.585	6118

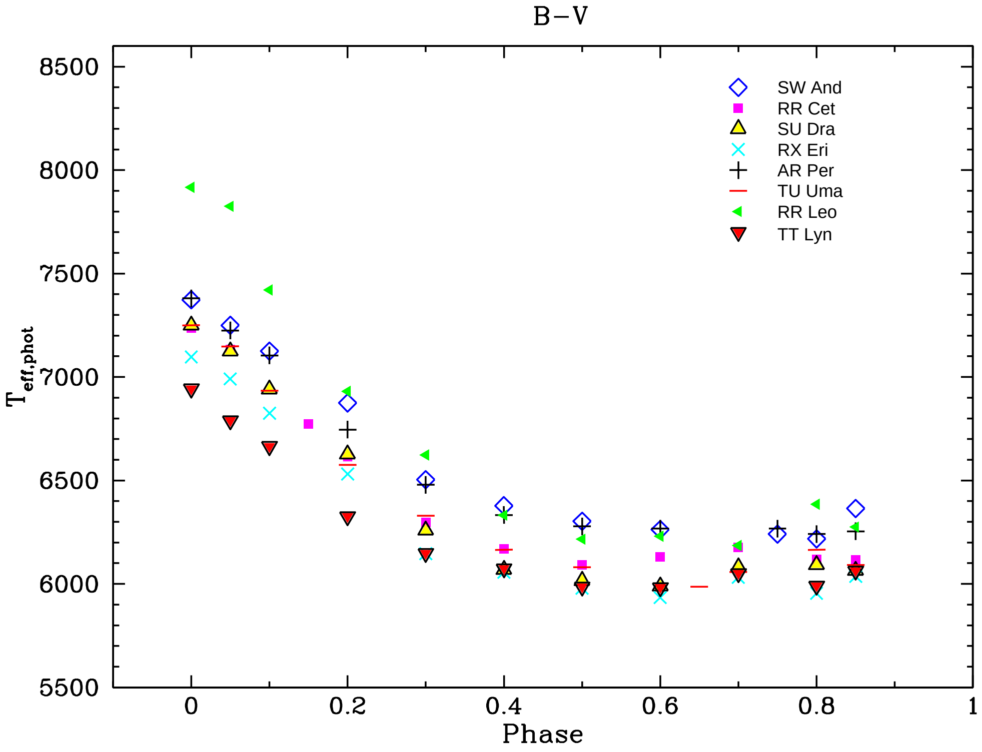

Figure 4.12 The effective temperatures transformed from $B-V$ color indices as a function of phase. The different symbols represent the 8 RRab variables (SW And, RR Cet, SU Dra, RX Eri, AR Per, TU Uma, RR Leo and TT Lyn) selected from LJ89 and LJ90. They are used as our "calibration stars".

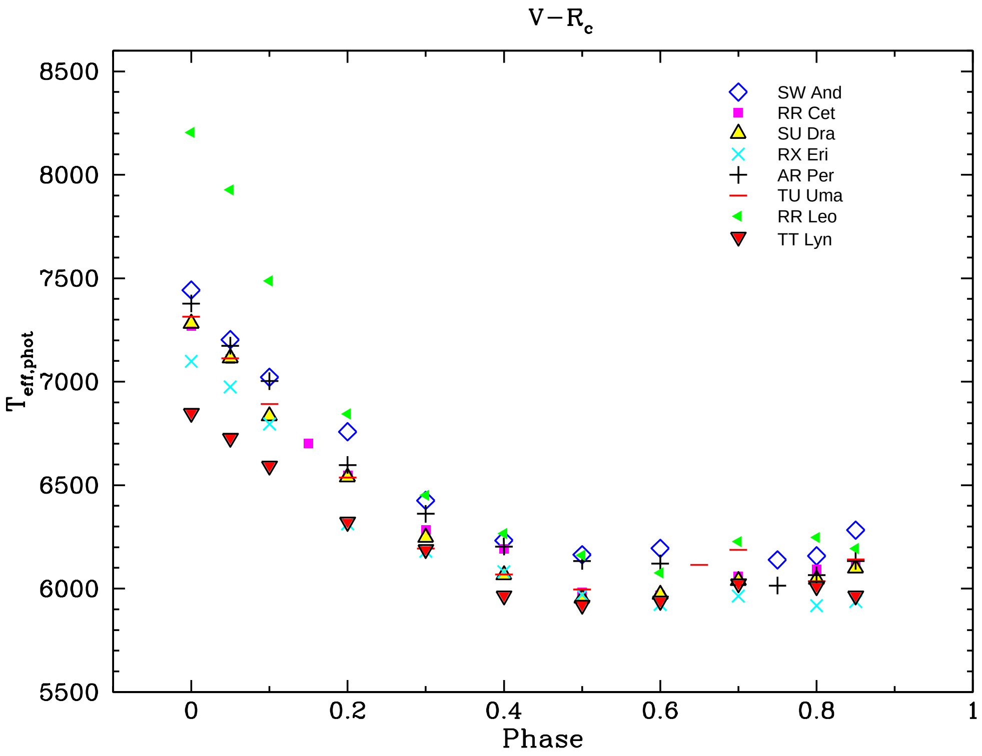

Figure 4.13 The effective temperatures transformed from $V-R_c$ color indices as a function of phase. The different symbols represent the same RR-ab variables as shown in Figure 4.12.

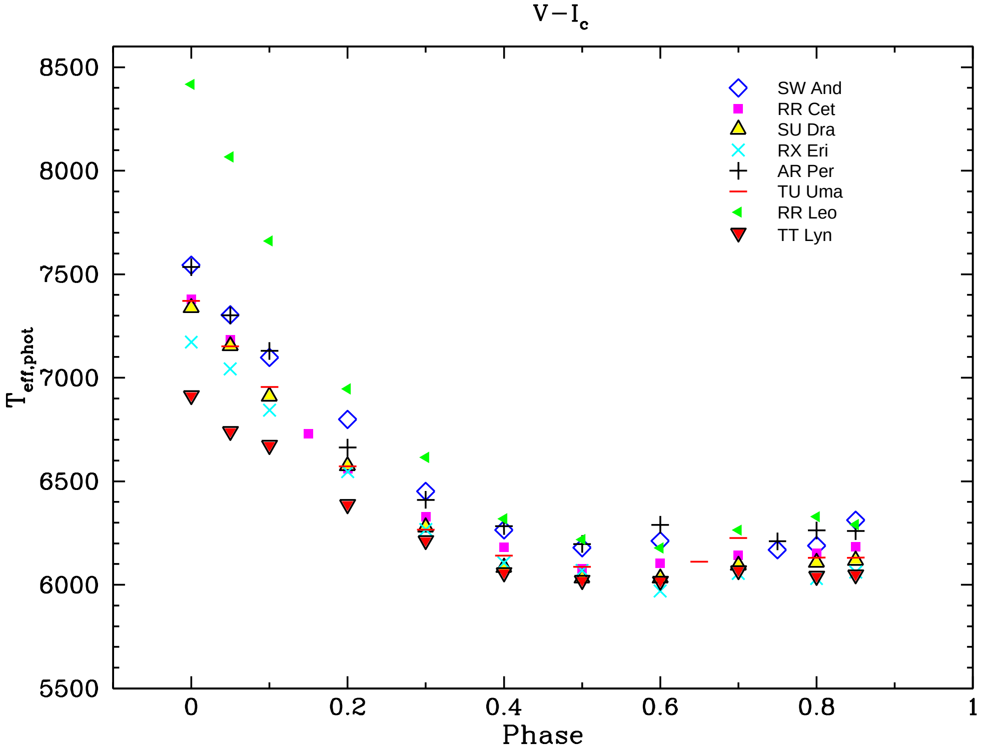

Figure 4.14 The effective temperatures transformed from $V-R_c$ color indices as a function of phase. The different symbols represent the same RR-ab variables as shown in Figure 4.12. Individual $V-I_c$ vs phase relations are used to fit 4th-order polynomial curves, which are treated as our "calibration curves".

Table 4.4. Coefficients for the fit of $T_{\mathrm{eff}} = a_4\phi^4 + a_3\phi^3 + a_2\phi^2 + a_1\phi + a_0$, where ϕ is phase.

Eq	Star	a_4	a_3	a_2	a_1	a_0
1	SW And	-1049.6	600.08	4153.8	-4808.7	7542.7
2	AR Per	-5174.6	4654.8	4167.1	-5275.8	7554.7
3	RR Leo	-6583.7	5248.0	7718.5	-8830.7	8444.6
4	RR Cet	-3483.1	2780.7	4418.3	-5061.1	7394.3
5	TU Uma	-10916	14340	-960.06	-4324.7	7373.8
6	TT Lyn	-7213.9	10633	-2121.4	-2464.3	6902.5
7	RX Eri	-6602.1	9883.2	-1303.9	-3315.4	7186.2
8	SU Dra	-8545.3	12001	-860.84	-4142.2	7343.4

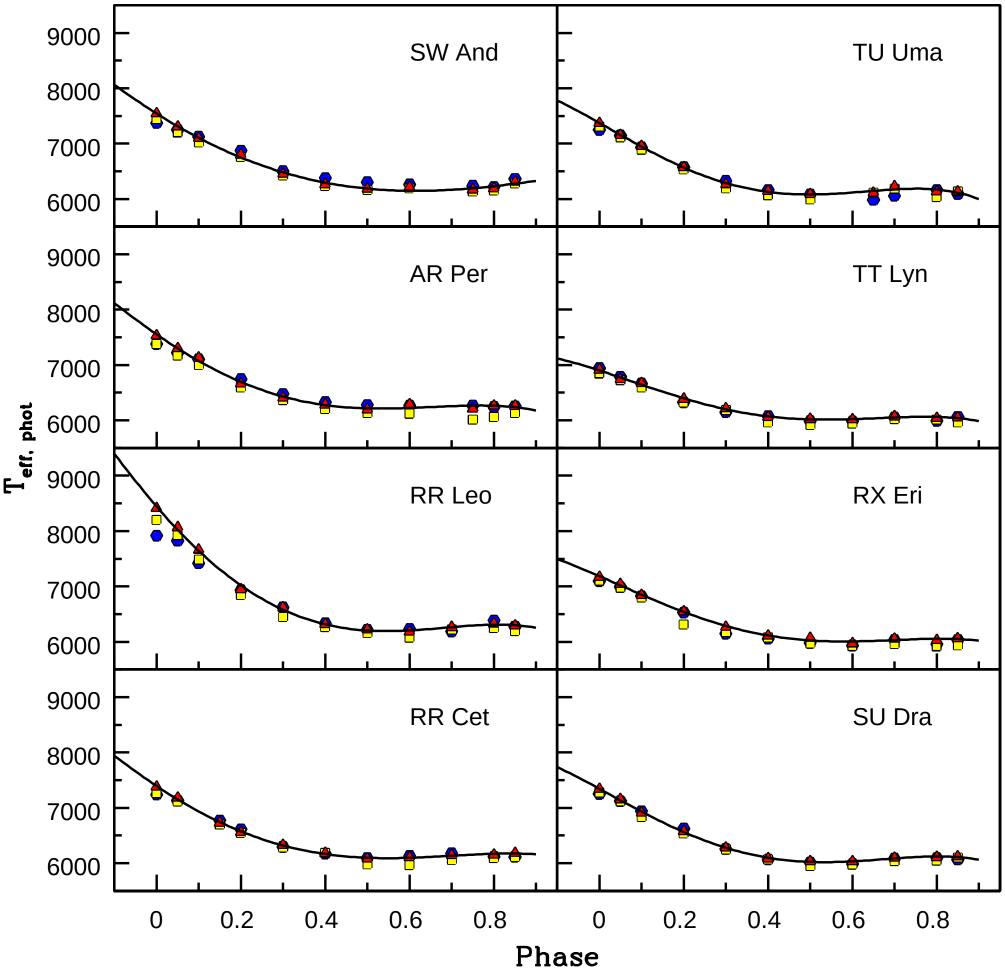

Figure 4.15 The transformed $T_{\rm eff}$ from different color indices as a function of phase for the selected 8 RR-ab variables from LJ89 and LJ90. The solid lines are fitted 4$^{\rm th}$-order polynomials to the $V - I_{\rm c}$ curves. Symbols refer to $T_{\rm eff}$ values derived from the color indices: $B - V$ (blue hexagons); $V - R_{\rm c}$ (yellow squares) and $V - I_{\rm c}$ (red triangles).

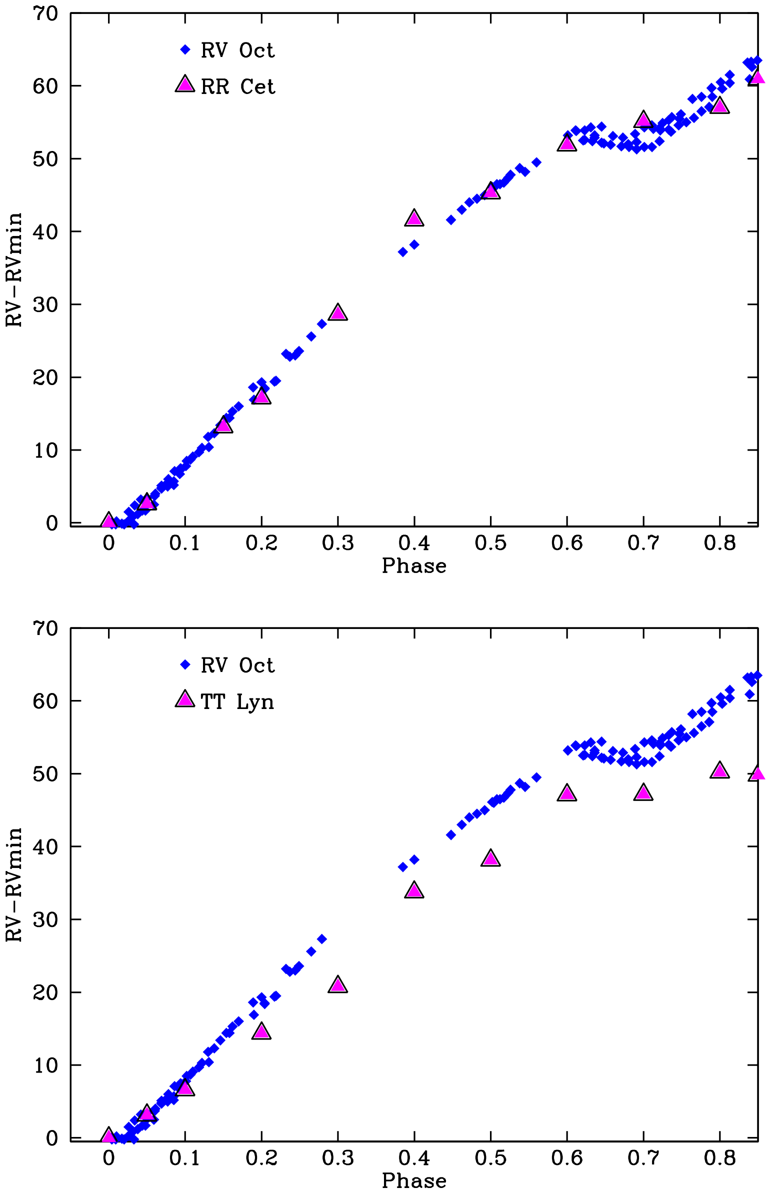

Figure 4.16 Demonstration of selecting the best calibration curves by comparing the RV−RVmin curve of our RV Oct to RV−RVmin curves of RR Cet (top panel) and TT Lyn (bottom panel). The top panel shows the best match pulsational behavior. Symbols refer to RV Oct (blue diamonds) and RR Cet & TT Lyn (magenta triangles).

4.5.2 Surface Gravity

Due to pulsation, the gravity of RR Lyr varies throughout the pulsational cycle. Therefore, the observed gravity at a given phase is referred as the effective gravity and can be described by:

$$g_{\text{eff}} = \frac{GM}{R^2} + \frac{d^2R}{dt^2}, \tag{4.3}$$

where M and R are the mass and the radius of the star in $M_\odot$. The first term represents the mean gravity of the star, which can be derived from its mass and mean radius. The second term represents the variation of gravity, which takes into account the acceleration of the moving atmosphere. It can be determined by differentiating the radial velocity curve.

The mass and mean radius can be derived via BW method, for which photometric information is required. Since we do not have lightcurves for our RR Lyr, a mean log g = 2.0 that is consistent with the chosen model atmosphere grid was adopted as initial guess for performing the spectroscopic analysis.

4.5.3 Metallicity and Microturbulence

We adopted the [Fe/H] as listed in Table 1 of Preston (2009) as our initial metallicity estimate. There is no previous derived metallicity for DT Hya and CD Vel in the literature. For these stars we employed [M/H] $= -1.5$, which is similar to the mean [M/H] of our other program stars.

A constant microtubulence is generally assumed throughout the layers of stellar atmospheres. Apart from simplicity, there is no evidence to support this assumption for real stars. In fact, some studies suggested that non-constant microturbulence is more appropriate to physically describe a stellar atmosphere (e.g., Hardorp & Scholz 1967; Kolenberg et al. 2010). In addition, the presence of shock waves during the RR Lyr pulsational cycle makes v_{t} unlikely to be constant in their atmospheres (see theorectical work by Fokin et al. 1999a). We cannot provide insight into this question with our data, and so we adopted $v_{\mathrm{t}} = 3$ km s^{-1} as an initial guess for the spectroscopic analysis. The variation of microturbulence as a function of phase/T_{eff} is discussed in the following sections.

4.6 Derived Model Atmosphere Parameters

We present the derived stellar parameters vs pulsational phase of each of our program stars in Figures 4.17–4.27. The dashed lines represent the mean values. The top and second panels show the typical T_{eff} and log g changes in the atmosphere of RR Lyr during the pulsational cycle. The third panel shows the consistency of our derived [M/H]. The bottom panel shows the variation of v_{t} as a function of phase. The derived model atmosphere parameters are given in Table 4.5, which we used them to derive the chemical abundances of each star.

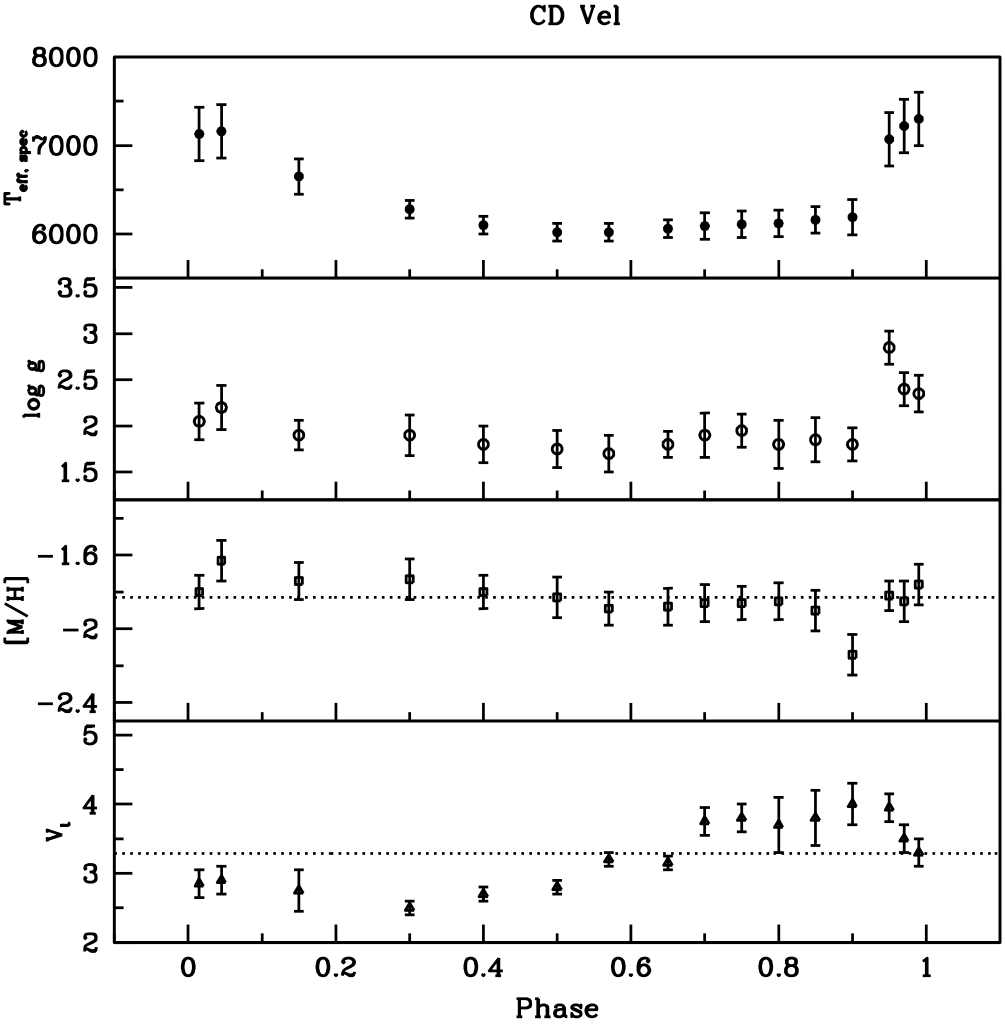

Figure 4.17 Derived stellar parameters (T_{eff}, log g, [M/H] and v_{t}) based on spectroscopic constraints as a function of phase. The dashed lines represent the mean values. Different color symbols represent different cycles being considered for combining the spectra.

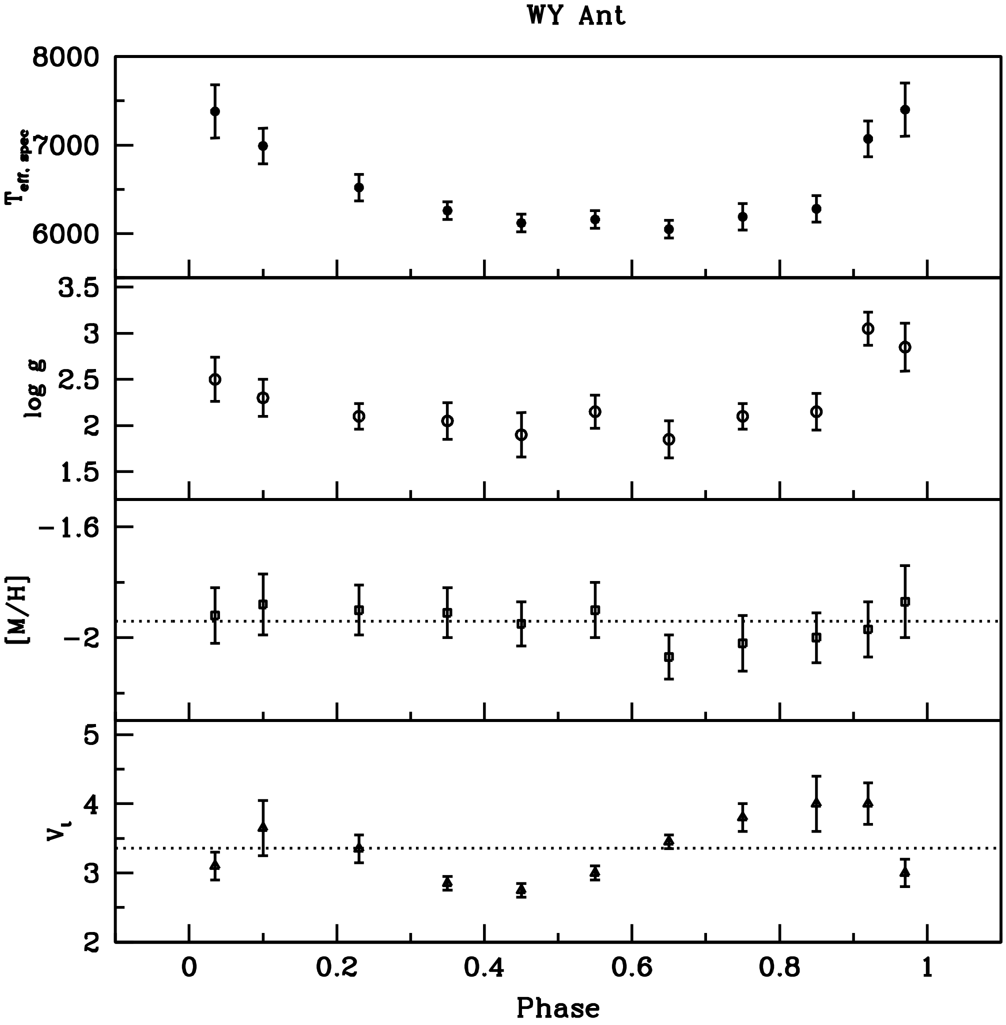

Figure 4.18 Same as Figure 4.17.

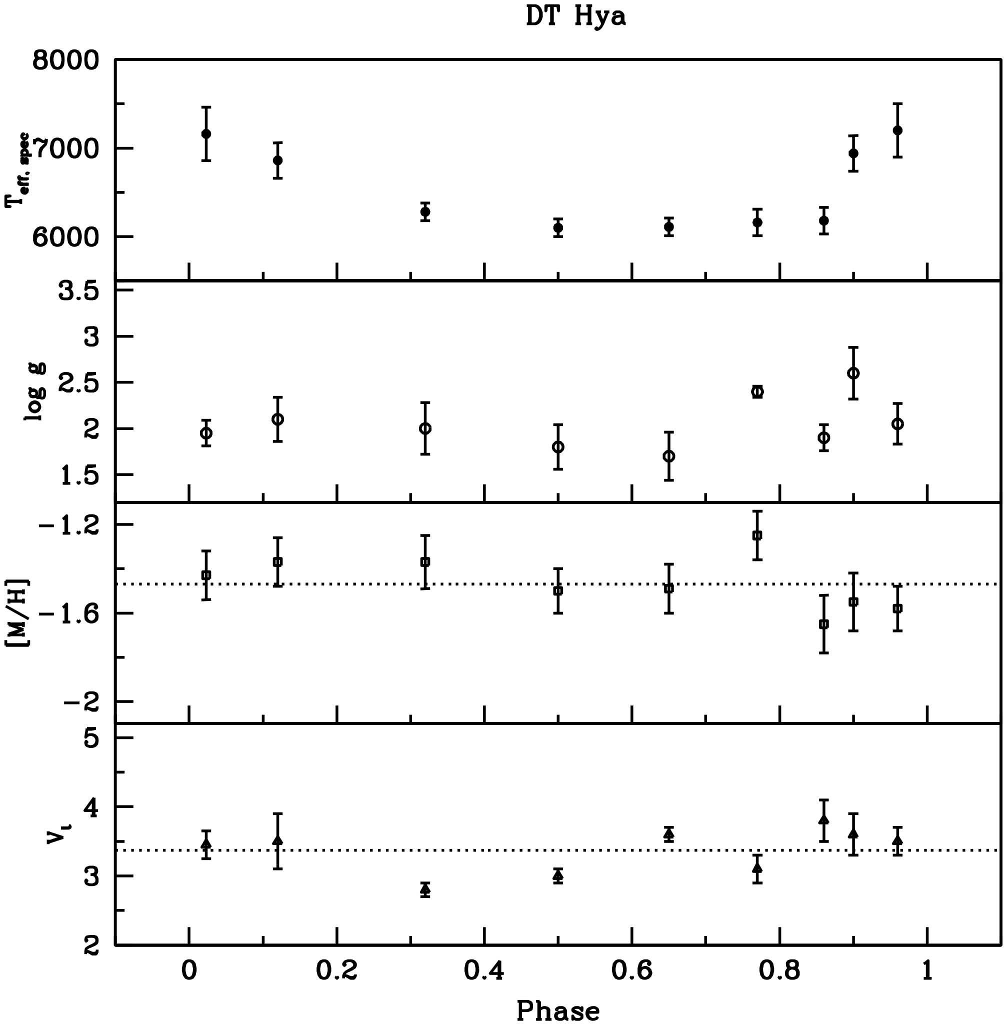

Figure 4.19 Same as Figure 4.17.

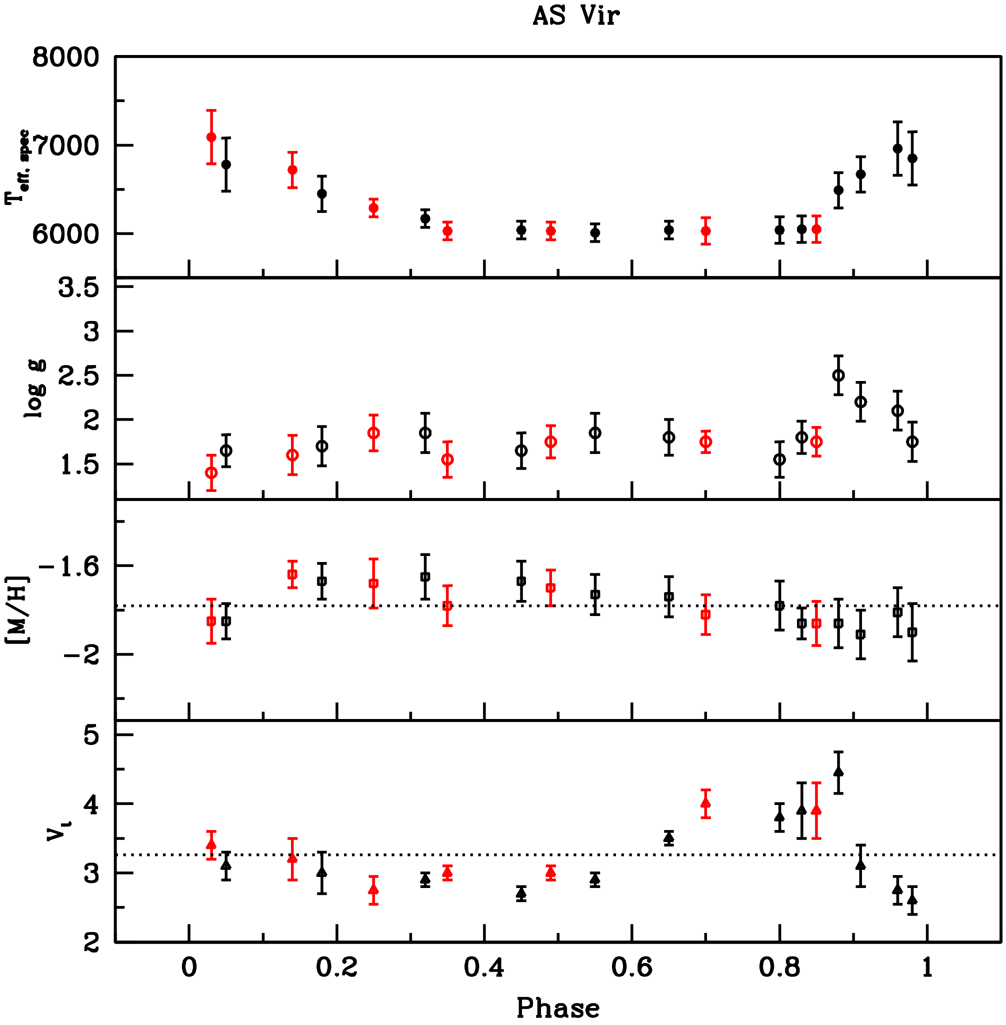

Figure 4.20 Same as Figure 4.17.

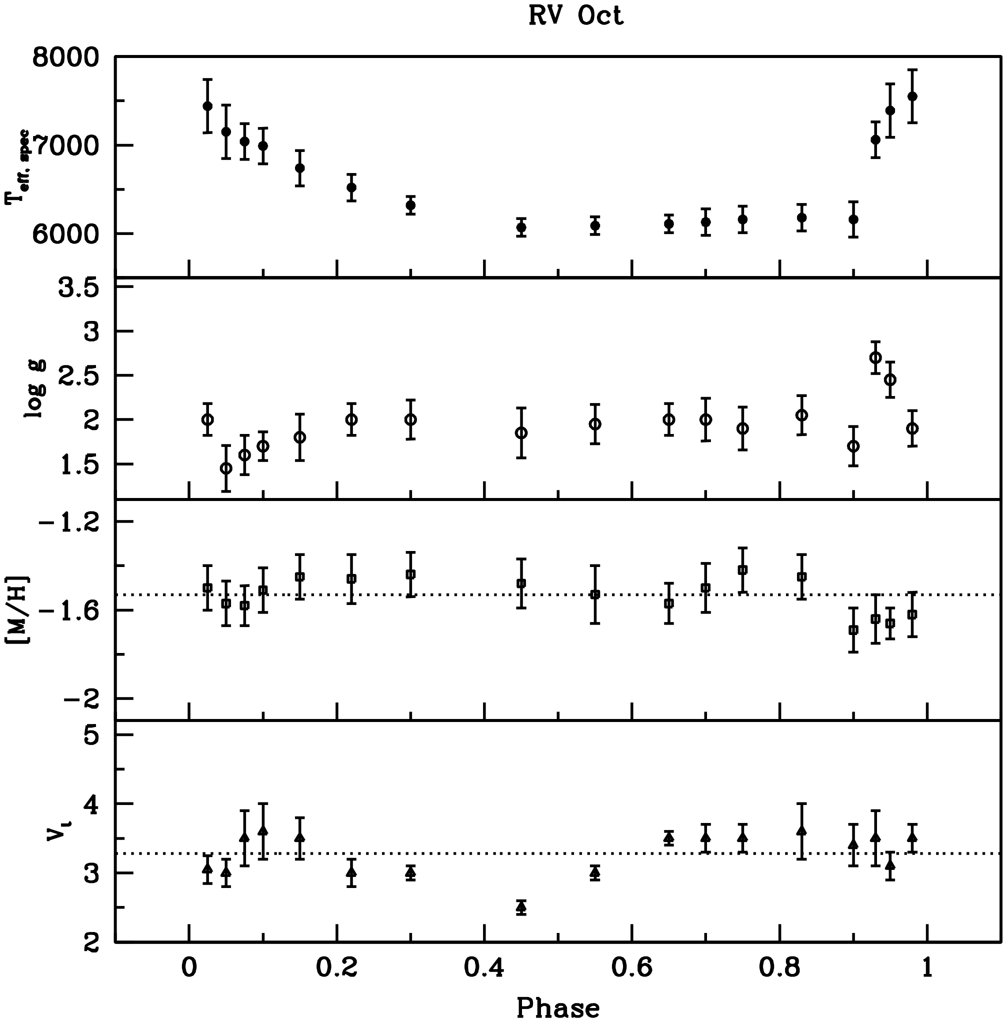

Figure 4.21 Same as Figure 4.17.

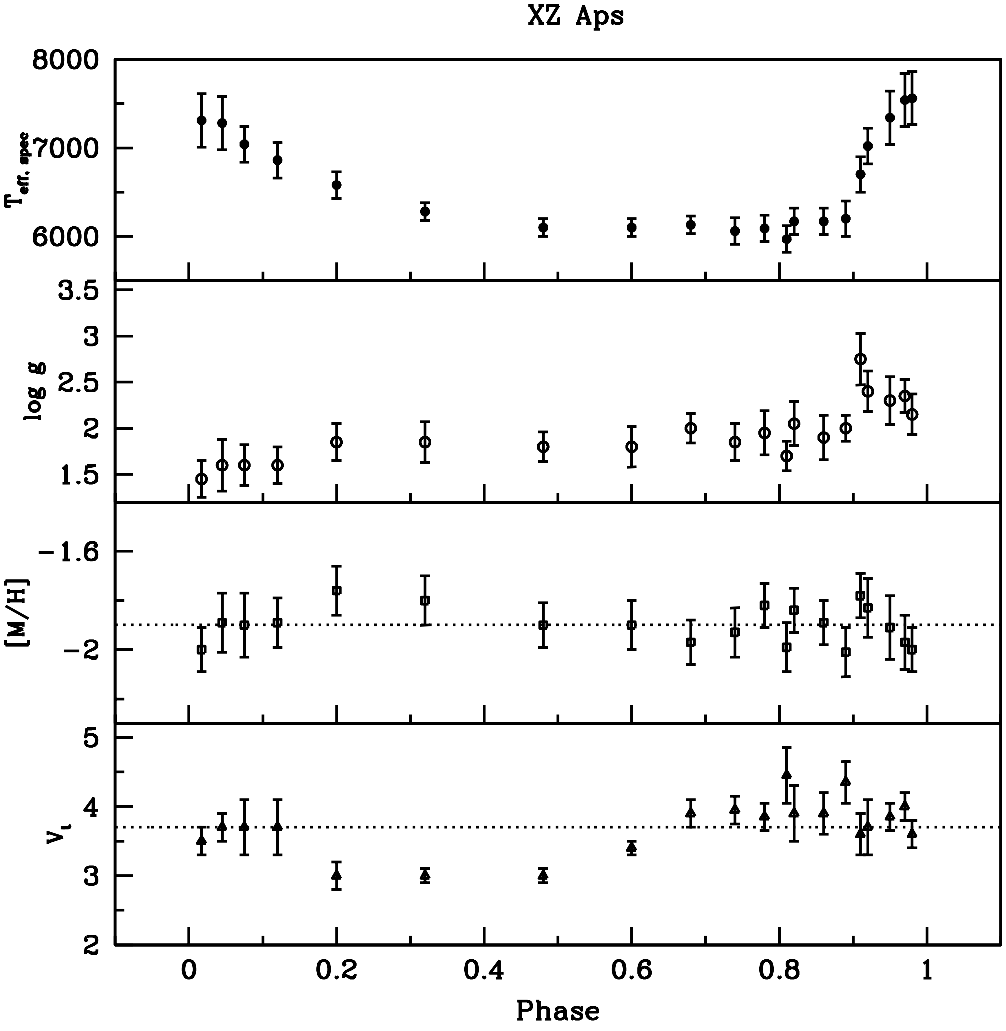

Figure 4.22 Same as Figure 4.17.

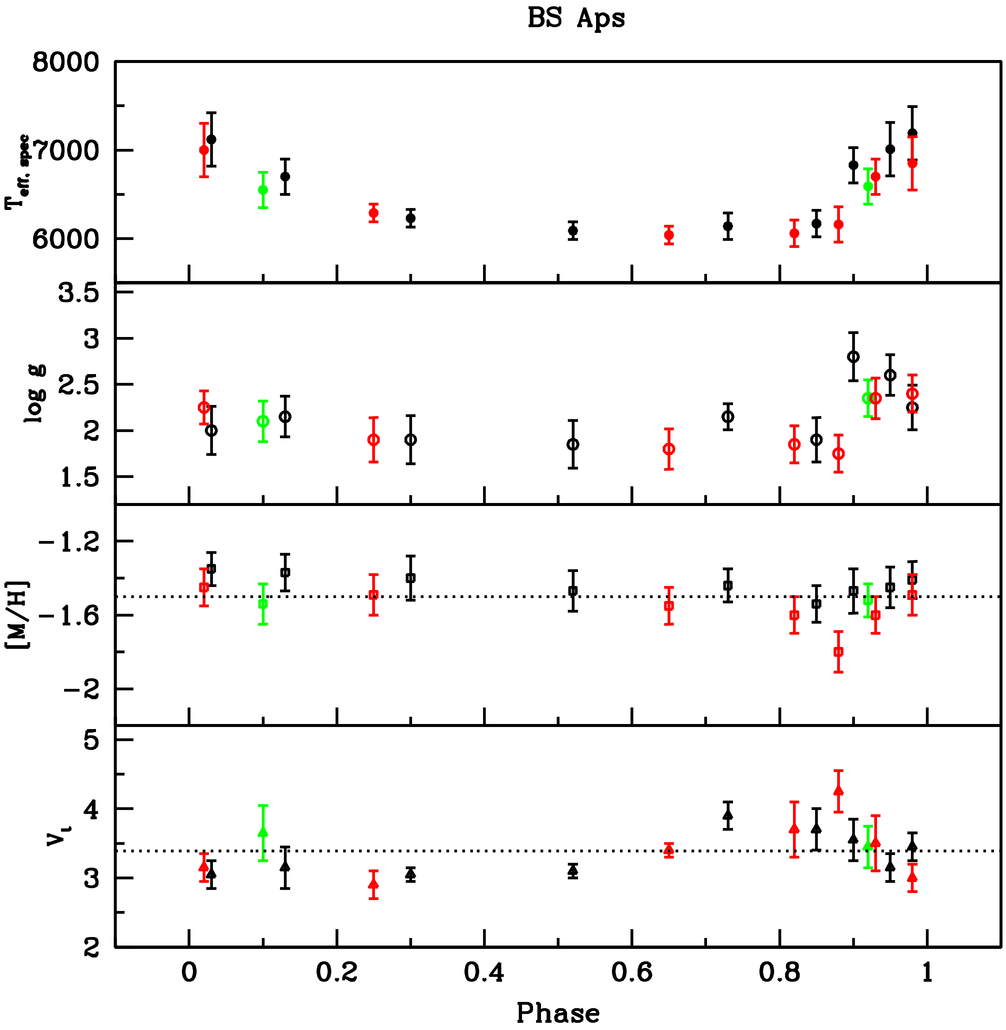

Figure 4.23 Same as Figure 4.17.

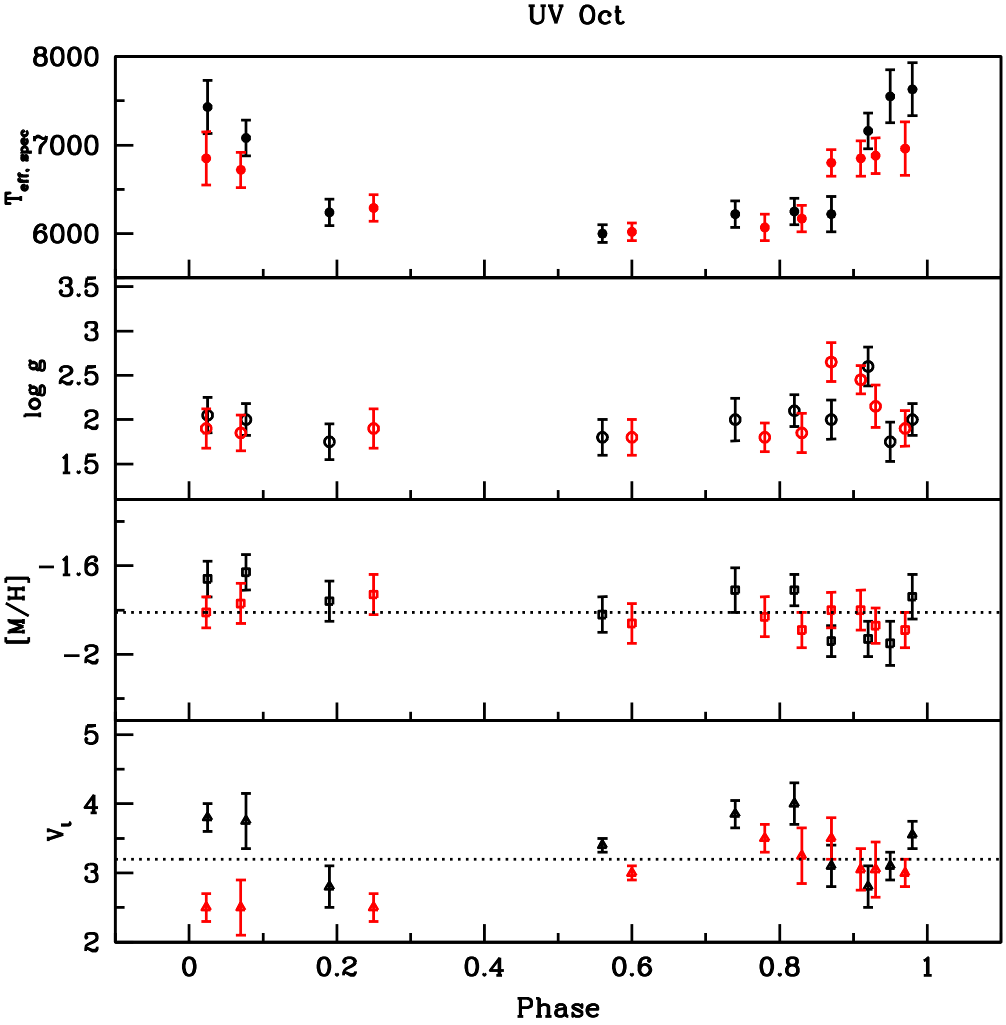

Figure 4.24 Same as Figure 4.17.

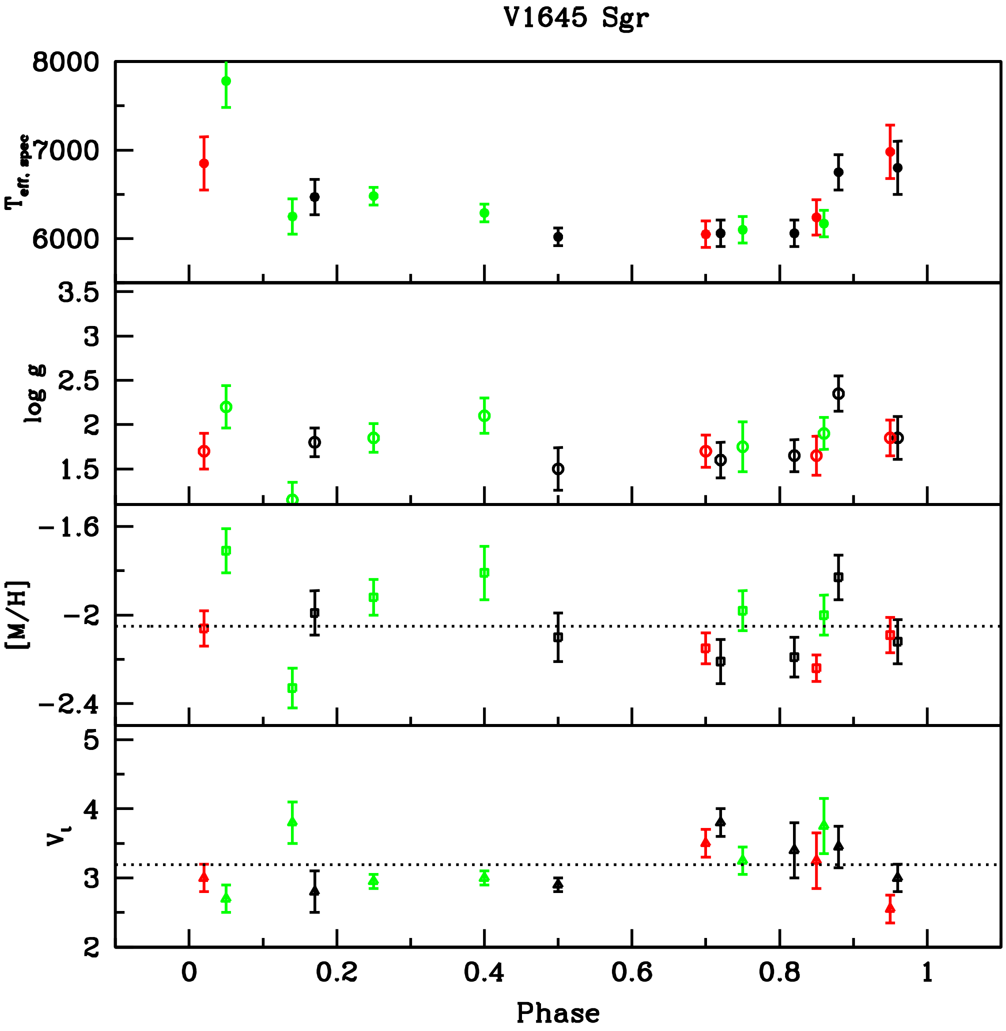

Figure 4.25 Same as Figure 4.17.

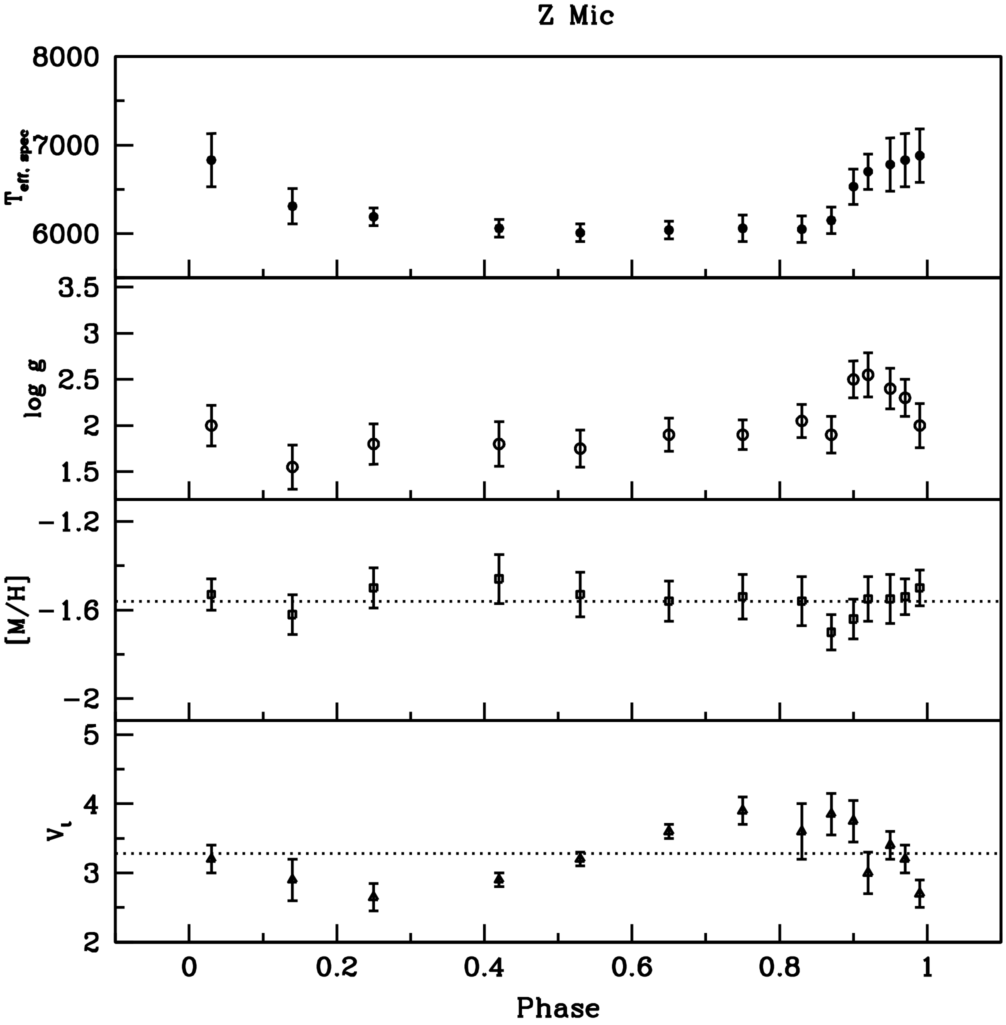

Figure 4.26 Same as Figure 4.17.

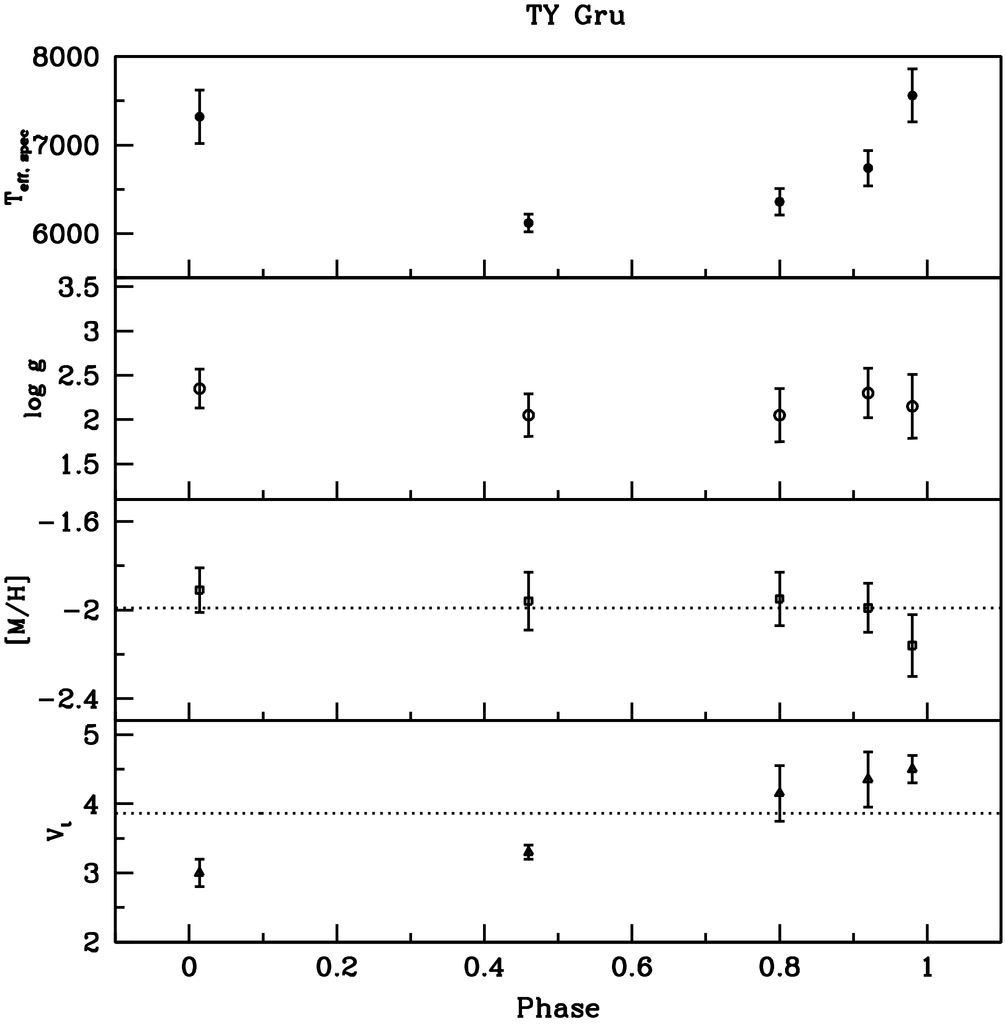

Figure 4.27 Same as Figure 4.17.

Table 4.5. Input stellar atmosphere parameters and derived Fe metallicities throughout the pulsational cycle.

Mid Phase	T_{eff} (K)	err	log g (dex)	err	[M/H] (dex)	v_{t} (km s^{-1})	err (dex)	[Fe I/H]	err	N	[Fe II/H] (dex)	err	N
CD Vel													
0.015	7130	300	2.05	0.20	−1.80	2.85	0.20	−1.80	0.09	30	−1.81	0.10	25
0.045	7160	300	2.20	0.24	−1.63	2.90	0.20	−1.63	0.11	26	−1.62	0.12	16
0.150	6650	200	1.90	0.16	−1.74	2.75	0.30	−1.74	0.10	68	−1.73	0.08	23
0.300	6280	100	1.90	0.22	−1.73	2.50	0.10	−1.73	0.11	82	−1.73	0.11	29
0.400	6100	100	1.80	0.20	−1.80	2.70	0.10	−1.80	0.09	80	−1.80	0.10	23
0.500	6020	100	1.75	0.20	−1.83	2.80	0.10	−1.83	0.11	76	−1.83	0.10	29
0.570	6020	100	1.70	0.20	−1.89	3.20	0.10	−1.89	0.09	63	−1.89	0.10	20
0.650	6060	100	1.80	0.14	−1.88	3.15	0.10	−1.88	0.10	55	−1.89	0.07	25
0.700	6090	150	1.90	0.24	−1.86	3.75	0.20	−1.86	0.10	53	−1.87	0.12	16
0.750	6110	150	1.95	0.18	−1.86	3.80	0.20	−1.86	0.09	50	−1.86	0.09	19
0.800	6120	150	1.80	0.26	−1.85	3.70	0.40	−1.85	0.10	49	−1.86	0.13	23
0.850	6160	150	1.85	0.24	−1.90	3.80	0.40	−1.90	0.11	58	−1.89	0.12	19
0.900	6190	200	1.80	0.18	−2.14	4.00	0.30	−2.14	0.11	42	−2.12	0.09	15
0.950	7070	300	2.85	0.18	−1.82	3.95	0.20	−1.82	0.08	35	−1.82	0.09	21
0.970	7220	300	2.40	0.18	−1.85	3.50	0.20	−1.85	0.11	23	−1.86	0.09	19
0.990	7300	300	2.35	0.20	−1.76	3.30	0.20	−1.76	0.11	30	−1.77	0.10	18
WY Ant													
0.035	7380	300	2.50	0.24	−1.92	3.10	0.20	−1.92	0.10	29	−1.92	0.12	20
0.100	6990	200	2.30	0.20	−1.88	3.65	0.40	−1.89	0.11	49	−1.90	0.10	28
0.230	6520	150	2.10	0.14	−1.90	3.35	0.20	−1.91	0.09	84	−1.92	0.07	33
0.350	6260	100	2.05	0.20	−1.91	2.85	0.10	−1.92	0.09	101	−1.93	0.10	36
0.450	6120	100	1.90	0.24	−1.95	2.75	0.10	−1.95	0.08	97	−1.96	0.12	36
0.550	6160	100	2.15	0.18	−1.90	3.00	0.10	−1.91	0.10	98	−1.91	0.09	33
0.650	6050	100	1.85	0.20	−2.07	3.45	0.10	−2.07	0.08	78	−2.06	0.10	26
0.750	6190	150	2.10	0.14	−2.02	3.80	0.20	−2.02	0.10	62	−2.03	0.07	23
0.850	6280	150	2.15	0.20	−2.00	4.00	0.40	−2.00	0.09	50	−2.01	0.10	26
0.920	7070	200	3.05	0.18	−1.97	4.00	0.30	−1.98	0.10	32	−1.99	0.09	17
0.970	7400	300	2.85	0.26	−1.87	3.00	0.20	−1.87	0.13	27	−1.88	0.13	17
DT Hya													
0.023	7160	300	1.95	0.14	−1.43	3.45	0.20	−1.43	0.11	26	−1.44	0.07	18
0.120	6860	200	2.10	0.24	−1.37	3.50	0.40	−1.38	0.11	50	−1.39	0.12	22
0.320	6280	100	2.00	0.28	−1.37	2.80	0.10	−1.38	0.12	87	−1.38	0.14	27
0.500	6100	100	1.80	0.24	−1.50	3.00	0.10	−1.50	0.10	65	−1.50	0.12	25
0.650	6110	100	1.70	0.26	−1.49	3.60	0.10	−1.49	0.11	44	−1.50	0.13	11
0.770	6160	150	2.40	0.06	−1.25	3.10	0.20	−1.25	0.11	27	−1.27	0.03	5
0.860	6180	150	1.90	0.14	−1.65	3.80	0.30	−1.65	0.13	26	−1.64	0.07	8
0.900	6940	200	2.60	0.28	−1.55	3.60	0.30	−1.55	0.13	37	−1.55	0.14	13
0.960	7200	300	2.05	0.22	−1.58	3.50	0.20	−1.58	0.10	41	−1.59	0.11	23
AS Vir 1													
0.050	6780	300	1.65	0.18	−1.85	3.10	0.20	−1.84	0.08	25	−1.84	0.09	14
0.180	6450	200	1.70	0.22	−1.67	3.00	0.30	−1.67	0.08	46	−1.67	0.11	20
0.320	6170	100	1.85	0.22	−1.65	2.90	0.10	−1.65	0.10	78	−1.65	0.11	30
0.450	6040	100	1.65	0.20	−1.67	2.70	0.10	−1.66	0.09	64	−1.67	0.10	23
0.550	6010	100	1.85	0.22	−1.73	2.90	0.10	−1.73	0.09	55	−1.72	0.11	17
0.650	6040	100	1.80	0.20	−1.74	3.50	0.10	−1.74	0.09	44	−1.74	0.10	11
0.800	6040	150	1.55	0.20	−1.78	3.80	0.20	−1.78	0.11	38	−1.79	0.10	8
0.830	6050	150	1.80	0.18	−1.86	3.90	0.40	−1.86	0.07	30	−1.86	0.09	5
0.880	6490	200	2.50	0.22	−1.86	4.45	0.30	−1.86	0.11	16	−1.87	0.11	2
0.910	6670	200	2.20	0.22	−1.91	3.10	0.30	−1.91	0.11	17	−1.92	0.11	6
0.960	6960	300	2.10	0.22	−1.81	2.75	0.20	−1.82	0.11	16	−1.81	0.11	11
0.980	6850	300	1.75	0.22	−1.90	2.60	0.20	−1.90	0.13	25	−1.89	0.11	12
AS Vir 2													
0.030	7090	300	1.40	0.20	−1.85	3.40	0.20	−1.85	0.10	11	−1.86	0.10	15
0.140	6720	200	1.60	0.22	−1.64	3.20	0.30	−1.65	0.06	31	−1.65	0.11	11

Table 4.5 (cont'd)

Mid Phase	$T_{\rm eff}$ (K)	err	log g (dex)	err	[M/H] (dex)	$v_{\rm t}$ (km s^{-1})	err (dex)	[Fe I/H]	err	N	[Fe II/H] (dex)	err	N
0.250	6290	100	1.85	0.20	−1.68	2.75	0.20	−1.68	0.11	38	−1.68	0.10	13
0.350	6030	100	1.55	0.20	−1.78	3.00	0.10	−1.78	0.09	70	−1.78	0.10	21
0.490	6030	100	1.75	0.18	−1.70	3.00	0.10	−1.70	0.08	65	−1.70	0.09	20
0.700	6030	150	1.75	0.12	−1.82	4.00	0.20	−1.82	0.09	50	−1.82	0.06	16
0.850	6050	150	1.75	0.16	−1.86	3.90	0.40	−1.86	0.10	40	−1.87	0.08	16
RV Oct													
0.025	7440	300	2.00	0.18	−1.50	3.05	0.20	−1.50	0.10	44	−1.51	0.09	30
0.050	7150	300	1.45	0.26	−1.57	3.00	0.20	−1.57	0.10	46	−1.58	0.13	25
0.075	7040	200	1.60	0.22	−1.58	3.50	0.40	−1.58	0.09	33	−1.59	0.11	23
0.100	6990	200	1.70	0.16	−1.51	3.60	0.40	−1.50	0.10	43	−1.50	0.08	25
0.150	6740	200	1.80	0.26	−1.45	3.50	0.30	−1.46	0.10	48	−1.47	0.13	20
0.220	6520	150	2.00	0.18	−1.46	3.00	0.20	−1.46	0.11	91	−1.45	0.09	33
0.300	6320	100	2.00	0.22	−1.44	3.00	0.10	−1.44	0.10	99	−1.44	0.11	37
0.450	6070	100	1.85	0.28	−1.48	2.50	0.10	−1.50	0.11	92	−1.51	0.14	25
0.550	6090	100	1.95	0.22	−1.53	3.00	0.10	−1.53	0.13	63	−1.52	0.11	21
0.650	6110	100	2.00	0.18	−1.57	3.50	0.10	−1.57	0.09	67	−1.57	0.09	19
0.700	6130	150	2.00	0.24	−1.50	3.50	0.20	−1.50	0.11	70	−1.49	0.12	19
0.750	6160	150	1.90	0.24	−1.42	3.50	0.20	−1.42	0.10	54	−1.41	0.12	19
0.830	6180	150	2.05	0.22	−1.45	3.60	0.40	−1.46	0.10	75	−1.45	0.11	20
0.900	6160	200	1.70	0.22	−1.69	3.40	0.30	−1.69	0.10	50	−1.69	0.11	21
0.930	7060	200	2.70	0.18	−1.64	3.50	0.40	−1.64	0.11	38	−1.63	0.09	14
0.950	7390	300	2.45	0.20	−1.66	3.10	0.20	−1.66	0.07	29	−1.67	0.10	18
0.980	7550	300	1.90	0.20	−1.62	3.50	0.20	−1.62	0.10	19	−1.63	0.10	19
XZ Aps													
0.017	7310	300	1.45	0.20	−2.00	3.50	0.20	−2.00	0.09	6	−2.02	0.10	15
0.045	7280	300	1.60	0.28	−1.89	3.70	0.20	−1.86	0.12	15	−1.88	0.14	17
0.075	7040	200	1.60	0.22	−1.90	3.70	0.40	−1.88	0.13	27	−1.91	0.11	25
0.120	6860	200	1.60	0.20	−1.89	3.70	0.40	−1.87	0.10	42	−1.88	0.10	35
0.200	6580	150	1.85	0.20	−1.76	3.00	0.20	−1.76	0.10	60	−1.75	0.10	23
0.320	6280	100	1.85	0.22	−1.80	3.00	0.10	−1.80	0.10	78	−1.80	0.11	25
0.480	6100	100	1.80	0.16	−1.90	3.00	0.10	−1.87	0.09	65	−1.89	0.08	27
0.600	6100	100	1.80	0.22	−1.90	3.40	0.10	−1.92	0.10	62	−1.92	0.11	17
0.680	6130	100	2.00	0.16	−1.97	3.90	0.20	−1.97	0.09	46	−1.99	0.08	12
0.740	6060	150	1.85	0.20	−1.93	3.95	0.20	−1.93	0.10	44	−1.93	0.10	16
0.780	6090	150	1.95	0.24	−1.82	3.85	0.20	−1.87	0.09	43	−1.84	0.12	17
0.810	5970	150	1.70	0.16	−1.99	4.45	0.40	−1.99	0.10	38	−2.01	0.08	13
0.820	6170	150	2.05	0.24	−1.84	3.90	0.40	−1.84	0.09	39	−1.86	0.12	21
0.860	6170	150	1.90	0.24	−1.89	3.90	0.30	−1.89	0.09	42	−1.92	0.12	21
0.890	6200	200	2.00	0.14	−2.01	4.35	0.30	−2.00	0.10	41	−2.00	0.07	13
0.910	6700	200	2.75	0.28	−1.78	3.60	0.30	−1.78	0.09	25	−1.80	0.14	6
0.920	7020	200	2.40	0.22	−1.83	3.70	0.40	−1.83	0.12	16	−1.84	0.11	5
0.950	7340	300	2.30	0.26	−1.91	3.85	0.20	−1.92	0.13	13	−1.92	0.13	14
0.970	7540	300	2.35	0.18	−1.97	4.00	0.20	−1.97	0.11	13	−1.98	0.09	14
0.980	7560	300	2.15	0.22	−2.00	3.60	0.20	−2.00	0.09	13	−1.99	0.11	11
BS Aps 1													
0.030	7120	300	2.00	0.26	−1.35	3.05	0.20	−1.35	0.09	34	−1.36	0.13	16
0.130	6700	200	2.15	0.22	−1.37	3.15	0.30	−1.37	0.10	52	−1.38	0.11	25
0.300	6230	100	1.90	0.26	−1.40	3.05	0.10	−1.40	0.12	74	−1.40	0.13	28
0.520	6090	100	1.85	0.26	−1.47	3.10	0.10	−1.47	0.11	75	−1.47	0.13	20
0.730	6140	150	2.15	0.14	−1.44	3.90	0.20	−1.44	0.09	43	−1.45	0.07	11
0.850	6170	150	1.90	0.24	−1.54	3.70	0.30	−1.54	0.10	42	−1.54	0.12	13
0.900	6830	200	2.80	0.26	−1.47	3.55	0.30	−1.47	0.12	34	−1.47	0.13	11
0.950	7010	300	2.60	0.22	−1.45	3.15	0.20	−1.45	0.11	40	−1.46	0.11	19
0.980	7190	300	2.25	0.24	−1.41	3.45	0.20	−1.41	0.10	34	−1.42	0.12	20
BS Aps 2													
0.020	7000	300	2.25	0.18	−1.45	3.15	0.20	−1.45	0.10	33	−1.46	0.09	21
0.250	6290	100	1.90	0.24	−1.49	2.90	0.20	−1.49	0.11	70	−1.49	0.12	27

Table 4.5 (cont'd)

Mid Phase	$T_{\rm eff}$ (K)	err	log g (dex)	err	[M/H] (dex)	$v_{\rm t}$ (km s^{-1})	err (dex)	[Fe I/H]	err	N	[Fe II/H] (dex)	err	N
0.650	6040	100	1.80	0.22	−1.55	3.40	0.10	−1.55	0.10	52	−1.54	0.11	21
0.820	6060	150	1.85	0.20	−1.60	3.70	0.40	−1.60	0.10	60	−1.59	0.10	14
0.880	6160	200	1.75	0.20	−1.80	4.25	0.30	−1.80	0.11	43	−1.80	0.10	19
0.930	6700	200	2.35	0.22	−1.60	3.50	0.40	−1.60	0.10	48	−1.59	0.11	23
0.980	6850	300	2.40	0.20	−1.49	3.00	0.20	−1.49	0.11	46	−1.48	0.10	24
BS Aps 3													
0.100	6550	200	2.10	0.22	−1.54	3.65	0.40	−1.54	0.11	30	−1.54	0.11	24
0.920	6590	200	2.35	0.20	−1.52	3.45	0.30	−1.52	0.09	46	−1.53	0.10	17
UV Oct 1													
0.025	7430	300	2.05	0.20	−1.66	3.80	0.20	−1.66	0.08	21	−1.66	0.10	22
0.077	7080	200	2.00	0.18	−1.63	3.75	0.40	−1.64	0.08	33	−1.64	0.09	21
0.190	6240	150	1.75	0.20	−1.76	2.80	0.30	−1.76	0.09	87	−1.77	0.10	28
0.560	6000	100	1.80	0.20	−1.82	3.40	0.10	−1.82	0.08	71	−1.81	0.10	21
0.740	6220	150	2.00	0.24	−1.71	3.85	0.20	−1.70	0.10	69	−1.71	0.12	21
0.820	6250	150	2.10	0.18	−1.71	4.00	0.30	−1.72	0.07	57	−1.73	0.09	20
0.870	6220	200	2.00	0.22	−1.94	3.10	0.30	−1.95	0.07	41	−1.94	0.11	15
0.920	7160	200	2.60	0.22	−1.93	2.80	0.30	−1.93	0.08	32	−1.94	0.11	19
0.950	7550	300	1.75	0.22	−1.95	3.10	0.20	−1.95	0.10	16	−1.96	0.11	16
0.980	7630	300	2.00	0.18	−1.74	3.55	0.20	−1.75	0.10	13	−1.75	0.09	16
UV Oct 2													
0.023	6850	300	1.90	0.22	−1.81	2.50	0.20	−1.81	0.07	45	−1.80	0.11	29
0.070	6720	200	1.85	0.20	−1.77	2.50	0.40	−1.77	0.09	58	−1.76	0.10	29
0.250	6290	150	1.90	0.22	−1.73	2.50	0.20	−1.73	0.09	75	−1.73	0.11	30
0.600	6020	100	1.80	0.20	−1.86	3.00	0.10	−1.86	0.09	65	−1.85	0.10	27
0.780	6070	150	1.80	0.16	−1.83	3.50	0.20	−1.83	0.09	66	−1.84	0.08	28
0.830	6170	150	1.85	0.22	−1.89	3.25	0.40	−1.89	0.08	53	−1.88	0.11	21
0.870	6800	150	2.65	0.22	−1.80	3.50	0.30	−1.80	0.08	40	−1.80	0.11	19
0.910	6850	200	2.45	0.16	−1.80	3.05	0.30	−1.80	0.09	36	−1.81	0.08	18
0.930	6880	200	2.15	0.24	−1.87	3.05	0.40	−1.88	0.08	44	−1.87	0.12	21
0.970	6960	300	1.90	0.20	−1.89	3.00	0.20	−1.89	0.08	40	−1.90	0.10	25
V1645 Sgr 1													
0.170	6470	200	1.8	0.16	−1.99	2.80	0.30	−1.99	0.10	49	−1.98	0.08	14
0.500	6020	100	1.5	0.24	−2.10	2.90	0.10	−2.10	0.11	27	−2.10	0.12	12
0.720	6060	150	1.6	0.20	−2.21	3.80	0.20	−2.21	0.10	30	−2.21	0.10	11
0.820	6060	150	1.65	0.18	−2.19	3.40	0.40	−2.19	0.09	28	−2.20	0.09	15
0.880	6750	200	2.35	0.20	−1.83	3.45	0.30	−1.83	0.10	20	−1.83	0.10	9
0.960	6800	300	1.85	0.24	−2.12	3.00	0.20	−2.12	0.10	24	−2.12	0.12	17
V1645 Sgr 2													
0.020	6850	300	1.70	0.20	−2.06	3.00	0.20	−2.06	0.08	33	−2.06	0.10	18
0.700	6050	150	1.70	0.18	−2.15	3.50	0.20	−2.15	0.07	37	−2.15	0.09	14
0.850	6240	200	1.65	0.22	−2.24	3.25	0.40	−2.24	0.06	23	−2.24	0.11	10
0.950	6980	300	1.85	0.20	−2.09	2.55	0.20	−2.09	0.08	25	−2.09	0.10	14
V1645 Sgr 3													
0.050	7780	300	2.20	0.24	−1.71	2.70	0.20	−1.71	0.10	7	−1.71	0.12	11
0.140	6250	200	1.15	0.20	−2.33	3.80	0.30	−2.33	0.09	15	−2.32	0.10	15
0.250	6480	100	1.85	0.16	−1.92	2.95	0.10	−1.92	0.08	53	−1.92	0.08	15
0.400	6290	100	2.10	0.20	−1.81	3.00	0.10	−1.81	0.12	50	−1.80	0.10	18
0.750	6100	150	1.75	0.28	−1.98	3.25	0.20	−1.98	0.09	17	−1.98	0.14	2
0.860	6170	150	1.90	0.18	−2.00	3.75	0.40	−2.00	0.09	29	−2.00	0.09	7
Z Mic													
0.030	6830	300	2.00	0.22	−1.53	3.20	0.20	−1.53	0.07	60	−1.54	0.11	27

Table 4.5 (cont'd)

Mid Phase	$T_{\rm eff}$ (K)	err	log g (dex)	err	[M/H] (dex)	$v_{\rm t}$ (km s^{-1})	err (dex)	[Fe I/H]	err	N	[Fe II/H] (dex)	err	N
0.140	6310	200	1.55	0.24	−1.62	2.90	0.30	−1.62	0.09	63	−1.63	0.12	26
0.250	6190	100	1.80	0.22	−1.50	2.65	0.20	−1.50	0.09	72	−1.51	0.11	22
0.420	6060	100	1.80	0.24	−1.46	2.90	0.10	−1.46	0.11	81	−1.47	0.12	24
0.530	6010	100	1.75	0.20	−1.53	3.20	0.10	−1.54	0.10	52	−1.53	0.10	18
0.650	6040	100	1.90	0.18	−1.56	3.60	0.10	−1.56	0.09	65	−1.57	0.09	22
0.750	6060	150	1.90	0.16	−1.54	3.90	0.20	−1.54	0.10	66	−1.54	0.08	21
0.830	6050	150	2.05	0.18	−1.56	3.60	0.40	−1.56	0.11	63	−1.57	0.09	17
0.870	6150	150	1.90	0.20	−1.70	3.85	0.30	−1.70	0.08	47	−1.70	0.10	23
0.900	6530	200	2.50	0.20	−1.64	3.75	0.30	−1.64	0.09	51	−1.64	0.10	13
0.920	6700	200	2.55	0.24	−1.55	3.00	0.30	−1.55	0.10	57	−1.55	0.12	21
0.950	6780	300	2.40	0.22	−1.55	3.40	0.20	−1.55	0.11	53	−1.55	0.11	25
0.970	6830	300	2.30	0.20	−1.54	3.20	0.20	−1.54	0.08	43	−1.54	0.10	23
0.990	6880	300	2.00	0.24	−1.50	2.70	0.20	−1.50	0.08	43	−1.50	0.12	18
TY Gru													
0.014	7320	300	2.35	0.22	−1.91	3.00	0.20	−1.90	0.10	3	−1.91	0.11	5
0.460	6120	100	2.05	0.24	−1.96	3.30	0.10	−1.95	0.13	45	−1.96	0.12	14
0.800	6360	150	2.05	0.30	−1.95	4.15	0.40	−1.95	0.12	26	−1.95	0.15	10
0.920	6740	200	2.30	0.28	−1.99	4.35	0.40	−1.99	0.11	17	−1.99	0.14	8
0.980	7560	300	2.15	0.36	−2.16	4.50	0.20	−2.16	0.14	7	−2.16	0.18	6

4.6.1 Parameter Uncertainties

To estimate the effects of uncertainties in our spectroscopically–based $T_{\rm eff}$ values on derived abundances, we varied the derived $T_{\rm eff}$ of RV Oct (as an example) by raising different amount of $T_{\rm eff}$ for all phases. The uncertainty of $T_{\rm eff}$ was determined for a particular phase when the raised $T_{\rm eff}$ produced a large trend of derived log ϵ(Fe) (Δ log ϵ(Fe) $> \pm 0.1$) with excitation potential. This yielded $T_{\rm eff}$ errors of 100–300 K throughout the cycle.

4.6.2 Reliability of Derived Stellar Parameters

4.6.2.1 Derived Effective Temperature

We compare our derived spectroscopic $T_{\rm eff}$'s with the initial values that were derived from the calibration curves, in Figure 4.28 and 4.29 for non-Blazhko and Blazhko stars, respectively. The scatter with respect to the unity line for the non-Blazhko stars is $\Delta(T_{\rm eff,phot} - T_{\rm eff,spec}) = 4 \pm 10$ K, $\sigma = 92$ K, $N = 87$, and it is somewhat larger for the Blazhko stars, $\Delta(T_{\rm eff,phot} - T_{\rm eff,spec}) =$

8 ± 17 K, $\sigma = 151$ K, $N = 78$. Most cases of exact agreement (i.e., $\Delta T_{\rm eff} = 0$) were artificially caused by the spectroscopic constraints method that we used. Those initial $T_{\rm eff}$ values either yielded no trend or small trend (Δ log ϵ(Fe) = 0.05) with EP during first iteration. Based on the overall calculated $\Delta T_{\rm eff}$, we concluded that even though the RV curves of Blazhko stars might not match the RV curves of calibration stars, the initial $T_{\rm eff}$ values derived from the calibration curves worked reasonably well. We also showed in a previous section that the selected initial $T_{\rm eff}$ yielded consistent stellar parameters throughout the pulsational phase for any cycle in Blazhko stars (see Figure 4.20 for example).

We also made another comparison with the study of TY Gru in (Preston et al. 2006b), which they used the MIKE Magellan spectra for analysis. Their derived stellar parameters near minimum light for TY Gru were $T_{\rm eff}$=6250±150 K, log g=2.3±0.2 dex, [M/H]=$-$2.0±0.2, and $v_{\rm t}$=4.1±0.2 km s^{-1}. Our derived stellar parameters at phase 0.8 were $T_{\rm eff}$=6360±150 K, log g=2.05±0.30 and $v_{\rm t}$=4.15±0.4 km s^{-1}, which were within the uncertainties with the Preston et al. (2006b) study.

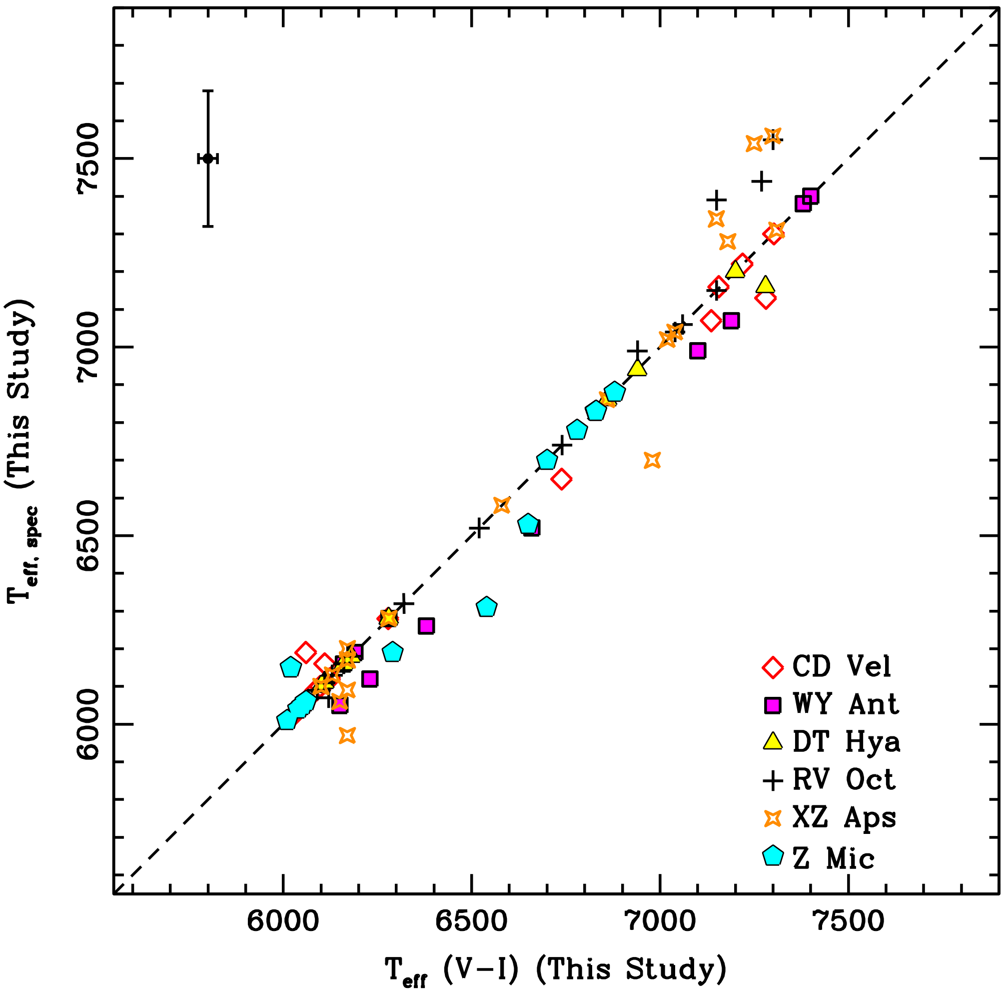

Figure 4.28 Comparison of derived spectroscopic $T_{\rm eff}$ with photometric $T_{\rm eff}$. It shows comparison for non-Blazhko stars. Symbols represent our program stars that are given in the legend. For the clarity of the figure, we do not plot the error bar for each value, but instead indicate typical uncertainties for $T_{\rm eff,spec}$ and $T_{\rm eff}(V - I)$.

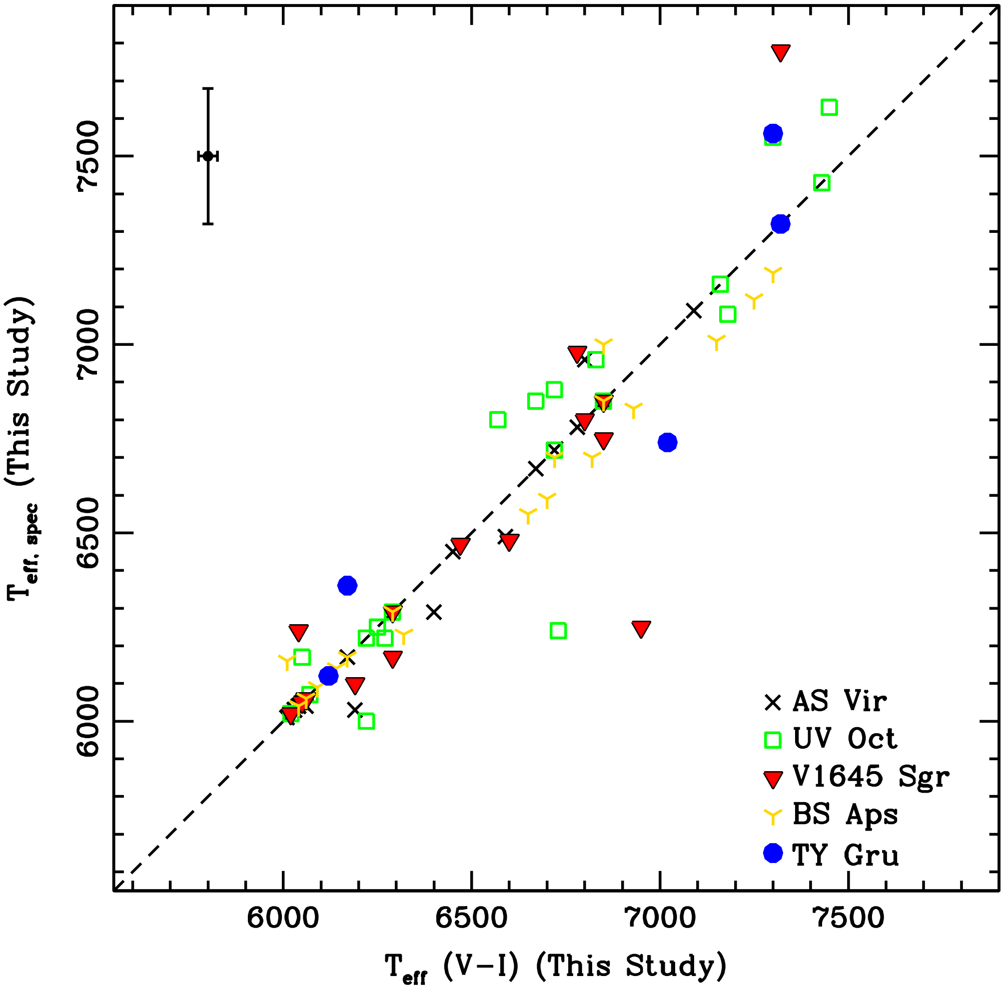

Figure 4.29 Same as Figure 4.28, except for Blazhko stars.

4.6.2.2 Derived Surface Gravity

It is known that the spectroscopic log g derived from using standard spectroscopic constraints, i.e., the ionization balance between neutral and ionized species, may be lower than the trigonometric log g (see e.g., Allende Prieto et al. 1999). The detailed abundance study of HB stars by For & Sneden (2010) also found lower derived spectroscopic log g than photometric.

The initial concern of significant low spectroscopic log g values forced us to re-evaluate the methods of reducing the spectra. To justify that the issue was not caused by the scattered light correction, we obtained a spectrum of a well studied metal-poor star, HD 140283, and reduced it in the same manner as we did for our RR Lyr. In Table 4.6, we summarize the results and comparison with other studies. We find that spectroscopic $T_{\rm eff}$ and log g values derived in Hosford et al. (2009) study show to be lower than other methods and essentially within errors of our values for HD 140283. We also show that the scattered light correction essentially has no effect on the derived stellar parameters. Thus, the derived low log g values for our RR Lyr and HD 140283 cannot be caused by the scattered light correction. In any case, despite the lower derived log g values for our RR Lyr throughout the pulsational cycle, the trend of our derived log g variation (see e.g., Figure 4.17) is quite similar to the effective gravity variation as shown in Figure 1 of LJ90.

Ideally we would compare the derived spectroscopic log g with physical or trigonometric log g that can be derived from stellar parallaxes. However, this is not possible in our case because either the reported parallaxes have large error or no parallax data are available. Nevertheless, we may evaluate the physical log g by making assumptions for the following equation:

$$\log\, g = \log(M/M_\odot) + 4\log(T_{\rm eff,spec}) - \log(L/L_\odot) - 10.607, \tag{4.4}$$

Table 4.6. Comparison of derived $T_{\rm eff}$ and log g values of HD 140283 in various studies.

Reference	Method	$T_{\rm eff}$ (K)	log g (dex)
Hosford et al. (2009)	Spectroscopic	5573±75	3.1±0.15
Asplund et al. (2006)	Balmer line wing fitting	5753±30	3.7±0.04
Ryan et al. (1996)	Photometry	5750	3.4
Alonso et al. (1996)	Infrared flux	5691±69	4.0±0.50
This study[a]	Spectroscopic	5400±150	2.6±0.16
This study[b]	Spectroscopic	5400±150	2.6±0.16
This study	Trigonometric[c]	5400[d]	3.7

[a] Without scattered light correction

[b] With scattered light correction

[c] Assuming $M = 0.8\ M_{\odot}$, $\pi = 17.44$ mas and $E(B-V) = 0$

[d] Adopted spectroscopic $T_{\rm eff}$

in which the constant was calculated by using the solar $T_{\rm eff}$ and log g values, $M = 0.5\ M_{\odot}$ as typical mass of an HB star and absolute magnitude of $M_V = +0.6$ as value consistent with RR Lyr (Beers et al. 1992). We note that the absolute magnitude is metallicity-dependent, in that a lower metallicity would result in brighter absolute magnitude (see e.g., Gratton 1998).

Comparing our derived log g values throughout pulsational cycle with calculated physical log g values, we found that they are systematically lower, Δlog g(calculated$-$us) $= 0.67 \pm 0.02$ dex, $\sigma = 0.28$ dex, $N = 165$. The large deviation is directly related to the assumptions we made for stellar mass, absolute magniture, and treatment of gravity as mean gravity instead of effective gravity that was decribed in §4.5.2.

4.6.2.3 Derived Metallicity

There are many methods to estimate metallicities of RR Lyr. One method is to use the well known ΔS–[Fe/H] relation. Another method is to use the period–metallicity relation: as an RR-ab variable's metallicity increases, its period decreases. Such a relation is generally derived via lightcurve fitting (see e.g., Jurcsik & Kovacs 1996) and an improvement of the relation by a recent study of Sarajedini et al. 2006)

We may compare our derived mean [Fe I/H] metallicities with [Fe I/H] values derived from the above methods. The values were extracted from Layden (1994), and were calculated with the period–metallicity relation. The comparison is summarized in Table 4.7, in which the periods are adopted from chapter 3.

In Figure 4.30, we show that the values extracted from Layden (1994), who employed the ΔS–[Fe/H] relation, are systematically larger than ours (Δ(Layden-us) $= 0.25 \pm 0.03$ dex, $\sigma = 0.08$, $N = 8$). We also show that there is no correlation between our mean [M/H] values and values calculated with the period–metallitiy relation (Sarajedini et al. 2006). However, we warn the reader that the dispersion of the derived period–metallicity relation is very large ($\sigma \sim 0.45$). Comparing metallicity of TY Gru between Preston et al and us, in which we both employed spectroscopic constraints to obtain the metallicity, they are in good agreement.

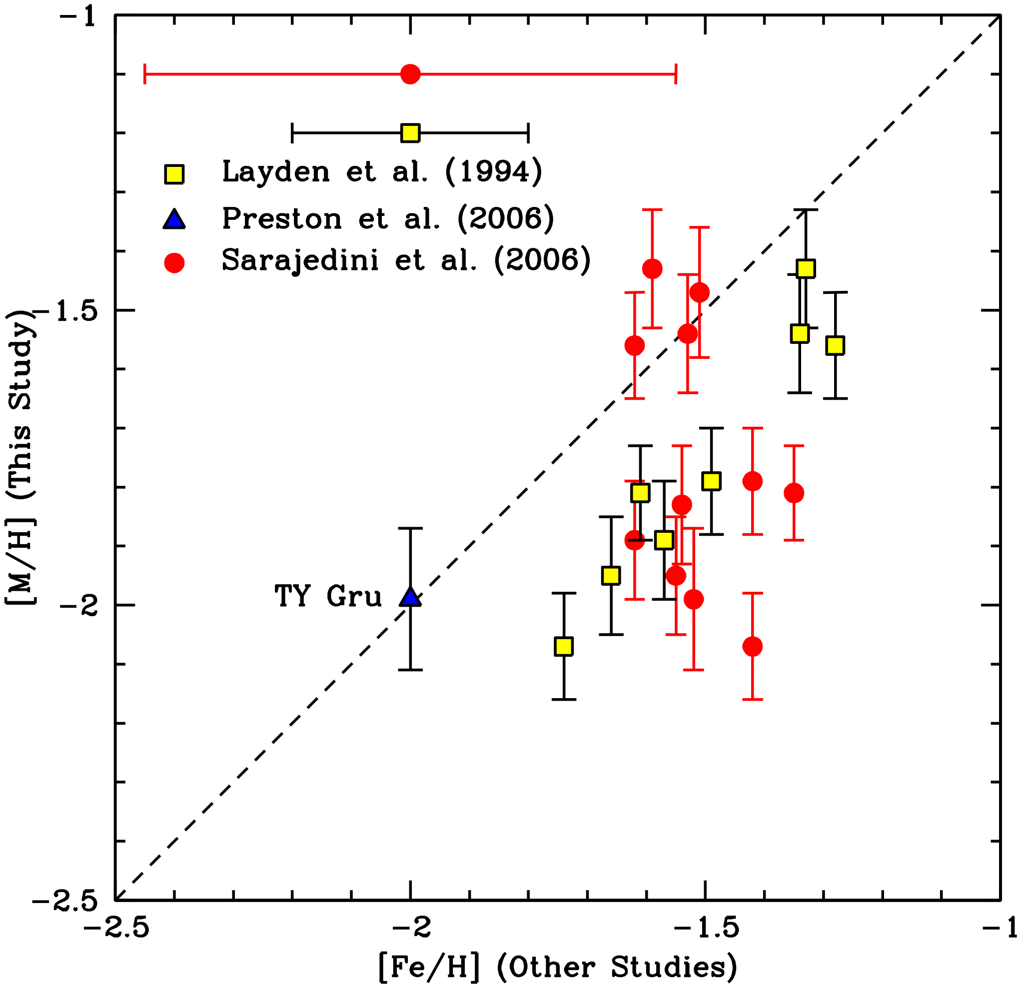

Figure 4.30 Comparison of derived [M/H] with [Fe/H] of other studies. The symbols represent the values derived from period–metallicity relation by Sarajedini et al. (2006) (red dots); from ΔS–metallicity relation by Layden (1994) (yellow squares) and from spectroscopic method by Preston et al. (2006b). For clarity in the figure, we do not plot error bars for each star, but instead indicate typical uncertainties of 0.2 dex and 0.4 dex for Layden (1994) and Sarajedini et al. (2006) studies.

Table 4.7. Comparison of derived metallicities with various methods.

P^{a} (day)	[M/H]^{b} (dex)	[Fe/H]^{c} (dex)	[Fe/H]^{d} (dex)
0.573510	-1.83 ± 0.10	-1.54 ± 0.45	···
0.574344	-1.95 ± 0.10	-1.55 ± 0.45	-1.66 ± 0.20
0.567978	-1.47 ± 0.11	-1.51 ± 0.45	···
0.553412	-1.79 ± 0.09	-1.42 ± 0.45	-1.49 ± 0.20
0.571170	-1.54 ± 0.10	-1.53 ± 0.45	-1.34 ± 0.20
0.587264	-1.89 ± 0.10	-1.62 ± 0.45	-1.57 ± 0.20
0.582561	-1.43 ± 0.10	-1.59 ± 0.45	-1.33 ± 0.20
0.542578	-1.81 ± 0.08	-1.35 ± 0.45	-1.61 ± 0.20
0.552948	-2.07 ± 0.09	-1.42 ± 0.45	-1.74 ± 0.20
0.586926	-1.56 ± 0.09	-1.62 ± 0.45	-1.28 ± 0.20
0.570065	-1.99 ± 0.12	-1.52 ± 0.45	-2.00 ± 0.20

[a] For et al. (2011)

[b] This study

[c] Calculated from period-metallicity relation of Sarajedini et al. (2006)

[d] From Layden (1994), except TY Gru from Preston et al. (2006b)

4.6.3 Microturbulence vs Effective Temperature

In this section, we revisit the correlation and anti-correlation between $v_{\rm t}$ and $T_{\rm eff}$ for RHB and BHB stars that was suggested in Figure 7 of For & Sneden (2010). The relationship was inconclusive in the RR Lyr instability strip region at the time because the data for these stars came from heterogeneous sources. Now, with our internally-consistent data and analyses, we have better control to investigate the trends. In Figure 4.31, we overplotted the derived $v_{\rm t}$ and $T_{\rm eff}$ of RV Oct onto the $v_{\rm t}$–$T_{\rm eff}$ plane published in For & Sneden (2010). It clearly shows that the correlation and anti-correlation with a transition near 6500 K.

In Figure 4.32, we enlarged on the RR Lyr instability strip region. It shows the $v_{\rm t}$ values as a function of $T_{\rm eff}$ of all the RR Lyr in our program. The trends are less obvious here and the $v_{\rm t}$ varies between 2.5 to 4.5 km s^{-1}, which is similar to the spread of $v_{\rm t}$ for RR Lyraes studied by Clementini et al. (1995) and Lambert et al. (1996) (refer to Figure 7 of For & Sneden 2010). The range in $v_{\rm t}$ for each RR Lyr is real, produced by systematic variation during pulsation cycles as we discuss in the next section.

4.6.4 Microturbulence vs Phase

The microturbulence variations as seen in the previous sections are undoubtedly related to the atmosphere instabilities of RR Lyraes. Such variations are believed to be caused by the strong shock waves propagating through the line formation region, which produce compression of the turbulent gas (Fokin et al. 1999b). Theoretical line profile studies of Fokin & Gillet (1997) and Fokin et al. (1999b) have shown that hydrodynamical RR Lyr models are consistent with the line profile variations (see Figures 1 and 4 of Fokin et al.

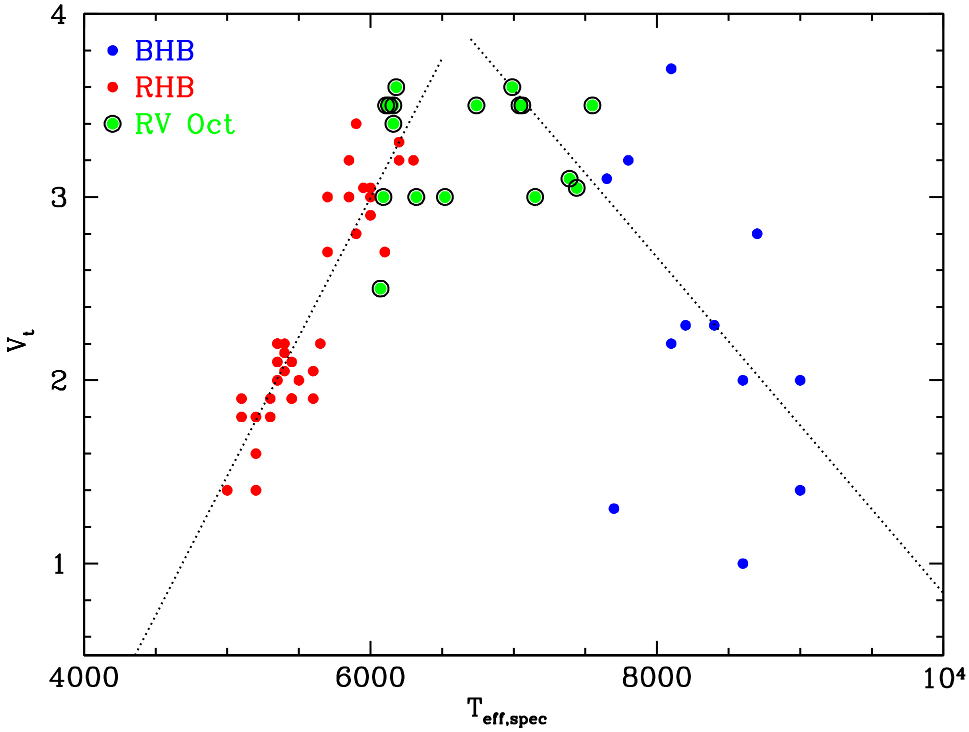

Figure 4.31 The microturbulence as a function of $T_{\rm eff}$. It shows $v_{\rm t}$ and $T_{\rm eff}$ of RV Oct on the $v_{\rm t}$-$T_{\rm eff}$ plane, with additional data of RHB and BHB stars from For & Sneden (2010). The dashed lines show the correlation and anti-correlation. A transition near 6500 K is shown. The symbols represent the same stars as labeled in Figure 4.28 and 4.29.

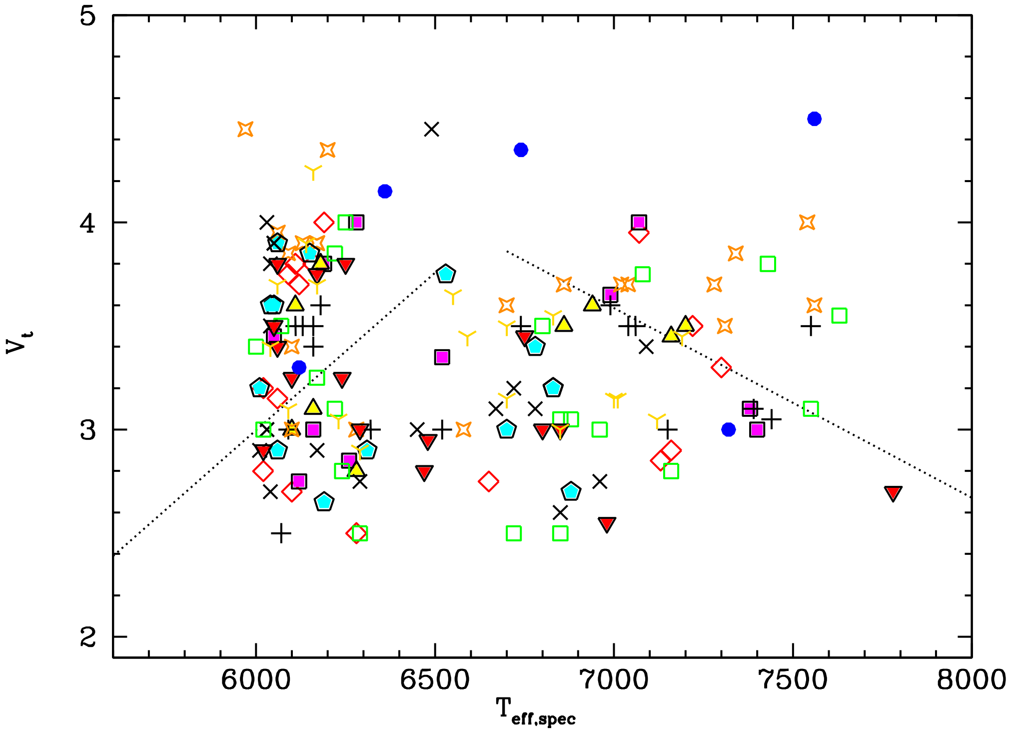

Figure 4.32 The microturbulence as a function of $T_{\rm eff}$. It shows all the $v_{\rm t}$ and $T_{\rm eff}$ of all of our program stars on the $v_{\rm t}$-$T_{\rm eff}$ plane near the instability strip region. The symbols represent the same stars as labeled in Figure 4.28 and 4.29.

1999b).

In our study, we set the microturbulence by demanding that the abundances of individual Fe I and Fe II lines show no trend with reduced width log RW. This is a simple compensation for the complex line width variations that occur throughout the pulsational cycle. To demonstrate such effects, we show the measured full width half maximum (FWHM) of four metal lines throughout the pulsational cycle of XZ Aps in Figure 4.33. The minimum occurrance of FWHM is near phase 0.3 and with increasing FHWM after ∼ phase 0.6. A visible peak occurs near phase 0.9 during the rising light that is caused by the shock wave. The general trend of FWHM vs phase is very similar to Figure 4 of the Kolenberg et al. (2010) study of Blazhko star RR Lyr.

In Figure 4.34, we present all the derived $v_{\rm t}$ as shown in the bottom panel of Figure 4.17–4.27. When the metal lines appear to be the sharpest near phase 0.35, the $v_{\rm t}$ is at its lowest. The $v_{\rm t}$ increases again as the atmosphere contracts and reaches another high point between phase 0.7 and 0.9. The scatter is relatively large between phase 0.7 and 1.0, which is observationally hard to dissect due to the complexity of shock waves phenomenon during these phases. However, we have shown for the first time that the observational variation of $v_{\rm t}$ versus phase is similar to the theoretical calculated turbulence velocity variation with phase, as shown in Figure 4 of Fokin et al. (1999b) and kinetic energy variation with phase in Figure 1 of Kolenberg et al. (2010).

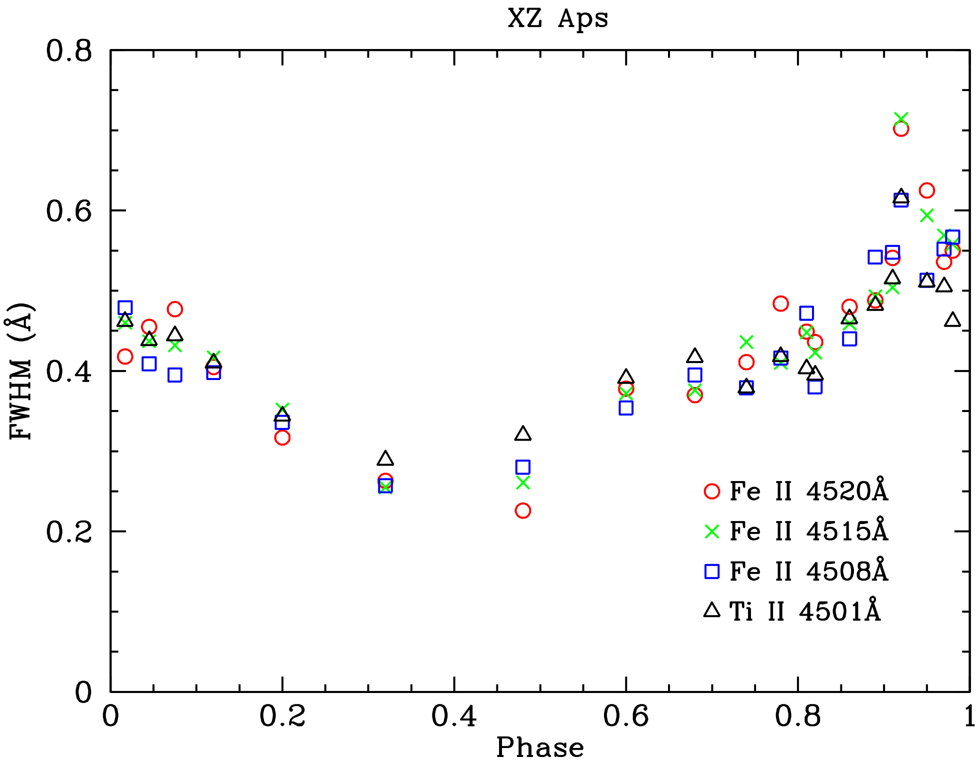

Figure 4.33 The full width half maximum (FWHM) of four metal lines of XZ Aps throughout the pulsational cycle. The FWHM appears to be lowest near phase 0.3 and a peak associated with the shock wave near phase 0.9.

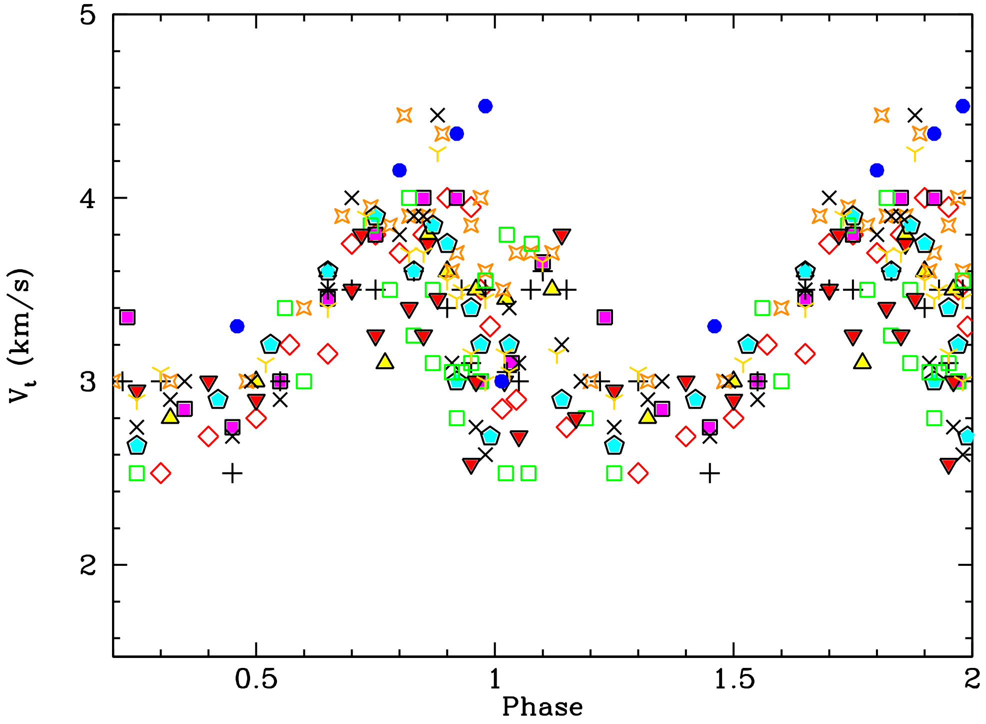

Figure 4.34 The microturbulence as a function of phase of all of our program stars. The symbols represent the same stars as labeled in Figure 2.6. It shows a general trend of v_t variation throughout the pulsational cycle. The v_t reaches ~ 2.7 km s^{-1} near phase 0.3 (minimum), and ~ 4 km s^{-1} near phase 0.85.

4.7 The Optimal Phases

In this section, we briefly describe the physical changes of RR Lyr atmosphere during the pulsational cycle. Then, we discuss the optimal phases for chemical abundances analysis.

It is generally defined the maximum light of a RR Lyr lightcurve as phase 0. At this phase, the RR Lyr atmosphere continues to expand and reaches its maximum radius at around phase 0.3. Then, to restore its thermal equilibrium, the star starts to contract. When it is about to reach its minimum radius (or minimum light), the first shock wave occurs at around phase 0.7, which caused by the rapid deceleration of infalling material collides with the accelerating outward atmosphere layer (Gillet et al. 1989; Gillet & Crowe 1988). A prominent bump feature is seen on the lightcurve of RR Lyr. After it reaches its minimum radius at around phase 0.8, the expansion of the atmosphere begins. The changes in the atmosphere is fast as can be seen through the sharp rising branch of the lightcurve. At around phase 0.9, a halt in the atmosphere occurs, which caused by the rapid accelerating outward atmosphere layer collides with the infalling material, a second shock wave is produced (Gillet et al. 1989; Gillet & Crowe 1988). A hump feature is detected in the lightcurve.

The dramatical changes in the atmosphere of RR Lyr during the pulsational cycle complicates the line profile, in which line broadening, line doubling and line emission have been reported in previous studies (see Preston 2009 and references therein). With the large number of spectra we collected throughout the cycles, we can identify possible quiescent phases, i.e., phases without the influence of shock wave phenomenon and no line profile distortion. Examining Figures 4.1–4.4, we find the metal spectral line is at its sharpest near phase

0.3, and phase ∼0.2–0.5 considered to be phases with minima line distortion. The FWHM of metal lines and v_{t} vs phase plots also show a similar range, ∼0.2–0.5, as optimal phases (see Figures 4.33 and 4.34).

During these optimal phases, the effective temperatures of RR Lyr are similar to those of RHB stars (6500 K $< T_{\mathrm{eff}} <$ 6000 K). Thus, we expect to see many formed metal lines in the spectra, which make these phases ideal for chemical abundances analysis. Nevertheless, we did not exclude the use of other phases for the following analysis. In fact, the descending and rising branches of RR Lyr have their advantage. The effective temperatures range are similar to the BHB stars (7400 K $< T_{\mathrm{eff}} <$ 6200 K), which certain low EP metal lines are less likely to saturate in these phases and can be measured. The sharpest line phase ∼0.3, which also corresponds to RR Lyr's maximum radius, is the only ideal phase for performing spectrum synthesis. The finding is contradict to previous assumption of quiescent phase at minimum light but in accord with the conclusion of Kolenberg et al. (2010).

4.8 Chemical Abundances

By the use of model atmosphere parameters derived in §4.5 (listed in Table 4.5), we computed chemical abundances for 22 species of 19 elements in ∼165 phase bins. Abundances of most elements were derived from EW measurements, i.e., by forcing the individual lines abundances to match the EW and averaging over all lines. In the cases of Mn I, Sr II, Zr II, Ba II, La II, and Eu II, we employed spectrum synthesis method to handle the blending, or hyperfine and/or isotopic substructure presence in these lines. We computed theoretical spectra for a variety of assumed abundances for each line, then the assumed abundances were changed iteratively until the theoretical spectra match the observed ones. Synthesis was performed only for phase (optimal phase) of each star, with the exception of AS Vir which we have optimal phase spectra for Blazhko and non-Blazhko cycles.

We show the derived relative abundance ratios, [X/Fe], of various elements as a function of phase in Figures 4.35–4.38 for RV Oct, a non-Blazhko star; and Figures 4.39–4.42 for AS Vir, a Blazhko star. In the case of a Blazhko star, we used different colors to represent different series of phase bins (see discussion in §3). Chemical abundances derived via spectrum synthesis are not presented as a function of phase because there were derived with only one phase as mentioned above. The error bars represent the internal error (line-to-line scatter). We adopted internal error of 0.2 dex for abundances derived from single line (for plots only). The mean relative abundance ratios are represented by the dashed lines. Examining these figures, we conclude that the abundances are consistent throughout the pulsational cycles in both Blazhko and non-Blazhko stars.

Tables 4.8–4.11 give the derived [X/Fe] of each phase for all program stars. The mean [X/Fe] values of each species for each RR-ab variable star (green dots) are presented as a function of metallicity in Figures 4.43–4.45. We overplot them with the results of RHB (red dots) and BHB (blue dots) stars presented in For & Sneden (2010). We summarize the mean [X/Fe] values in Tables 4.12 and comment on individual elements in the following subsections.

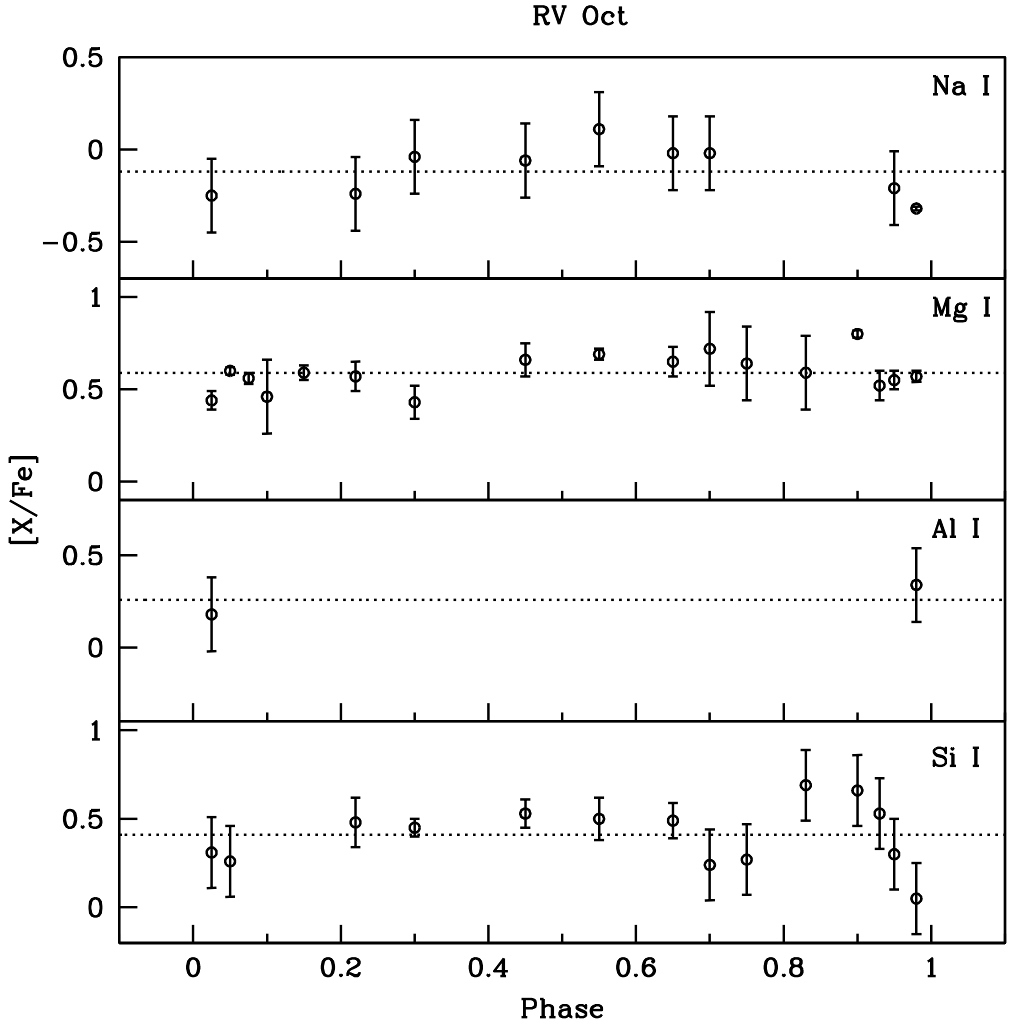

Figure 4.35 Abundance ratios, [X/Fe], of Na I, Mg I, Al I and Si I as a function of phase for a non-Blazhko effect star, RV Oct. The dashed line represent the mean values. The [X/Fe] values are generally consistent throughout the pulsational cycle. The small trend of [Si I/Fe] between phase 0.8 and 1.0 is discussed in §7.2.

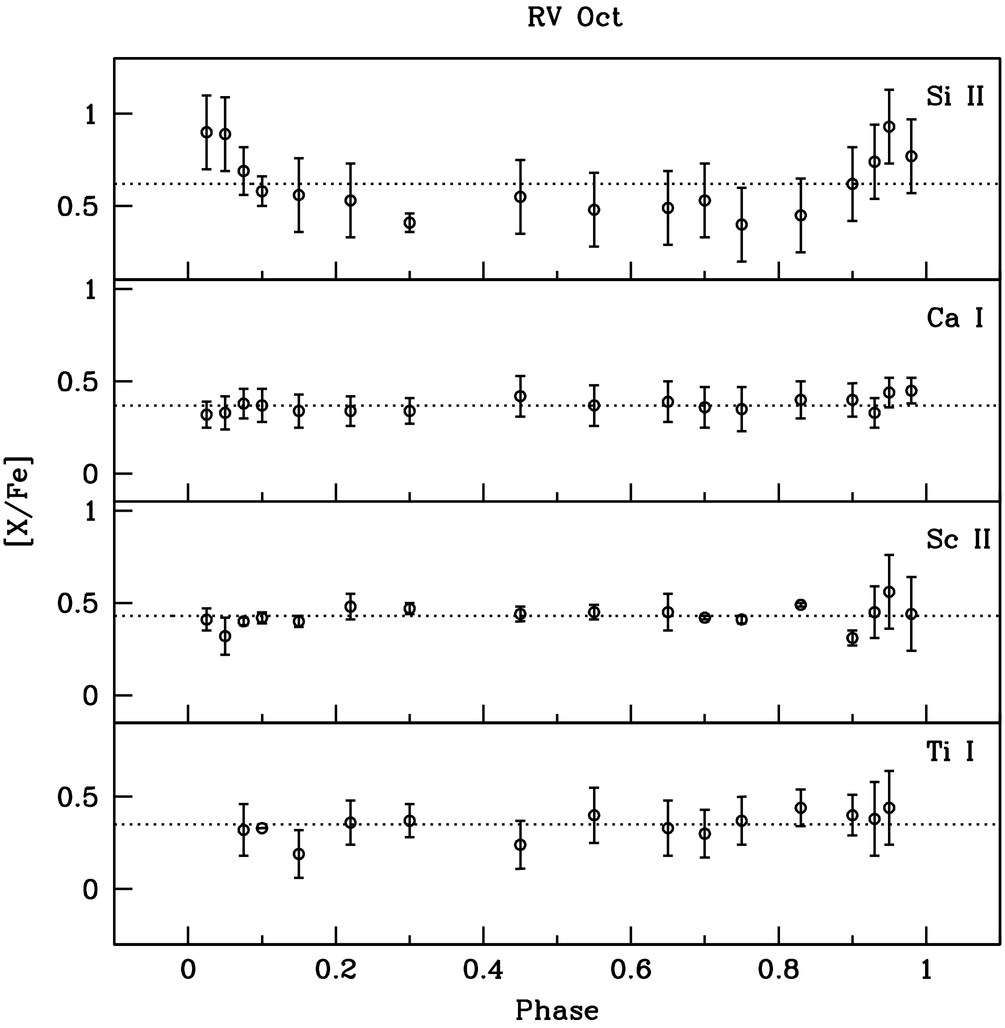

Figure 4.36 Same as Figure 4.35, except for Si II, Ca I, Sc II and Ti I. The trend of [Si II/Fe] is discussed in §7.2.

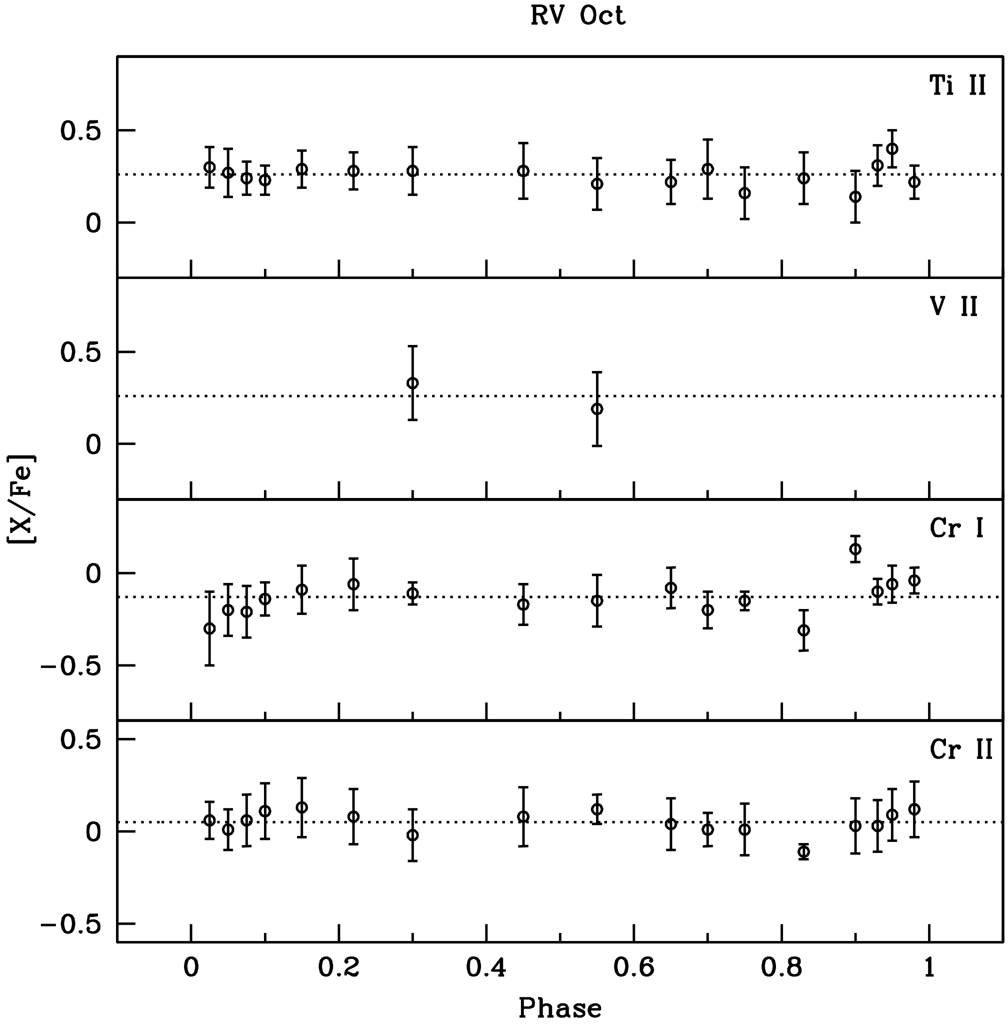

Figure 4.37 Same as Figure 4.35, except for Ti II, V II, Cr I and Cr II.

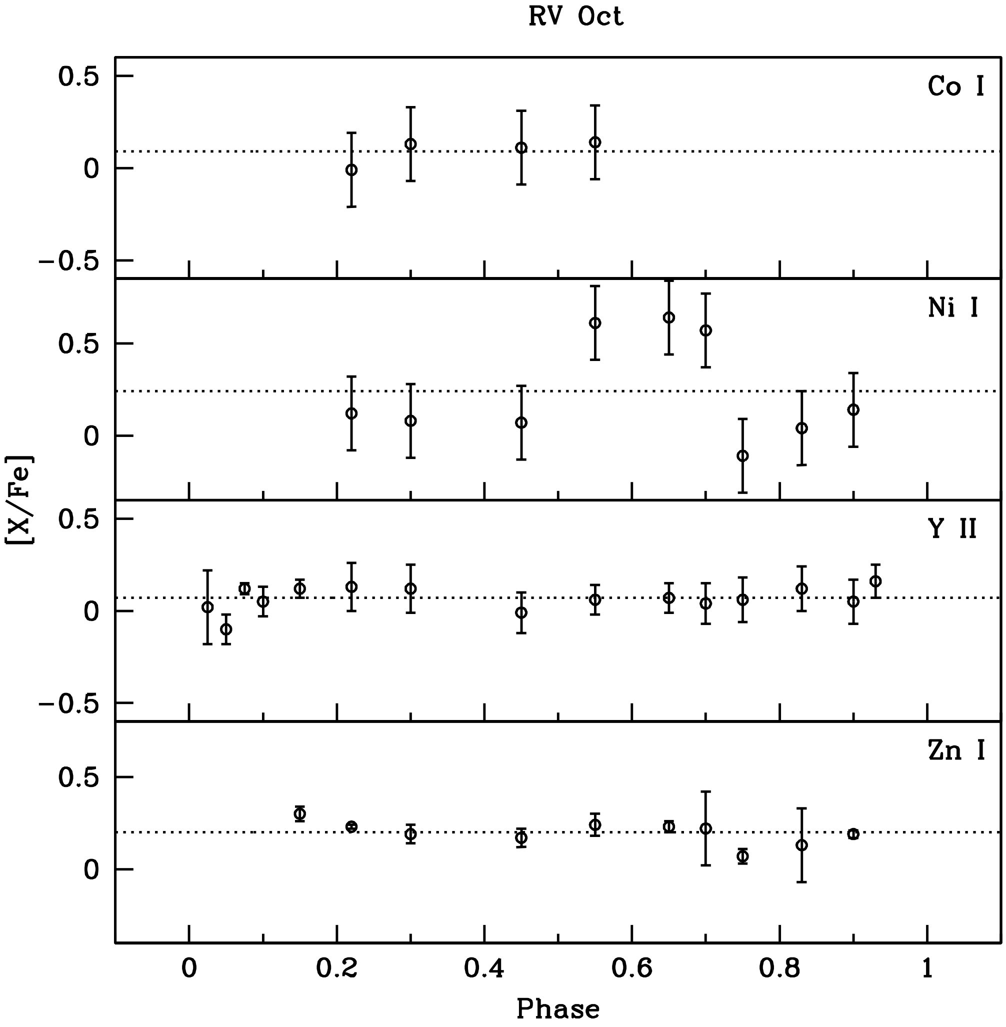

Figure 4.38 Same as Figure 4.35, except for Co I, Ni I, Y II and Zn I. The large phase-to-phase scatter of [Ni I/Fe] is due to the large uncertainties of the derived values.

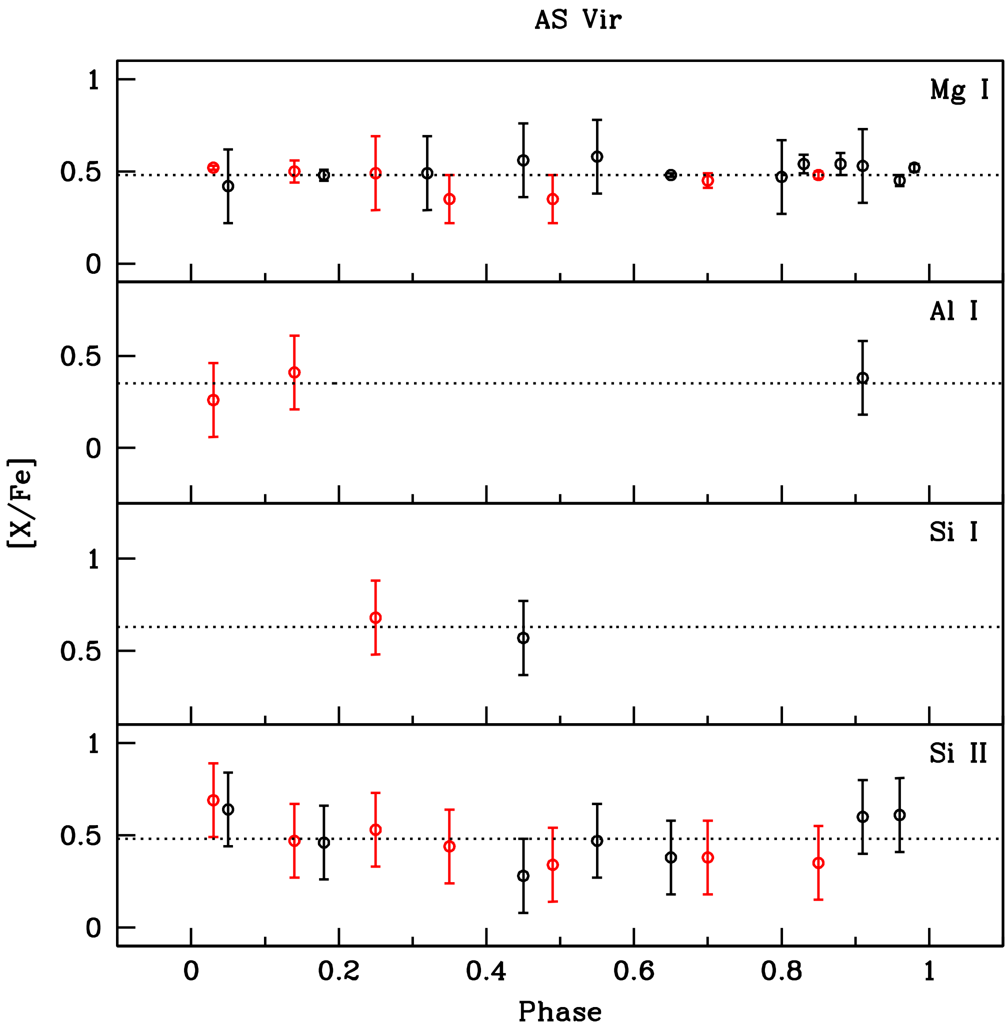

Figure 4.39 Abundance ratios, [X/Fe], of Mg I, Al I, Si I and Si II as a function of phase for a Blazhko effect star, AS Vir. The dashed lines and color symbols represent the mean values and different cycles being considered for combining the spectra, respectively. The [X/Fe] values are generally consistent throughout the pulsational cycle. The trend in [Si II/Fe] is discussed in §7.2.

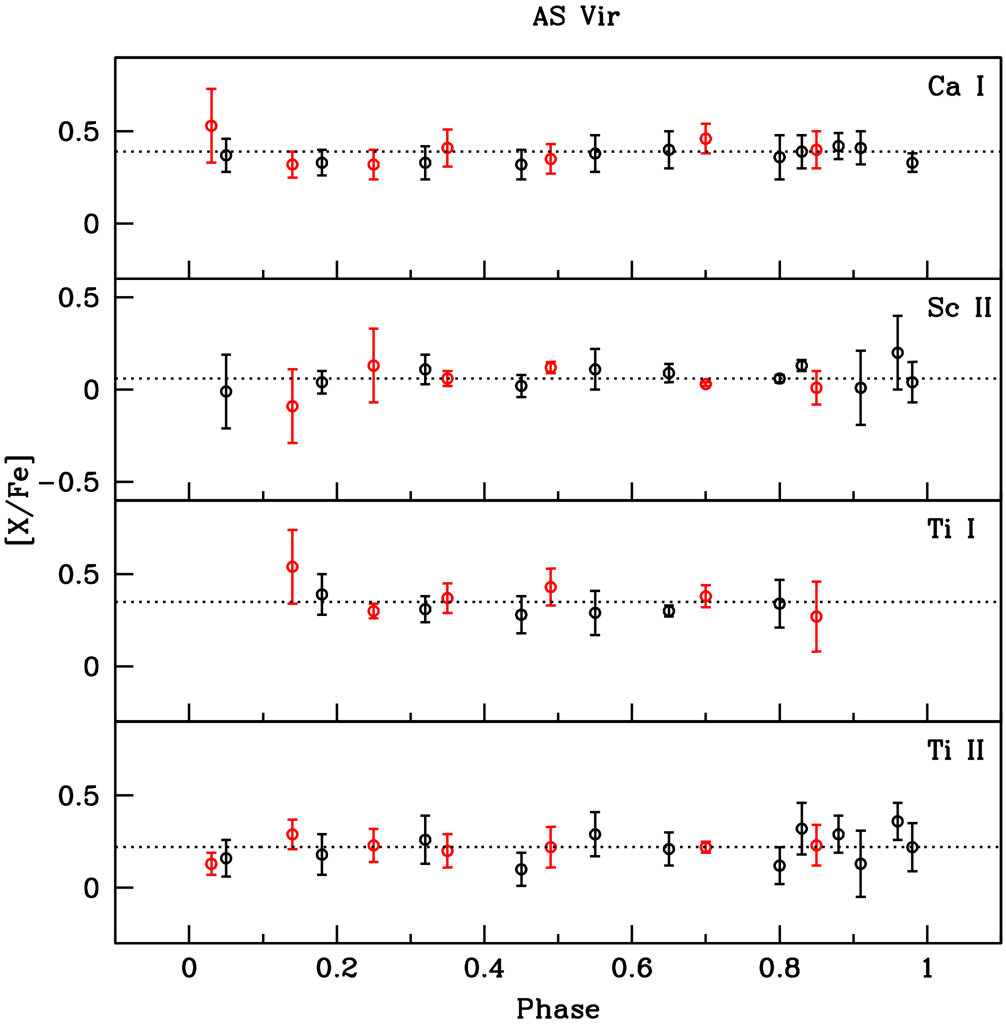

Figure 4.40 Same as Figure 4.39, except for Ca I, Sc II, Ti I and Ti II.

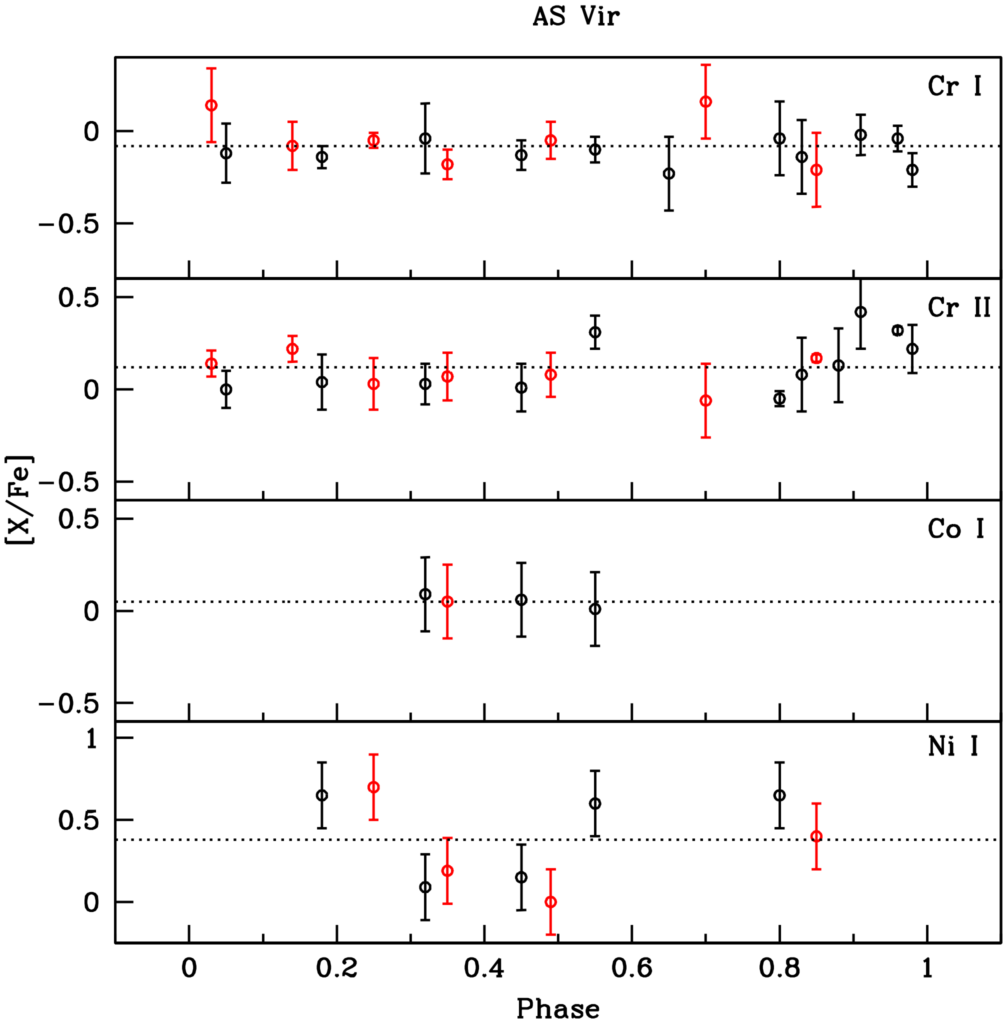

Figure 4.41 Same as Figure 4.39, except for Cr I, Cr II, Co I and Ni I. The large phase-to-phase scatter of [Ni I/Fe] is due to the large uncertainties of the derived values.

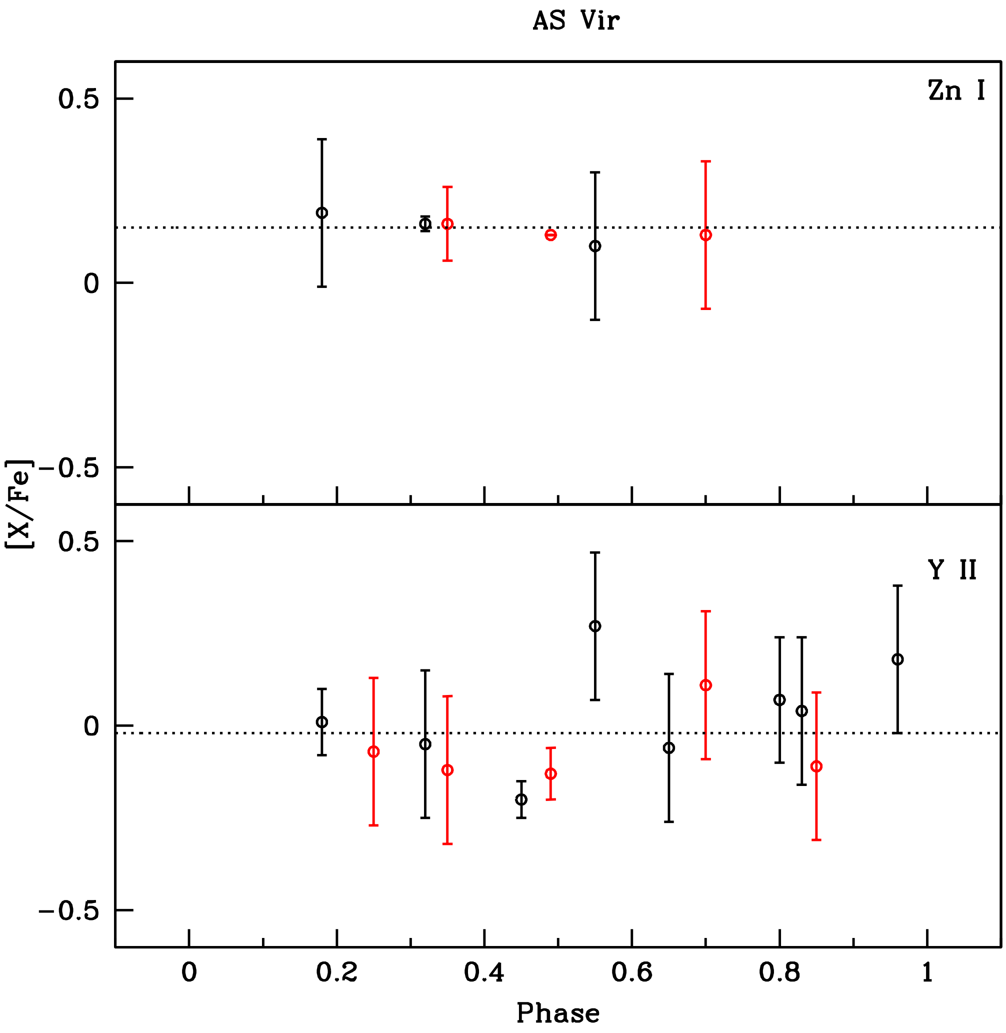

Figure 4.42 Same as Figure 4.39, except for Zn I, Y II.

Table 4.8. Abundance ratios of Na, Mg, Al, Si and Ca throughout the pulsational cycle.

Phase	[Na I/Fe]^{a}	σ	N	[Mg I/Fe]	σ	N	[Al I/Fe]^{a}	σ	N	[Si I/Fe]^{a}	σ	N	[Si II/Fe]^{a}	σ	N	[Ca I/Fe]	σ	N
									CD Vel									
0.015	-0.37^{a}	0.03	2	0.40	0.02	3	0.03^{a}	···	1	···	···	···	0.58^{a}	···	1	0.19	0.09	8
0.045	-0.23^{a}	0.07	2	0.31	0.04	2	0.26^{a}	···	1	···	···	···	0.31^{a}	···	1	0.22	0.10	7
0.150	···	···	···	0.44	0.03	2	0.18^{a}	0.08	2	···	···	···	0.47^{a}	···	1	0.26	0.06	11
0.300	···	···	···	0.41	0.06	2	0.48^{a}	0.22	2	0.66	···	1	···	···	···	0.33	0.10	13
.	.	.	.	.	.	.	.	.	.	.	.	.	.	.	.	.	.	.
.	.	.	.	.	.	.	.	.	.	.	.	.	.	.	.	.	.	.
.	.	.	.	.	.	.	.	.	.	.	.	.	.	.	.	.	.	.

[a] NLTE corrections.

Note. — Table 4.8 is published in its entirety in the electronic edition of the *Astrophysical Journal Supplement Series*. A portion is shown here for guidance regarding its form and content.

Table 4.9. Abundance ratios, [X/Fe], of Sc, Ti, V and Cr throughout the pulsational cycle.

Phase	Sc II	σ	N	Ti I	σ	N	Ti II	σ	N	V II	σ	N	Cr I	σ	N	Cr II	σ	N
CD Vel																		
0.015	0.24	0.10	3	···	···	···	0.41	0.11	10	···	···	···	−0.09	0.12	3	0.21	0.11	3
0.045	0.15	0.01	2	···	···	···	0.31	0.12	13	···	···	···	−0.12	0.13	4	0.16	0.13	6
0.150	0.06	0.05	3	0.30	0.05	3	0.27	0.14	17	0.08	···	1	−0.03	0.11	3	0.05	0.15	7
0.300	0.07	0.04	3	0.29	0.13	4	0.35	0.18	17	0.18	···	1	0.07	0.14	5	0.03	0.13	7
.	.	.	.	.	.	.	.	.	.	.	.	.	.	.	.	.	.	.
.	.	.	.	.	.	.	.	.	.	.	.	.	.	.	.	.	.	.
.	.	.	.	.	.	.	.	.	.	.	.	.	.	.	.	.	.	.

Note. — Table 4.8 will be published in its entirety in the electronic edition of the *Astrophysical Journal Supplement Series*. A portion is shown here for guidance regarding its form and content.

Table 4.10. Abundance ratios, [X/Fe], of Co, Ni, Zn and Y throughout the pulsational cycle.

Phase	Co I	σ	N	Ni I	σ	N	Zn I	σ	N	Y II	σ	N
CD Vel												
0.015	⋯	⋯	⋯	⋯	⋯	⋯	⋯	⋯	⋯	⋯	⋯	⋯
0.045	⋯	⋯	⋯	⋯	⋯	⋯	⋯	⋯	⋯	−0.06	⋯	1
0.150	0.05	⋯	1	⋯	⋯	⋯	⋯	⋯	⋯	0.11	0.14	2
0.300	−0.01	⋯	1	0.70	⋯	1	0.1	0.01	2	−0.18	0.15	2
.	.	.	.	.	.	.	.	.	.	.	.	.
.	.	.	.	.	.	.	.	.	.	.	.	.
.	.	.	.	.	.	.	.	.	.	.	.	.

Note. — Table 4.8 will be published in its entirety in the electronic edition of the *Astrophysical Journal Supplement Series*. A portion is shown here for guidance regarding its form and content.

Table 4.11. Derived abundance ratios, [X/Fe], of Mn, Sr, Zr, Ba, La and Eu via syntheses method.

Star	Phase	Mn I	σ	N	Sr II	σ	N	Zr II	σ	N	Ba II	σ	N	La II	σ	N	Eu II	σ	N
CD Vel	0.30	−0.48	0.15	3	0.57	0.21	2	0.36	0.14	2	0.06	0.17	3	···	···	···	0.25	···	2
WY Ant	0.35	−0.59	···	2	0.54	0.07	2	0.48	0.14	2	0.14	0.24	3	0.26	0.14	2	0.62	···	2
DT Hya	0.32	−0.57	0.14	2	0.72	0.14	2	0.48	···	1	0.36	0.13	4	0.04	0.13	2	0.27	···	1
AS Vir	0.32,0.35	−0.48	0.23	6	0.33	0.33	4	0.31	0.22	5	0.04	0.12	8	0.16	0.20	4	0.51	0.16	3
RV Oct	0.30	−0.34	0.15	4	0.57	0.21	2	0.61	0.12	3	0.06	0.15	4	−0.06	···	1	0.18	···	1
XZ Aps	0.32	−0.58	0.15	3	0.20	···	2	0.72	···	1	0.17	0.15	3	···	···	···	−0.10	···	1
BS Aps	0.30	−0.04	0.15	4	0.52	0.21	2	0.57	0.21	2	0.24	0.21	2	−0.13	···	1	0.17	0.07	2
UV Oct	0.25	−0.53	0.14	2	0.20	···	2	0.28	0.14	2	0.11	0.21	2	0.05	···	2	0.35	···	2
V1645 Sgr	0.25	−0.52	0.07	2	−0.05	···	2	0.22	0.15	3	0.02	0.10	3	0.44	0.14	2	0.51	···	1
Z Mic	0.25	−0.56	0.25	3	0.43	0.07	2	0.20	0.21	2	0.26	0.21	2	0.12	0.07	2	0.37	···	1
TY Gru	0.46	−0.64	···	1	0.04	0.07	2	0.32	···	1	1.05	0.17	3	0.85	0.21	2	···	···	···

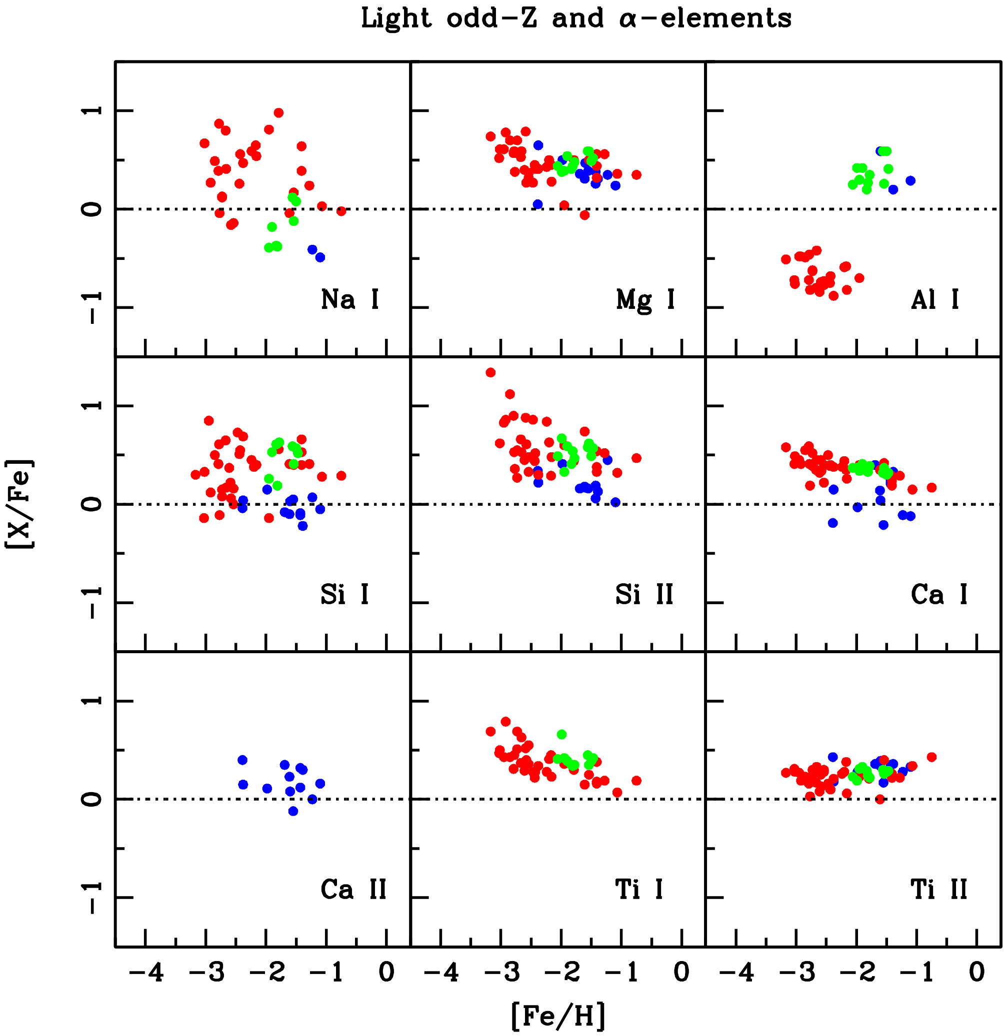

Figure 4.43 Abundance ratios of light odd-Z and α-elements as a function of metallicity. NLTE corrections applied to Na I, Al I, Si I and Si II whenever appropriate. The red and blue dots represent RHB and BHB stars from For & Sneden (2010). The green dots represent the mean abundance ratios of each RR Lyr in our program.

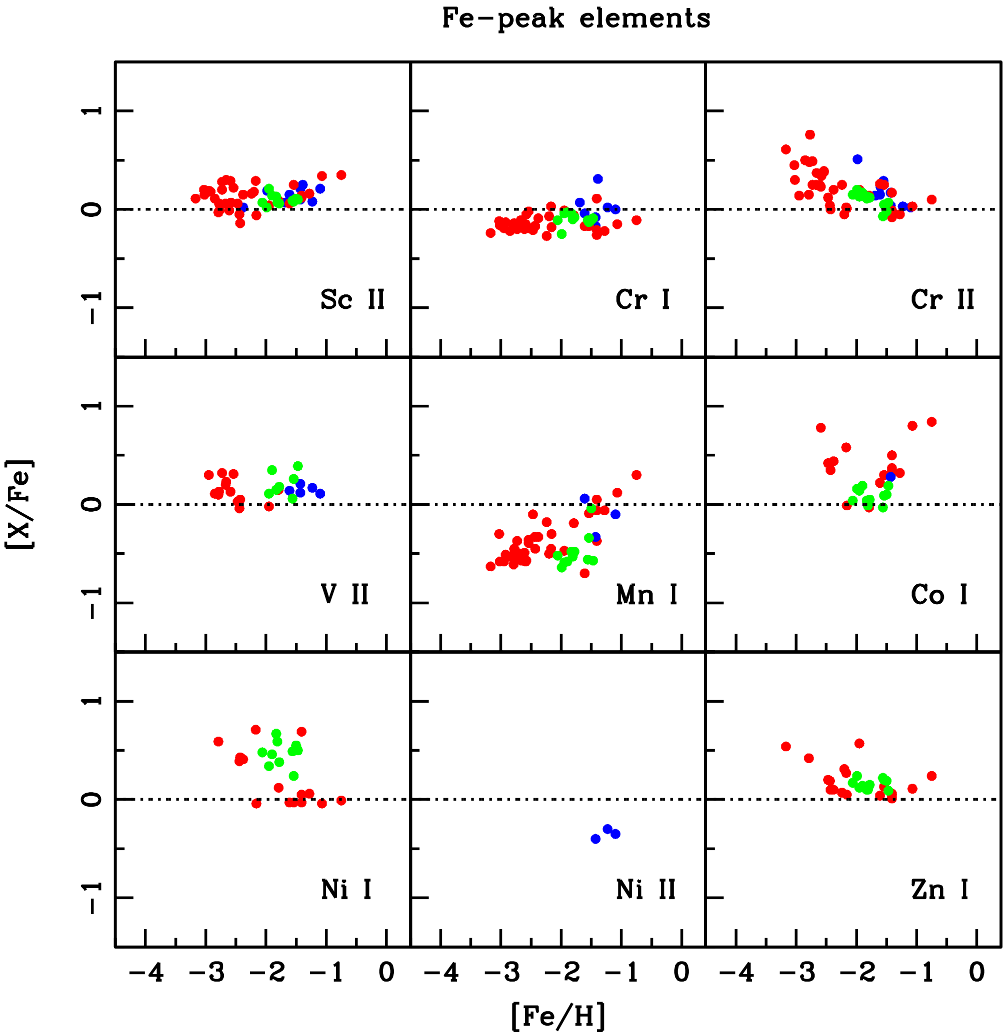

Figure 4.44 Abundance ratios of Fe-peak elements as a function of metallicity. The red and blue dots represent RHB and BHB stars from For & Sneden (2010). The green dots represent the mean abundance ratios of each RR Lyr in our program.

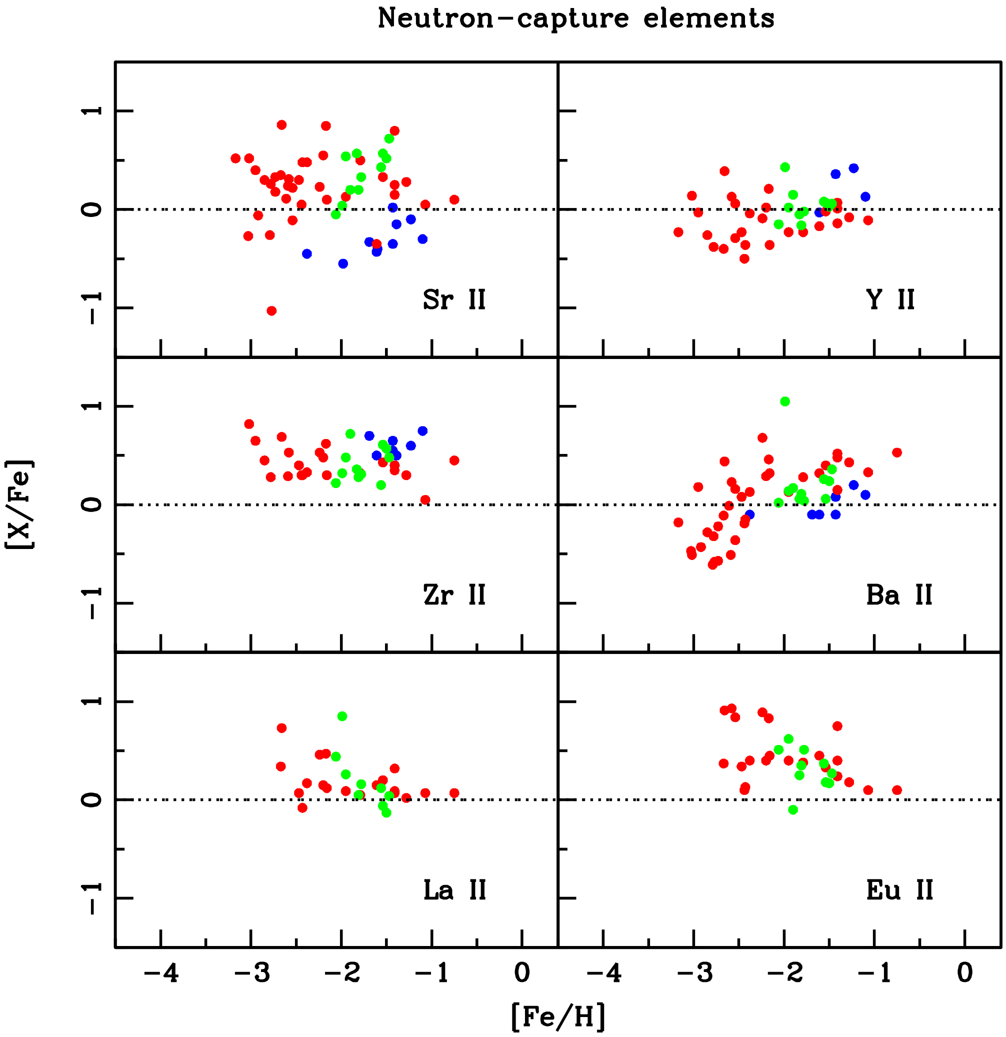

Figure 4.45 Abundance ratios of neutron-capture elements as a function of metallicity. The red and blue dots represent RHB and BHB stars from For & Sneden (2010). The green dots represent the mean abundance ratios of each RR Lyr in our program.

Table 4.12. Mean abundance ratios of various elements.

	CD Vel	WY Ant	DT Hya	AS Vir	RV Oct	XZ Aps	BS Aps	UV Oct	V1645 Sgr	Z Mic	TY Gru
Na I	−0.37	−0.39	...	...	−0.12	−0.18	0.08	−0.38	...	0.12	...
N^{a}	3	3	...	...	9	8	2	9	...	2	...
Mg I	0.41	0.39	0.52	0.48	0.59	0.54	0.49	0.44	0.44	0.59	0.38
N^{a}	16	11	9	19	17	20	18	20	16	14	4
Al I	0.20	0.30	0.41	0.35	0.26	0.42	0.59	0.27	0.25	0.59	0.42
N^{a}	10	9	2	3	2	4	3	12	6	3	1
Si I	0.61	0.26	0.52	0.63	0.41	0.53	0.59	0.19	...	0.59	...
N^{a}	3	6	2	2	14	2	6	10	...	8	...
Si II	0.41	0.33	0.57	0.47	0.62	0.59	0.49	0.54	0.49	0.58	0.67
N^{a}	11	11	6	14	17	14	17	19	11	13	2
Ca I	0.34	0.34	0.32	0.39	0.37	0.41	0.3	0.33	0.37	0.32	0.37
N^{a}	16	11	9	18	17	19	18	20	14	14	3
Ti I	0.35	0.42	0.42	0.35	0.35	0.39	0.39	0.34	0.41	0.45	0.66
N^{a}	11	7	6	12	14	11	12	10	8	14	2
Ti II	0.29	0.31	0.29	0.22	0.26	0.33	0.28	0.24	0.23	0.3	0.19
N^{a}	16	11	8	19	17	20	18	20	16	14	5
Sc II	0.13	0.21	0.1	0.06	0.08	0.14	0.11	0.07	0.07	0.09	0.02
N^{a}	16	11	9	17	17	17	18	20	13	14	5
Cr I	-0.04	-0.04	-0.09	-0.08	-0.13	-0.03	-0.11	-0.1	-0.11	-0.11	-0.25
N^{a}	16	11	9	18	17	19	18	20	15	14	4
Cr II	0.11	0.13	0.07	0.12	0.05	0.17	-0.02	0.13	0.15	-0.07	0.2
N^{a}	16	11	9	18	17	18	18	20	15	13	5
V II	0.15	0.11	0.39	0.18	0.26	0.35	...	...	...	0.06	...
N^{a}	3	4	1	1	2	1	...	...	...	5	...
Mn I	-0.48	-0.59	-0.57	-0.48$^{\mathrm{c}}$	-0.34	-0.58	-0.04	-0.53	-0.52	-0.56	-0.64
N^{b}	3	2	2	6$^{\mathrm{d}}$	4	3	4	2	2	3	1
Co I	0.04	0.14	0.19	0.05	0.09	0.19	0.1	-0.01	0.04	-0.03	0.16
N^{a}	6	4	1	4	4	3	9	3	3	2	1
Ni I	0.67	0.34	0.5	0.38	0.24	0.46	0.55	0.59	0.48	0.49	...
N^{a}	3	6	4	9	9	4	4	6	2	10	...
Zn I	0.1	0.12	0.09	0.15	0.2	0.14	0.19	0.1	0.17	0.22	0.24
N^{a}	4	6	3	6	10	4	9	6	1	12	1
Sr II	0.57	0.54	0.72	0.33$^{\mathrm{c}}$	0.57	0.2	0.52	0.2	-0.05	0.43	0.04
N^{b}	2	2	2	4$^{\mathrm{d}}$	2	2	2	2	2	2	2

Table 4.12 (cont'd)

	CD Vel	WY Ant	DT Hya	AS Vir	RV Oct	XZ Aps	BS Aps	UV Oct	V1645 Sgr	Z Mic	TY Gru
Y II	-0.05	0.02	0.06	-0.02[c]	0.07	0.15	0.03	-0.16	-0.15	0.08	0.43
N[b]	12	8	8	13[d]	15	13	15	11	3	12	2
Zr II	0.36	0.48	0.48	0.31[c]	0.61	0.72	0.57	0.28	0.22	0.2	0.32
N[b]	2	2	1	5[d]	3	1	2	2	3	2	1
Ba II	0.06	0.14	0.36	0.04[c]	0.06	0.17	0.24	0.11	0.02	0.26	1.05
N[b]	3	3	4	8[d]	4	3	2	2	3	2	3
La II	···	0.26	0.04	0.16[c]	-0.06	···	-0.13	0.05	0.44	0.12	0.85
N[b]	···	2	2	4[d]	1	···	1	2	2	2	2
Eu II	0.25	0.62	0.27	0.51[c]	0.18	-0.1	0.17	0.35	0.51	0.37	···
N[b]	2	2	1	3[d]	1	1	2	2	1	1	···
[Fe I/H]	-1.83	-1.95	-1.47	-1.78	-1.54	-1.9	-1.5	-1.81	-2.06	-1.56	-1.99
N[a]	16	11	9	19	17	20	15	20	16	14	5
[Fe II/H]	-1.83	-1.96	-1.47	-1.78	-1.54	-1.91	-1.5	-1.81	-2.06	-1.56	-1.99
N[a]	16	11	9	19	17	20	15	20	16	14	5

[a] Total number of phases for averaging.

[b] Total number of lines for averaging.

[c] Averaged with two phases.

[c] Total number of lines in two phases.

4.8.1 The Alpha Elements: Magnesium, Calcium and Titanium

The scatter of our derived light α-elements abundances is small for our RR-ab stars over the metallicities (see Figure 4.43). We calculated <[Mg I/Fe]> $\simeq$+0.48 for RR-ab stars, which is consistent with the typical α-enhancement in field metal-poor stars within that metallicity range.

An offset of [Ca I/Fe] between RHB and BHB stars, $\sim$ 0.3 dex, was reported by For & Sneden (2010). Our derived [Ca I/Fe] values are consistent throughout the cycles as shown in both Blazhko and non-Blazhko stars (see Figures 4.36 and 4.40). Thus, the cause of such offset is still unknown considered that we have [Ca I/Fe] values of RR-ab stars that cover all phases in most cases, including an overlap with the coolest $T_{\rm eff}$ range of some BHB stars ($\sim$ 7400 K). Unfortunately, we could not perform synthesis for Ca II 3933Å K-line in our RR-ab stars to further investigate this issue because the phases with similar $T_{\rm eff}$ as BHB stars have spectra with line distortion problem. In addition, this line is is extremely strong in optimal phase of RR-ab stars, which is not suitable for synthesis. We also note that the reported trend of decreasing [Ca/Fe] with increasing $T_{\rm eff}$ for BHB stars as shown in Figure 11 of For & Sneden (2010) is not detected in this study.

There are no Ti I lines detectable in the hottest phases of RR-ab stars, i.e., during those early and late phases of a cycle when $T_{\rm eff}$ overlap with the coolest $T_{\rm eff}$ of the sample BHB stars ($T_{\rm eff}$$\sim$7400). Thus, the <[Ti I/Fe]> values showing here assemble similar $T_{\rm eff}$ range as RHB stars. The overall trend of [Ti II] exhibits differently than those of the other α-elements, in which they do not decline as the metallicity increases. However, if we only consider abundances of Ti I and Ti II derived for RR-ab stars, we find both exhibits a rather flat distribution with a relatively small scatter in this metallicity range (excluding the large deviate [Ti I/Fe] of TY Gru). Investigation of larger sample of RR-ab stars that covers larger metallitiicy range might further justify if the flat distribution of [Ti II/Fe] is actually real. We note that there is a small offset, ~ 0.15 dex, between the mean abudances of Ti I and Ti II in RR-ab stars. The cause is unknown because both mean titanium-based abundances were calculated with large number of phases for each RR-ab star. We also find no trend of [Ti I/Fe] with increasing $T_{\rm eff}$ (see e.g., Figure 4.40 of AS Vir) in contrast to the previous conclusion of For & Sneden (2010) and findings by others (see Lai et al. 2008 and references therein).

4.8.2 The Alpha Element Silicon: Revisiting A Special Case

It has been shown that there is a significant dependence of [Si I/Fe] with temperature in metal-poor field stars in previous studies (see Cayrel et al. 2004, Cohen et al. 2004, Preston et al. 2006a, Sneden & Lawler 2008, and Lai et al. 2008). The effect seems to solely depends on $T_{\rm eff}$ but not with log g. To investigate this issue, Shi et al. (2009) performed an analysis of NLTE effects in warm metal-poor stars ($T_{\rm eff} \geq 6000$ K). They concluded that the NLTE effects differ from line-to-line and are substantially larger in the blue-spectral region (e.g., 3905Å line) than the red-spectral region (e.g., 5690Å and 6155Å lines) of Si I. Departure from NLTE in warm metal-poor stars is also expected for Si II 6347Å and 6371Å lines.

We revisit the issue of $T_{\rm eff}$ dependent with our RR-ab stars because derivation of silicon abundances over a large effective temperature range can be achieved. The [Si I/Fe] values were derived either solely from 3905Å line or lines in red-spectral region throughout the cycle. The selection of lines depends on the $T_{\rm eff}$. To avoid possible blending of 3905Å line with a weak CH transition Cohen et al. (2004), which presence in cool stars, we only employed 3905Å line during the early or late phases of a pulsational cycle when $T_{\rm eff}$ is similar to the BHB stars ($T_{\rm eff} \geq 7400$ K).

As shown in Figure 4.36, the trend of [Si II/Fe] resembles a similar "shape" as the $T_{\rm eff}$ vs phase plot in Figure 4.21, which suggests a dependence of $T_{\rm eff}$. It is less obvious in the case of [Si I/Fe] between phase 0–0.8 for RV Oct. However, we detect a significant declining trend as the $T_{\rm eff}$ increases after ∼phase 0.8 (see Figure 4.35). To investigate if NLTE effects could be the cause of such trend, we applied the suggested NLTE corrections of +0.1 dex and −0.1 dex by Shi et al. (2009) to the Si I and Si II abundances derived from 3905Å, 6347Å and 6371Å lines. In Figures 4.46 and 4.47, we extend For & Sneden's Figures 14 and 15 by adding all measured [Si I/Fe] and [Si II/Fe] values that had been corrected for NLTE effects, whenever appropriate. While the scatter of [Si I/Fe] is large, we find a possible declining trend with increasing $T_{\rm eff}$ if the two outliers (in box) are ignored. On the contrary, the [Si II/Fe] values show possible inclining trend with increasing $T_{\rm eff}$. However, we caution the reader that most [Si II/Fe] values were derived with 1–2 lines, which large uncertainties are expected.

To further investigate the NLTE effects on the trends, we present the silicon abundances as a function of phase for RV Oct and WY Ant in Figure 4.48, where the blue and red dots represent lines in the blue and red spectral regions, respectively. To emphasize, all values of [Si II/Fe] and only the blue dots of [Si I] have been corrected for NLTE effects. We find that the NLTE corrections do not resolve the puzzle of $T_{\rm eff}$ dependency in silicon abundances. In fact, lower [Si I/Fe] values (as seen in the obvious case of WY Ant) were yielded by the use of 3905Å line in warm metal-poor RR-ab stars suggest a possible different cause of such trend than the NLTE affects. A discussion about the line transitions of blue and red spectral lines of Si I is given in Sneden & Lawler (2008). The resolution of this issue is unsatisfactory and beyond the scope of this study.

The overall silicon abundances of RR-ab stars exhibit a large star-to-star scatter, which is similar to the results of RHB and BHB stars (see Figure 4.43). The <[Si I/Fe]>≈+0.48 dex and <[Si II/Fe]>≈+0.52 dex are consistent with the mean of typical α-enhancement in metal-poor stars.

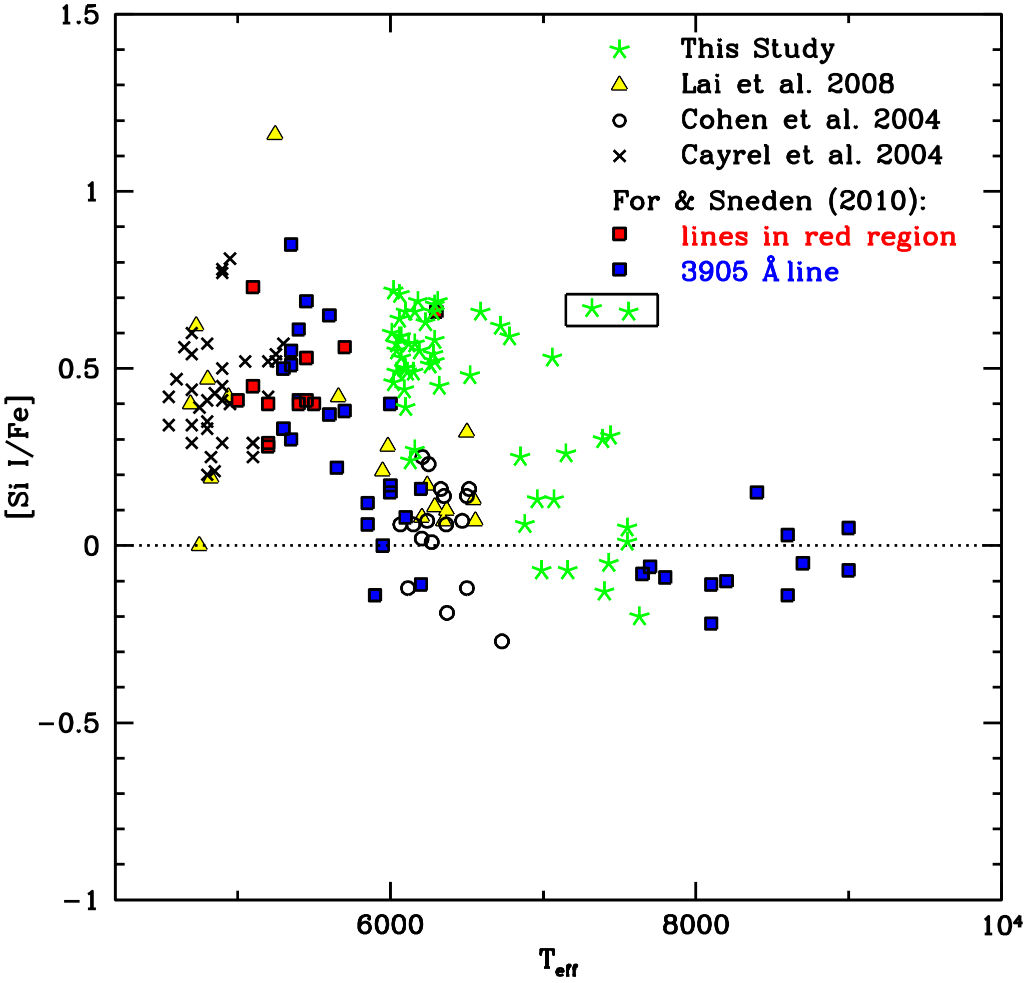

Figure 4.46 Abundance ratios of [Si I/Fe] of all our program stars in all phases (green stars) vs. spectroscopic $T_{\rm eff}$, with additional data from Cayrel et al. (2004) (crosses), Cohen et al. (2004) (open circles), Lai et al. (2008) (yellow triangles), and For & Sneden (2010) (blue and red squares). The box marks the two outliers. NLTE correction applied to [Si I/Fe] whenever appropriate.

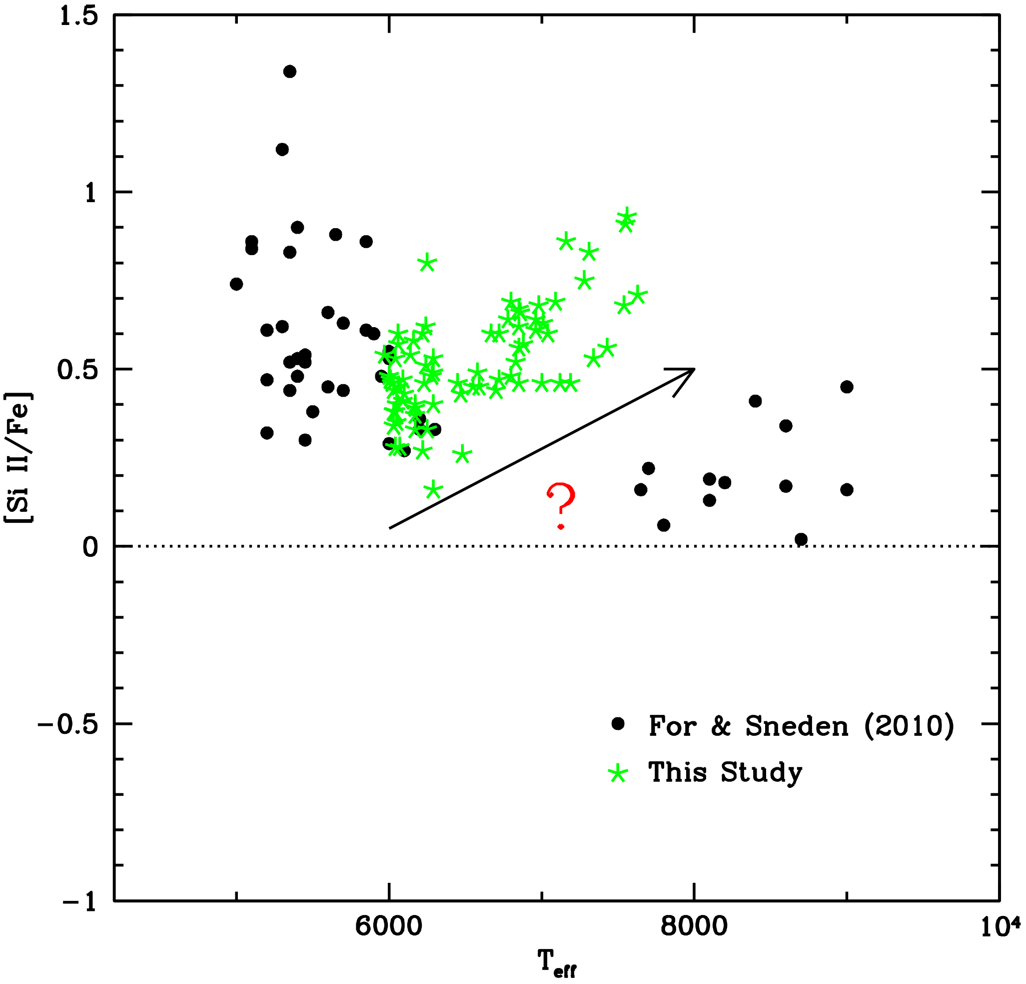

Figure 4.47 Abundance ratios of [Si II/Fe] of all our program stars in all phases (green stars) vs. spectroscopic $T_{\rm eff}$. NLTE correction applied to [Si II/Fe] whenever appropriate. The black dots and green stars represent values in For & Sneden (2010) and this study, respectively. The ambigious trend of increasing [Si II/Fe] as a function of $T_{\rm eff}$ is discussed in §7.2.

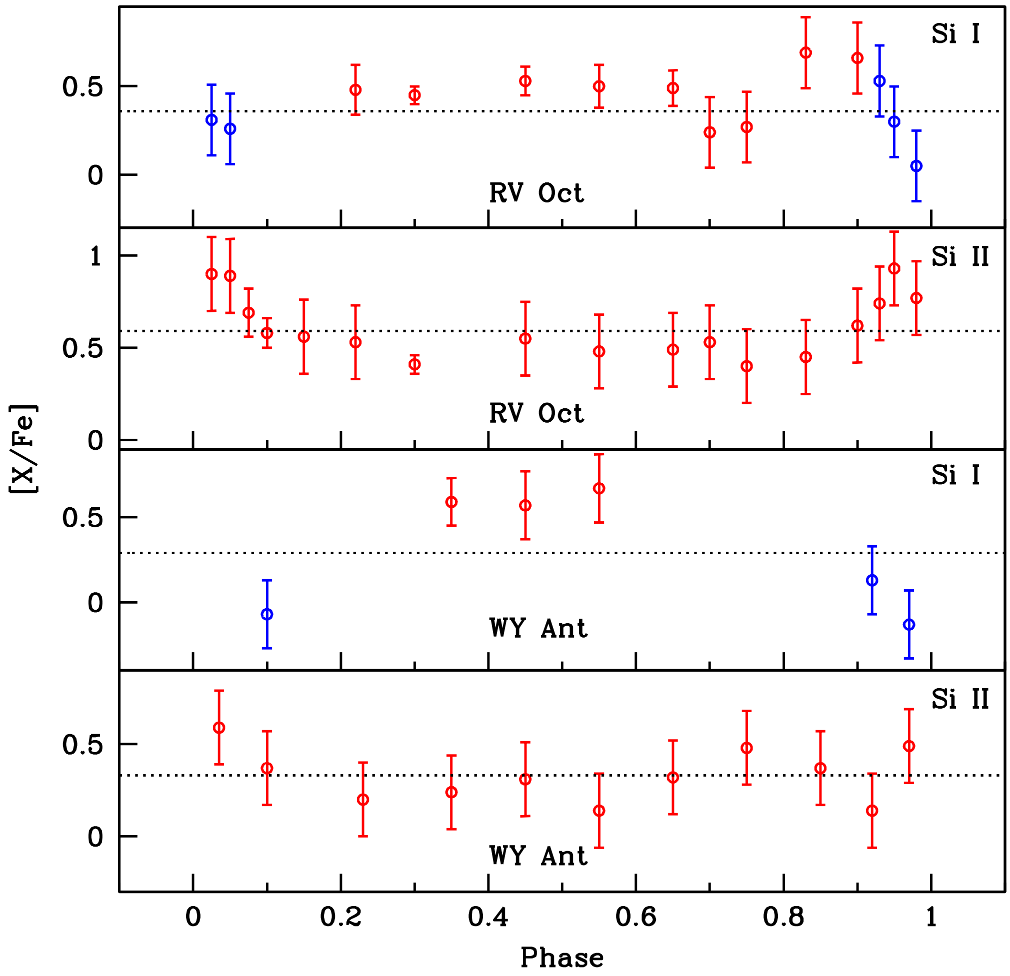

Figure 4.48 Silicon abundance ratios as a function of phase for RV Oct (first and second panels) and WY Ant (third and forth panels). The blue and red open circles represent lines used to derive the abundances in blue and red spectral regions, respectively. Only the blue open circles have been corrected for NLTE effects.

4.8.3 Light Odd-Z Elements Sodium and Aluminum

For sodium abundances, we used the Na I resonance D-lines (5889.9 Å, 5895.9 Å) and higher excitation Na I lines (the 5682.6 Å, 5688.2 Å and the 6154.2 Å, 6160.7Å doublets) whenever available. The resonance D-lines are generally detected and not saturated in the spectra of early and late phases of RR-ab pulsational cycle. The mid phases possess similar T_{eff} range as RHB stars, as such albeit weak higher excitation Na I lines are detected and used in these phases. There are only two Al II lines, 3944 Å and 3961 Å available for this study.

It has been known that Na D-lines and the Al I blue resonance spectral region can be significantly affected by NLTE effects (see e.g., Baumueller et al. 1998; Baumueller & Gehren 1997). The NLTE corrections are particularly important for warm, metal-poor stars because the statistical equilibrium is dominated by collisions. We applied the suggested NLTE corrections of −0.5 dex (Baumueller et al. 1998) and +0.65 dex (Baumueller & Gehren 1997) for Na and Al abundances derived from those lines, respectively. We warn the reader that these corrections can be different from different studies. For example, recent NLTE calculations by Andrievsky et al. (2007) estimate a correction of ~ -0.15 dex for Na D-lines. An estimation of +0.7 dex for Al blue-resonance lines (Andrievsky et al. 2008).

Considering only the derived [Na I/Fe] and [Al I/Fe] values of RR-ab stars, the mean abundances are −0.18 dex and 0.37 dex, respectively (see Figure 4.43). Sodium abundances show a large star-to-star scatter with a dispersion of 0.2 dex. Alunimum abundances of RR-ab stars are overabundant, similar to those derived for BHB stars. We warn the reader that we did not have many Na and Al measurements throughout the cycle. If any, there were generally derived with 1–2 lines. We find no trend of Al abundances with $T_{\rm eff}$. As such, we do not have an explanation for the discrepancy of [Al I/Fe] between RHB and BHB/RR-ab stars.

4.8.4 The iron-peak elements: Scandium through Zinc

As noted by Prochaska & McWilliam (2000), scandium lines can be affected by hypefine substructure. However, the test performed in For & Sneden (2010) has shown that the effect is small. Thus, we proceeded using the same method as decribed in For & Sneden (2010), i.e., EW method, to derive Sc II abundances. Both [Sc II/Fe] and [V II/Fe] values are roughly solar with <[Sc II/Fe]>$\simeq$+0.1 dex and <[V II/Fe]>$\simeq$+0.2 dex for RR-ab stars (see Figure 4.44). They are also in accord with the results derived for RHB and BHB stars. We note that there are not many detectable V II lines available for analysis throughout the cycle. We also find no trends of [Sc II/Fe] and [V II/Fe] with either [Fe/H] or $T_{\rm eff}$.

The derived [Cr I/Fe] and [Cr II/Fe] values show similar discrepancy as found by other metal-poor stars studies (see Sobeck et al. 2007, and references therein). The [Cr I/Fe] values are $\simeq -0.2$ dex lower than the [Cr II/Fe] values (see Figure 4.44) for RR-ab stars. This issue was re-examined by Sobeck et al. (2007) using recent derived Cr I transition probabilities on solar abundance. They found that the [Cr I/Fe] value was 0.15–0.20 dex lower than the [Cr II/Fe], which suggested that the problem was not due to the NLTE effects. As shown in Figure 4.37, our chronium abundances are consistent throughout the cycle. It supports the finding of Sobeck et al. (2007) but different than the the conclusion made in For & Sneden (2010), which a trend of increasing [Cr I/Fe] as increasing $T_{\rm eff} < 7000$ K was found for RHB stars.

Manganese abundances show a large star-to-star scatter with a dispersion of 0.17 dex for our RR-ab star (see Figure 4.44). In general, only 1–3 lines were employed for synthesis. The [Mn I] values presented here are not an average value throughout the cycle but the abundance of a single phase (optimal phase). The overall manganese abundances trend of increasing [Mn I/Fe] with at higher [Fe/H] metallicities is in accord with previous studies (see Sobeck et al. 2006, Lai et al. 2008, and reference therein).

The derived [Co I/Fe] values for RR-ab stars have smaller star-to-star scatter ($\sigma \simeq 0.08$) as compared to those derived for RHB stars ($\sigma \simeq 0.26$) (see Figure 4.44). This is due to the fact that many [Co I/Fe] values have been derived throughout the cycle and used to give the average [Co I/Fe] for each star presented in Figure 4.44. Similar conclusion is also drawn for [Ni I/Fe]. The <[Ni I/Fe]>≃+0.47 dex for RR-ab stars suggest an enchancement. However, we warn the reader that abundances of Co I and Ni I of each phase were determined with only 1–2 lines and show large phase-to-phase scatter, in particularly for [Ni I/Fe] (see Figure 4.38 and 4.41). Interpretation of these abundances should be treated with caution. The determination of Ni II abundances was not possible due to the distorted 4067 Å line, which is only detectable in early and late phases of a pulsational cycle.

The dispersion of [Zn I/Fe] is small and with <[Zn I/Fe]>≃+0.16 dex for RR-ab stars (see Figure 4.44). The enchancement of Zn abundances toward the low metallicity range as seen in the RHB stars is inconclusive. A larger sample of RR-ab stars in [Fe/H]< -2.0 regime might help to resolve this puzzle.

4.8.5 The neutron capture elements: Strontium, Yttrium, Zirconium, Barium, Lanthanum and Europium

We were able to derive abundances of light *n*-capture elements (Sr, Y and Zr) and heavy *n*-capture elements (Ba, La and Eu) in most of our RR-ab stars. The derived abundances of these elements show large star-to-star scatter with respect to iron (see Figure 4.45).

Strontium abundances were derived using available Sr II 4077 Å, 4161 Å and 4215 Å lines. These lines are generally strong and/or blended in cool stars. A large dispersion of 0.25 dex is shown for RR-ab stars and such variations are intrinsic to the stars (For & Sneden 2010). The overall [Sr II/Fe] distribution is similar to those of RHB stars, which does not aid in explaning the presence of Sr abundances offset between RHB and BHB stars

Equivalent width analysis and synthesis were performed to obtain Yttrium and Zirconium abundances, respectively. Both [Y II/Fe] and [Zr II/Fe] exhibit a large star-to-star scatter with dispersions $\simeq$ 0.17 dex. Zirconium abundances are overabundant as compared to other light *n*-capture elements, i.e., Sr and Y. We note that the Zr II lines are generally very weak, and there are not many phases per star have detected Zr lines. Hence, the reader should be caution with the interpretation of Zr abundances.

Barium lines are affected by both hyperfine substructure and isotopic splitting (see a line list given by McWilliam 1998). The solar abundance ratio distribution among the $^{134--138}$Ba isotopes (Lodders 2003) was adopted for synthesizing the Ba II 4554 Å, 5853 Å, 6141 Å, and 6496 Å lines, whenever present in the spectra. We note that the 4554 Å line is always substantially stronger than the other lines, and Ba abundances derived from this line can also be larger due to severely affected by microturbulence and damping. Synthesis were performed on La II 4086 Å and 4123 Å lines, and Eu II 4129Å and 4205 Å lines, whenever present in the spectra. These lines are very weak and only 1–2 lines are available for analysis. The overall barium, lanthum and europium abundances for RR-ab stars are in accord to those derived for RHB and BHB stars in the same metallicity range.

4.9 Evolutionary State

4.9.1 $T_{\rm eff} - \log g$ Plane

We compared the physical properties of our RR-ab stars with the RR Lyr samples of Lambert et al. (1996) and Clementini et al. (1995). In Figure 4.49, we extend Figure 19 of For & Sneden (2010) by adding the derived spectroscopic $T_{\rm eff}$ and log g values of two of our RR-ab stars, CD Vel and WY Ant, on the $T_{\rm eff}$-log g plane. The $T_{\rm eff}$ and log g values of field RR Lyr samples of Lambert et al. (1996) are based on spectroscopic derivation and photometric $T_{\rm eff}$ and Baade-Wesselink log g for Clementini et al. (1995) study. We show that our log g values derived from spectroscopic ionization balance are generally lower than the Baade-Wesselink method. However, they follow the general physical $T_{\rm eff}$ and log g change with the RHB and BHB population across the $T_{\rm eff}$-log g plane.

In Figure 4.50, we enlarge Figure 4.49 near the RR Lyr instability strip region and overlaid on α-enhanced HB tracks of [M/H]$= -1.79$, $Z = 0.0003$ and $Y = 0.245$ in different model masses. These HB tracks are adopted from Pietrinferni et al. (2006), which have been implemented with low T-opacities of Ferguson et al. (2005) and an α-enhanced distribution that represents typical Galatic halo and bulge stars. We employed Eq. 4 to convert the bolometric luminosities in the model to log g values. It shows a large star-to-star scatter for Lambert et al's samples and our RR Lyrs follow the general trend of a single mass evolutionary track (within log g uncertainties) except near 7000–7500 K region. The scatter in this $T_{\rm eff}$ range is due to the fast moving and complex nature of RR Lyr atmosphere during the rising and descending branch of the cycle.

4.10 Summary and Conclusion

We present the first detailed chemical abundances study of field variable horizontal branch RR Lyrae stars throughout the pulsational cycles. The high resolution spectra were obtained with the du Pont 2.5-m telescope at the Las Campanas Observatory. The samples were selected based on the study of Preston (2011). A new, indirect method to estimate initial $T_{\rm eff}$ values for the analysis was developed. The estimated initial $T_{\rm eff}$ values work reasonably well for both Blazhko and non-Blazhko effect stars.

We derived the model stellar atmospheric parameters, $T_{\rm eff}$, log g, [M/H] and $v_{\rm t}$ for all our program stars throughout the pulsational cycles based on the spectroscopic constraints. Variations of microturbulence as a function of $T_{\rm eff}$ and phase were found. We show that the correlation and anti-correlation with a transition near 6500 K on the $v_{\rm t}$-$T_{\rm eff}$ plane. We also show for the first time observationally that the variation of $v_{\rm t}$ as a function of phase is similar to the theoretical $v_{\rm t}$ and kinetic energy calculations of Fokin et al. (1999b) and Kolenberg et al. (2010), respectively.

Employing the derived model stellar atmospheric parameters, we derived elemental abundance ratios, [X/Fe], of the α-elements, light odd-Z elements, Fe-peak elements, and n-capture elements. The elemental abundance ratios show consistency throughout the pulsational cycles for both Blazhko and

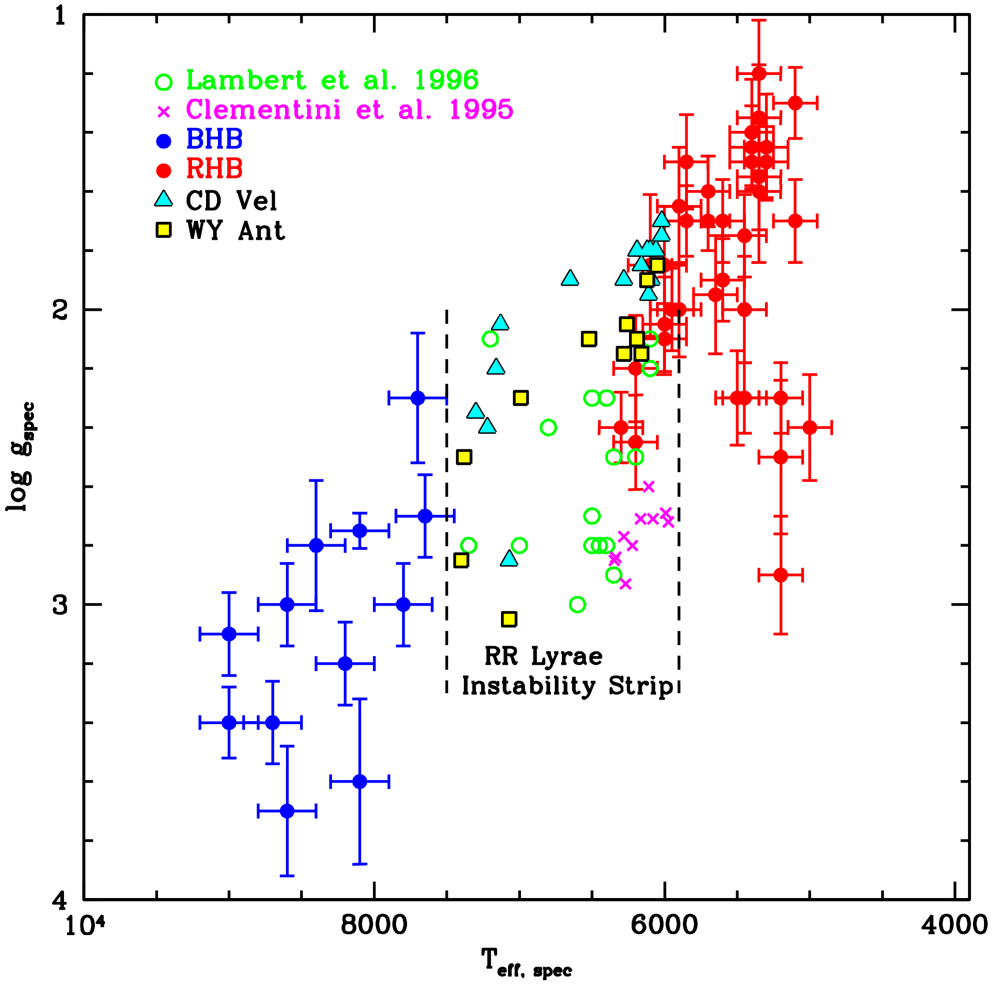

Figure 4.49 Spectroscopic $T_{\rm eff}$ and log g of CD Vel and WY Ant, with additional data from For & Sneden (2010) (RHB: red dots; BHB: blue dots), Lambert et al. (1996) (green open circles) and Clementini et al. (1995) (magenta crosses) on the $T_{\rm eff}$-log g plane.

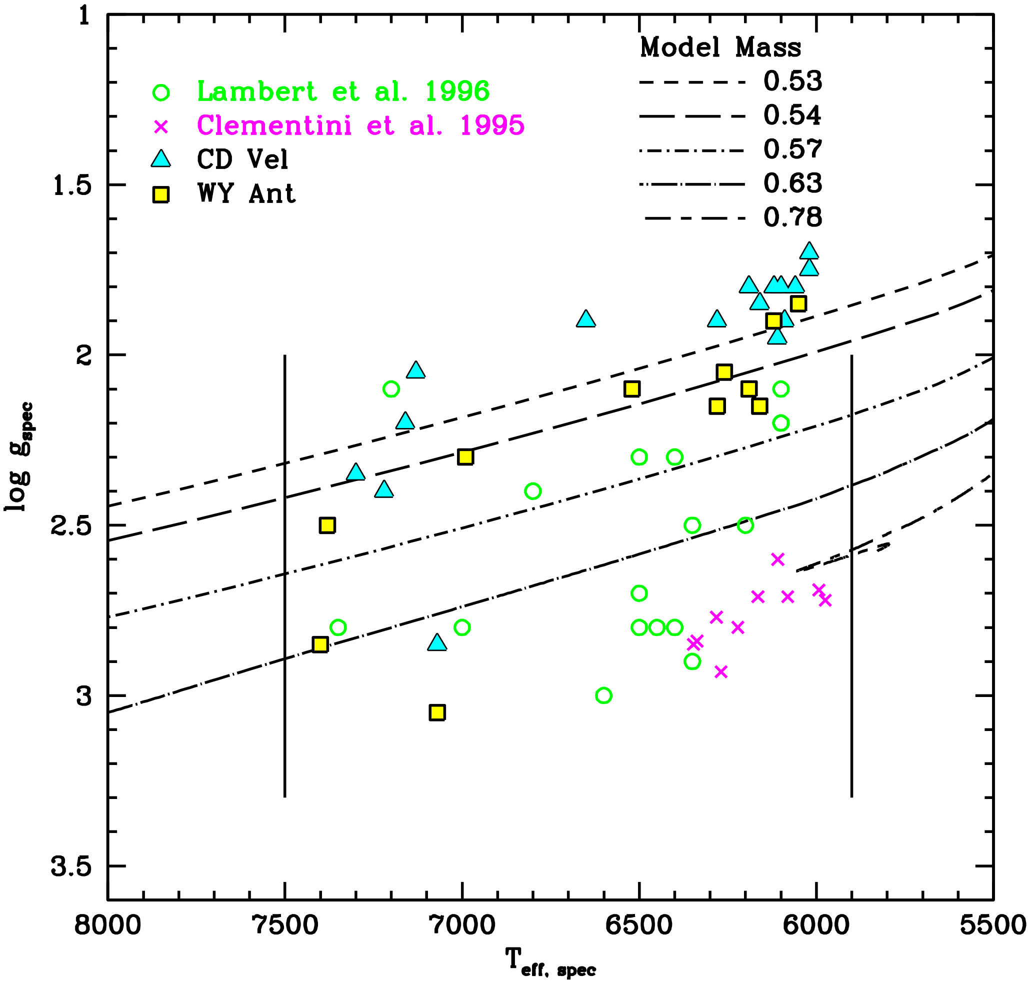

Figure 4.50 An enlarged version of Figure 4.49 near instability strip region with an overlaid of α-enhanced HB tracks of [M/H] = -1.79, $Z = 0.0003$, $Y = 0.245$.

non-Blazhko effect stars. The mean abundance ratios vs metallicity of our program stars are also generally in accord with the RHB and BHB stars. We did not obtain satisfactory solution for the known trend of Silicon abundances as a function of $T_{\rm eff}$ with our RR Lyr stars.

Finally, we investigated the physical properties of our RR Lyr stars by comparing them with those presented in Lambert et al. (1996) and Clementini et al. (1995) onto the $T_{\rm eff}$-log g plane. A large star-to-star scatter on the $T_{\rm eff}$-log g plane was found for Lambert et al's sample in contrast to our RR Lyr, which follow the general trend of a single mass evolutionary track. The Clementini et al's sample possess lower log g values which correlate with the use of BW method.

Chapter 5

Medium-resolution Survey: The Identification of Field Horizontal Branch Stars and Other A-Type Stars

5.1 Introduction

Field horizontal branch (FHB) stars play an important role in studying the early formation and evolution of our Milky Way. They are generally used as a tracer for the kinematic properties of the stellar component and population. Many surveys have led to studies of these aspects, for example, the HK objective-prism survey (Beers et al. 1988) that observed $\sim 10,000$ FHB candidates in the northern and southern hemisphere; the Hamburg/ESO survey (Reimers & Wisotzki 1997) that went deeper than the HK survey, and the recent Sloan Digitized Sky Survey that has identified even more FHB stars. While these surveys provide a large number of FHB candidates, the actual classification can be difficult and uncertain due to their color similarity with the high-gravity main-sequence A-type stars.

The idea of using stellar rotation for classification has been proposed by Peterson (1983) and Green & Morrison (1993). However, this method requires high-resolution and high signal-to-noise spectra that are only feasible with the brightest of these stars for observations with moderate-size telescopes. To explore a different method, Wilhelm et al. (1999) made use of the spectra taken by the HK survey and employed a method based on the combination of broadband photometry and medium-resolution spectra. A grid of spectral line profiles and broadband UBV colors was constructed. Then, the stellar parameters were determined iteratively until the created synthetic spectrum matched the observed one. This method has proved to be quite successful in separating the FHB and main-sequence A-type stars.

The aim of this work is to identify a large sample of bright FHB stars for a follow up high-resolution spectroscopic study. It is a work in conjuction with the chemical abundances study of RHB and BHB stars as described in chapter 2. In this survey, we plan to employ similar techniques as described by Wilhelm et al. (1999) on a large sample of potential FHB candidates ($V < 10$ mag) that are selected from the *Hipparcos* catalog. The magnitude limit is brighter than that of the HK survey, which makes high-resolution follow-up observations feasible to be carried out with the medium-size 2.7-m telescope at the McDonald Observatory or any other 3-m class telescope. In this chapter, we describe the target selection criteria in §5.2 and observations and data reduction in §5.3.

5.2 Target Selection

The potential FHB candidates were selected from the *Hipparcos* catalog[1] based on the following selection criteria:

- color index of $-0.1 < B - V < +0.8$ mag, which corresponds to A0–G9 spectral type;
- absolute magnitude of $-1.0 < M_{\mathrm{V}} < +3.2$ mag;

---

[1] http://heasarc.gsfc.nasa.gov/cgi-bin/W3Browse/w3browse.pl

- and parallax error less than 3 times the parallax (π).

The *Hipparcos* catalog does not provide absolute magnitudes directly but they can be easily calculated with the distance module equation using V and π information,

$$M_{\rm V} = V + 5 - 5\log\left(\frac{1}{\pi}\right). \tag{5.1}$$

The lower limit of $B-V$ for BHB stars corresponds to HB stars with $T_{\rm eff}<$ 10,500 K, in which abundances are known to be affected by gravitational settling above this $T_{\rm eff}$ (see e.g., Behr 2003a). This limit is also set to be consistent with our selection criterion for the study of chemical compositions in HB stars (see chapter 2). The upper limit of $B-V$ for RHB stars is based on a study by Preston & Sneden (2000b). We adopted the $T_{\rm eff}$–color transformation of Reed (1998).

Using the above selection criteria, we retrieved more than 8000 stars that include RHB, BHB and RR Lyrae stars. While these stars are bright and the spectra can be obtained with relatively short exposure time, there are still too many stars for a reasonable telescope time request. Thus, we select ∼300 stars randomly from this compilation for the observations.

5.3 Observations and Data Reduction

The observations were made with the McDonald observatory's 2.1 m Otto Struve telescope in three observing seasons to maximize the hour angle coverage. We used the Cassegrain spectrometer (es2) with the 1200 mm^{-1} grating and a 1.6$''$ slit to obtain spectra with a resolving power of $R \equiv \lambda/\Delta\lambda \sim 2,600$. The spectrograph was tilted to an angle covering the spectral features of the CaII K line, and the Balmer Hδ, Hϵ absorption lines. The spectrum of an

Argon comparison lamp was taken immediately after each stellar exposure(s) for wavelength calibration. We performed tests of collimator focus and check tilt angle with the solar spectrum before each night of observing. These were non-trivial tasks as we found that the spectrograph was mechanically unstable. The projected lines of the observed solar spectrum were shifted spatially from day-to-day. In addition, we also could not reproduce the result of the best collimator focus after it had been determined from the focus test. The spectrograph also seemed to suffer severe internal reflection that projected onto the CCD when exposing on a bright star. In any case, we were able to obtain ~ 300 spectra thoughout the seasons before the observatory decommissioned the spectrograph in early 2010. We also observed 2 known RHB stars and 1 BHB star for the analysis.

The spectra were bias-subtracted, flat-fielded, background-subtracted, wavelength-calibrated and extracted using IRAF. We show examples of the reduced spectra in Figure 5.1, in which the spectra of FHB candidates (HIP 75163 and HIP 67447) are compared to known RHB star (BD+09° 3223) and BHB star (HD 167105). Basic information for our observed stars is given in Table 5.1.

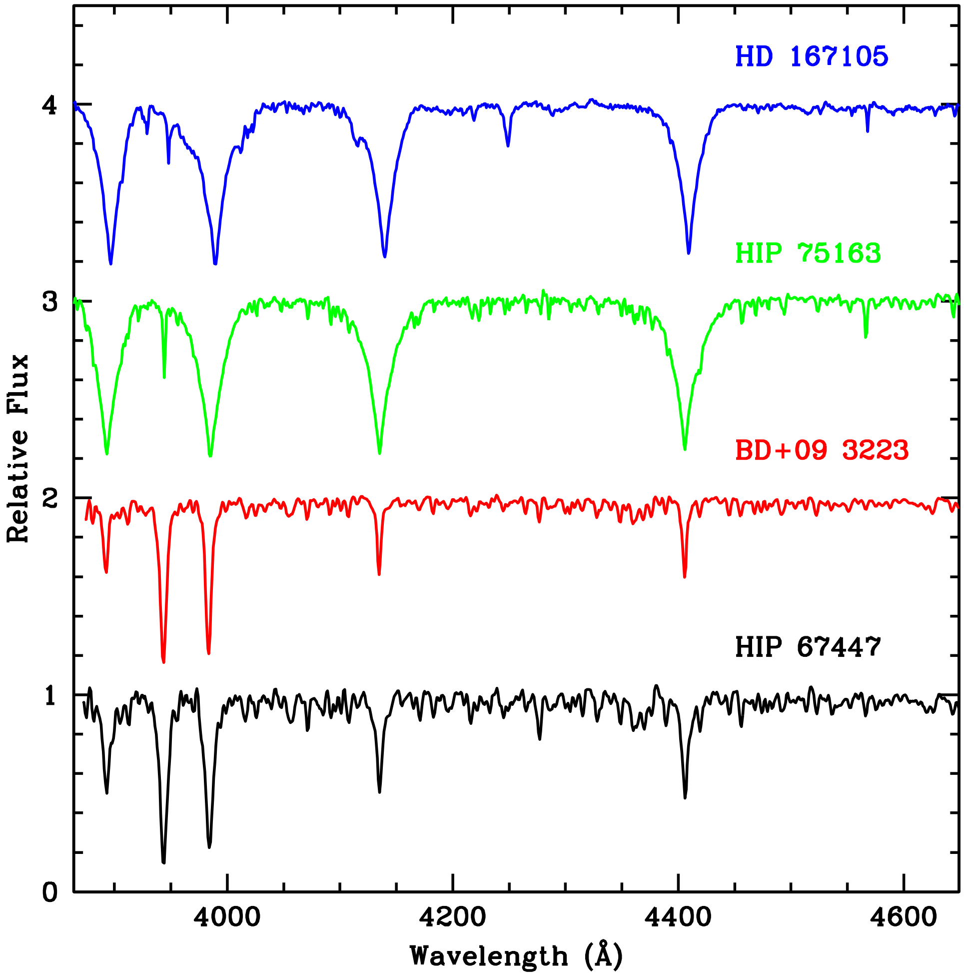

Figure 5.1 Examples of our observed spectra. HD 167105 (blue) and BD+09°3223 (red) are known BHB and RHB stars, respectively. HIP 75163 (green) and HIP 67447 (black) are FHB candidates of this survey.

Table 5.1. Basic parameters of observed program stars.

Star	Other ID	R.A.(J2000) (hr m s)	Decl.(J2000) (° ′ ″)	π (mas)	σ_π (mas)	d (pc)	V^{a} (mag)	$B-V^{\mathrm{a}}$ (mag)
HIP 81078	BD+09 3223	16 33 35.5	+09 06 16.3	···	···	···	9.25	0.56
HIP 66956	HD 119516	13 43 26.7	+15 34 31.0	···	···	···	9.13	0.39
HIP 89012	HD 167105	18 11 06.3	+50 47 32.4	3.02	0.78	331	8.95	0.02
HIP 11	HD 224720	00 00 08.9	+46 56 23.9	4.29	0.84	233	7.34	0.08
HIP 244	HD 225054	00 03 02.1	+39 59 42.5	3.49	0.74	287	7.9	0.67
HIP 397	HD 225275	00 04 54.0	+52 14 56.1	3.73	1.1	268	8.72	0.08
HIP 1496	HD 1448	00 18 40.7	+44 37 47.9	9.28	0.75	108	7.05	0.12
HIP 1722	HD 1714	00 21 38.5	+36 15 10.8	4.9	1.03	204	8.48	0.35
HIP 2535	HD 2836	00 32 09.8	+47 07 22.2	4.79	1.04	209	8.3	0.06
HIP 4612	HD 5704	00 59 06.5	+32 27 20.7	4.77	0.84	210	7.37	0.18
HIP 5425	HD 6812	01 09 17.3	+34 48 21.2	6.39	0.92	156	7.54	0.23
HIP 6059	HD 7744	01 17 45.6	+41 00 49.0	3.56	1.12	281	8.7	−0.01
HIP 8108	HD 10577	01 44 13.7	+48 12 40.7	3.98	0.78	251	7.01	0.03
HIP 8357	HD 10852	01 47 42.3	+54 00 16.1	3.34	0.89	299	7.44	−0.06
HIP 9204	HD 11925	01 58 25.5	+49 54 54.1	4.24	1.2	236	8.82	0.14
HIP 9501	HD 12389	02 02 13.4	+33 24 31.7	3.4	1.03	294	7.98	0.20
HIP 9513	HD 12314	02 02 21.9	+53 37 43.7	3.99	0.73	251	7.61	0.17
HIP 10098	HD 13225	02 09 50.9	+26 29 04.2	4.37	1.1	229	8.5	0.51
HIP 10369	HD 13609	02 13 37.4	+31 55 08.5	5.32	1.04	188	8.29	0.53
HIP 12861	HD 17044	02 45 19.6	+38 04 07.3	4.26	1.07	235	8.31	0.09
HIP 13232	HD 17690	02 50 20.3	+00 57 49.9	5.62	1.52	178	7.64	0.50
HIP 13980	HD 18439	03 00 04.1	+55 11 17.1	6.24	0.93	160	7.33	0.13
HIP 13994	HD 18594	03 00 10.9	+25 14 44.8	3.79	1.1	264	8.48	0.38
HIP 14348	HD 19155	03 05 02.7	+02 56 28.2	4.49	1.13	223	8.41	0.73
HIP 14404	HD 19208	03 05 47.7	+14 16 03.4	3.64	1.11	275	8.94	0.52
HIP 14842	HD 19846	03 11 42.0	+08 07 07.6	3.65	1.07	274	8.55	0.05
HIP 15238	HD 20284	03 16 32.4	+26 12 31.0	4.49	1.27	223	8.57	0.30
HIP 15922	HD 21134	03 25 04.5	+10 58 35.2	8.77	0.94	114	7.29	0.15
HIP 16201	HD 21555	03 28 43.0	+04 21 25.5	6.59	0.97	152	7.68	0.19
HIP 16214	HD 21581	03 28 54.4	−00 25 03.1	4.27	1.2	234	8.7	0.79
HIP 17003	HD 22653	03 38 42.8	+02 43 40.2	5.27	1.05	190	7.84	0.15
HIP 17234	HD 22916	03 41 26.3	+19 23 18.9	4.39	1.14	228	8.09	0.15
HIP 17733	HD 23810	03 47 49.5	−07 01 33.2	3.93	0.97	254	8.04	−0.04
HIP 17804	HD 23824	03 48 38.8	+15 30 19.2	5.1	1.08	196	8.17	0.22
HIP 18832	HD 25400	04 02 13.1	+00 04 50.5	5.09	1.25	196	8.35	0.36
HIP 19049	HD 25752	04 04 53.3	−02 25 37.6	7.36	0.81	136	7.07	0.00
HIP 19239	HD 25819	04 07 24.3	+43 16 41.0	4.71	1.11	212	8.41	0.12
HIP 19548	HD 26399	04 11 10.4	+15 37 34.4	4.24	0.94	236	7.73	0.21
HIP 19831	HD 26885	04 15 08.5	+03 57 26.6	6.93	1.17	144	7.7	0.09
HIP 20367	HD 27448	04 21 41.9	+41 24 26.7	4.15	1.02	241	7.99	0.10
HIP 20835	HD 28083	04 27 54.7	+43 19 51.9	4.17	0.94	240	7.74	0.03
HIP 21342	HD 28794	04 34 45.9	+50 07 28.2	4.47	0.86	224	7.08	0.08
HIP 21485	HD 29132	04 36 50.5	+37 26 20.5	6.96	1.1	144	7.63	0.07
HIP 21679	HD 29418	04 39 14.4	+31 44 29.2	6.37	1.03	157	7.92	0.45
HIP 21739	HD 29634	04 40 05.5	+00 33 02.4	4.72	1.14	212	8.57	0.09
HIP 22415	HD 30409	04 49 26.5	+44 14 22.6	4.73	1.12	211	8.33	0.07
HIP 22877	HD 31252	04 55 16.4	+25 16 37.7	4.42	1.33	226	8.48	0.32

Table 5.1 (cont'd)

Star	Other ID	R.A.(J2000) (hr m s)	Decl.(J2000) ($^\circ\ '\ ''$)	π (mas)	σ_π (mas)	d (pc)	$V^{\rm a}$ (mag)	$B-V^{\rm a}$ (mag)
HIP 22936	HR 1561	04 56 07.0	+52 52 11.1	6.82	0.84	147	5.75	0.11
HIP 23477	HD 32050	05 02 46.6	+46 39 36.8	2.91	0.89	344	7.74	0.02
HIP 23633	HD 32509	05 04 50.1	+26 43 14.7	6.63	1.09	151	7.51	0.20
HIP 24049	HD 33217	05 10 05.2	+31 55 49.9	5.24	0.98	191	8.01	0.26
HIP 24587	HD 34095	05 16 28.9	+36 04 18.5	6.26	0.96	160	7.22	0.16
HIP 25236	HD 35333	05 23 50.8	−04 34 04.0	4.02	1.11	249	8.23	0.35
HIP 25696	HD 35898	05 29 16.7	+32 11 58.0	8.91	1.14	112	7.06	0.50
HIP 26116	HD 36468	05 34 09.5	+43 56 14.8	7.12	0.93	140	7.21	0.04
HIP 26782	HD 37804	05 41 21.1	+02 21 40.6	3.71	1.22	270	8.63	0.64
HIP 26838	HD 37670	05 41 56.7	+35 37 52.7	9.63	1.08	104	6.85	0.02
HIP 27116	HD 38263	05 45 01.2	+12 53 17.9	9.38	1.03	107	6.47	0.23
HIP 27597	HD 39079	05 50 35.8	+10 32 32.5	4.14	1.34	242	8.6	0.14
HIP 27619	HD 39141	05 50 52.6	+07 28 53.8	3.2	1.06	313	8.57	0.67
HIP 27702	HD 39065	05 51 56.3	+39 33 46.7	5.25	1.25	190	7.85	0.42
HIP 28446	HD 40712	06 00 22.1	−05 13 25.5	3.74	1.09	267	8.47	0.21
HIP 28473	HD 40631	06 00 41.1	+14 57 24.9	5.23	1.07	191	8.17	0.25
HIP 28870	HD 41569	06 05 42.2	−06 06 39.6	4.38	1.22	228	8.66	0.21
HIP 29481	HD 42292	06 12 41.6	+51 41 10.8	3.29	0.95	304	7.99	0.17
HIP 29758	HD 43338	06 16 00.9	+06 32 09.2	5.35	0.96	187	7.64	0.38
HIP 30029	HD 43692	06 19 08.0	+33 47 43.5	4.35	1.01	230	7.85	0.37
HIP 30191	HD 44236	06 21 06.1	+07 32 07.8	3.75	1.08	267	7.57	0.11
HIP 31517	HD 46949	06 35 57.7	−03 58 39.5	4.39	0.9	228	7.59	0.16
HIP 31651	HD 47031	06 37 29.3	+22 08 55.6	4.5	1.16	222	7.68	0.08
HIP 31853	HD 47376	06 39 33.7	+30 18 14.2	5.44	1.13	184	8.05	0.13
HIP 32443	HD 48710	06 46 16.1	+49 22 28.4	5.6	1.08	179	8.26	0.14
HIP 32451	HD 48864	06 46 21.0	+18 50 15.6	3.33	0.82	300	7.07	−0.06
HIP 33251	HD 50633	06 55 04.4	+22 33 37.0	4.43	0.98	226	7.67	0.27
HIP 33752	HD 52124	07 00 39.1	+16 57 33.0	2.68	0.87	373	7.11	−0.05
HIP 33768	HD 51909	07 00 46.8	+37 07 42.5	3.61	1.17	277	8.34	0.43
HIP 34030	HD 52764	07 03 36.8	+27 00 19.8	3.66	1.12	273	8.46	0.56
HIP 34651	HD 54806	07 10 34.1	+05 49 03.5	4.43	1.32	226	8.53	0.51
HIP 34745	HD 54800	07 11 37.7	+31 22 38.9	5.53	1.18	181	8.11	0.11
HIP 35137	HD 55746	07 15 50.4	+36 47 08.7	5.09	1.16	196	8.02	0.20
HIP 35640	HD 57047	07 21 15.7	+39 05 30.6	4.6	1.24	217	8.48	0.01
HIP 36031	HD 58370	07 25 28.2	+04 33 43.6	3.37	1.07	297	8.53	0.08
HIP 36185	HD 58271	07 27 07.9	+47 38 45.3	4.58	0.91	218	7.66	0.09
HIP 36197	HD 58578	07 27 16.8	+27 17 55.4	4.6	1.14	217	8.01	0.15
HIP 37274	HD 61422	07 39 15.2	+00 06 37.3	4.51	1.17	222	8	0.10
HIP 37365	HD 61252	07 40 13.5	+41 09 48.5	8.19	0.9	122	6.83	−0.05
HIP 37517	HD 61806	07 42 00.2	+24 03 01.6	3.89	1.12	257	8.14	0.27
HIP 38419	HD 63629	07 52 14.1	+49 37 36.5	5.23	1.19	191	8.41	0.32
HIP 38891	HD 64934	07 57 32.6	+32 39 24.1	8.61	1.13	116	7.13	0.23
HIP 39141	HD 65778	08 00 22.5	+03 14 56.1	4.13	1.01	242	7.94	0.26
HIP 39148	HD 65602	08 00 26.1	+25 02 02.3	6.17	1.07	162	7.96	0.09
HIP 39466	HD 66197	08 04 01.0	+38 38 22.1	4.21	1.29	238	8.62	0.13
HIP 40421	HD 68849	08 15 08.9	+23 44 49.2	3.47	1.1	288	9.19	0.19
HIP 40522	HD 69028	08 16 25.8	+35 33 02.5	3.28	1.02	305	7.99	−0.02

Table 5.1 (cont'd)

Star	Other ID	R.A.(J2000) (hr m s)	Decl.(J2000) (° ′ ″)	π (mas)	σ_π (mas)	d (pc)	$V^{\rm a}$ (mag)	$B-V^{\rm a}$ (mag)
HIP 41073	HD 70631	08 22 49.0	−06 41 41.0	5.76	0.99	174	7.64	0.02
HIP 41133	HD 70568	08 23 31.3	+23 32 04.1	6.28	1.15	159	7.99	0.20
HIP 41356	HD 70988	08 26 13.8	+34 12 28.6	4.42	1.14	226	8.63	0.43
HIP 41868	HD 72114	08 32 14.1	+32 10 12.8	5.64	1.01	177	7.79	0.41
HIP 42598	HD 73821	08 40 54.5	+16 29 58.9	6.1	1.07	164	7.82	0.30
HIP 42960	HD 74701	08 45 24.2	−03 40 53.5	3.5	1.03	286	8.33	0.10
HIP 42994	HD 74389	08 45 46.9	+48 52 43.5	7.74	0.88	129	7.47	0.08
HIP 43817	HD 76192	08 55 27.4	+26 24 35.3	6.53	1.07	153	7.36	0.03
HIP 44078	HD 76733	08 58 45.3	+23 58 00.1	7.07	1.09	141	7.59	0.22
HIP 44421	HD 77227	09 03 02.8	+49 56 53.6	7.64	0.85	131	6.87	0.08
HIP 44574	HR 3606	09 04 55.0	+32 22 36.5	12.6	0.8	79	6.46	0.24
HIP 44603	HD 77874	09 05 15.3	+02 24 50.8	5.78	1.37	173	7.38	0.16
HIP 44908	HD 78463	09 08 54.3	+17 14 03.3	4.31	1.23	232	8.44	0.49
HIP 45327	HD 79374	09 14 15.8	+18 15 27.5	4.29	1.15	233	8.71	0.57
HIP 46125	HR 3727	09 24 22.4	+36 35 13.5	10.59	0.86	94	6.68	0.22
HIP 46359	HD 81709	09 27 08.7	−04 45 18.9	3.92	1.18	255	8.5	0.11
HIP 47034	HD 82817	09 35 08.8	+26 11 33.3	5.8	0.96	172	7.66	0.05
HIP 47781	HD 84337	09 44 30.4	−04 39 26.1	5.38	0.98	186	7.75	0.23
HIP 48013	HD 84526	09 47 16.2	+48 02 05.7	3.97	1.07	252	8.56	0.18
HIP 48312	HD 85269	09 50 56.8	+10 52 56.9	5.09	0.98	196	8.3	0.13
HIP 48963	HD 86579	09 59 18.5	−03 04 29.5	7.57	1.02	132	7.41	0.37
HIP 49010	BD+15 2146	09 59 53.9	+14 52 39.3	3.99	1.24	251	8.9	0.42
HIP 49113	HD 86777	10 01 24.7	+30 35 14.3	6.81	0.92	147	7.83	0.17
HIP 49398	HD 87358	10 05 05.5	+29 44 57.7	4.32	0.96	231	8.57	0.33
HIP 49545	HD 87742	10 06 58.9	−03 17 02.4	4.77	0.94	210	7.76	0.07
HIP 50093	HD 88460	10 13 42.2	+26 09 02.1	5.69	0.93	176	7.55	0.12
HIP 50404	HD 89226	10 17 31.7	−03 32 01.8	3.99	1.02	251	8.32	0.40
HIP 50459	HR 4041	10 18 10.5	+27 24 55.7	7.83	0.73	128	6.53	−0.02
HIP 51250	HD 90651	10 28 05.5	+03 18 56.4	4.51	1.04	222	7.84	0.08
HIP 51591	HD 91220	10 32 17.3	+24 26 32.1	7.94	0.99	126	7.18	0.25
HIP 51603	HD 91181	10 32 28.6	+44 10 54.2	8.16	0.89	123	7.36	0.21
HIP 51644	HD 91349	10 33 05.3	+19 33 59.3	5.46	1.03	183	8.31	0.50
HIP 52415	HD 92748	10 42 52.6	+18 22 55.8	6.97	1.01	143	7.69	0.41
HIP 52460	HD 92868	10 43 27.4	+02 09 53.1	4.37	1.31	229	8.28	0.33
HIP 52659	HD 93167	10 46 05.6	+39 29 40.5	5.01	0.92	200	8.36	0.37
HIP 53419	HD 94653	10 55 38.0	+00 07 22.3	4.89	0.91	204	8.11	0.29
HIP 53606	HD 94938	10 57 59.1	+31 04 57.0	3.86	1.05	259	8.43	0.24
HIP 53959	HD 95607	11 02 23.7	+23 40 29.3	4.64	1.08	216	8.46	0.29
HIP 54107	HD 95884	11 04 18.1	+38 52 05.6	8.77	0.83	114	7.14	0.22
HIP 54208	HD 96128	11 05 28.6	+28 58 38.1	4.08	1.27	245	8.94	0.49
HIP 54323	HD 96327	11 06 45.9	+44 06 55.4	6.22	0.8	161	7.55	0.22
HIP 54343	HD 96370	11 07 01.6	+36 44 11.5	5.46	0.98	183	8.16	0.24
HIP 54592	HD 97005	11 10 21.0	+22 42 06.9	7.15	1.06	140	7.5	0.34
HIP 54654	HD 97198	11 11 16.1	−05 28 12.6	5	1.25	200	8.22	0.17
HIP 54714	HD 97324	11 12 10.0	+11 06 02.7	5.32	1.3	188	8.37	0.59
HIP 55382	HD 98547	11 20 26.4	+17 18 40.6	6.34	0.99	158	7.14	0.12
HIP 55391	HD 98526	11 20 31.9	+44 59 53.8	10.23	0.74	98	6.73	0.34

Table 5.1 (cont'd)

Star	Other ID	R.A.(J2000) (hr m s)	Decl.(J2000) (° ′ ″)	π (mas)	σ_π (mas)	d (pc)	V^{a} (mag)	$B-V^{\mathrm{a}}$ (mag)
HIP 55764	HD 99222	11 25 34.9	+54 24 30.6	3.89	1.03	257	8.55	0.24
HIP 55960	HD 99665	11 28 03.5	−00 53 52.2	8.38	0.92	119	7.11	0.03
HIP 56105	HD 99928	11 30 01.5	+42 39 41.4	4.41	1.02	227	8.36	0.36
HIP 56147	HD 99966	11 30 29.8	+48 56 08.5	4.94	0.82	202	7.39	−0.04
HIP 56263	HD 100237	11 31 59.7	−01 46 56.5	4.8	1.17	208	7.34	0.00
HIP 56584	HD 100775	11 36 03.3	+27 54 08.8	5.12	1.1	195	8.26	0.53
HIP 56679	HD 100974	11 37 17.8	+06 16 12.1	6	1	167	7.12	0.22
HIP 56708	HD 100972	11 37 36.7	+44 42 58.7	6.16	0.76	162	6.84	0.03
HIP 57133	HD 101784	11 42 49.9	−03 32 42.4	7.15	0.85	140	7.55	−0.01
HIP 57158	HD 101846	11 43 19.9	+00 11 06.6	6.71	1.11	149	7.83	0.14
HIP 57406	HD 102223	11 46 08.5	+50 33 48.8	5.15	0.89	194	7.68	0.28
HIP 57604	HD 102589	11 48 36.5	+28 47 59.7	6.42	0.85	156	7.05	0.08
HIP 57743	HD 102841	11 50 28.9	+09 46 37.3	4.29	1.13	233	8.38	0.27
HIP 57831	HD 102998	11 51 34.7	+36 35 14.7	3.93	1.13	254	8.96	0.48
HIP 58044	HD 103378	11 54 14.2	−07 23 01.8	4.17	1.3	240	8.63	0.24
HIP 58552	HD 104241	12 00 24.4	+44 37 49.2	5.7	0.88	175	7.57	0.07
HIP 58723	HD 104573	12 02 40.0	+35 43 38.4	4.19	0.89	239	8.15	0.25
HIP 59005	HD 105076	12 05 54.6	−02 27 47.7	5.14	1.02	195	8.25	0.37
HIP 59766	HD 106557	12 15 20.7	+38 44 09.0	3.56	0.98	281	8.15	0.06
HIP 59783	HD 106593	12 15 29.0	+38 39 35.3	5.57	0.9	180	7.67	0.31
HIP 60124	HD 107254	12 19 50.9	+14 23 00.3	4	1.21	250	8.95	0.46
HIP 60156	HD 107324	12 20 10.4	+41 24 24.7	3.64	1.07	275	8.9	0.34
HIP 60933	HD 108714	12 29 20.4	+17 19 18.9	4.51	0.92	222	7.71	0.11
HIP 61018	HD 108835	12 30 19.5	−01 56 33.0	3.91	1.1	256	8.8	0.02
HIP 62344	HD 111056	12 46 30.7	+21 03 09.2	3.63	0.99	275	8.57	0.23
HIP 62606	HD 111540	12 49 43.6	+29 09 21.8	10.43	2.96	96	9.52	0.61
HIP 62874	HD 112002	12 53 10.4	+12 27 57.3	5.54	1.02	181	7.96	0.14
HIP 63096	HD 112396	12 55 39.0	+54 57 40.4	6.68	0.63	150	6.78	0.04
HIP 63225	HD 112504	12 57 19.0	−08 54 38.9	5.12	0.84	195	6.93	0.09
HIP 63285	HD 112732	12 58 09.6	+52 33 11.6	4.48	0.92	223	8.39	0.18
HIP 63551	HD 113168	13 01 20.2	+38 02 53.5	5.01	0.92	200	7.83	0.01
HIP 64220	HD 114325	13 09 42.7	+20 08 02.2	5.31	1.54	188	8.31	0.28
HIP 64648	HD 115197	13 15 08.5	+35 26 44.8	7.15	1.13	140	6.8	0.18
HIP 64722	HD 115301	13 15 57.7	+21 22 54.4	5.89	0.87	170	7.39	0.03
HIP 64943	HD 115752	13 18 45.2	+32 10 11.5	5.8	0.91	172	8.16	0.30
HIP 66684	HD 119146	13 40 11.6	+53 06 37.3	6.49	0.81	154	7.65	0.22
HIP 66718	HD 119170	13 40 33.1	+46 16 51.3	6.5	0.89	154	7.54	0.52
HIP 66877	HD 119424	13 42 22.9	+38 50 14.2	3.52	1.08	284	8.66	0.37
HIP 67229	HD 120049	13 46 34.7	+27 56 33.4	5.07	1.06	197	8.32	0.27
HIP 67447	HD 120931	13 49 20.9	+72 06 02.3	5.08	0.7	197	8.3	0.45
HIP 67729	HD 121048	13 52 28.6	+35 40 46.0	3.56	1.02	281	8.76	0.26
HIP 68196	HD 122007	13 57 42.8	+53 54 36.2	6.94	0.6	144	6.94	0.30
HIP 69274	HD 124170	14 10 52.4	+42 10 00.2	2.58	0.86	388	8.63	0.16
HIP 69492	HD 124693	14 13 39.9	+51 17 47.3	3.14	0.8	318	8.47	0.43
HIP 69650	HR 5345	14 15 16.9	+52 32 09.3	10.83	0.63	92	6.56	0.10
HIP 69942	HD 125657	14 18 46.2	+58 59 50.7	3.72	0.75	269	8.64	0.46
HIP 70029	HR 5373	14 19 47.7	+38 47 38.5	7.3	0.6	137	6.33	0.05

Table 5.1 (cont'd)

Star	Other ID	R.A.(J2000) (hr m s)	Decl.(J2000) (° ′ ″)	π (mas)	σ_π (mas)	d (pc)	V^{a} (mag)	$B-V^{\mathrm{a}}$ (mag)
HIP 70247	HD 126229	14 22 22.9	+56 53 15.5	3.55	0.78	282	8.76	0.53
HIP 70630	HD 126968	14 26 51.5	+56 02 10.7	3.84	0.75	260	7.53	−0.05
HIP 71432	HD 128590	14 36 25.4	+44 00 57.4	3.14	0.84	318	8.72	0.15
HIP 71468	HD 128579	14 36 57.0	+27 50 10.5	4.64	1.13	216	8.54	0.26
HIP 71687	HD 129025	14 39 47.0	+22 10 52.8	3.64	0.98	275	8.7	0.04
HIP 71945	HD 129632	14 42 53.3	+29 05 16.9	4.54	1.07	220	8.21	0.06
HIP 72193	HD 130370	14 45 57.7	+51 37 35.5	3.69	0.75	271	8.56	0.18
HIP 72953	HD 131764	14 54 35.6	+30 03 49.1	10.72	0.81	93	6.84	0.43
HIP 73283	HD 132890	14 58 39.3	+61 40 00.8	3.65	0.61	274	7.22	0.08
HIP 73549	HD 133230	15 01 53.9	+43 32 30.6	5.23	0.79	191	8.15	0.49
HIP 73915	HD 134301	15 06 18.2	+59 49 30.4	6.35	0.94	157	7.67	0.46
HIP 74173	HD 134588	15 09 20.2	+39 25 48.6	3.08	1.02	325	8.85	0.21
HIP 74359	HD 134854	15 11 47.7	+10 12 59.6	8.21	0.87	122	6.89	0.05
HIP 74551	HD 135558	15 13 58.9	+47 58 08.5	7.31	0.66	137	7.47	0.23
HIP 74639	HD 135613	15 15 01.7	+33 30 46.1	4.96	0.99	202	8.2	0.34
HIP 75163	HD 136754	15 21 34.5	+24 20 36.1	7.55	0.81	132	7.25	0.04
HIP 75345	HD 137444	15 23 47.3	+53 41 08.3	3.19	0.81	313	9.02	0.42
HIP 75537	HD 137426	15 25 53.9	+05 57 03.0	3.01	0.99	332	8.37	0.16
HIP 76010	HD 138512	15 31 26.0	+32 35 32.2	3.7	0.96	270	8.52	0.47
HIP 76773	HD 140101	15 40 30.2	+37 01 01.1	7.36	0.64	136	7.16	0.01
HIP 76831	HD 140396	15 41 14.1	+50 12 13.8	4.09	0.8	244	8.76	0.48
HIP 77016	HD 140770	15 43 30.6	+46 54 13.9	2.48	0.74	403	8.38	0.05
HIP 77922	HD 142553	15 54 49.0	+11 30 55.0	4.65	1.08	215	7.69	0.22
HIP 78565	HD 144129	16 02 34.5	+42 30 20.5	3.07	0.98	326	9.48	0.43
HIP 78856	HD 145021	16 05 50.0	+56 41 01.2	3.04	0.86	329	9.32	0.20
HIP 79272	HD 145871	16 10 45.4	+52 08 13.4	3.8	0.78	263	8.56	0.23
HIP 79472	HD 146010	16 13 07.9	+21 33 58.2	11.21	0.83	89	6.69	0.18
HIP 79574	HD 146469	16 14 09.1	+50 04 32.6	4.27	0.76	234	8.8	0.44
HIP 80622	HD 148493	16 27 43.7	+20 50 36.0	3.6	1.06	278	8.39	0.42
HIP 81718	HD 150812	16 41 31.2	+41 19 24.2	4.49	0.78	223	8.67	0.52
HIP 82002	HD 151353	16 45 05.7	+40 38 17.4	5.78	0.78	173	8.16	0.14
HIP 82893	HD 153145	16 56 22.6	+31 00 40.5	2.5	0.83	400	8.14	0.17
HIP 82939	HD 238628	16 56 56.1	+57 08 32.2	2.96	0.82	338	9.32	0.32
HIP 83050	HD 153436	16 58 12.8	+33 42 02.3	4.32	0.9	231	8.49	0.36
HIP 83130	HD 153649	16 59 18.5	+34 51 51.5	4.1	0.85	244	8.46	0.22
HIP 83354	HD 154344	17 02 08.2	+51 56 32.3	6.15	0.6	163	7.85	0.23
HIP 83724	HD 154888	17 06 41.6	+35 19 24.2	7.04	0.65	142	7.36	0.04
HIP 83860	HD 155178	17 08 19.8	+37 46 47.2	2.85	0.8	351	8.82	0.11
HIP 83905	HD 155227	17 08 53.9	+33 18 02.7	4.72	0.69	212	7.56	−0.02
HIP 84254	HD 155978	17 13 22.7	+35 25 51.3	2.53	0.75	395	8.11	0.11
HIP 84464	HD 156535	17 16 04.3	+42 16 04.8	2.74	0.76	365	8.52	0.29
HIP 84615	HD 156757	17 17 48.8	+36 05 38.7	3.49	0.73	287	7.57	0.27
HIP 84845	HD 157579	17 20 27.2	+59 11 56.1	3.69	0.71	271	8.36	0.17
HIP 85303	HD 158098	17 25 54.5	+33 59 52.2	3.72	0.81	269	8.01	0.14
HIP 85841	HD 159303	17 32 26.8	+35 46 23.2	3.17	0.66	315	7.8	−0.07
HIP 87098	HD 162093	17 47 45.5	+34 55 23.6	4.74	0.71	211	8	0.12
HIP 87724	HD 163439	17 55 08.3	+24 13 54.5	4.57	0.92	219	8.44	0.05

Table 5.1 (cont'd)

Star	Other ID	R.A.(J2000) (hr m s)	Decl.(J2000) (° ′ ″)	π (mas)	σ_π (mas)	d (pc)	$V^{\rm a}$ (mag)	$B-V^{\rm a}$ (mag)
HIP 87749	HD 163590	17 55 25.3	+32 26 18.0	2.64	0.64	379	7.44	0.03
HIP 88376	HD 164760	18 02 47.4	−01 20 10.9	5.15	1	194	7.97	0.14
HIP 88890	HD 165991	18 08 46.0	−03 59 27.2	4.15	1.04	241	7.64	0.16
HIP 89336	HD 167560	18 13 41.8	+42 52 45.9	3.92	0.67	255	8.12	0.28
HIP 89415	HD 168129	18 14 49.1	+58 00 09.3	5.57	0.57	180	7.97	0.10
HIP 89765	HD 168620	18 19 04.4	+37 39 30.1	3.6	0.74	278	8.6	−0.02
HIP 90031	HD 169487	18 22 11.8	+51 32 30.8	6.73	0.5	149	6.84	0.13
HIP 90209	HD 169668	18 24 25.5	+32 07 50.9	3.41	0.78	293	8.15	0.03
HIP 90536	HD 170274	18 28 24.0	+03 46 47.3	4.55	1	220	7.88	0.34
HIP 90912	HD 171070	18 32 41.1	+00 34 39.0	3.57	1.19	280	8.76	0.47
HIP 90960	HD 171364	18 33 18.5	+30 09 40.5	2.93	0.85	341	8.67	−0.03
HIP 91705	HD 172806	18 42 06.2	+04 02 03.6	3.83	0.96	261	8.01	0.09
HIP 91927	HD 173666	18 44 23.3	+44 53 23.9	3.6	0.75	278	8.13	0.37
HIP 93329	HD 176869	19 00 34.2	+39 50 41.8	4.21	0.91	238	7.86	−0.06
HIP 93549	HD 177487	19 03 13.0	+37 21 14.2	3.49	0.84	287	8.65	0.06
HIP 93833	HD 177959	19 06 33.6	+06 53 25.6	8.15	0.95	123	7.28	0.19
HIP 94324	HD 179817	19 11 56.5	+43 53 25.8	2.65	0.66	377	8.01	0.02
HIP 95115	HD 181986	19 20 59.1	+38 47 23.8	4.52	0.72	221	8.38	0.43
HIP 95161	HD 181831	19 21 37.8	+10 26 59.5	3.76	1.16	266	8.31	0.20
HIP 96029	HD 184058	19 31 29.9	+28 43 02.2	7.45	0.75	134	7.6	0.33
HIP 96268	HD 184566	19 34 28.5	+17 58 52.4	4.28	1.15	234	8.66	0.27
HIP 97311	HD 187122	19 46 35.9	+39 30 40.2	4.52	0.63	221	7.46	0.13
HIP 97555	HD 187406	19 49 42.8	+02 57 14.1	5.61	1.11	178	7.65	0.52
HIP 99505	HD 191879	20 11 38.1	+14 38 55.9	7.41	1.06	135	7.57	0.13
HIP 99713	HD 192387	20 14 00.3	+16 51 29.0	3.46	0.96	289	8.19	0.13
HIP 99748	HD 192327	20 14 19.9	+00 08 39.9	5.47	1.28	183	8.15	0.40
HIP 100237	HD 193328	20 19 47.4	−00 54 25.7	7.06	1.05	142	7.48	0.13
HIP 100408	HD 194007	20 21 39.9	+42 14 05.6	3.52	0.81	284	8.31	0.00
HIP 101486	HD 196196	20 33 58.2	+46 24 58.6	2.46	0.72	407	7.67	−0.03
HIP 101486	HD 196196	20 33 58.2	+46 24 58.6	2.46	0.72	407	7.67	−0.03
HIP 102038	HD 197040	20 40 42.4	+14 31 36.8	5.69	0.94	176	7.85	0.09
HIP 103322	HD 199479	20 55 59.0	+44 22 26.1	5.61	0.69	178	6.83	−0.05
HIP 103418	HD 199455	20 57 11.7	+02 28 03.0	4.04	1.18	248	8.56	0.40
HIP 104090	HD 200747	21 05 19.2	+00 43 37.5	6.25	0.88	160	7.78	0.39
HIP 104091	HD 200778	21 05 19.3	+09 10 10.0	5.7	1.19	175	8.02	0.40
HIP 104233	HD 201274	21 07 07.5	+38 18 53.7	2.6	0.84	385	7.95	0.01
HIP 104845	HD 202243	21 14 18.9	+06 57 54.4	5.56	1.05	180	8.07	0.08
HIP 106388	HD 205201	21 32 50.7	+32 46 36.0	2.53	0.73	395	7.41	−0.06
HIP 107013	HD 206295	21 40 24.5	+34 12 36.6	3.82	1	262	8.54	0.27
HIP 107063	HD 206298	21 41 02.2	+05 01 14.2	8.13	0.98	123	7.23	0.16
HIP 107902	HD 207829	21 51 42.5	+09 02 31.2	4.67	1.08	214	8.37	0.31
HIP 108287	HD 208714	21 56 19.1	+58 24 44.3	6.24	0.66	160	7.89	0.31
HIP 109121	HR 8429	22 06 12.2	+45 14 55.2	10.09	0.61	99	6.19	0.08
HIP 109341	HD 210265	22 09 04.1	+09 27 04.2	4.47	1.14	224	7.92	0.09
HIP 110522	HD 212318	22 23 27.6	+00 36 31.0	8.96	0.78	112	6.94	0.18
HIP 110684	HD 212713	22 25 25.6	+47 06 12.4	2.82	0.83	355	8.41	−0.02
HIP 111789	HD 214588	22 38 33.7	+44 40 08.4	6.45	0.75	155	7.18	0.04

Table 5.1 (cont'd)

Star	Other ID	R.A.(J2000) (hr m s)	Decl.(J2000) (° ′ ″)	π (mas)	σ_π (mas)	d (pc)	V^{a} (mag)	$B-V^{\mathrm{a}}$ (mag)
HIP 112099	HD 215043	22 42 21.1	+05 10 25.3	7.77	0.97	129	7.37	0.22
HIP 112125	HD 215077	22 42 42.5	+00 04 15.6	5.83	0.89	172	7.19	0.38
HIP 112474	HD 215772	22 46 54.9	+47 10 52.6	4.5	1.02	222	8.71	0.45
HIP 113551	HD 217398	22 59 53.2	+38 37 40.4	3.41	1.1	293	8.92	0.02
HIP 114315	HD 218567	23 09 04.1	−02 27 09.5	5.89	0.93	170	7.62	0.43
HIP 114480	HD 218869	23 11 05.7	+28 33 29.9	3.56	1.02	281	8.58	0.15
HIP 114488	HD 218845	23 11 13.3	+03 09 10.8	6.24	1.1	160	7.92	0.24
HIP 115428	HD 220337	23 22 53.2	+02 49 05.9	7.54	0.88	133	7.04	0.03

[a] Magnitudes extracted directly from *Hipparcos* catalog, except magnitudes of BD+09 3223, HD 119516 and HD 167105 are adopted from SIMBAD.

Chapter 6

Modeling the System Parameters of 2M 1533+3759: A New Longer-Period Low-Mass Eclipsing sdB+dM Binary

6.1 Introduction

Subdwarf B (sdB) stars are evolved, hot, compact stars ($23,000$ K $< T_{\text{eff}} < 37,000$ K; $5.2 < \log g < 6.0$), commonly found in the disk and halo of our Galaxy (Saffer et al. 1994)[1]. They are believed to ascend the first red giant branch (RGB) following the exhaustion of central hydrogen, somehow experiencing sufficient mass loss prior to the RGB tip to remove nearly all of their envelopes. They subsequently evolve blueward from the RGB before igniting helium in their cores. From an evolutionary point of view, sdB stars are also known as extreme horizontal branch (EHB) stars (Heber 1986). Their helium burning cores, generally expected to be just under 0.5 $M_{\odot}$, are essentially identical to those of normal horizontal branch (HB) stars. However, their hydrogen envelopes are too thin and inert (< 0.01 $M_{\odot}$) (Saffer et al. 1994; Heber 1986) to support double shell burning, so they never make it to the asymptotic giant branch. Following core helium exhaustion, they evolve directly into sdO stars before proceeding down the white dwarf cooling track (Dorman et al. 1993).

---

[1] Significant portions of this chapter have been published previously in For, B.-Q.; Green, E.M.; Fontaine, G.; Drechsel, H. et al. 2010, ApJ, 708, 253.

In the context of understanding Galaxy evolution and cosmology, sdB stars play an important role because their large UV flux appears to be the dominant source of the "UV upturn" phenomenon observed in elliptical galaxies and the centers of spiral bulges (de Boer 1982; Greggio & Renzini 1999; Brown et al. 1997). The UV excess in old stellar populations has been used as an age indicator in evolutionary population synthesis (Yi et al. 1997, 1999), although more recent work has begun to consider alternative binary scenarios that would have quite different effects (Podsiadlowski et al. 2008).

Various evolutionary scenarios have been proposed for sdB stars, but the details of the formation mechanisms are not yet well determined. Possible formation channels can be divided into single star evolution with enhanced mass loss at the tip of RGB (Castellani & Castellani 1993; D'Cruz et al. 1996) and close binary evolution, first suggested by Mengel et al. (1976). Recently, Han et al. (2002, 2003) conducted an in-depth theoretical investigation through binary population synthesis. They found that common-envelope evolution, resulting from dynamically unstable mass transfer near the tip of the first RGB, should produce short-period binaries ($P \approx 0.1 - 10$ day) with either a main sequence (MS) or white dwarf (WD) companion. If a red giant star loses nearly all of its envelope prior to the red giant tip via stable mass transfer, a long-period sdB binary with a MS companion can be produced ($P \approx 10 - 500$ day). A most interesting feature of Han et al.'s models is that they predict a much larger range of sdB progenitor masses than had previously been considered, including stars sufficiently massive to avoid a helium flash and instead undergo quiescent helium ignition in non-degenerate cores (see also Hu et al. 2007; Politano et al. 2008).

Binary formation scenarios appear likely to be responsible for the majority of observed field sdB stars, as a large fraction are observed to occur in binaries (e.g., Lisker et al. 2005; Morales-Rueda et al. 2003; Maxted et al. 2001; Saffer et al. 2001; Green et al. 1997; Allard et al. 1994). Nevertheless, the same studies show that there are a sizable fraction of sdB stars, 30% or more, that do not now appear to be in binaries: there is no sign of a companion in high S/N optical spectra or infrared colors, and their radial velocities are constant to within the observational errors (a few km s^{-1}) over many months. Moni Bidin et al. (2008) also found a significant fraction, 96%, of sdB stars in globular clusters to be single stars, in contrast to observed field sdB stars. Han et al. (2002, 2003) investigated the possibility of forming single sdB stars by merging two helium white dwarfs, which would allow the formation of more massive sdB stars ($0.4 - 0.65\ M_{\odot}$), and Politano et al. (2008) considered the possibility that some sdB stars might form from mergers during common envelope evolution, followed by rotationally-induced mass loss. Still, unusually high mass loss in single red giant stars cannot yet be ruled out.

The distribution of sdB masses is clearly one of the most important constraints on the several possible formation channels. Different observational techniques provide different windows of opportunity for investigating these masses.

More sdB masses have been derived by asteroseismology than by any other method to date. Asteroseismology provides an extremely high level of precision (and is the only way to determine envelope masses, in addition to total masses), but it has so far been successfully applied only to the relatively rare short-period sdB pulsators. Two different types of multimode sdB pulsators have been discovered: short-period V361 Hya pulsators (originally, EC 14026 stars, Kilkenny et al. 1997) which comprise a rather small percentage of the hotter sdB stars, and longer period V1093 Her pulsators (PG 1716 stars, Green et al. 2003), which seem to be fairly common among cooler sdB stars. The rapid oscillations of V361 Hya stars are interpreted as low-order pressure modes (p-modes) that are driven by a κ-mechanism associated with the radiative levitation of iron in the thin diffusion-dominated envelopes (Charpinet et al. 1996, 1997). The same mechanism has also been shown to explain the excitation of high-order gravity modes (g-modes) in the V1093 Her stars (Fontaine et al. 2003). Asteroseismological modeling has so far been extremely successful with p-mode pulsations in the envelopes of sdB stars, and the resulting stellar parameters are generally in very good agreement with theoretical expectations (e.g., Fontaine et al. 2008; Charpinet et al. 2007, and references therein). On the other hand, g-mode pulsations, which extend much more deeply into the stellar cores, will require more sophisticated interior models before they can be satisfactorily analyzed by asteroseismology (Randall et al. 2007).

The list of p-mode pulsators whose parameters have been derived by asteroseismology is presented in Table 6.1. Most of the derived masses are within a few hundredths of a solar mass of the canonical sdB mass of 0.48 $M_{\odot}$, except for PG 0911+456 (Randall et al. 2007), which will be discussed further in §6.7. Interestingly, the only post-common envelope binaries in this list are Feige 48 (van Grootel et al. 2008a) and PG 1336−018 (Charpinet et al. 2008). Indeed, the large majority of V1093 Her stars exhibit low or negligible radial velocity variations, of the order of a few km s^{-1} or less, and thus must be single stars, or have extremely low mass companions, or else occur in long-period binaries with a main sequence F, G, or K star primary. This is not surprising, since sdB stars whose radial velocity variations are clearly indicative of post-common envelope binaries are preferentially found at temperatures cooler than most V1093 Her stars (Green et al. 2008).

Traditional methods of deriving masses by exploiting binary properties are therefore quite important. For one thing, binaries provide a vital test of asteroseismology in the rare cases where the sdB primary is a pulsator. More importantly, until improved asteroseismic models and extensive satellite observations make it possible to successfully model g-mode sdB pulsators, the only way to derive masses for a larger sample of post-common envelope sdB stars is to analyze their binary properties. Finally, there are simply a large number of binaries that contain non-pulsating sdB stars.

The difficulty with most sdB stars in post-common envelope systems is that they are single-lined spectroscopic binaries with essentially invisible compact secondaries. In principle, precise measurements of the sdB surface gravity and rotational velocity in a tidally locked system will yield the orbital inclination, allowing the individual component masses to be determined from the mass function (e.g., Geier et al. 2008), but the accuracy of this approach has not yet been proven. There are, however, a small number of rare post-common envelope sdB+dM binaries (Maxted et al. 2004), which have been identified by their reflection effects – e.g., the sinusoidal variation observed in the light curve due to reradiated light from the heated side of the tidally locked M dwarf – that are more promising. The known sdB+dM systems are summarized in Table 6.2. If narrow lines originating from the cool secondary could be detected, then masses of both components could be derived from the double-lined spectroscopic solution. Again, this should be possible in principle, especially in binaries with the shortest orbital periods, where the heated face of the secondary is brighter than it otherwise would be, but results so far have been ambiguous. Vučković et al. (2008) detected emission lines from the secondary in PG 1336-018, by subtracting the spectrum of the hot primary from spectra taken at other phases, but the S/N of the spectra were only sufficient to claim general consistency with the orbital solution described in Vučković et al. (2007). Using much higher S/N spectra of a similar sdO+dM binary, AA Dor, Vučković et al. (2008) were able to determine a velocity amplitude for the secondary, but their derived primary mass has now been vigorously disputed by Rucinski (2009). Wood & Saffer (1999) presented a good argument for the detection of $H\alpha$ absorption lines from the secondary in HW Vir, again by subtracting the spectrum near minimum light from spectra near maximum light, and obtained reasonable velocities, but it is perplexing that absorption lines and no emission lines should have been seen.

An apparently more successful method is to model the light variations in sdB+dM binaries exhibiting reflection effects, especially the eclipsing systems, in order to determine the system parameters. This is a very complex endeavor. The models have many free parameters, and there are large uncertainties that typically require additional information to constrain the solution. Often, the light curves provide more than one high quality solution. For example, Drechsel et al. (2001) had to make use of a mass–radius relation for the secondary star to decide between two solutions that implied quite different sdB masses for HS 0705+6700 (0.483 and < 0.3 $M_\odot$). Heber et al. (2004) needed to use their spectroscopic $\log g$ and mass–radius relations to discriminate between two solutions with different secondary albedos and inclinations in HS 2333+3927. Vučković et al. (2007) found three possible solutions modeling the light curves PG 1336−018, and it was not possible to choose between two of them until Charpinet et al. (2008) derived a consistent primary mass by asteroseismological modeling. Furthermore, even when a single family of solutions can be identified, there still remain unavoidable ambiguities in choosing one "best" model (Drechsel et al. 2001). Even in the most favorable cases of eclipsing sdB+dM binaries, the eclipses are not flat-bottomed, leading to a small range of nearly equivalent solutions in the vicinity of the deepest minimum. The resulting small variations in the mass mass ratio, q, lead to a significant range in the derived sdB mass. The uncertainties are obviously larger when there is no eclipse. Still, light curve modeling provides valuable information, and when the derived sdB mass can be verified – rarely by asteroseismology, more often from consistency with the spectroscopic surface gravity or projected rotational velocity – our confidence in the results is greatly increased. It is clearly important to investigate as many sdB+dM binaries as possible, especially the eclipsing systems, in order to build up a more comprehensive picture of sdB masses produced by post-common envelope evolution and to compare with the distribution of masses from other formation channels.

In this chapter, we report on the system parameters of 2M 1533+3759 ($15^h33^m49.44^s$, $+37°59'28.2''$, J2000), a new eclipsing sdB+dM binary with a longer orbital period than any eclipsing sdB+dM discovered so far. This star was first recognized as an sdB in 2005 (although it remained unpublished) during a continuing spectroscopic survey (Green et al. 2008) of bright blue stellar candidates selected from a variety of sources, including the 2MASS survey (Skrutskie et al. 2006). The current investigation was motivated by Kelley & Shaw (2007), who discovered that 2M 1533+3759 is an eclipsing binary, NSVS 07826147, through their work with the Northern Sky Variability Survey (NSVS; Wozniak et al. 2004). Kelley & Shaw (2007) identified a group of nine eclipsing binaries with short periods and relatively narrow eclipse widths, indicating very small radii for the components. Since their list

Table 6.1. sdB stars with masses determined by asteroseismology

Name	log g (cm s^{-2})	$T_{\rm eff}$ (K)	M_1 ($M_\odot$)	log $M_{\rm env}/M_*$	References
PG 1047+003	5.800±0.006	33150±200	0.490±0.014	−3.72±0.11	Charpinet et al. (2003)
PG 0014+067	5.775±0.009	34130±370	0.477±0.024	−4.32±0.23	Charpinet et al. (2005a)
PG 1219+534	5.807±0.006	33600±370	0.457±0.012	−4.25±0.15	Charpinet et al. (2005b)
PG 1325+101	5.811±0.004	35050±220	0.499±0.011	−4.18±0.10	Charpinet et al. (2006)
EC 20117−4014	5.856±0.008	34800±2000	0.540±0.040	−4.17±0.08	Randall et al. (2006)
PG 0911+456	5.777±0.002	31940±220	0.390±0.010	−4.69±0.07	Randall et al. (2007)
Feige 48	5.462±0.006	29580±370	0.519±0.009	−2.52±0.06	van Grootel et al. (2008a)
BAL 090100001	5.383±0.004	28000±1200	0.432±0.015	−4.89±0.14	van Grootel et al. (2008b)
PG 1336−018	5.739±0.002	32740±400	0.459±0.005	−4.54±0.07	Charpinet et al. (2008)
PG 1605+072	5.226±0.005	32300±400	0.528±0.004	−5.88±0.04	van Spaandonk et al. (2008)
EC 09582−1137	5.788±0.004	34805±230	0.485±0.011	−4.39±0.10	Randall et al. (2009)

includes the well-known HW Vir (Lee et al. 2009 and references therein), as well as 2M 1533+3759, which we confirmed to be a spectroscopic near-twin of HW Vir, Kelley & Shaw (2007) proposed that the other objects in their Table 6.3 might also be sdB+dM binaries. §6.2 presents the results from our follow-up spectra for these stars.

In §6.3, we describe new spectroscopy and photometry for 2M 1533+3759. The data analyses are given in §6.4 and §6.5, and the system parameters are derived in §6.6. We discuss possible selection effects and consider the unusually low derived mass for the sdB mass in §6.7. §6.8 looks at the evolution of 2M 1533+3759, and §6.9 contains our conclusions.

6.2 NSVS Eclipsing sdB+dM Candidates

We have obtained high S/N low resolution spectra for Kelley & Shaw's (2007) proposed sdB+dM stars (their Table 3). All were observed with the same telescope and instrumental setup (§6.3) that we used to obtain our initial

Table 6.2. Currently known sdB+dM binaries

Name	Alternate Name	Period (day)	M_1 ($M_\odot$)	M_2 ($M_\odot$)	References	Comments
Reflection Effect/Eclipsing Binaries						
HS 0705+6700		0.0956466	0.48	0.13	Drechsel et al. (2001)	light curve
PG 1336−018	NY Vir	0.101015999	0.466/0.389	0.122/0.110	Vuckovic et al. 2007	light curve, two solutions
			0.459	–	Charpinet et al. (2008)	asteroseismology
NSVS 14256825	J 2020+0437	0.1104	0.46	0.21	Wils et al. (2007)	no spectroscopy
HS 2231+2441		0.11058798	< 0.3	–	Østensen et al. (2008)	uncertain $\log g$
PG 1241−084	HW Vir	0.11676195	0.485	0.142	Lee et al. (2009)	light curve
BUL–SC16 335		0.125050278	–	–	Polubek et al. (2007)	
2M 1533+3759	NSVS 07826147	0.16177042	0.377	0.113	this paper	light curve
Reflection Effect/Non-Eclipsing Binaries						
PG 1017−086	XY Sex	0.073	–	–	Maxted et al. (2002)	
HS 2333+3927		0.1718023	0.38	0.29	Heber et al. (2005)	light curve
PG 1329+159	Feige 81, PB 3963	0.249699	–	–	Maxted et al. (2004)	
		0.249702	–	–	Green et al. (2004)	
2M 1926+3720	KBS 13	0.2923	–	–	For et al. (2008)	
PG 1438−029		0.33579	–	–	Green et al. (2004)	
HE 0230−4323		0.4515	–	–	Koen (2007)	

spectrum of 2M 1533+3759.

Table 6.3 of this chapter presents the results of our spectroscopic follow-up. The NSVS numbers, V magnitudes and orbital periods from Kelley & Shaw are listed in the first three columns. Columns 4, 5, and 6 give the $J-H$ color, RA, and Dec from the 2MASS All-Sky Point Source Catalog (Skrutskie et al. 2006) for the objects that we observed. The seventh column lists our best estimate of their spectral types. For the non-sdB stars, the spectral types were determined by cross-correlating their continuum-subtracted spectra with template spectra of known main sequence spectral standards (Gray & Corbally 2009), acquired with the same instrument and spectroscopic setup, in order to find the best match. Since the binary spectra are composite, the best matches indicate either the dominant or the effective spectral type.

NSVS 04818255 deserves further comment. Its NSVS coordinates are $08^h40^m59.8^s$, $+39°56'02''$; this is close, but not quite coincident with the brightest star in the immediate area. Kelley & Shaw identified NSVS 04818255 with the sdB star PG 0837+401. However, according to the finder chart in Green et al. (1986), PG 0837+401 is the fainter star at $08^h41^m01.3^s$, $+39°56'18''$, approximately $24''$ northeast; our spectrum confirms that it is indeed an sdB star. We initially observed the bright F9–G0 star nearest to the NSVS coordinates, since it has the same 2MASS $J-H$ value that Kelley & Shaw give for NSVS 04818255. However, S. Bloemen and I. Decoster (Leuven) and M. Godart (Liège) recently obtained time-series photometry indicating that neither PG 0837+401 nor the bright F9–G0 star are variable (R. Østensen, priv. comm.). The eclipsing system that they identify with NSVS 04818255 is the intermediate brightness object almost $40''$ west northwest of PG 0837+401. We obtained a spectrum for the variable star and found it to have a G0 spectral type, in agreement with its somewhat redder $J - H$.

HW Vir and 2M 1533+3759 are therefore, unfortunately, the only two bonafide sdB stars in Kelley & Shaw's (2007) list. Figure 6.1 shows our flux-calibrated spectrum for 2M 1533+3759, along with the bluest and reddest of the non-sdB spectra from Table 6.3, for comparison. It is clear from the decreasing flux blueward of the Balmer jump that there are not any sdB stars hidden in any of the seven binaries with overall A, F, or G spectral types. $J - H$ colors are a good indicator for the presence of an sdB star in a suspected sdB+dM binary, since M dwarfs later than about M2 are too faint relative to sdB stars to have much of an effect on the $J - H$ colors. All of the known sdB+dM binaries have $-0.2 < J - H < 0.0$; their distribution in $J - H$ is only slightly redder than the overall distribution of moderately unreddened sdB+WD binaries and non-binary sdB stars plotted in Green et al.'s (2008) Figure 5.

6.3 Observations and Reductions

6.3.1 Spectroscopy

Low-resolution spectra for 2M 1533+3759 were obtained with the Boller & Chivens (B&C) Cassegrain spectrograph at Steward Observatory's 2.3 m Bok telescope on Kitt Peak. The 400 mm^{-1} first order grating was used with a $2.5''$ slit to obtain spectra with a typical resolution of 9 Å over the wavelength interval 3620–6900 Å. The instrument rotator was set prior to each exposure, to align the slit within $\sim 2^\circ$ of the parallactic angle at the midpoint of the exposure. HeAr comparison spectra were taken immediately following each stellar exposure. The spectra were bias-subtracted, flat-fielded, background-subtracted, optimally extracted, wavelength-calibrated and flux-

Table 6.3. NSVS sources identified by Kelley & Shaw (2007) as potential sdB stars

NSVS ID[a]	V[a] (mag)	Period[a] (day)	$J-H$[b] (mag)	RA (J2000)[b] (h m s)	DEC (J2000)[b] (° ′ ″)	Spectral Type[c]	Comments
02335765	10.69	9.744983	0.224	06:31:02.7	+61:14:29	F2–F5	
03259747	11.22	1.239805	0.274	20:57:27.7	+56:46:06	F9–G0	
04818255	12.10	0.1600359	0.392	08:40:58.4	+39:56:28	G0	late-type eclipsing binary star
			0.343	08:41:00.2	+39:55:54	F9–G0	star nearest to NSVS coords
04963674	10.63	3.6390769	0.297	11:03:36.4	+41:36:02	F9–G0	
07826147	13.61	0.16177	−0.084	15:33:49.4	+37:59:28	sdB	2M 1533+3759; FBS 1531+381
08086052	11.94	1.853631	0.255	18:03:11.9	+32:11:14	F8–F9	
09729507	11.77	4.740887	0.094	06:05:18.4	+20:44:32	A0–A2	
15864165	12.65	1.232349	0.111	11:05:06.6	−09:01:33	A6–A7	
15972828	11.21	0.116719	−0.119	12:44:20.2	−08:40:16	sdB	HW Vir

[a] Table 3 of Kelley & Shaw (2007).

[b] 2MASS All-Sky Point Source Catalog (Skrutskie et al. 2006).

[c] Steward 2.3 m spectra.

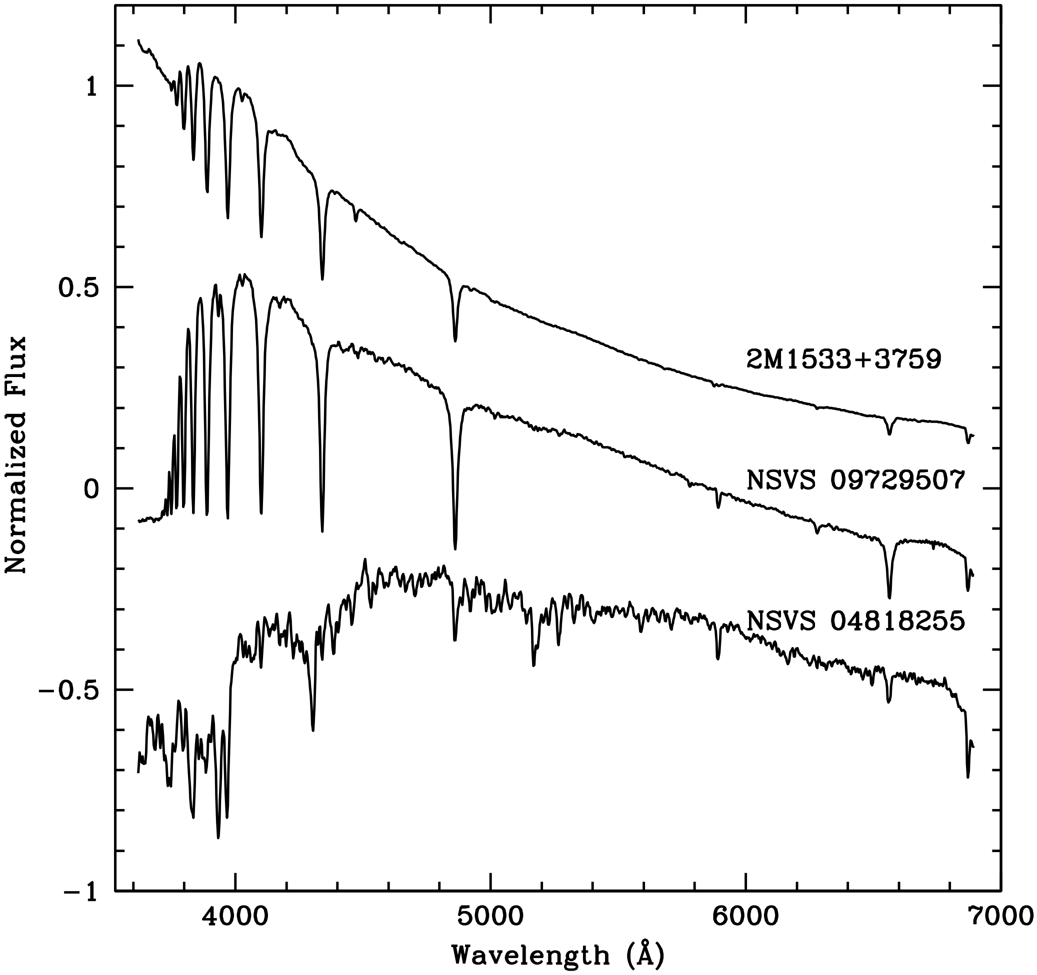

Figure 6.1 Flux-calibrated 2M 1533+3759 spectrum compared to the bluest and reddest non-sdB spectra from Table 6.3.

calibrated using standard IRAF tasks. Details of the individual low resolution spectra are given in Table 6.4. The orbital phases in the last column are discussed in §6.5.1.

We acquired additional medium resolution spectra in 2008 and 2009 for radial velocities, again with the B&C spectrograph on the 2.3 m Bok telescope. For these, we used an 832 mm^{-1} grating in second order with a 1.5$''$ slit to achieve 1.8 Å resolution over a wavelength range of 3675–4520 Å. The slit was aligned with the parallactic angle at the midpoint of each exposure, the same as for the low resolution spectra, but comparison HeAr spectra were taken before and after each stellar spectrum. The spectra were reduced in a similar manner, except that they were not flux-calibrated. After wavelength calibration, the radial velocity spectra were interpolated onto a log-wavelength scale. The continuum was removed from each spectrum by dividing through by a spline fit to the continuum, and then subtracting a constant equal to unity in order to get a continuum value of zero. Table 6.5 lists the details of the medium resolution spectra. The radial velocities are described in §6.4.1 and the orbital phases in §6.5.1.

6.3.2 Differential Photometry

Differential *BVRI* light curves for 2M 1533+3759 were obtained at the Steward Observatory 1.55 m Kuiper telescope on Mt. Bigelow, Arizona, between February and June of 2008 and in 2009 March. We used the Mont4K facility CCD camera[2] with Harris *BVR* and Arizona *I* filters. Several hundred bias images and dome flats were obtained each day to reduce the error budget

---

[2] See http://james.as.arizona.edu/ psmith/61inch/instruments.html for a description of the Mont4K CCD imager and filters.

Table 6.4. Low resolution 2.3 m spectra

UT Date	HJD at midpoint (2450000+)	Exp Time (s)	S/N	Orbital Phase
27 Jun 2005	3548.82037	550	165	0.72
30 Dec 2007	4465.04391	480	174	0.44
31 Dec 2007	4466.03402	400	161	0.56
19 Jan 2008	4485.02730	490	162	0.97
19 Sep 2008	4728.61983	450	179	0.76

due to calibrations to less than 0.001 magnitude. The time stamp for each image is written by the clock on the CCD computer, which is synchronized with the on-site GPS system every 120 s, so that the times are always correct to better than a couple of tenths of a second. To reduce the observational sampling time, we used on-chip 3×3 binning and read out only 2/3 of the CCD rows, resulting in a readout time of 22 s per image. (For 2009, the readout time was reduced to 14 s, as a result of improvements to the electronics.) The remaining overhead time between images was 7 s, including 6 s for the filter change. We alternated between two filters each night in order to obtain two coeval light curves while maintaining adequate sampling of the eclipses. Table 6.6 summarizes the photometric observations.

The images were reduced with a pipeline constructed from standard IRAF tasks. The bias-subtracted images were flat-fielded with the appropriate $BVRI$ dome flat and corrected for bad columns and cosmic rays. Images in the I filter were further corrected by subtracting a scaled, high S/N, zero-mean fringe frame. The fringe frame was constructed from 31 dithered I images, 600 s each, in fields with low stellar density, taken between 2008 March and

Table 6.5. Medium resolution 2.3 m spectra and the derived radial velocities

UT Date	HJD at midpoint (2450000+)	Exp Time (s)	S/N	V (km s^{-1})	$V_{\rm err}$ (km s^{-1})	Orbital Phase
19 Feb 2008	4516.02529	750	83.5	27.15	4.99	0.58
18 Mar 2008	4543.99112	550	80.7	−24.90	5.54	0.46
18 Mar 2008	4544.01329	550	80.0	30.54	4.73	0.59
27 Mar 2008	4552.97753	500	47.3	−9.29	6.68	0.01
17 Apr 2008	4573.93042	600	68.9	15.07	4.80	0.53
18 Apr 2008	4574.94859	550	61.3	68.75	5.65	0.82
25 Apr 2008	4581.88679	500	77.5	73.37	5.03	0.71
25 Apr 2008	4581.98355	625	79.0	−69.29	3.69	0.31
26 Apr 2008	4582.87608	550	77.9	55.20	3.76	0.83
26 Apr 2008	4582.96181	500	81.9	−57.65	3.96	0.36
05 Feb 2009	4868.02541	525	69.7	−2.92	4.54	0.51
14 Mar 2009	4904.83567	725	89.0	−34.43	4.18	0.05
14 Mar 2009	4904.84734	575	78.8	−50.58	3.84	0.13
14 Mar 2009	4904.85772	550	75.2	−68.20	4.23	0.19
14 Mar 2009	4904.86738	550	77.9	−78.37	4.74	0.25
14 Mar 2009	4904.87654	550	80.0	−71.28	4.86	0.31
15 Mar 2009	4905.83299	600	71.6	−66.07	4.46	0.22
15 Mar 2009	4905.84391	600	78.2	−76.04	5.03	0.29
15 Mar 2009	4905.89487	550	79.0	36.78	5.24	0.60
15 Mar 2009	4905.90420	500	75.8	60.08	4.26	0.66
15 Mar 2009	4905.91322	500	74.7	64.20	4.29	0.71
15 Mar 2009	4905.92344	500	74.0	66.27	4.19	0.78
15 Mar 2009	4905.93239	500	73.5	63.25	4.07	0.83
15 Mar 2009	4905.94190	500	71.5	43.94	3.87	0.89
15 Mar 2009	4905.95137	575	73.7	16.80	3.93	0.95
15 Mar 2009	4905.96212	700	59.1	−19.75	4.70	0.02
15 Mar 2009	4905.97491	625	78.1	−38.16	4.60	0.10
16 Mar 2009	4906.82916	575	89.5	−52.76	3.39	0.38
16 Mar 2009	4906.86126	525	86.6	27.75	4.86	0.57
16 Mar 2009	4906.87078	490	79.2	44.75	3.83	0.63
16 Mar 2009	4906.88020	490	80.5	62.30	4.13	0.69
16 Mar 2009	4906.88876	490	81.6	63.09	4.88	0.74
16 Mar 2009	4906.90777	490	82.3	51.32	3.20	0.86
16 Mar 2009	4906.91653	490	83.3	35.74	4.19	0.92
16 Mar 2009	4906.92530	490	70.8	19.09	4.43	0.97
16 Mar 2009	4906.93541	650	82.2	−22.00	4.08	0.03
16 Mar 2009	4906.94885	650	92.3	−48.09	3.14	0.12
16 Mar 2009	4906.97131	575	87.4	−74.59	4.20	0.25

May; the fringe pattern was very stable over that time interval. Aperture photometry was performed for the sdB and a set of reference stars, with the aperture radius set to 2.25 times the average FWHM in each image. The same set of eight, apparently nonvariable, reference stars was used with every filter; the reference stars were chosen to be distributed as closely and symmetrically as possible around 2M 1533+3759 (Figure 6.2). The differential magnitudes (sdB minus the average of the reference stars) were converted to relative fluxes and normalized to 1.0 near the quarter phase of the star's orbit.

The resulting light curves, shown below in Figure 6.6 and further discussed in §6.7, have well-defined primary and secondary eclipses. The peak-to-peak amplitudes of the reflection effect are 0.10, 0.13, 0.15, and 0.19 magnitudes, respectively, in the $BVRI$ filters.

6.4 Spectroscopic Analysis

6.4.1 Radial Velocities

We derived the radial velocities iteratively using a double-precision version of the IRAF task FXCOR. The initial velocity template was constructed by combining and median-filtering all 38 medium resolution spectra. The individual spectra were cross-correlated against the template by fitting a Gaussian to the cross-correlation peak to determine the velocity shifts. The spectra were then Doppler-shifted to the same velocity and recombined into an improved template. Five iterations were required to reach convergence. Columns 5 and 6 in Table 6.5 list the derived radial velocities and their associated errors. Since FXCOR velocity errors are only known to within a scale factor, the final step was to scale the FXCOR errors so that the average error matches the standard deviation of the observed points about the fitted velocity curve.

Table 6.6. Photometric observations at the Steward Observatory 1.55 m Mt. Bigelow telescope

UT Date	Start HJD (2450000+)	End HJD (2450000+)	Filter	Exp time (s)
27 Feb 2008	4523.879786	4523.982705	B,R	30,25
28 Feb 2008	4524.943268	4525.031564	B,R	30,25
06 Mar 2008	4531.902243	4532.025496	B,R	30,25
07 Mar 2008	4532.896078	4533.016714	B,R	30,25
10 Mar 2008	4535.898112	4536.025827	B,R	30,25
11 Mar 2008	4536.942407	4537.022719	B,R	30,25
29 Mar 2008	4554.843844	4555.016093	B,R	30,25
12 Apr 2008	4568.787329	4568.974478	V,I	30,45
13 Apr 2008	4569.831345	4569.994764	V,I	30,45
26 Apr 2008	4582.818149	4582.981342	V,I	30,45
27 Apr 2008	4583.752365	4583.926433	B,R	35,30
22 Jun 2008	4639.674751	4639.710198	B,R	35,30
28 Mar 2009	4639.674751	4639.710198	B,R	30,25

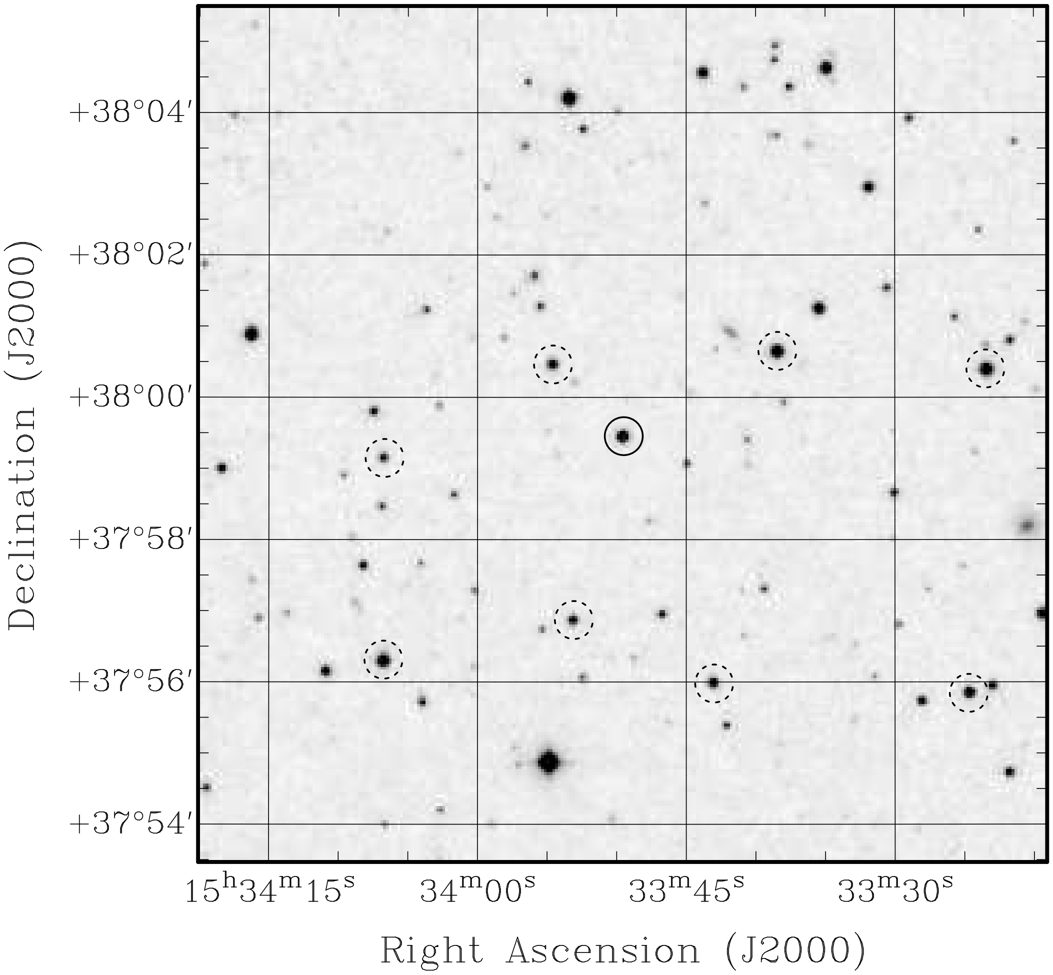

Figure 6.2 Finder chart for 2M 1533+3759. The solid circle in the center of the chart is 2M 1533+3759. The dashed circles are the adopted reference stars.

The radial velocity solution was determined using a weighted least-squares procedure to fit a sine curve. The orbital period was fixed at the value derived from the eclipse times in the following section, since the photometric period is much more precise than the period derived from the velocities. The radial velocity solution is shown in Figure 6.3. The velocity semi-amplitude is $K_1 = 71.1 \pm 1.0$ km s^{-1}. The systemic velocity, $\gamma = -3.4 \pm 5.2$ km s^{-1}, was determined relative to three sdB radial velocity "standards", PG 0101+039, PG 0941+280, and PG 2345+318, one or two of which were observed each night[3].

6.4.2 Spectroscopic Parameters

We fit the Balmer lines from Hβ to H11 and the strongest helium lines (4922 Å, 4471 Å, and 4026 Å) in our low-resolution spectra to synthetic line profiles calculated from a grid of zero-metallicity non NLTE (NLTE) atmospheric models. Our expectation was that the reflection effect in 2M 1533+3927 would introduce negligible contamination from the secondary. The only sdB+dM binary whose spectroscopic parameters have previously been reported to vary with orbital phase is HS 2333+3927 (Heber et al. 2004), and its reflection effect is more than twice as large as that of 2M 1533+3927. We were therefore surprised to find that our individual low resolution spectra for 2M 1533+3927 do in fact give significantly different temperatures at different orbital phases, amounting to the better part of 1000 K.

We therefore returned to our more numerous medium resolution spec-

---

[3] These are actually short-period sdB+WD binaries with large velocity amplitudes that we have observed for 10 to 15 years, whose velocities are known to 1–2 km s^{-1} at any given time.

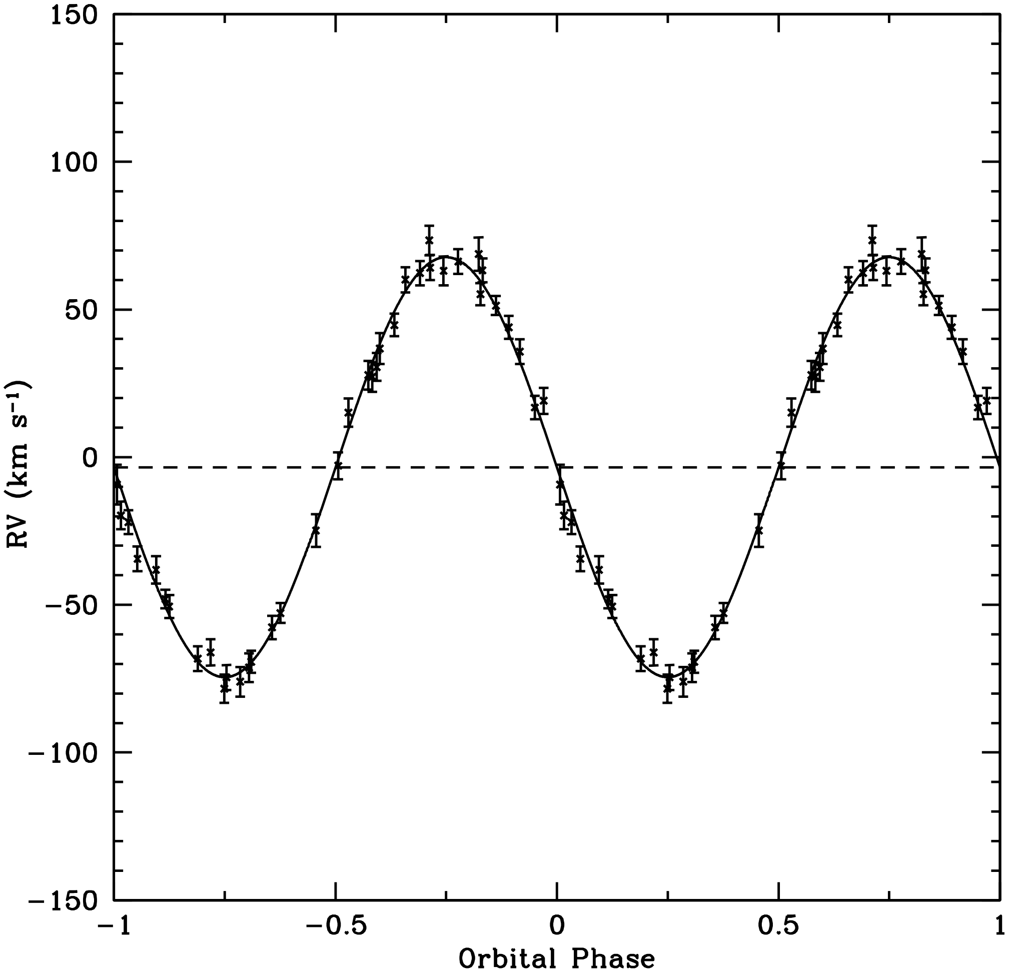

Figure 6.3 Radial velocity solution for 2M 1533+3759 as a function of orbital phase, superimposed on the observed velocities. The velocity amplitude and systemic velocity are $K_1 = 71.1 \pm 1.0$ km s^{-1} and $\gamma = -3.4 \pm 5.2$ km s^{-1}.

tra, and (after reinterpolating onto a linear wavelength scale) fit Hγ through H11, He 4471 Å, and 4026 Å, again using zero metallicity NLTE models. The medium resolution spectra show the same orbital temperature effect (Figure 6.4), with about the same amplitude, even though they exclude Hβ (which suffers the most from contamination by the secondary of all the lines we considered). The lowest derived temperatures are found from spectra taken near minimum light. The unexpected prominence of the temperature variations with orbital phase is probably due to the high S/N noise of our spectra (70–90 per pixel). There is also a suggestion of a similar trend with gravity, but the derived helium abundances were negligibly affected. (For unknown reasons, our temperature variations are in the same sense as those derived by Heber et al. (2004) using only helium lines (their Figure. 7b), and in the opposite sense from what they found when fitting both Balmer and helium lines, although naturally we see smaller amplitude variations for 2M 1533+3759.)

To be safe, we adopted atmospheric parameters determined from 14 spectra observed near minimum light, i.e., orbital phases between 0.8 and 1.2, not including the two points closest to the center of the eclipse. (The temperature derived at the midpoint of the primary eclipse was surprisingly discrepant, possibly due to absorption of some of the uneclipsed sdB light near the limb of the secondary; discrepant gravity values were also seen during both eclipses.) The excellent quality of the fit can be seen in Figure 6.5. Our adopted spectroscopic parameters are $T_{\rm eff} = 29230 \pm 125$ K, $\log g = 5.58 \pm 0.03$, and log $N(\mathrm{He})/N(\mathrm{H}) = -2.37 \pm 0.05$, where the errors are the standard deviations of the values from the individual spectra. This $T_{\rm eff}$ was used as the initial value for the primary temperature in our light curve modeling in §6.5.2.

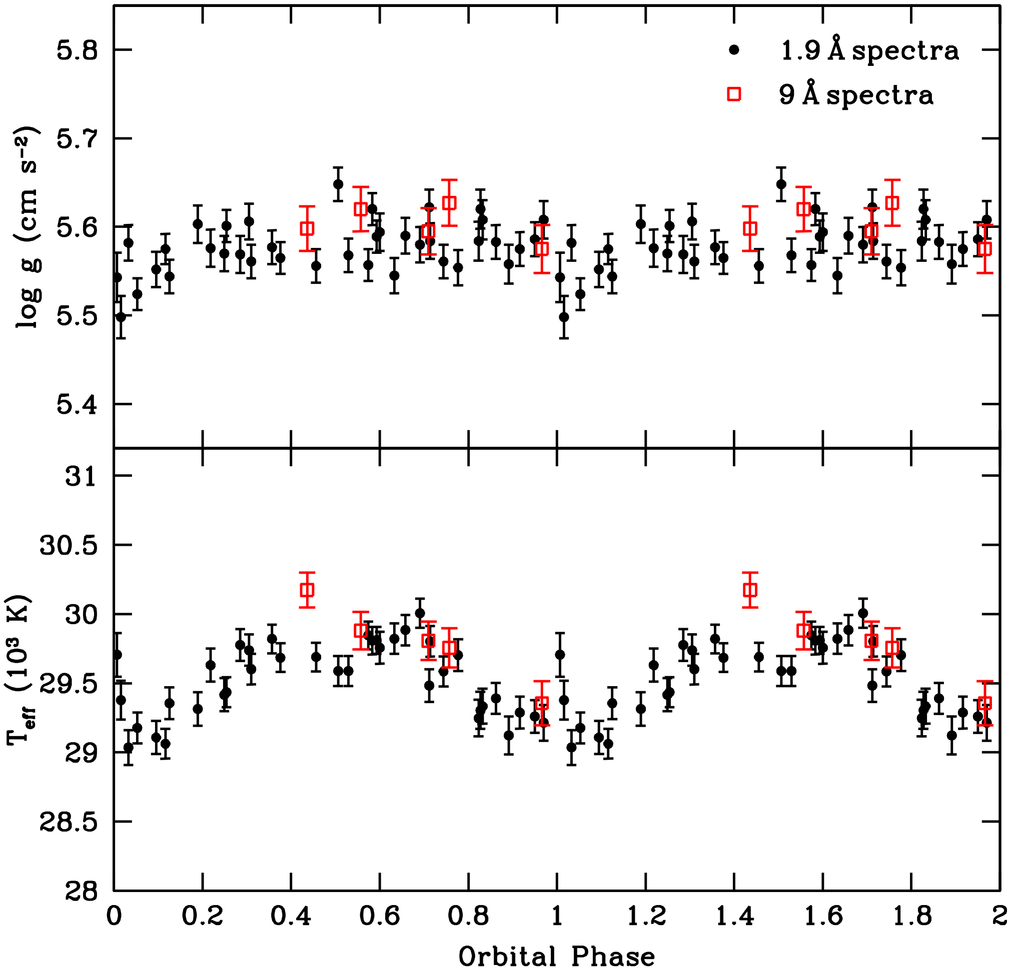

Figure 6.4 Derived gravities (above) and effective temperatures (below) as a function of orbital phase, from fits to Balmer and helium lines in 2M 1533+3759.

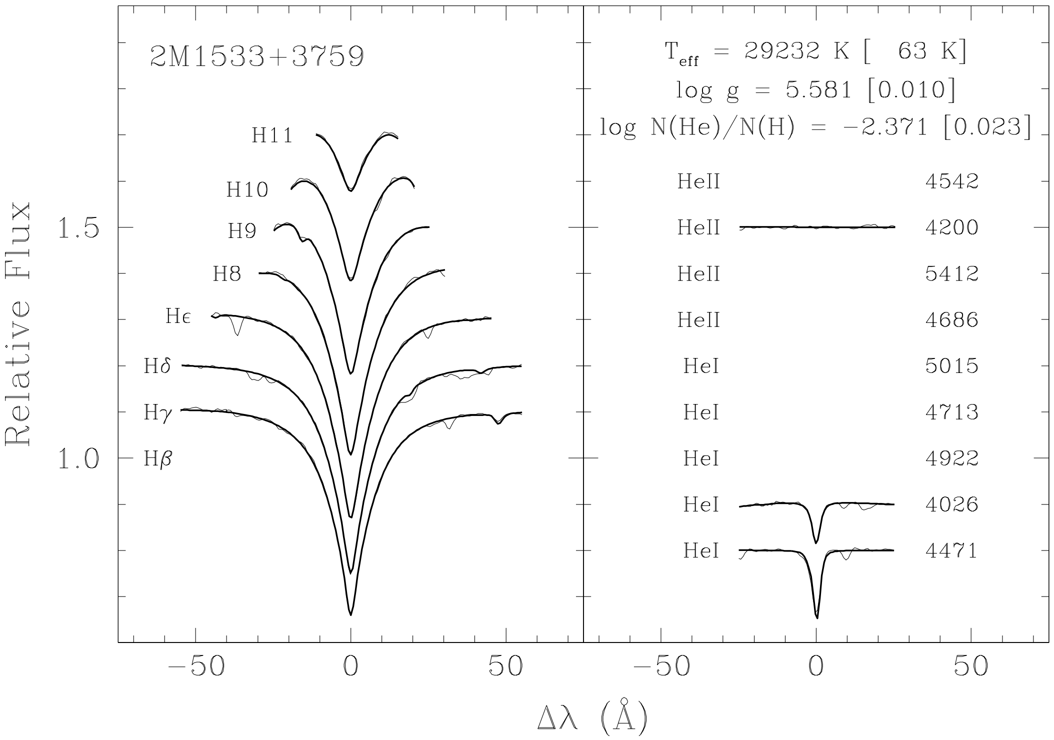

Figure 6.5 Fits of the Balmer and helium lines in the combined 2M 1533+3759 minimum light spectrum to synthetic zero metallicity NLTE line profiles.

6.5 Photometric Analysis

6.5.1 Ephemeris

We solved for the orbital period using a linear least-squares fit to the well-defined times of primary and secondary eclipse minima in the V and R light curves, in the equation $T_{min} = T_0 + nP$, where T_{min} are the times of the eclipse minima, T_0 is the reference HJD for the primary eclipse at $n = 0$, n are the cycle numbers, and P is the orbital period in units of a day.

The time of minimum for each observed primary and secondary eclipse was determined by fitting an inverse Gaussian to the eclipse shape. The results are listed in Table 6.7, along with the corresponding cycle numbers, the instrumental filter, and the $O - C$ time residuals. The standard deviation of the $O - C$ values is 3.3 s. The derived ephemeris for the primary eclipses is

$$\mathrm{HJD} = (2454524.019552 \pm 0.000009) + (0.16177042 \pm 0.00000001) \times \mathrm{E}.$$

6.5.2 Light Curve Modeling

The $BVRI$ light curves were phased with the ephemeris and orbital period derived from the photometry. Small vertical flux differences equivalent to a few hundredths of a magnitude remained in the phased light curves. These could be due to slight long term variability in one or more of the reference stars, but are more likely to be caused by subtle variations in the dome flats from different runs. We therefore shifted the light curves in the same filter vertically by a small constant to minimize the standard deviation of the total phased light curves for that filter. The light curves for all four filters were analyzed simultaneously with the MOdified ROche (MORO) code (Drechsel et al. 1995).

The MORO code adopts the Wilson-Devinney monochromatic light, synthetic light curve calculation approach (Wilson & Devinney 1971), but has

Table 6.7. Times of minima of 2M 1533+3759

Mid Eclipse (HJD 2450000+)	Error	Epoch	Type	Filter	$O-C$ (s)
4523.93875	2.5×10^{-5}	−0.5	sec.	R	7.2
4524.99017	1.5×10^{-5}	6.0	pri.	R	−0.4
4531.94631	1.5×10^{-5}	49.0	pri.	R	0.6
4532.91693	1.5×10^{-5}	55.0	pri.	R	0.4
4532.99788	2.5×10^{-5}	55.5	sec.	R	6.0
4535.90970	2.5×10^{-5}	73.5	sec.	R	1.9
4535.99054	1.5×10^{-5}	74.0	pri.	R	−2.0
4536.96115	1.5×10^{-5}	80.0	pri.	R	−3.1
4554.91769	1.5×10^{-5}	191.0	pri.	R	−1.1
4554.99860	2.5×10^{-5}	191.5	sec.	R	1.0
4568.82995	1.5×10^{-5}	277.0	pri.	V	−0.8
4568.91082	2.5×10^{-5}	277.5	sec.	V	−2.1
4569.88151	2.5×10^{-5}	283.5	sec.	V	3.7
4569.96228	1.5×10^{-5}	284.0	pri.	V	−6.2
4582.82312	2.5×10^{-5}	363.5	sec.	V	1.7
4582.90399	1.5×10^{-5}	364.0	pri.	V	0.3
4583.79377	2.5×10^{-5}	369.5	sec.	R	4.0
4583.87460	1.5×10^{-5}	370.0	pri.	R	−0.7
4639.68546	1.5×10^{-5}	715.0	pri.	R	4.8
4918.90113	1.5×10^{-5}	2441.0	pri.	R	−2.1
4918.98208	2.5×10^{-5}	2441.5	sec.	R	3.5

implemented a modified Roche model that takes into account radiation pressure effects in close binaries with hot components. It also replaces the classical Wilson-Devinney grid search differential corrections method with a more powerful $SIMPLEX$ optimization algorithm. This provides several advantages: in particular, the fitting procedure improves with each iteration and is not allowed to diverge. For details of the numerical procedure and the radiation pressure implementation, we refer the reader to the description in Drechsel et al. (1995).

Light curve modeling becomes a challenging task when information about the secondary is limited, as is the case in all single-lined spectroscopic binaries. Since the modeling requires a large set of parameters, it is important to constrain as many as possible based on additional spectroscopic and theoretical information. We assumed the orbit is circular and the stellar rotation is synchronized with the orbit, since the timescales for both circularization and synchronization are a few decades (Zahn 1977), very much shorter than the helium burning lifetime of a horizontal branch star. We adopted the spectroscopic T_{eff} of the sdB as an initial parameter, and took the linear limb darkening coefficients (x_1) of 0.305, 0.274, 0.229 and 0.195 from Diaz-Cordoves et al. (1995) and Wade & Rucinski (1985) for the B, V, R, and I filters, respectively. These values correspond to the nearest available stellar atmosphere model, a star with $T_{\text{eff}} = 30,000$ K and $\log g = 5.0$, and should be very close to the correct values (Wood et al. 1993), since the dependence on the surface gravity is weak. Previous experience with light curve modeling of similar systems (Hilditch et al. 1996) indicates that the limb-darkening coefficient of the cool secondary star (x_2) can deviate highly from normal values for cool dwarf stars, so we decided to treat x_2 as an adjustable parameter. Due to the irradiation effect, the limb-darkening can be expected to be more extreme than for single stars, and thus we employed initial values of 0.7, 0.8, 1.0 and 1.0, for the B, V, R, and I filters, respectively. The primary albedo (A_1) was fixed to 1.0 and its gravity darkening exponent (β_1) was set to 1.0, appropriate for a radiative outer envelope (von Zeipel 1924). The enormous reflection effect suggests a mirror-like surface on the heated side facing the primary, indicating complete reradiation of the primary light; therefore a secondary albedo (A_2) of 1.0 was adopted. We set the gravity darkening exponent (β_2) to 0.32 for the convective secondary (Lucy 1967). The radiation pressure parameter for the secondary star (δ_2) was set to zero because the radiation pressure forces exerted by the cool companion are negligible. A blackbody approximation was used to treat the irradiation of the secondary by the primary. We input central wavelengths of 4400, 5500, 6400, and 7900Å for our $BVRI$ passbands, which are a fair match to the filter passbands convolved with the CCD sensitivity.

The simultaneous light curve modeling was performed with the Wilson-Devinney mode 2 option, for a detached system. The remaining free parameters for the fitting procedure include the orbital inclination, i; the effective temperature of the secondary, T_2; the Roche surface potential, Ω_1 and Ω_2; the mass ratio, $q = M_2/M_1$; the color-dependent luminosity of the primary, L_1; the radiation pressure parameter for the primary, δ_1; and l_3, a potential third light contribution due to a possible unresolved field star or an extended source. The color-dependent luminosity of the secondary, L_2, was not adjusted but was recomputed from the secondary's radius and temperature.

Degeneracy is a common problem encountered in light curve modeling. A high degree of correlation between several parameters (e.g., i, q) can result in several equally good solutions with different families of parameters. Therefore, it is necessary to test for the presence of multiple good solutions over a wide range of mass ratios. The usual procedure is to run a series of initial trials at discrete mass ratios, keeping them fixed. Unfortunately, our first set of trials did not produce any good solutions for mass ratios in the range $1.2 < q < 0.2$, corresponding to either an sdB mass of 0.49 $M_{\odot}$ and M dwarf masses in the range 0.6-0.1 $M_{\odot}$ (M0-M5.5), or to smaller sdB masses and later M spectral types – i.e., there were no solutions that matched the shapes of our observed light curves – because the reflection effect was underestimated by about 30% in all of the models. The trial runs did however suggest that there was no third light contribution, so we set that parameter to zero for the rest of the runs.

A similar, although less extreme, problem was encountered in previous attempts to model the light curves of eclipsing sdB+dM binaries (Kilkenny et al. 1998, PG 1336−018; Drechsel et al. 2001, HS 0705+6700), especially with redder filters, and for the same reason: theoretical models are not sophisticated enough in their treatment of the reflected/reradiated light. Both Kilkenny et al. (1998) and Drechsel et al. (2001) found that if the secondary albedo was treated as a free parameter, their solutions converged to physically unrealistic values, $A_2 > 1.0$, although they were able to find acceptable solutions when A_2 was held fixed at a value of 1.0. Vučković et al. (2007) and Lee et al. (2009), both using Wilson-Devinney synthesis codes, noted that their biggest difficulty concerned the temperature of the heated secondary. This appears to be an alternate version of the same basic problem, i.e. correctly treating the light from the secondary star, which manifests differently in different adaptations of the Wilson-Devinney code. Vučković et al. (2007) were able to find good solutions with $A_2 = 0.92$ by simply fixing their secondary temperature at the average of the values found separately in their two passbands. Lee et al. (2009) had to resort to mode 0 instead of mode 2, allowing L_2 and T_2 to be separate free parameters (rather than computing L_2 from T_2 and R_2), in addition to fixing $A_2 = 1.0$. Since we could not find any acceptable fits to our light curves with MORO when A_2 was set to 1.0, we decided to treat it as an adjustable scale factor, accepting that it would converge to an unphysically high value.

When A_2 was no longer kept fixed, good fits to the light curve shapes were found for the following mass ratios: q =0.301, 0.586, 0.697, 0.800, and 0.888. To discriminate between the possible solutions, we calculated the sdB mass corresponding to each value of q, using the mass function, which can be expressed as

$$\frac{M_1 \times (q \sin i)^3}{(1+q)^2} = \frac{{K_1}^3 P}{9651904}, \tag{6.1}$$

where i is the corresponding inclination angle, which was always $86.6° \pm 0.2°$, and with $K_1 = 71.1$ km s^{-1} and $P = 0.16177042$ day, as derived above. The resulting sdB masses are 0.376, 0.076, 0.052, 0.038, and 0.031 $M_\odot$, respectively. According to evolutionary models, core helium burning sdB stars must have masses substantially larger than 0.08 $M_\odot$, leaving only one reasonable solution, $q = 0.301$.

Once q was constrained to a single approximate value, the problem was reduced to finding the deepest minimum in the surrounding multidimensional parameter space. The *SIMPLEX* algorithm is a very powerful numerical tool, but it is always possible for any algorithm to converge into a less-than-optimal local minimum. To verify that the converged $q = 0.301$ solution was the deepest minimum in the local vicinity, we varied the set of starting parameters over $0.27 < q < 0.35$ ($0.26 < M_1 < 0.50\ M_\odot$) in multiple additional runs, to make sure that they all converged to the same solution within a small error margin, which they did. Table 6.8 lists the best light curve solution for 2M 1533+3759 for all the filters. The standard deviations of the various fits are at the bottom. The observed $BVRI$ light curves are shown together with the calculated theoretical curves in Figure 6.6.

Throughout the previous runs, the temperature of the primary, T_1, was initialized to the spectroscopic value, but it was allowed to be an adjustable parameter. The converged results showed a consistent preference for a higher-than-observed effective temperature, by 1200 K or so. However, once we isolated the best model, we reran the solution while keeping T_1 fixed at 29230 K. The resulting values of the mass ratio, inclination angle, fractional radii, etc., in Table 6.8 are the same, within the errors, whether T_1 is 30400 K or 29230 K.

Figure 6.7 is a series of snapshots from a three-dimensional animation of 2M 1533+3759 at different orbital different phases.

6.6 Geometry and System Parameters

The light curve solution allows us to calculate the absolute system parameters. Substituting the values of K_1 and P from §6.4.1 and §6.5.1 into Eq. (1), along with $q = 0.301$ and $i = 86.6°$, results in component masses $M_1 = 0.376 \pm 0.055\ M_\odot$ and $M_2 = 0.113 \pm 0.017\ M_\odot$. Kepler's law tells us the orbital separation of the two stars, $a = 0.98 \pm 0.04\ R_\odot$, which can then be used to scale the fractional radii from the model solution in order to get the actual radii, $R_1 = 0.166 \pm 0.007\ R_\odot$ and $R_2 = 0.152 \pm 0.005\ R_\odot$.

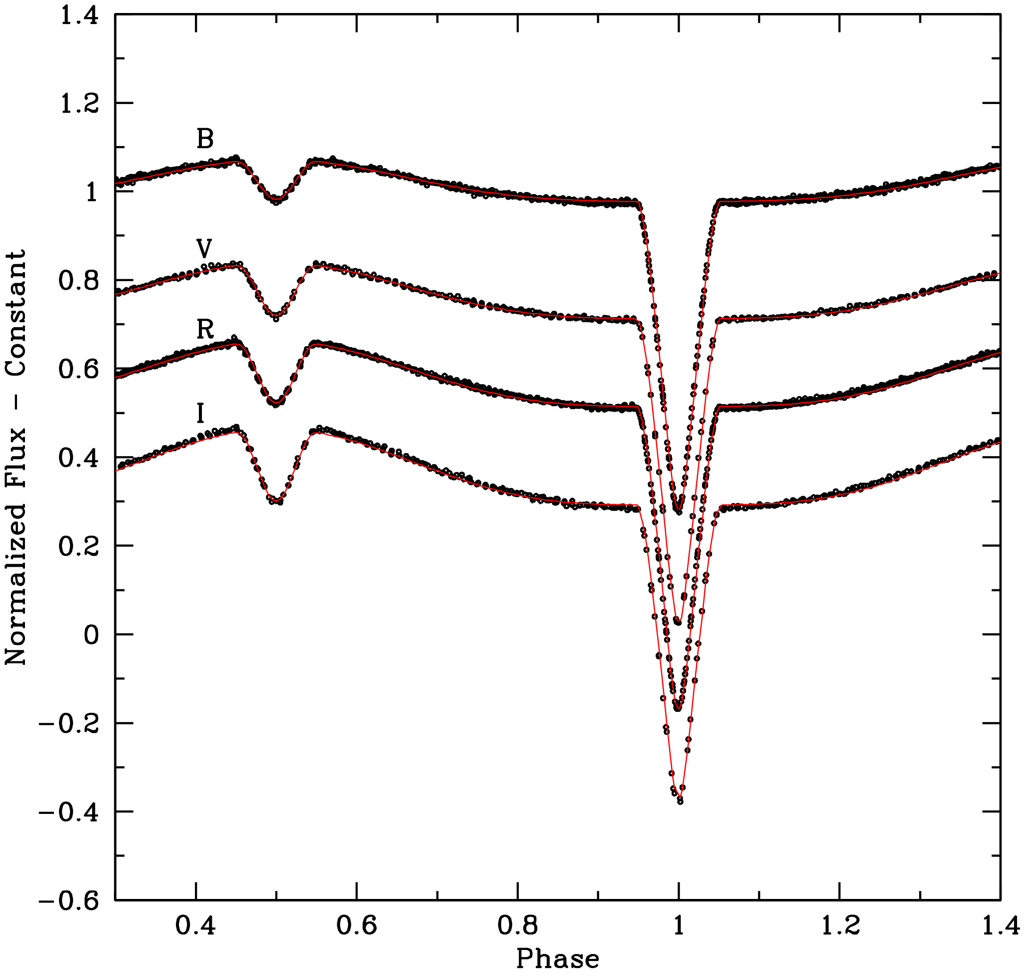

Figure 6.6 The observed light curves superimposed onto the calculated theoretical light curves (solid red lines). The VRI light curves are each offset by a constant with respect to the B light curve.

Table 6.8 Light curve solution for 2M 1533+3759 and goodness of fit.

Fixed Parameters	Value
β_1^a	1.0
β_2^a	0.32
A_1^b	1.0
$x_1(B)^c$	0.305
$x_1(V)^c$	0.274
$x_1(R)^c$	0.229
$x_1(I)^c$	0.195
δ_2^d	0.0
$l_3(B, V, R, I)^e$	0.0
Adjusted Parameters	Value
i	$86.6° \pm 0.2°$
A_2^b	2.0 ± 0.2
$q(M_2/M_1)$	0.301 ± 0.014
Ω_1^f	6.049 ± 0.230
Ω_2^f	3.305 ± 0.098
δ_1^d	0.035 ± 0.043
$T_{\mathrm{eff}}(1)$	30400 ± 500
$T_{\mathrm{eff}}(2)$	3100 ± 600
$x_2(B)^c$	0.83 ± 0.17
$x_2(V)^c$	0.91 ± 0.09
$x_2(R)^c$	0.95 ± 0.05
$x_2(I)^c$	1.00 ± 0.02
$L1(B)^g$	0.99996 ± 0.00004
$L1(V)^g$	0.99978 ± 0.00017
$L1(R)^g$	0.99941 ± 0.00043
$L1(I)^g$	0.99821 ± 0.00116
Fractional Roche Radii^h	Value
r_1(pole)	0.168 ± 0.003
r_1(point)	0.169 ± 0.003
r_1(side)	0.168 ± 0.002
r_1(back)	0.169 ± 0.002
r_2(pole)	0.153 ± 0.001
r_2(point)	0.154 ± 0.004
r_2(side)	0.154 ± 0.001
r_2(back)	0.157 ± 0.003
Standard Deviation	
σ_B	0.0072
σ_V	0.0061
σ_R	0.0069
σ_I	0.0080

[a] Gravity darkening exponent.

[b] Bolometric albedo.

[c] Limb darkening coefficient.

[d] Radiation pressure parameter.

[e] Fraction of third light at maximum.

[f] Roche surface potential.

[g] Relative luminosity, $L_1/(L_1 + L_2)$.

[h] In units of separation of mass centers.

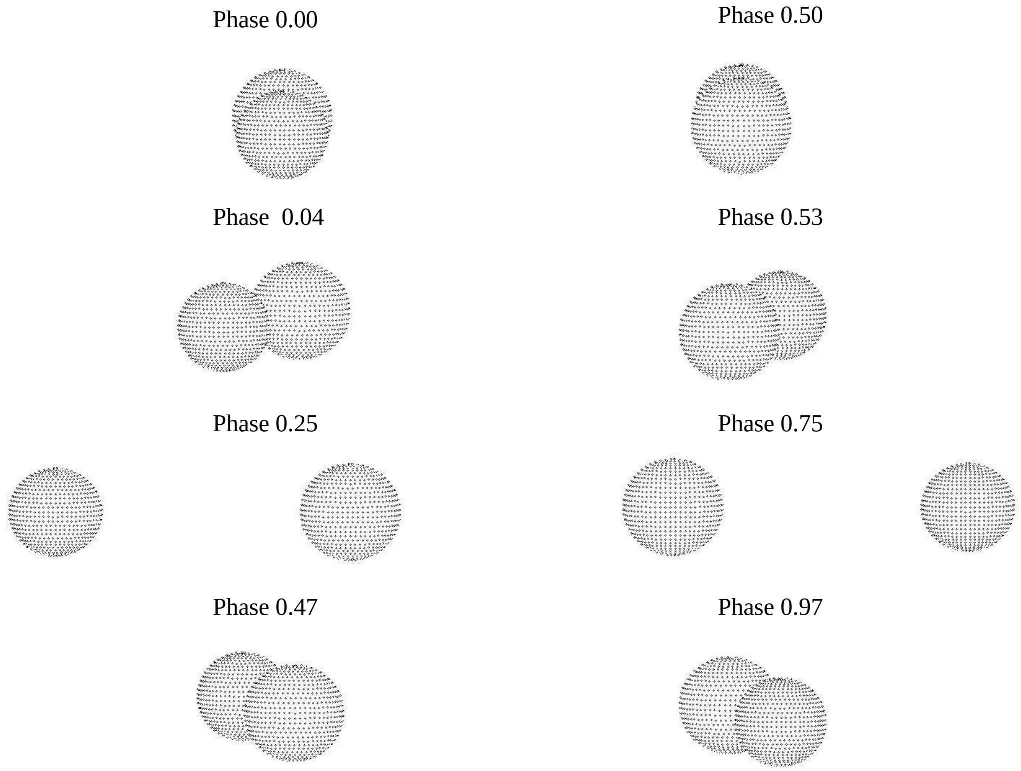

Figure 6.7 Snapshots of 2M 1533+3759 at various orbital phases, as viewed from an inclination angle of 86.6°. Left column, top to bottom: phase 0.00 (primary eclipse), 0.04, 0.25 and 0.47. Right column, top to bottom: phase 0.50 (secondary eclipse), 0.53, 0.75 and 0.97.

The light curve modeling is completely independent of the observed spectroscopic gravity, which therefore provides a nice consistency check. The calculated $\log g$ corresponding to our derived M_1 and R_1 turns out to be 5.57 ± 0.07, essentially identical with our adopted spectroscopic value of 5.58.

In the past, error bars have not usually been attached to masses derived from modeling light curves of sdB+dM binaries, but we found it to be a very instructive exercise. The formal error propagation for the primary mass, according to equation (1), includes the uncertainties on q, i, and K_1, and P. Although the mass depends on the cubic power of both K_1 and q, the error in K_1 is small enough in our case that the mass uncertainties are dominated by the uncertainty in q, as small as it is. Ninety five percent of the error in M_1 is due to the $3M_1\Delta q/q$ term. Our inability to more tightly constrain the sdB mass is a dramatic illustration of why useful mass constraints from light curve modeling can usually be obtained only for eclipsing systems (unless, of course, good radial velocities can be obtained from both components). Furthermore, even with an eclipsing sdB+dM binary, the light curve shapes and velocity amplitude must be sufficiently precisely observed to adequately minimize the other error terms, or else the uncertainty in the mass will be even larger.

The temperature of the secondary is somewhat more uncertain, 3100 ± 600 K, since it contributes almost negligibly to the total light, aside from the reflection effect. Nevertheless, our model value for T_2 is quite acceptable. According to the theoretical $T_{\rm eff}$-mass-luminosity relation of Baraffe & Chabrier (1996), the predicted temperature and radius of a 0.113 $M_\odot$ main-sequence star should be 2854 K and 0.138 $R_\odot$, respectively, corresponding to an M5 dwarf. The empirical mass-radius relation of Bayless & Orosz (2006) for low mass main sequence stars gives an identical radius of 0.138 $R_\odot$. Our value of

Table 6.9. Fundamental parameters of 2M 1533+3975

Parameter	Value
T_{eff_1} (K)	29230 ± 125
$\log g$ (cm s^{-2})	5.58 ± 0.03
$\log N(\mathrm{He})/N(\mathrm{H})$	-2.37 ± 0.05
Period (days)	$0.16177042 \pm 0.00000001$
T_0 (days)	$2454524.019552 \pm 0.000009$
K_1 (km s^{-1})	71.1 ± 1.0
γ (km s^{-1})	-3.4 ± 5.2
M_1 ($M_\odot$)	0.376 ± 0.055
M_2 ($M_\odot$)	0.113 ± 0.017
a ($R_\odot$)	0.98 ± 0.04
R_1 ($R_\odot$)	0.166 ± 0.007
R_2 ($R_\odot$)	0.152 ± 0.005
T_{eff_2} (K)	3100 ± 600
V_{rot_1} (km s^{-1})	52 ± 2
L_1 ($L_\odot$)	18.14 ± 1.84
M_{V_1}	4.57 ± 0.21
d (pc)	644 ± 66

0.152 $R_\odot$ is slightly larger (although still within the 3σ error), but it would not be unexpected if the highly heated and already slightly distorted secondary in a system like 2M 1533+3759 turned out to be a little larger than an isolated M dwarf of the same mass.

Table 6.9 summarizes the system parameters for 2M 1533+3759, beginning with our adopted spectroscopic parameters and the photometric and radial velocity solutions described in the previous sections.

6.7 Discussion

We examined several possible systematic effects, beginning with our spectroscopic parameters. Under the reasonable assumption that the primary's rotation is synchronized with the orbital period, its rotational velocity should be $V_{\mathrm{rot}_1} = 2\pi R_1/P = 52 \pm 2$ km s^{-1}. This corresponds to 1.0 pixel in our medium resolution spectra, which have an instrumental FWHM of 2.75 pixels. We reanalyzed our combined minimum-light spectrum after broadening the synthetic spectra by this extra amount, and found that the expected rotation has a negligible effect on the spectroscopic parameter determination. The derived temperature was reduced by 10 K and the gravity was reduced by 0.002 dex.

Next, we investigated the effects of using zero metallicity NLTE atmospheres to derive our spectroscopic parameters, since metal lines are observed to be present in sdB atmospheres, especially in the UV. Two of us (G.F. and P.C.) conducted an experiment in which TLUSTY was used to construct a synthetic model atmosphere at a temperature of 28000 K, $\log g = 5.35$, log $N(\mathrm{He})/N(\mathrm{H}) = -2.70$, and solar abundances of C, N, O, S, and Fe. Using our zero metallicity NLTE grid, the derived parameters were found to be $T_{\mathrm{eff}} = 30096$ K, $\log g = 5.54$, and log $N(\mathrm{He})/N(\mathrm{H}) = -2.72$. At these abundances, we would have overestimated the effective temperature by about 2000 K and the surface gravity by almost 0.2 dex, so the true values for 2M 1533+3759 would be about 27300 K and 5.40, respectively. Happily, the light curve solution is amazingly robust. The model results obtained by further lowering the primary temperature to a fixed value of 27300 K are only negligibly different from our original solution. Thus, the system parameters would remain essentially the same: $q = 0.303$, $i = 86.5°$, $M_1 = 0.370\ M_\odot$,

$M_2 = 0.112\ M_\odot$, $R_1 = 0.165\ R_\odot$, $R_2 = 0.152\ R_\odot$, and $a = 0.98\ R_\odot$. The calculated sdB surface gravity would also be unchanged, $\log g = 5.57 \pm 0.03$, but would no longer be as consistent with the expected gravity of 5.40. This implies that the atmospheric abundances in 2M 1533+3759 are not as large as the solar values assumed above.

We spent considerable time worrying about the very large secondary albedo, $A_2 \sim 2$, that was required to obtain a solution which fits the observed shapes of the 2M 1533+3759 light curves, since all previous sdB+dM analyses were able to find acceptable light curve solutions with $A_2 \sim 1$. We tested the version of MORO running at the University of Texas using Drechsel et al.'s (2001) input datafile, and found exactly the same solution that they did. We verified that an independent Steward V light curve data for HS 0705+6700, in the same format as our 2M 1533+3759 data, produced a curve that fell exactly between Drechsel et al.'s (2001) normalized B and R data for HS 0705+6700, thus eliminating problems with our input format. We shifted the $BVRI$ effective wavelengths specified to MORO by up to 200 Å, with no effect on the output solution.

Our dataset is unique among published sdB+dM light curve analyses in extending to the I filter. Drechsel et al. (2001) fit only B and R data, Heber et al. (2004) fit BVR, Vučković et al. (2007) used g' (intermediate between B and V) and r' (close to R), and Lee et al. (2009) had only V and R. We therefore reanalyzed our 2M 1533+3759 data using only the B and R light curves. The results were the same as before: when A_2 is allowed to be a free parameter, the solution always converges to A_2 near 2. Furthermore, no new solutions appear for other q values, and the solution for $q = 0.301$ is nearly identical to our previous best solution. If A_2 is forced to have a value of 1, the

B and R solutions fail to fit the observed light curve shapes in nearly the same manner as our original trial solutions at the same A_2 and q. The amplitude of the theoretical reflection effect with $A_2 = 1$ using current models simply is not large enough to fit 2M 1533+3759.

An alternate way to look at this problem is to compare the reflection effect amplitudes in 2M 1533+3759 versus HW Vir. HW Vir was selected because it has the next longest orbital period of well-studied eclipsing sdB+dM systems besides 2M 1533+3759, and because our high S/N spectra give essentially identical temperatures and gravities for these stars when analyzed in a homogeneous manner. However complicated the physics of the reflection effect may be, the actual processes ought to be similar in both systems. Thus, to first order, the reflection effect amplitudes should be proportional to the luminosity of the primary and the surface area of the heated face of the secondary, and inversely proportional to the distance between the two stars. Using our values of R_1, $T_{\mathrm{eff}\,1}$, R_2, and a for 2M 1533+3759, and Lee et al.'s (2009) values for HW Vir (0.183 $R_\odot$, 28490 K, 0.175 $R_\odot$, and 0.86 $R_\odot$, respectively) to calculate the ratio of $R_1^2 T_{\mathrm{eff}\,1}^4 R_2^2 / a^2$ for the two binaries, we find that the amplitude in 2M 1533+3759 ought to be 53% of the amplitude in HW Vir. Instead, it is observed to be 95% of the HW Vir amplitude. It seems that the reflection effect in 2M 1533+3759 really is stronger than would be expected, compared to other known eclipsing sdB+dM binaries. Another light curve solution might give a different result, but an exhaustive search of parameter space failed to find any other solution that fit our data.

The most interesting result of our modeling is the unusually low mass obtained for the sdB star in 2M 1533+3759. The vast majority of sdB masses derived previously from asteroseismology of sdB pulsators (Table 6.1) or by modeling sdB+dM binaries (Table 6.2) are clustered near the canonical value of 0.48 $M_{\odot}$, i.e. near the mass of the degenerate He core at helium ignition in low mass red giants. However, there are at least one or two other hot subdwarfs for which masses lower than 0.4 $M_{\odot}$ have also been found.

The first anomalously low mass for a hot subdwarf was found for the eclipsing sdO+dM binary, AA Dor, although this result continues to be the subject of debate (Rucinski 2009; Fleig et al. 2008; Vučković et al. 2008, and references therein). The most recent values for the sdO mass, 0.25 $M_{\odot}$ (Rucinski 2009) and 0.24 $M_{\odot}$ (from Fleig et al.'s values for the surface gravity, 5.30, and radius, 0.181 $R_{\odot}$) are too low for a core helium burning star, implying that AA Dor is on a post-RGB cooling track, as originally suggested by Paczynski (1980). This is consistent with the fact that AA Dor (42000 K) is much hotter than sdB stars.

Heber et al. (2004, 2005) used the MORO code to model light curves of HS 2333+3927, the non-eclipsing sdOB+dM binary with the largest known reflection effect, and found two good solutions with quite different secondary albedos, $A_2 = 0.39$ and $A_2 = 1.00$. Interestingly, their spectroscopic $\log g$ and mass–radius relations convincingly argued that the lower albedo solution should be preferred - the opposite of what has been required for all other sdB+dM light curve modeling - resulting in a primary mass of 0.38 ± 0.09 $M_{\odot}$ for HS 2333+3927. However, Heber et al. pointed out that a mass of 0.47 $M_{\odot}$ corresponds to $\log g = 5.86$, only 0.16 dex larger than their observed spectroscopic $\log g = 5.70$, leaving room for doubt about the mass. While it is clear that a non-eclipsing system is inherently more uncertain than an eclipsing one, there are two further pieces of evidence in favor of a lower mass for HS 2333+3927. Heber et al.'s gravity was derived using zero metallicity NLTE atmospheres, and if the metallicity corrections at 36000 K go in the same direction as they do at several thousand degrees cooler, then any such corrections should reduce the gravity, and therefore lower the derived mass. We can also corroborate their observed surface gravity from our own independent measurements of multiple high S/N spectra taken within 15 minutes of the minimum of the reflection effect (Green et al. 2008), similarly analyzed with zero-metal NLTE synthetic atmospheres. While optical spectra are not as free from the secondary contamination as ultraviolet spectra, our derived $\log g$ of 5.70 is nevertheless identical to Heber et al.'s value, supporting their lower value for the mass. (Heber et al. alternately suggested that HS 2333+3927 might be on a post-RGB cooling track, although that would require an even lower mass of 0.29 $M_\odot$.)

Østensen et al. (2008) reported a very low mass ($< 0.3\ M_\odot$) for the eclipsing sdB, HS 2231+2441, but their result is rather uncertain, as it depends strongly on the spectroscopic $\log g = 5.39$, which was determined using solar abundances. Our independent estimate of the gravity for this star, using the same homogeneous zero-metal NLTE atmospheric models that we used for 2M 1533+3927 and HS 2333+3927, is 5.51, consistent with a mass of 0.47 $M_\odot$. The true value is presumably somewhere in between. Further investigation is required to better assess the sdB mass in HS 2231+2441.

Randall et al. (2007) utilized the completely different technique of asteroseismology to derive a mass of $0.39 \pm 0.01\ M_\odot$ for the p-mode sdB pulsator, PG 0911+456. The high precision is due to the fact that the envelope pulsations are extremely sensitive to the surface gravity. It turns out that any systematic metallicity corrections would also tend to reduce the mass in this case, as well. This is because the asteroseismic models were calculated for a fixed temperature, the observed spectroscopic value of 31940 K, which was once again determined by fits to synthetic zero metal NLTE atmospheres. There is a known degeneracy in mass versus temperature (and gravity) for similar sdB asteroseismic solutions (Charpinet et al. 2005b). For PG 0911+456, every 400 K decrease in the assumed effective temperature due to metallicity corrections would lower the derived sdB mass by about 0.01 $M_{\odot}$.

Given the robustness of our light curve solution, the mass of 0.376 ± 0.055 $M_{\odot}$ for 2M 1533+3927 appears rather firm. Thus, there is now significant evidence from two completely independent observational and analytical techniques, asteroseismology and light curve modeling in binary stars, for the existence of sdB stars with masses around 0.38 $M_{\odot}$.

Even one or two sdB stars with masses less than $0.40 - 0.43$ $M_{\odot}$, out of about 16 whose masses are fairly well determined, constitute an important fraction. One such star might conceivably lie on a post-RGB cooling track but the odds are very much against it. For example, 2M 1533+3927, PG 0911+456, and HS 2333+3927 all fall near the extremely fast loop at the beginning of Althaus et al.'s (2001) 0.406 $M_{\odot}$ cooling track (between C and D in their Figure 1), but the few years spent in that early phase are insignificant compared to typical core helium burning lifetimes ($\sim 10^8$ yr). The only post-RGB stars with any reasonable likelihood of being seen at the temperatures and gravities of typical sdB stars have masses less than 0.30 $M_{\odot}$ (Althaus et al. 2001; see also Figure 10 of Heber et al. 2004). The evidence therefore suggests that sdB stars with masses near 0.38 $M_{\odot}$ are bonafide core helium burning horizontal branch stars.

The mass of PG 0911+456 is more precisely known and therefore the evolutionary history is more interesting. It does not now appear to be in a binary system (Randall et al. 2007), and it is not clear why some, but not all, single $\sim 2\ M_\odot$ progenitors would lose their entire envelopes. The merger of two helium white dwarfs is not a completely satisfactory alternative – Han et al.'s sdB models give a lower limit of $0.4\ M_\odot$ for the product of such a merger – unless some of the mass in the two white dwarfs can somehow manage to escape during the merger. Politano et al's (2008) common envelope merger model predicts a lower mass limit ($\leq 0.32\ M_\odot$), in better agreement with the observed mass of PG 0911+456. Their model also hypothesizes that since fast rotators lose more envelope mass, a significant fraction of the envelope angular momentum would be carried away, slowing down the star's rotation. However, PG 0911+456 has an unusually low rotational velocity, less than 0.1 km s^{-1}, and it is not clear if a common envelope merger could explain the loss of essentially all the envelope mass as well as nearly all the angular momentum.

2M 1533+3759 has clearly been through an initial common envelope. Theoretical investigations, from the first in-depth study by Sweigart et al. (1989) to recent work aimed specifically at binary systems expected to produce hot subdwarfs (Han et al. 2002, 2003; Hu et al. 2007), indicate that helium burning cores somewhat less than $0.40\ M_\odot$ are produced by stars with initial masses greater than about $2\ M_\odot$, which undergo non-degenerate helium ignition. Of course, 2M 1533+3759 might still have had a degenerate helium flash if the mass of the sdB is toward the upper end of the possible range. Still, either way, a helium core mass less than about $0.43\ M_\odot$ ought to have evolved from a main sequence progenitor with an initial mass of at least $1.8 - 2.0\ M_\odot$, which corresponds to a main sequence A star (Binney & Merrifield 1998). 2M 1533+3759 therefore presents the best observational evidence so far that stars with initial main sequence masses this large can be sdB progenitors. (The situation in sdB binaries with compact companions is less clear, since mass may have been transferred to the sdB progenitor during the evolution of the original primary.)

Previously, the upper limit to the mass of an sdB progenitor could only be estimated from the fact that sdB stars have not been found in any galactic clusters younger than NGC 188, which has an age of 6–7 Gyr and a turnoff mass of 1.1 $M_\odot$ (Meibom et al. 2009). Small number statistics clearly play an important role here, since there are only two hot subdwarfs in NGC 188, and half a dozen or so in NGC 6791 (Landsman et al. 1998), the only other old open cluster known to contain such stars, and the majority of younger open clusters are even less massive than these two.

Indeed, at a mass of 0.38 $M_\odot$, 2M 1533+3759 (and perhaps also HS 2333+3927, if the latter's mass is in fact less than 0.4 $M_\odot$) would fall at the low mass end of Han et al.'s (2003) preferred distribution for the first common envelope ejection channel (see their Figure 12). The existence of a binary like 2M 1533+3759 therefore may also provide support for Han et al's (2002, 2003) assumption that a fraction of the ionization energy contained in the progenitor red giant's envelope combines with the liberated gravitational potential energy to enable the ejection of the common envelope. Without this extra energy, it would be more difficult to eject the envelope around such a massive red giant and a 0.1 $M_\odot$ M dwarf secondary, and the two might well merge (Sandquist et al. 2000).

6.8 Subsequent Evolution

We consider the possible CV scenario for the subsequent evolution of 2M 1533+3759. If we assume gravitational radiation is the only acting mechanism for angular momentum loss and the secondary has not evolved on this timescale, the orbital period will decrease until the Roche lobe comes into contact with the secondary, initiating mass transfer and the beginning of the cataclysmic variable (CV) stage. The orbital period at contact, P_c can be calculated using Kepler's law and the fact the ratio of the Roche lobe radius to the orbital separation is constant prior to contact: $P_c = P(a_c/a)^{1.5} = P(R_2/R_{L2})^{1.5}$, where a_c is the orbital separation at the beginning of contact, a is the current orbital separation, $R_2 = 0.152\ R_\odot$ is the radius of the secondary (which is assumed not to change significantly), and $R_{L2} = 0.276\ R_\odot$ is the current Roche lobe of the secondary Eggleton (1983).

The resulting P_c, 0.066 d (1.6 h), will be above the mininum orbital period (1.27 hr) for a cataclysmic variable and below the period gap (Knigge 2006). If any additional mechanisms, such as magnetic braking, have a significant effect (see Sills et al. 2000), the timescale for Roche lobe contact would be reduced.

6.9 Conclusion

The sdB star 2M 1533+3759 is the seventh eclipsing sdB+dM binary discovered to date. Its orbital period of 0.16177042 ± 0.00000001 d is 29% longer than the 0.12505 day period of the next longest eclipsing sdB+dM, BUL−SC16 335. The amplitude of the reflection effect in 2M 1533+3759 is surprisingly strong, only about 0.05 mag weaker than the amplitude observed in HW Vir, in spite of the longer orbital period and the fact that the temperatures of the primary stars are similar.

2M 1533+3759 is the only new sdB binary among the eclipsing systems that were proposed to be sdB+dM by Kelley & Shaw (2007) on the basis of their narrow eclipse widths. This result is consistent with the 2MASS colors of other known reflection-effect sdB+dM systems, all of which have $J - H < 0$. 2M 1533+3759 and the archetypal HW Vir (Menzies & Marang 1986) are the only two binaries in Kelley & Shaw's (2007) Table 6.3 that have similarly blue IR colors, and the only two that contain sdB stars.

Spectroscopic parameters 2M 1533+3759 were derived by fitting Balmer and helium line profiles in high S/N spectra to a grid of zero-metallicity NLTE model atmospheres. The effective temperatures derived from low (9Å) and medium (1.9Å) resolution spectra exhibit clear variations with orbital phase. Phase variations are much less significant for the surface gravities, and completely negligible for the helium abundance fraction. Our adopted parameters for the sdB star, $T_{\rm eff} = 29230 \pm 125\,{\rm K}$, $\log g = 5.58 \pm 0.03$, $\log N({\rm He})/N({\rm H}) = -2.37 \pm 0.05$, were determined from medium resolution spectra taken when the reflection effect was near minimum. The inferred rotational velocity has a negligible affect on the derivation of these parameters.

Light curve modeling with the MORO code produced only one well-fitting solution consistent with a core helium burning primary. The system mass ratio, q (M_2/M_1), is 0.301 ± 0.014 and the inclination angle, i, is $86.6^\circ \pm 0.2^\circ$. The robustness and precision of these numbers are due to the high precision of the light curves and the fact that the system is eclipsing. Radial velocities for the sdB component were used to derive the velocity amplitude, $K_1 = 71.1 \pm 1.0\,{\rm km\,s^{-1}}$, leading to component masses of $M_1 = 0.376 \pm 0.055\ M_\odot$ and $M_2 = 0.113 \pm 0.017\ M_\odot$. The errors in the masses are dominated by the uncertainty in q. Since the mass ratio and inclination are even more uncertain in non-eclipsing systems, our inability to more tightly constrain the primary mass provides a strong illustration for why useful sdB masses from light curve modeling can usually be obtained only from eclipsing binaries.

The orbital separation derived from the masses and the period is $a = 0.98 \pm 0.04\ R_\odot$. The individual radii, $R_1 = 0.166 \pm 0.007\ R_\odot$, $R_2 = 0.152 \pm 0.005\ R_\odot$ were then calculated from the relative radii, R_1/a and R_2/a, determined by the light curve solution. Both radii are consistent with theoretical expectations, and the resulting sdB surface gravity, $\log g = 5.57 \pm 0.07$, is completely consistent with the adopted spectroscopic value above.

We constructed a synthetic line-blanketed spectrum to investigate potential systematic effects caused by our use of zero metallicity NLTE atmospheres to derive the spectroscopic parameters. If 2M 1533+3759 had solar abundances of C, N, O, S, and Fe in its atmosphere, our assumption of zero metals would have overestimated the effective temperature by about 2000 K, and the surface gravity by almost 0.2 dex. Thus, the true $T_{\rm eff}$ and $\log g$ abundances would have been about 27300 K and 5.40, respectively. The modeled light curve solution at this lower temperature is only negligibly different from our original solution, and thus the resulting system parameters remain essentially unchanged. However, in this case, the calculated sdB surface gravity, $\log g = 5.57$, would be much less consistent with the expected value of 5.40. This suggests that the full correction to solar metallicites assumed above is not appropriate for 2M 1533+3759.

An important conclusion is that there is now significant observational evidence, from two completely independent techniques, asteroseismology (PG 0911+456) and modeling of eclipsing/reflection effect light curves (2M 1533+3759 and perhaps HS 2333+3927), for the existence of sdB stars with masses significantly lower than the canonical $0.48 \pm 0.02\ M_\odot$.

2M 1533+3759 must have formed via the first common-envelope channel, since the companion is an M dwarf. With a probable sdB mass in the range $0.32 - 0.43\ M_\odot$, this star is expected to have evolved from a main-sequence A star with an initial mass $> 1.8 - 2.0\ M_\odot$. The existence of such a binary might support recent theoretical predictions that sdB stars can be produced by such massive progenitors, including the assumption that the ionization energy of the red giant envelope contributes to the ejection of the common envelope (Han et al. 2002, 2003). If the primary mass of 2M 1533+3759 could be measured more precisely, or if the separation between the two components could be measured independently, this system ought to provide a very useful observational constraint for the upper limit to the main sequence mass of an sdB progenitor.

If 2M 1533+3759 becomes a cataclysmic variable (CV) after orbital shrinkage due to gravitational radiation brings the Roche lobe into contact with the M dwarf secondary, its orbital period of the CV at the onset of mass transfer will be 1.6 hours, below the CV period gap.

Chapter 7

Outlook

In the study presented here, we have enhanced our understanding in the following areas: (1) observational studies of chemical compositions of field horizontal branch stars, especially throughout the pulsational cycles of Blazhko and non-Blazhko effect RR Lyrae stars; (2) observational study of line profile variation in the dynamical atmosphere of RR Lyrae stars; (3) empirical study of the red and blue edges of the instability strip; and finally (4) observational studies of masses of FHB stars. We were seeking to connect the chemical abundance patterns of various elements as seen in FHB stars with other metal-poor stars in different evolutionary stages. These studies have shown that FHB stars are a useful tool for studying Galactic chemical evolution, Galactic structure and formation, the physics of dynamical atmospheres, and HB morphology.

Thanks to the wealth of photometric and/or spectroscopic data generated by the HK objective-prism survey, ESO-Hamburg survey and Sloan Digital Sky Survey (SDSS), new metal-poor stars, stellar streams and faint dwarf galaxies have been discovered. The science coming out of these surveys has had a significant impacted on the field and advanced our understanding of the formation of the Galactic halo. We should also acknowledge the ESA *Hipparcos* mission, which has revolutionized the field of stellar astronomy.

The future looks bright for Galactic astronomy with the ESA GAIA satellite mission, SkyMapper survey, and HERMES projects. GAIA is due to launch in 2012 and will map all stars brighter than $V > 20$ mag, measure proper motions with errors down to 3 μas, determine precise trigonometric parallaxes and radial velocities, and perform photometry of all observed stars. These data will be used for ancillary science cases of other studies, such as kinematics and precise distance measurements to stellar streams, which cannot be achieved with the current *Hipparcos* data.

SkyMapper is a new telescope that will conduct an all-sky survey to cover the southern sky. It is an anolog to the northern SDSS but will go slightly deeper in magnitude. The key science programs include searching for new ultra-faint dwarf galaxies via overdensity method and extremely metal-poor stars via photometrically derived metallicity as indicator. Blue horizontal branch stars will be used as a primary dynamical tracer to probe the distribution of dark matter in the Galatic halo.

HERMES is a state of the art instrument, which will provide a wide field of view fibre spectrograph to collect millions of high-resolution and high S/N spectra of the Galactic disk and halo stars with $V \leq 14$ mag in the southern hemisphere. The primary science goal is to chemically tag the metal-poor stars in the halo. which will lead to the understanding of ISM enrichment during early stages of galaxy assembly and possible mergers or accretion events. In conjunction with the GAIA mission, the resulting ages from the parallaxes/distances will allow us to determine the Galactic chemical evolution in the disk as a function of time. Subsequently, the results can be compared to theoretical Galactic chemical evolution models.

All of these projects will provide us with a huge amount of data in the future and finally allow us to solve many of the remaining questions about the structure and evolution of our Galaxy.

Bibliography

Adelman, S. J., & Hill, G. 1987, MNRAS, 226, 581

Adelman, S. J., & Philip, A. G. D. 1990, MNRAS, 247, 132

Allard, F., Wesemael, F., Fontaine, G., Bergeron, P., & Lamontagne, R. 1994, AJ, 107, 1565

Allende Prieto, C. 2001, ArXiv Astrophysics e-prints

Allende Prieto, C., García López, R. J., Lambert, D. L., & Gustafsson, B. 1999, ApJ, 527, 879

Alonso, A., Arribas, S., & Martinez-Roger, C. 1994, A&A, 282, 684

—. 1996, A&A, 313, 873

Alonso, A., Arribas, S., & Martínez-Roger, C. 1999, A&AS, 140, 261

Althaus, L. G., Serenelli, A. M., & Benvenuto, O. G. 2001, MNRAS, 323, 471

Altmann, M. & de Boer, K. S. 2000, A&A, 353, 135

Anders, E., & Grevesse, N. 1989, Geochim. Cosmochim. Acta, 53, 197

Andrievsky, S. M., Spite, M., Korotin, S. A., Spite, F., Bonifacio, P., Cayrel, R., Hill, V., & François, P. 2007, A&A, 464, 1081

—. 2008, A&A, 481, 481

Aoki, W., et al. 2005, ApJ, 632, 611

Arlandini, C., Käppeler, F., Wisshak, K., Gallino, R., Lugaro, M., Busso, M., & Straniero, O. 1999, ApJ, 525, 886

Arpigny, C., & Magain, P. 1983, A&A, 127, L7

Asplund, M., Lambert, D. L., Nissen, P. E., Primas, F., & Smith, V. V. 2006, ApJ, 644, 229

Baraffe, I., & Chabrier, G. 1996, ApJL, 461, L51+

Barklem, P. S., & O'Mara, B. J. 1998, MNRAS, 300, 863

Barklem, P. S., et al. 2005, A&A, 439, 129

Baumueller, D., Butler, K., & Gehren, T. 1998, A&A, 338, 637

Baumueller, D., & Gehren, T. 1997, A&A, 325, 1088

Bayless, A. J., & Orosz, J. A. 2006, ApJ, 651, 1155

Beers, T. C., Preston, G. W., & Shectman, S. A. 1988, ApJS, 67, 461

—. 1992, AJ, 103, 1987

Behr, B. B. 2003a, ApJS, 149, 67

—. 2003b, ApJS, 149, 101

Binney, J., & Merrifield, M. 1998, Galactic astronomy (Princeton University Press: Princeton series in astrophysics, p. 110)

Blackwell, D. E., & Shallis, M. J. 1977, MNRAS, 180, 177

Blažko, S. 1907, Astronomische Nachrichten, 175, 325

Brown, T. M., Ferguson, H. C., Davidsen, A. F., & Dorman, B. 1997, ApJ, 482, 685

Burstein, D., & Heiles, C. 1982, AJ, 87, 1165

Busso, M., Gallino, R., & Wasserburg, G. J. 1999, ARA&A, 37, 239

Butler, D. 1975, ApJ, 200, 68

Carney, B. W., & Jones, R. 1983, PASP, 95, 246

Cassisi, S., Castellani, M., Caputo, F., & Castellani, V. 2004, A&A, 426, 641

Castellani, M., & Castellani, V. 1993, ApJ, 407, 649

Castelli, F., Gratton, R. G., & Kurucz, R. L. 1997, A&A, 318, 841

Castor, J. P. 1972, in The Evolution of Population II Stars, ed. A. G. D. Philip, 147–+

Catelan, M. 2004, ApJ, 600, 409

Cayrel, R., et al. 2004, A&A, 416, 1117

Charpinet, S., Fontaine, G., & Brassard, P. 2003, in NATO ASIB Proc. 105: White Dwarfs, ed. D. de Martino, R. Silvotti, J.-E. Solheim, & R. Kalytis, 69–+

Charpinet, S., Fontaine, G., Brassard, P., Billères, M., Green, E. M., & Chayer, P. 2005a, in Astronomical Society of the Pacific Conference Series, Vol. 334, 14th European Workshop on White Dwarfs, ed. D. Koester & S. Moehler, 619–+

Charpinet, S., Fontaine, G., Brassard, P., Chayer, P., Green, E. M., & Randall, S. K. 2007, Communications in Asteroseismology, 150, 241

Charpinet, S., Fontaine, G., Brassard, P., & Dorman, B. 1996, ApJl, 471, L103+

—. 1997, ApJl, 489, L149+

Charpinet, S., Fontaine, G., Brassard, P., Green, E. M., & Chayer, P. 2005b, A&A, 437, 575

Charpinet, S., van Grootel, V., Reese, D., Fontaine, G., Green, E. M., Brassard, P., & Chayer, P. 2008, A&A, 489, 377

Charpinet, S., et al. 2006, A&A, 459, 565

Clementini, G., Carretta, E., Gratton, R., Merighi, R., Mould, J. R., & McCarthy, J. K. 1995, AJ, 110, 2319

Clementini, G., Gratton, R. G., Bragaglia, A., Ripepi, V., Martinez Fiorenzano, A. F., Held, E. V., & Carretta, E. 2005, ApJ, 630, L145

Clementini, G., Merighi, R., Gratton, R., & Carretta, E. 1994, MNRAS, 267, 43

Cohen, J. G., et al. 2004, ApJ, 612, 1107

D'Cruz, N. L., Dorman, B., Rood, R. T., & O'Connell, R. W. 1996, ApJ, 466, 359

de Boer, K. S. 1982, A&AS, 50, 247

de Boer, K. S., Geffert, M., Tucholke, H., & Schmidt, J. H. K. 1997, in ESA Special Publication, Vol. 402, Hipparcos - Venice '97, ed. R. M. Bonnet, E. Høg, P. L. Bernacca, L. Emiliani, A. Blaauw, C. Turon, J. Kovalevsky, L. Lindegren, H. Hassan, M. Bouffard, B. Strim, D. Heger, M. A. C. Perryman, & L. Woltjer, 331–334

de Boer, K. S., Schmidt, J. H., & Heber, U. 1993, in Astronomische Gesellschaft Abstract Series, Vol. 9, Astronomische Gesellschaft Abstract Series, ed. G. Klare, 173–+

Demarque, P., Zinn, R., Lee, Y., & Yi, S. 2000, AJ, 119, 1398

Diaz-Cordoves, J., Claret, A., & Gimenez, A. 1995, A&AS, 110, 329

Dorman, B., Rood, R. T., & O'Connell, R. W. 1993, ApJ, 419, 596

Drechsel, H., Haas, S., Lorenz, R., & Gayler, S. 1995, A&A, 294, 723

Drechsel, H., et al. 2001, A&A, 379, 893

Eggleton, P. P. 1983, ApJ, 268, 368

Ferguson, J. W., Alexander, D. R., Allard, F., Barman, T., Bodnarik, J. G., Hauschildt, P. H., Heffner-Wong, A., & Tamanai, A. 2005, ApJ, 623, 585

Fernley, J., Barnes, T. G., Skillen, I., Hawley, S. L., Hanley, C. J., Evans, D. W., Solano, E., & Garrido, R. 1998, A&A, 330, 515

Fitzpatrick, M. J., & Sneden, C. 1987, in Bulletin of the American Astronomical Society, Vol. 19, Bulletin of the American Astronomical Society, 1129–+

Fleig, J., Rauch, T., Werner, K., & Kruk, J. W. 2008, A&A, 492, 565

Fokin, A. B., & Gillet, D. 1997, A&A, 325, 1013

Fokin, A. B., Gillet, D., & Chadid, M. 1999a, A&A, 344, 930

—. 1999b, A&A, 344, 930

Fontaine, G., Brassard, P., Charpinet, S., Green, E. M., Chayer, P., Billères, M., & Randall, S. K. 2003, ApJ, 597, 518

Fontaine, G., Brassard, P., Charpinet, S., Green, E. M., Chayer, P., Randall, S. K., & van Grootel, V. 2008, in Astronomical Society of the Pacific Conference Series, Vol. 392, Hot Subdwarf Stars and Related Objects, ed. U. Heber, C. S. Jeffery, & R. Napiwotzki, 231–+

For, B.-Q., Edelmann, H., Green, E. M., Drechsel, H., Nesslinger, S., & Fontaine, G. 2008, in Astronomical Society of the Pacific Conference Series, Vol. 392, Astronomical Society of the Pacific Conference Series, ed. U. Heber, C. S. Jeffery, & R. Napiwotzki, 203–+

For, B.-Q., Preston, G. W., & Sneden, C. 2011, ApJS, 194, 38

For, B.-Q., & Sneden, C. 2010, AJ, 140, 1694

François, P., et al. 2007, A&A, 476, 935

Francois, P. 1984, Academie des Science Paris Comptes Rendus Serie B Sciences Physiques, 299, 195

Fulbright, J. P. 2000, AJ, 120, 1841

Fusi Pecci, F., Ferraro, F. R., Bellazzini, M., Djorgovski, S., Piotto, G., & Buonanno, R. 1993, AJ, 105, 1145

Gautschy, A. 1987, Vistas in Astronomy, 30, 197

Geier, S., Karl, C., Edelmann, H., Heber, U., & Napiwotzki, R. 2008, MmSAI, 79, 608

Gillet, D., Burki, G., & Crowe, R. A. 1989, A&A, 225, 445

Gillet, D., & Crowe, R. A. 1988, A&A, 199, 242

Gould, A., & Popowski, P. 1998, ApJ, 508, 844

Gratton, R. G. 1998, MNRAS, 296, 739

Gratton, R. G., Fusi Pecci, F., Carretta, E., Clementini, G., Corsi, C. E., & Lattanzi, M. 1997, ApJ, 491, 749

Gratton, R. G., et al. 2007, A&A, 464, 953

Gray, R. O., & Corbally, C. 2009, Stellar Spectral Classification (Princeton University Press: Princeton), Appendix Tables A.1, A.6, and A.7).)

Green, E. M., Fontaine, G., Hyde, E. A., For, B.-Q., & Chayer, P. 2008, in Astronomical Society of the Pacific Conference Series, Vol. 392, Hot Subdwarf Stars and Related Objects, ed. U. Heber, C. S. Jeffery, & R. Napiwotzki, 75–+

Green, E. M., Liebert, J. W., & Saffer, R. A. 1997, in The Third Conference on Faint Blue Stars, ed. A. G. D. Philip, J. Liebert, R. Saffer, & D. S. Hayes, 417–+

Green, E. M., & Morrison, H. L. 1993, in Astronomical Society of the Pacific Conference Series, Vol. 48, The Globular Cluster-Galaxy Connection, ed. G. H. Smith & J. P. Brodie, 318–+

Green, E. M., et al. 2003, ApJl, 583, L31

—. 2004, Ap&SS, 291, 267

Green, R. F., Schmidt, M., & Liebert, J. 1986, ApJS, 61, 305

Greggio, L., & Renzini, A. 1999, Memorie della Societa Astronomica Italiana, 70, 691

Han, Z., Podsiadlowski, P., Maxted, P. F. L., & Marsh, T. R. 2003, MNRAS, 341, 669

Han, Z., Podsiadlowski, P., Maxted, P. F. L., Marsh, T. R., & Ivanova, N. 2002, MNRAS, 336, 449

Hansen, C. J., et al. 2011, A&A, 527, A65+

Hardorp, J., & Scholz, M. 1967, ZAp, 67, 312

Heber, U. 1986, A&A, 155, 33

—. 2009, ARA&A, 47, 211

Heber, U., et al. 2004, A&A, 420, 251

Heber, U., et al. 2005, in Astronomical Society of the Pacific Conference Series, Vol. 334, 14th European Workshop on White Dwarfs, ed. D. Koester & S. Moehler, 357–+

Hilditch, R. W., Harries, T. J., & Hill, G. 1996, MNRAS, 279, 1380

Hill, V., et al. 2002, A&A, 387

Hosford, A., Ryan, S. G., García Pérez, A. E., Norris, J. E., & Olive, K. A. 2009, A&A, 493, 601

Hoyle, F., & Schwarzschild, M. 1955, ApJS, 2, 1

Hu, H., Nelemans, G., Østensen, R., Aerts, C., Vučković, M., & Groot, P. J. 2007, A&A, 473, 569

Hubrig, S., Castelli, F., de Silva, G., González, J. F., Momany, Y., Netopil, M., & Moehler, S. 2009, A&A, 499, 865

Ibata, R. A., Gilmore, G., & Irwin, M. J. 1994, Nature, 370, 194

Ivezić, Ž., et al. 2004, in Astronomical Society of the Pacific Conference Series, Vol. 327, Satellites and Tidal Streams, ed. F. Prada, D. Martinez Delgado, & T. J. Mahoney, 104–+

Johnson, C. I., Kraft, R. P., Pilachowski, C. A., Sneden, C., Ivans, I. I., & Benman, G. 2005, PASP, 117, 1308

Jurcsik, J., & Kovacs, G. 1996, A&A, 312, 111

Kelley, N., & Shaw, J. S. 2007, Journal of the Southeastern Association for Research in Astronomy, 1, 13

Khalack, V. R., Leblanc, F., Behr, B. B., Wade, G. A., & Bohlender, D. 2008, A&A, 477, 641

Khalack, V. R., Leblanc, F., Bohlender, D., Wade, G. A., & Behr, B. B. 2007, A&A, 466, 667

Kilkenny, D., Koen, C., O'Donoghue, D., & Stobie, R. S. 1997, MNRAS, 285, 640

Kilkenny, D., O'Donoghue, D., Koen, C., Lynas-Gray, A. E., & van Wyk, F. 1998, MNRAS, 296, 329

Knigge, C. 2006, MNRAS, 373, 484

Koen, C. 2007, MNRAS, 377, 1275

Kolenberg, K., Fossati, L., Shulyak, D., Pikall, H., Barnes, T. G., Kochukhov, O., & Tsymbal, V. 2010, A&A, 519, A64+

Kovács, G., Zucker, S., & Mazeh, T. 2002, A&A, 391, 369

Kurucz, R. L. 1979, ApJS, 40, 1

Kwee, K. K., & van Woerden, H. 1956, Bull. Astron. Inst. Netherlands, 12, 327

Lai, D. K., Bolte, M., Johnson, J. A., Lucatello, S., Heger, A., & Woosley, S. E. 2008, ApJ, 681, 1524

Lambert, D. L., Heath, J. E., Lemke, M., & Drake, J. 1996, ApJS, 103, 183

Landsman, W., Bohlin, R. C., Neff, S. G., O'Connell, R. W., Roberts, M. S., Smith, A. M., & Stecher, T. P. 1998, AJ, 116, 789

Layden, A. C. 1994, AJ, 108, 1016

Lee, J. W., Kim, S.-L., Kim, C.-H., Koch, R. H., Lee, C.-U., Kim, H.-I., & Park, J.-H. 2009, AJ, 137, 3181

Lee, Y., & Demarque, P. 1990, ApJS, 73, 709

Lee, Y., Demarque, P., & Zinn, R. 1994, ApJ, 423, 248

Lisker, T., Heber, U., Napiwotzki, R., Christlieb, N., Han, Z., Homeier, D., & Reimers, D. 2005, A&A, 430, 223

Liu, T., & Janes, K. A. 1989, ApJS, 69, 593

—. 1990, ApJ, 354, 273

Lodders, K. 2003, ApJ, 591, 1220

Lucy, L. B. 1967, Zeitschrift fur Astrophysik, 65, 89

Majewski, S. R., Skrutskie, M. F., Weinberg, M. D., & Ostheimer, J. C. 2003, ApJ, 599, 1082

Manduca, A. 1981, ApJ, 245, 258

Maxted, P. f. L., Heber, U., Marsh, T. R., & North, R. C. 2001, MNRAS, 326, 1391

Maxted, P. F. L., Marsh, T. R., Heber, U., Morales-Rueda, L., North, R. C., & Lawson, W. A. 2002, MNRAS, 333, 231

Maxted, P. F. L., Morales-Rueda, L., & Marsh, T. R. 2004, Ap&SS, 291, 307

McWilliam, A. 1998, AJ, 115, 1640

McWilliam, A., Preston, G. W., Sneden, C., & Searle, L. 1995, AJ, 109, 2757

Meibom, S., et al. 2009, AJ, 137, 5086

Meléndez, J., Shchukina, N. G., & Vasiljeva, I. E. a nd Ramírez, I. 2006, ApJ, 642, 1082

Mengel, J. G., Norris, J., & Gross, P. G. 1976, ApJ, 204, 488

Menzies, J. W., & Marang, F. 1986, in IAU Symposium, Vol. 118, Instrumentation and Research Programmes for Small Telescopes, ed. J. B. Hearnshaw & P. L. Cottrell, 305–+

Möhler, S. 2004, in IAU Symposium, Vol. 224, The A-Star Puzzle, ed. J. Zverko, J. Ziznovsky, S. J. Adelman, & W. W. Weiss, 395–402

Moni Bidin, C., Catelan, M., Villanova, S., Piotto, G., Altmann, M., Momany, Y., & Moehler, S. 2008, in Astronomical Society of the Pacific Conference Series, Vol. 392, Hot Subdwarf Stars and Related Objects, ed. U. Heber, C. S. Jeffery, & R. Napiwotzki, 27–+

Morales-Rueda, L., Maxted, P. F. L., Marsh, T. R., North, R. C., & Heber, U. 2003, MNRAS, 338, 752

Nilsson, H., Ljung, G., Lundberg, H., & Nielsen, K. E. 2006, A&A, 445, 1165

Nissen, P. E., Akerman, C., Asplund, M., Fabbian, D., Kerber, F., Kaufl, H. U., & Pettini, M. 2007, A&A, 469, 319

Østensen, R. H., Oreiro, R., Hu, H., Drechsel, H., & Heber, U. 2008, in Astronomical Society of the Pacific Conference Series, Vol. 392, Astronomical Society of the Pacific Conference Series, ed. U. Heber, C. S. Jeffery, & R. Napiwotzki, 221–+

Paczynski, B. 1980, Acta Astronomica, 30, 113

Perryman, M. A. C., et al. 1997, A&A, 323, L49

Peterson, R. C. 1983, ApJ, 275, 737

Peterson, R. C., Rood, R. T., & Crocker, D. A. 1995, ApJ, 453, 214

Pietrinferni, A., Cassisi, S., Salaris, M., & Castelli, F. 2006, ApJ, 642, 797

Pilachowski, C. A., Sneden, C., & Kraft, R. P. 1996, AJ, 111, 1689

Podsiadlowski, P., Han, Z., Lynas-Gray, A. E., & Brown, D. 2008, in Astronomical Society of the Pacific Conference Series, Vol. 392, Hot Subdwarf Stars and Related Objects, ed. U. Heber, C. S. Jeffery, & R. Napiwotzki, 15–+

Pojmanski, G. 2002, Acta Astronomica, 52, 397

Politano, M., Taam, R. E., van der Sluys, M., & Willems, B. 2008, ApJL, 687, L99

Polubek, G., Pigulski, A., Baran, A., & Udalski, A. 2007, in Astronomical Society of the Pacific Conference Series, Vol. 372, 15th European Workshop on White Dwarfs, ed. R. Napiwotzki & M. R. Burleigh, 487–+

Preston, G. W. 1959, ApJ, 130, 507

—. 1961, ApJ, 134, 633

—. 2009, A&A, 507, 1621

—. 2011, AJ, 141, 6

Preston, G. W., Shectman, S. A., & Beers, T. C. 1991, ApJS, 76, 1001

Preston, G. W., & Sneden, C. 2000a, AJ, 120, 1014

—. 2000b, AJ, 120, 1014

Preston, G. W., Sneden, C., Thompson, I. B., Shectman, S. A., & Burley, G. S. 2006a, AJ, 132, 85

Preston, G. W., Thompson, I. B., Sneden, C., Stachowski, G., & Shectman, S. A. 2006b, AJ, 132, 1714

Prochaska, J. X., & McWilliam, A. 2000, ApJ, 537, L57

Ramírez, I., & Meléndez, J. 2005a, ApJ, 626, 446

—. 2005b, ApJ, 626, 465

Randall, S. K., Fontaine, G., Charpinet, S., Lynas-Gray, A. E., Lopes, I. P., O'Toole, S. J., & Brassard, P. 2006, ApJ, 648, 637

Randall, S. K., van Grootel, V., Fontaine, G., Charpinet, S., & Brassard, P. 2009, A&A, 507, 911

Randall, S. K., et al. 2007, A&A, 476, 1317

Reddy, B. E., Tomkin, J., Lambert, D. L., & Allende Prieto, C. 2003, MNRAS, 340, 304

Reed, B. C. 1998, JRASC, 92, 36

Reimers, D., & Wisotzki, L. 1997, The Messenger, 88, 14

Rood, R. T., & Seitzer, P. O. 1981, in IAU Colloq. 68: Astrophysical Parameters for Globular Clusters, ed. A. G. D. Philip & D. S. Hayes, 369–+

Rosenberg, A., Aparicio, A., Saviane, I., & Piotto, G. 2000, A&AS, 145, 451

Rosswog, S., Liebendörfer, M., Thielemann, F., Davies, M. B., Benz, W., & Piran, T. 1999, A&A, 341, 499

Rucinski, S. M. 2009, MNRAS, 395, 2299

Ryan, S. G., Norris, J. E., & Beers, T. C. 1996, ApJ, 471, 254

Saffer, R. A., Bergeron, P., Koester, D., & Liebert, J. 1994, ApJ, 432, 351

Saffer, R. A., Green, E. M., & Bowers, T. 2001, in Astronomical Society of the Pacific Conference Series, Vol. 226, 12th European Workshop on White Dwarfs, ed. J. L. Provencal, H. L. Shipman, J. MacDonald, & S. Goodchild, 408–+

Sandage, A. 1990, ApJ, 350, 603

Sandage, A., & Wallerstein, G. 1960, ApJ, 131, 598

Sandquist, E. L., Taam, R. E., & Burkert, A. 2000, ApJ, 533, 984

Sarajedini, A., Barker, M. K., Geisler, D., Harding, P., & Schommer, R. 2006, AJ, 132, 1361

Scargle, J. D. 1982, ApJ, 263, 835

Schlegel, D. J., Finkbeiner, D. P., & Davis, M. 1998, ApJ, 500, 525

Searle, L., & Zinn, R. 1978, ApJ, 225, 357

Shi, J. R., Gehren, T., Mashonkina, L., & Zhao, G. 2009, A&A, 503, 533

Sills, A., Pinsonneault, M. H., & Terndrup, D. M. 2000, ApJ, 534, 335

Simmerer, J., Sneden, C., Cowan, J. J., Collier, J., Woolf, V. M., & Lawler, J. E. 2004, ApJ, 617, 1091

Simon, G. W. 1966, AJ, 71, 190

Skrutskie, M. F., et al. 2006, AJ, 131, 1163

Smith, H. A., & Butler, D. 1978, PASP, 90, 671

Sneden, C., Cowan, J. J., & Gallino, R. 2008, ARA&A, 46, 241

Sneden, C., Gratton, R. G., & Crocker, D. A. 1991, A&A, 246, 354

Sneden, C., & Lawler, J. E. 2008, in American Institute of Physics Conference Series, Vol. 990, First Stars III, ed. B. W. O'Shea & A. Heger, 90–103

Sneden, C., et al. 2003, ApJ, 591, 936

Sneden, C. A. 1973, PhD thesis, THE UNIVERSITY OF TEXAS AT AUSTIN.

Sobeck, J. S., Ivans, I. I., Simmerer, J. A., Sneden, C., Hoeflich, P., Fulbright, J. P., & Kraft, R. P. 2006, AJ, 131, 2949

Sobeck, J. S., Lawler, J. E., & Sneden, C. 2007, ApJ, 667, 1267

Sobeck, J. S., et al. 2011, ArXiv e-prints

Stephens, A., & Boesgaard, A. M. 2002, AJ, 123, 1647

Stothers, R. B. 2006, ApJ, 652, 643

—. 2010, PASP, 122, 536

Sweigart, A. V. 1987, ApJS, 65, 95

—. 1997, ApJ, 474, L23+

Sweigart, A. V., Greggio, L., & Renzini, A. 1989, ApJS, 69, 911

Szczygieł, D. M., & Fabrycky, D. C. 2007, MNRAS, 377, 1263

Thévenin, F., & Idiart, T. P. 1999, ApJ, 521, 753

Timmes, F. X., Woosley, S. E., & Weaver, T. A. 1995, ApJS, 98, 617

Valcarce, A. A. R., & Catelan, M. 2008, A&A, 487, 185

van Grootel, V., Charpinet, S., Fontaine, G., & Brassard, P. 2008a, A&A, 483, 875

van Grootel, V., Charpinet, S., Fontaine, G., Brassard, P., Green, E. M., Chayer, P., & Randall, S. K. 2008b, A&A, 488, 685

van Spaandonk, L., Fontaine, G., Brassard, P., & Aerts, C. 2008, Communications in Asteroseismology, 156, 35

Venn, K. A., Irwin, M., Shetrone, M. D., Tout, C. A., Hill, V., & Tolstoy, E. 2004, AJ, 128, 1177

Vivas, A. K., et al. 2004, AJ, 127, 1158

von Zeipel, H. 1924, MNRAS, 84, 665

Vučković, M., Aerts, C., Östensen, R., Nelemans, G., Hu, H., Jeffery, C. S., Dhillon, V. S., & Marsh, T. R. 2007, A&A, 471, 605

Vučković, M., Østensen, R., Bloemen, S., Decoster, I., & Aerts, C. 2008, in Astronomical Society of the Pacific Conference Series, Vol. 392, Hot Subdwarf Stars and Related Objects, ed. U. Heber, C. S. Jeffery, & R. Napiwotzki, 199–+

Wade, R. A., & Rucinski, S. M. 1985, A&AS, 60, 471

Wallerstein, G., & Huang, W. 2010, Mem. Soc. Astron. Italiana, 81, 952

Wallerstein, G. qnd Greenstein, J. L., Parker, R., Helfer, H. L., & Aller, L. H. 1963, ApJ, 137, 280

Wilhelm, R., Beers, T. C., & Gray, R. O. 1999, AJ, 117, 2308

Wilhelm, R., Beers, T. C., Kriessler, J. R., Pier, J. R., Sommer-Larsen, J., & Layden, A. C. 1996, in Astronomical Society of the Pacific Conference Series, Vol. 92, Formation of the Galactic Halo...Inside and Out, ed. H. L. Morrison & A. Sarajedini, 171–+

Wils, P., di Scala, G., & Otero, S. A. 2007, Information Bulletin on Variable Stars, 5800, 1

Wilson, R. E., & Devinney, E. J. 1971, ApJ, 166, 605

Wood, J. H., & Saffer, R. 1999, MNRAS, 305, 820

Wood, J. H., Zhang, E.-H., & Robinson, E. L. 1993, MNRAS, 261, 103

Woolf, V. M., Tomkin, J., & Lambert, D. L. 1995, ApJ, 453, 660

Woosley, S. E., & Weaver, T. A. 1995, ApJS, 101, 181

Wozniak, P. R., et al. 2004, VizieR Online Data Catalog, 2287, 0

Yi, S., Demarque, P., & Oemler, A. J. 1997, ApJ, 486, 201

Yi, S., Lee, Y.-W., Woo, J.-H., Park, J.-H., Demarque, P., & Oemler, A. J. 1999, ApJ, 513, 128

York, D. G., et al. 2000, AJ, 120, 1579

Zahn, J.-P. 1977, A&A, 57, 383

Vita

Bi-Qing For grew up in Ulu Tiram, Johor, Malaysia. After graduating from Foon Yew High School in Malaysia in December 2000, she left her home country in June 2001 to pursue her study at the University of Arizona, Tucson. She was selected as a Starr Scholar with the Starr Foundation in New York awarding her 3 years of scholarship toward her undergraduate study. She received a B.S. in Physics and Astronomy in 2005 and began graduate school at the Astronomy Department of the University of Texas, Austin, in August 2006.

In her spare time, Bi-Qing enjoys going camping and hiking. She also does photography and enjoys various sports.

Permanent address: Department of Astronomy,
1 University Station, C 1400,
Austin, Texas 78712
USA

This dissertation was typeset with LaTeX[†] by the author.

[†] LaTeX is a document preparation system developed by Leslie Lamport as a special version of Donald Knuth's TeX Program.